

Decoherence in microscopic two-level systems
and
in analog quantum simulators

Zur Erlangung des akademischen Grades eines

DOKTORS DER NATURWISSENSCHAFTEN

von der Fakultät für Physik des Karlsruher Instituts für Technologie
Karlsruhe

genehmigte

DISSERTATION

von

Dipl. Phys. Sebastian Zanker
aus Ludwigsburg

Tag der mündlichen Prüfung: 14.07.2017

Referent: Prof. Dr. G. Schön

Korreferent: Prof. Dr. Frank Wilhelm-Mauch

1 Preface

The many-body system of interacting electrons is one of the most important and versatile quantum mechanical systems. Electronic structure calculations of atoms, molecules and solids allow us to understand and to predict phenomena vital to physics, chemistry, material science but also to life sciences. Unfortunately, a straightforward solution of the full Schrödinger equation is a numerically hard problem. The fundamental issue is the dimensionality of the Hilbert space of an interacting quantum system which grows exponentially with its size. Thus, the numerical solution of the full Schrödinger equation becomes unfeasible on conventional classical computers even for systems of moderate size [1].

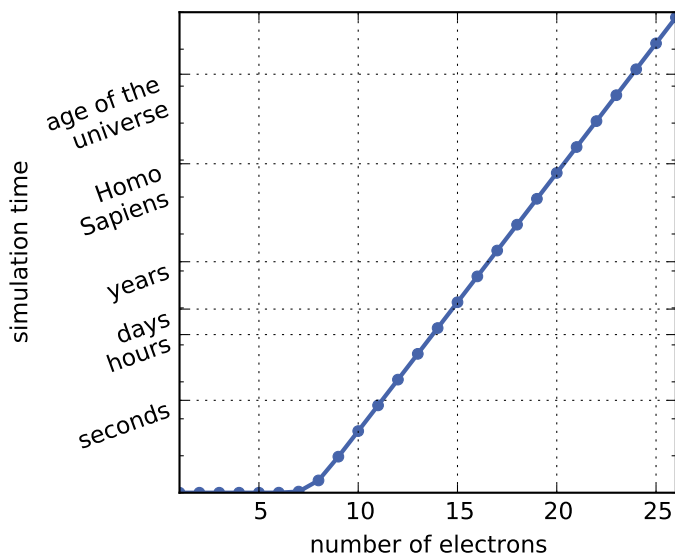


Figure 1: Estimate of the time required for numerically exact calculations of molecules containing N electrons on the Hermit supercomputer in Stuttgart with ~ 3.8 petaFLOPS.

The exponential growth of the Hilbert space and entanglement are inherent properties of all quantum mechanical systems. Consequently, except for a few exceptions quantum mechanical systems are hard to solve on conventional classical computers. Even on high-performance classical computers exact calculations are only feasible for systems comprising about fifteen electrons [2]. For systems with more electrons the time and memory required to exactly diagonalize the interacting-electron Hamiltonian increases extremely fast as depicted in Fig. 1. Thus, various phenomena such as high- T_c superconductivity [3] or properties of transition-metals [4] that are dominated by correlation effects are beyond the scope of simulation on classical computers.

In 1982 Richard Feynman proposed to utilize the inherent properties of quantum mechanical systems, that is, the exponential growth of the Hilbert space and entangle-

ment, in order to perform quantum simulations [5]. The idea is to use a well-controlled quantum system designed such that it mimics another quantum mechanical system. Measurements on this well-controlled system reveal properties of the physical system of interest [6–8]. Such a device is called a quantum simulator. For specific problems this approach promises an exponential speedup as compared to numerical calculations on classical computers [9, 10]. Among these specific problems are electronic structure calculations in quantum chemistry [11, 12], and systems of strongly correlated electrons [13–15]. Even some problems of information sciences such as search algorithms can profit from quantum simulation [16, 17].

While a quantum simulator was a purely theoretical concept at the time of Feynman’s suggestion a lot of progress has been achieved since the first proposal of a practical algorithm by Shor in 1997 [18]. Since that time quantum simulators have been realized using different physical systems such as cold gases [19, 20], trapped ions [21], photons [22], or superconducting circuits [13, 23–26]. Over the last years many fascinating proof-of-principle experiments demonstrating elementary quantum simulations have been performed. Ultracold atoms have been used to simulate Mott-insulator transitions in the Hubbard model [27] and the crossover from the superconducting BCS state to a Bose-Einstein condensate of Cooper pairs in a cold Fermi liquid [20]. Fig. 2a shows experimental data for the BCS-BEC crossover obtained with ^6Li atoms [28]. Quantum simulations of quantum magnets, i.e. interacting spins, and relativistic particles in 1+1 dimension have been realized using trapped ions [21] or cold atoms [29]. The hydrogen molecule and quantum stochastic walks have been simulated using photons [22], see also Fig. 2b, while small systems of interacting fermions and interacting spins have been realized by Barends et al. on superconducting circuits [13, 31]. This list of experiments is only a small excerpt of all the exciting progress that has already been achieved in the field of quantum simulation.

Despite all that success quantum supremacy, that is, superiority of a quantum simulation over a conventional simulation, has not yet been demonstrated. In an experimental setting quantum simulators are prone to imperfections such as noise emanating from interactions with the laboratory environment or imprecise fabrication processes [32]. Imprecise fabrication and quasi-static sources of noise induce long-time fluctuations of system parameters changing the effective Hamiltonian of the quantum simulator while coupling to dynamical noise disturbs phase coherence and eventually leads to errors in simulations performed by the quantum simulator. Hence, disorder and decoherence are among the major challenges on the way to quantum simulators that are able to simulate systems of academically relevant size.

Due to these imperfections a real-world quantum simulator does not simulate the desired quantum system but some disturbed system influenced by the environment.

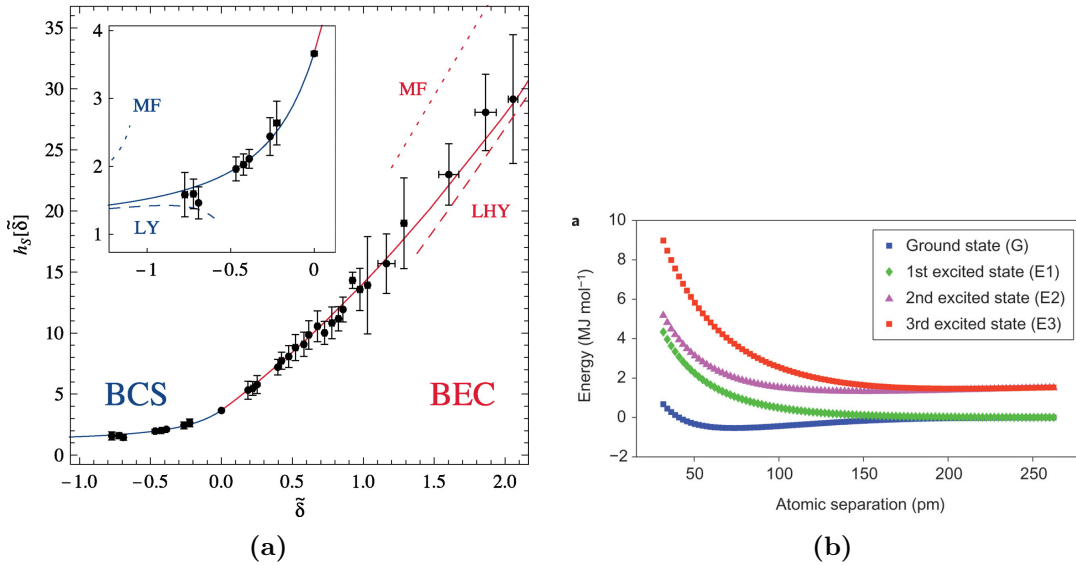


Figure 2: (a) Simulation of the BCS-BCE crossover in a cold Fermi liquid using ultracold ${}^6\text{Li}$ atoms. The graph shows the pressure of the system normalized to the ideal pressure, $2h = P/P_0$ as a function of the dimensionless interaction $1/k_F a$. Here, a is the s-wave scattering length. Dashed (dotted) lines are mean-field (LHY) theory. Reprint with permission from [28], © 2010 AAAS. (b) H_2 energy calculated on a photonic chip. Energies are calculated with a phase estimation algorithm. Reprint with permission from [30], © 2010 Nature Publishing Group.

This raises questions on the reliability of quantum simulations. Different ideas on how to validate results obtained from quantum simulators exist such as cross-validation using different physical realizations or numerical validation in parameter regimes solvable on conventional computers [32]. Another idea is to connect the disturbed result to the ideal result using theoretical system-bath approaches in order to make statements about the validity of a quantum simulation [VI].

In chapter 2 of this thesis we analyze the influence of decoherence and disorder on quantum simulators and discuss the questions formulated above. This part of the thesis led to the publication [V] and is closely related to the publications [VI, VII].

Superconducting quantum bits (qubits) based on the non-linear behavior of Josephson junctions are among the most promising candidates to building scalable quantum simulators [24]. Well-established microelectronics can be used to control, measure and couple superconducting qubits. Additionally, superconducting qubits can be produced using standard microelectronic fabrication processes. Qubits are quantum-mechanical two-level systems that form the basic building block of any quantum simulator. Superconducting quantum circuits at the fault-tolerance threshold for surface code error correction have been demonstrated by Barends et al. [33]. Companies with strong interest in cutting-edge research such as IBM or Google invest in the development of

superconducting qubits strongly pushing the progress in the field. Starting in 2017 IBM has provided public access to a chip comprising sixteen superconducting qubits which can be used by academic groups.

A major source of decoherence in superconducting qubits stems from defects in amorphous materials such as dielectric substrates, disordered interfaces, oxide surfaces, or tunneling barriers of Josephson junctions [34]. These defects lead to low-energy excitations that can be described as quantum mechanical two-level systems. The phenomenological two-level system (TLS) model was originally introduced by Phillips [35] and Anderson et al. [36] to explain “anomalous” properties of glasses at temperatures below approximately 1 K.

In superconducting qubits ensembles of low-energy two-level systems are a source of the omnipresent $1/f$ -noise limiting the performance of many devices while slowly fluctuating thermal two-level systems, so-called two-level fluctuators, induce long-time parameter shifts. Dielectric loss in amorphous materials can be accounted for by energy transfer from the electromagnetic field to the ensemble of two-level systems [37]. Although much effort has been put into understanding the microscopic origin and properties of two-level systems their nature remains unclear at present. Some possible explanations are single atoms or small groups of atoms tunneling between two energetically similar configurations [38], dangling bonds, hydrogen defects [39], or trapped electrons [40].

While in the past experiments were limited to measurements on large ensembles of two-level systems recent experiments by Lisenfeld et al. using superconducting qubits demonstrate the coherent control of single two-level systems [41]. This provides a new experimental tool to probe microscopic properties of individual two-level systems. For example, strain dependent spectroscopy on individual two-level systems yields the deformation potential of two-level systems [42] while strain-dependent measurements of spin-echo and Ramsey dephasing reveal an extraordinarily strong effect of spin-echo refocusing [III].

Another experiment by Lisenfeld et al. demonstrated a surprisingly strong temperature dependence of relaxation and dephasing rates of two-level system [43]. Scattering with quasiparticles of the superconducting material might explain these findings. In metallic glasses scattering of conduction electrons leads to strong relaxation of two-level systems [44]. In the ground state of a superconducting material, however, electrons are bound in Cooper pairs and do not participate in such scattering processes. Breaking of a Cooper pair and excitation of quasiparticles costs an energy of twice the superconducting gap. At temperatures well below the critical temperature of the superconductor the number of equilibrium quasiparticles is exponentially suppressed. With increasing temperature the amount of quasiparticles participating in scattering processes drastically increases. Hence, coupling to quasiparticles might explain the

strong temperature dependence of the relaxation rate. Additionally, from the decoherence of superconducting qubits it is understood that even at low temperatures a finite amount of excess or non-equilibrium quasiparticles remains in a superconducting device. In a follow-up experiment A. Bilmes explicitly analyzed the influence of quasiparticles on decoherence rates of two-level systems [IV].

In chapter 4 of this thesis we analyze decoherence of two-level systems in the amorphous layer of a Josephson junction. We develop a detailed theory of the interaction between two-level systems and quasiparticle excitations of the aluminum superconductor. In the frame of this theory we explain the results in the experiment by A. Bilmes [IV]. Additionally, we discuss decoherence of two-level systems due to different sources of noise in order to explain the findings in [III]. The results presented in this chapter led to the publications [I, II, III, IV] of the publication list.

List of publications

- I. [Zanker](#), S. & Marthaler, M. Qubit dephasing due to quasiparticle tunneling. *Phys. Rev. B* **91**, 174504 (2015) (cit. on pp. vii, 83, 93, 94, 110, 119, 127, 142, 143).
- II. [Zanker](#), S., Marthaler, M. & Schön, G. Decoherence and Decay of Two-Level Systems Due to Nonequilibrium Quasiparticles. *IEEE Transactions on Applied Superconductivity* **26**, 1–4 (2016) (cit. on pp. vii, 93, 94, 143).
- III. Lisenfeld, J., Bilmes, A., Matityahu, S., [Zanker](#), S., Marthaler, M., Schechter, M., Schön, G., Shnirman, A., Weiss, G. & Ustinov, A. V. Decoherence spectroscopy with individual two-level tunneling defects. *Scientific Reports* **6**, 23786 (2016) (cit. on pp. vi, vii, 77, 82, 83, 87, 88, 90–92, 128, 129, 140, 142–144).
- IV. Bilmes, A., [Zanker](#), S., Heimes, A., Marthaler, M., Schön, G., Weiss, G., Ustinov, A. V. & Lisenfeld, J. Electronic decoherence of two-level systems in a Josephson junction. *Phys. Rev. B* **96**, 064504 (2017) (cit. on pp. vii, 82, 83, 87–89, 93, 94, 101, 103, 105, 115, 117, 118, 127, 142, 143).
- V. [Zanker](#), S., Schwenk, I., Reiner, J.-M., Leppäkangas, J. & Marthaler, M. Analyzing the spectral density of a perturbed analog quantum simulator using Keldysh formalism. *ArXiv e-prints*. arXiv: 1705.02325 [quant-ph] (2017) (cit. on pp. v, 22).
- VI. Schwenk, I., [Zanker](#), S., Reiner, J.-M., Leppäkangas, J. & Marthaler, M. Estimating the error of an analog quantum simulator by additional measurements. *ArXiv e-prints*. arXiv: 1612.03767 (2016) (cit. on pp. v, 22, 145).
- VII. Schwenk, I., Reiner, J.-M., [Zanker](#), S., Tian, L., Leppäkangas, J. & Marthaler, M. Reconstructing the ideal results of a perturbed analog quantum simulator. *ArXiv e-prints*. arXiv: 1701.02683 [quant-ph] (2017) (cit. on pp. v, 22, 145).

Contents

1	Preface	iii
I	Application of many-body non-equilibrium methods to analog quantum simulators	1
1	Theoretical background I: Non-equilibrium theory	3
1.1	Time dependent expectation values	4
1.2	Non-equilibrium Green's functions	6
1.3	Perturbation theory	7
1.3.1	Dyson equation	7
1.3.2	Contour diagrammatics	8
1.4	Continuation to real times	11
1.4.1	Kadanoff-Baym equations	13
1.5	From Keldysh to master equation	16
2	Analyzing a perturbed quantum simulator using many-body theory	21
2.1	Introduction	21
2.2	Motivation of the idea	23
2.3	Decoherence in a quantum simulator - general discussion	24
2.3.1	Wick's theorem and spin operators	25
2.3.2	Mapping qubits onto fermions - the Jordan-Wigner transformation	26
2.3.3	Dephasing	28
2.3.4	Relaxation	29
2.3.5	Disorder	29
2.3.6	Summary	31
2.4	Model	31
2.5	Dephasing due to a bosonic bath	33
2.5.1	Dephasing rate-function from a diagrammatic expansion	34
2.5.2	Analysis for environments characterized by a power-law spectral density	38
2.5.3	Comparison with master equation	43
2.5.4	Effect of decoherence in large systems	46

2.6	Relaxation due to an ensemble of TLS	49
2.6.1	Adiabatic approach	51
2.6.2	Time dependence	53
2.6.3	Comparison with master equation	56
2.7	Disorder	57
2.7.1	Disorder in on-site energies and transversal qubit couplings . .	58
2.7.2	Outlook I: Disorder in the interaction	63
2.8	Outlook II: Decoherence in interacting systems	65
II	Decoherence of microscopic two-level systems	69
3	Theoretical background II: Dynamics of two-level systems	71
3.1	Isolated TLS	71
3.1.1	TLS coupled to the environment - decoherence	72
3.2	Dephasing and refocusing techniques	75
4	Decoherence of Two-Level Systems	81
4.1	Introduction	81
4.2	Microscopic TLS - the standard tunneling model	83
4.2.1	Artificial TLS - Current biased Phase Qubit	86
4.2.2	Experiments with TLS	87
4.3	Decoherence Due to Quasiparticles	93
4.3.1	Model	94
4.3.2	Quasiparticle dynamics	97
4.3.3	Quasiparticle spectral density	108
4.3.4	Direction Averaged Interaction	111
4.3.5	TLS relaxation due to quasiparticles	114
4.3.6	Dephasing: Ramsey and spin-echo protocol	118
4.3.7	Rabi Decay Rates	125
4.3.8	Decoherence of superconducting qubits due to quasiparticles . .	127
4.4	Decoherence due to different sources of noise	128
4.4.1	Decoherence due to acoustic phonons	130
4.4.2	Decoherence due to TLS	132
4.4.3	Quasiparticle induced decoherence	140
5	Conclusion	141

Part I

Application of many-body non-equilibrium methods to analog quantum simulators

1 Chapter 1

Theoretical background I: Non-equilibrium theory

During an experiment a quantum simulator usually is far away from equilibrium: time-dependent driving, ramping of qubit-qubit couplings, but also the influence of the environment drive the quantum simulator out of equilibrium. Consequently, we are concerned with time-dependent averages of systems away from equilibrium when theoretically describing quantum simulators.

Quantum systems out of equilibrium are conveniently described in terms of an oriented time-contour instead of the physical time evolving along the real axes. In many-body physics Green's functions defined on such a contour are routinely applied to describe non-equilibrium phenomena such as transport [45].

In this work, we apply non-equilibrium many-body methods to describe large quantum simulators in contact with the environment. Hence, we give a short introduction into the contour formalism and the non-equilibrium Green's function formalism in this chapter following the introductory textbook on non-equilibrium many body theory by Stefanucci and van Leeuwen [46] and the classic introduction by Rammer and Smith [45]. We employ the formalism presented here to analyze analog quantum simulators in chapter 2.

Master equation methods are the state-of-the-art tool used to simulate open quantum systems. In particular they are usually used in order to analyze effects of the environment on qubit systems. However, master equation calculations become numerically demanding for larger systems. In the last part of the present chapter, we show the connection between quantum master equations and the contour formalism.

If not stated otherwise we use $\hbar = 1$ throughout the thesis.

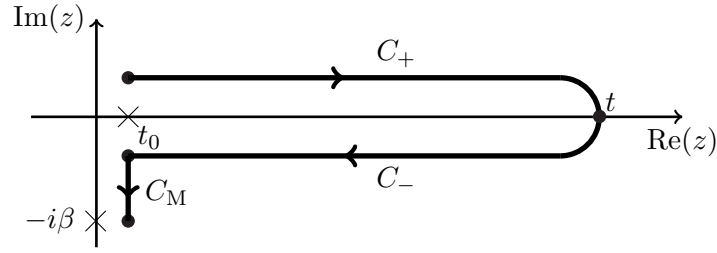


Figure 1.1: Full contour $C = C_+ \oplus C_- \oplus C_M$ for interacting initial states.

1.1 Time dependent expectation values

A quantum simulator returns time dependent expectation values of observables $\langle \hat{A}_{\mathcal{H}}(t) \rangle$. Here, $\hat{A}_{\mathcal{H}}(t) = \hat{U}_{\mathcal{H}}(t_0, t) \hat{A}(t) \hat{U}_{\mathcal{H}}(t, t_0)$ is the operator in the Heisenberg picture and $\hat{U}_{\mathcal{H}}(t, t')$ is the time evolution operator from t' to t . For a system initially prepared in a state described by the density matrix $\rho(t_0)$ the expectation value of an observable \hat{A} is given by

$$A(t) = \langle \hat{A}_{\mathcal{H}}(t) \rangle = \text{Tr}\{\rho(t_0) \hat{U}_{\mathcal{H}}(t_0, t) \hat{A}(t) \hat{U}_{\mathcal{H}}(t, t_0)\}, \quad (1.1)$$

The most general form of the initial density matrix can be written resulting from a time evolution along the imaginary time axis with a preparation Hamiltonian \mathcal{H}^M [46]

$$\rho(t_0) = \frac{1}{Z} e^{-\beta \mathcal{H}^M} = \frac{1}{Z} \mathcal{T} \exp \left\{ -i \int_{t_0}^{t_0 - i\beta} dt' \mathcal{H}^M(t') \right\} = \frac{\hat{U}_{\mathcal{H}^M}(t_0 - i\beta, t_0)}{\text{Tr}\{\hat{U}_{\mathcal{H}^M}(t_0 - i\beta, t_0)\}}. \quad (1.2)$$

In this expression \mathcal{H}^M is chosen in such a way that $\rho(t_0)$ correctly represents the initial state, $\rho(t_0) = |\psi(t_0)\rangle\langle\psi(t_0)|$. For a system initially in equilibrium the relation $\mathcal{H}^M = \mathcal{H} - \mu \hat{N}$ holds while for a general initial state the preparation Hamiltonian \mathcal{H}^M is not related to the Hamiltonian \mathcal{H} of the system. The expectation value Eq. (1.1) takes the form

$$A(t) = \frac{\text{Tr}\{\hat{U}_{\mathcal{H}^M}(t_0 - i\beta, t_0) \hat{U}_{\mathcal{H}}(t_0, t) \hat{A}(t) \hat{U}_{\mathcal{H}}(t, t_0)\}}{\text{Tr}\{\hat{U}_{\mathcal{H}^M}(t_0 - i\beta, t_0)\}}, \quad (1.3)$$

Reading this expression from right to left corresponds to a forward time evolution from t_0 to t followed by the action of \hat{A} and a subsequent backward evolution to the initial time and a final evolution along the imaginary axis. We can combine the different steps of the time evolution into a single time evolution along the oriented contour in the complex time plane depicted in Fig. 1.1. Denoting time variables on the contour with z and reserving the letter t for real times we define the contour time evolution

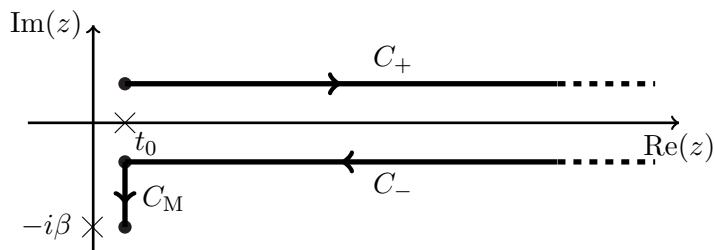


Figure 1.2: Full contour $C = C_+ \oplus C_- \oplus C_M$ for interacting initial states.

operator $\hat{U}_{\mathcal{H}}(z, z_0)$ with respect to \mathcal{H} ,

$$\hat{U}_{\mathcal{H}}(z, z_0) = \begin{cases} \mathcal{T}_D e^{-i \int_{z_0}^z dz' \mathcal{H}(z')}, & z > z_0 \\ \bar{\mathcal{T}}_D e^{i \int_z^{z_0} dz' \mathcal{H}(z')}, & z < z_0 \end{cases} \quad (1.4)$$

with the Hamiltonian

$$\mathcal{H}(z) = \begin{cases} \mathcal{H}(t = z), & z \in C_{\pm} \\ \mathcal{H}^M, & z \in C_M \end{cases} \quad (1.5)$$

The contour Dyson-time-ordering operator \mathcal{T}_D sorts contour arguments according to the premise *latest to the left*,

$$\mathcal{T}_D \{\hat{A}(z_1) \hat{B}(z_2)\} = \theta(z_1, z_2) \hat{A}(z_1) \hat{B}(z_2) + \theta(z_2, z_1) \hat{B}(z_2) \hat{A}(z_1) \quad (1.6)$$

where $z_1 > z_2$ in the contour sense if z_2 is closer to the starting point than z_1 . The contour Heaviside function is defined as $\theta(z, z') = 1$ if $z > z_1$ and $\theta(z, z') = 0$ otherwise. Thus, every contour argument on the forward branch is earlier than an argument on the backward branch. For two arguments on the forward (backward) branch \mathcal{T}_D is identical to the time (anti time) ordering \mathcal{T} ($\bar{\mathcal{T}}$). Each argument on the vertical track is later than any argument on one of the horizontal branches. The contour ordering is defined to produce the correct order of operators in Eq. (1.1). We define the operator in the contour Heisenberg picture $\hat{A}_{\mathcal{H}}(z) = \hat{U}(z_i, z) \hat{A}(z) \hat{U}_{\mathcal{H}}(z, z_i)$. With the contour Heisenberg picture and extending the definition (1.1) for the expectation value to arguments defined on the contour we find

$$A(z) = \frac{\text{Tr}[\hat{U}_{\mathcal{H}}(z_f, z_i) \hat{A}_{\mathcal{H}}(z)]}{\text{Tr}[\hat{U}_{\mathcal{H}}(z_f, z_i)]} = \frac{\text{Tr}[\mathcal{T}_D \{\mathcal{S}_{\mathcal{H}} \hat{A}(z)\}]}{\text{Tr}[\mathcal{T}_D \{\mathcal{S}_{\mathcal{H}}\}]} \quad (1.7)$$

with $\mathcal{S}_{\mathcal{H}} = \exp\left(-i \int_C \mathcal{H}(z') dz'\right)$. We note that the closed time contour as shown in Fig. 1.1 explicitly depends on the time t . However, adding the representation of unity

$\mathbb{I} = \hat{U}(t, \infty)\hat{U}(\infty, t)$ we can extend the contour to infinity as depicted in Fig. 1.2. With the contour Heisenberg representation we can define contour Green's functions $G_{AB}(z, z') = \langle \mathcal{T}_D \{ \hat{A}_{\mathcal{H}}(z) \hat{B}_{\mathcal{H}}(z') \} \rangle$ similar to their real-time counterparts. We will introduce contour Green's function for many-body systems in the next section and show how to use them to find real time non-equilibrium functions which in turn contain many information on a noisy quantum simulator.

1.2 Non-equilibrium Green's functions

In this section we introduce the many body non-equilibrium Green's functions (NEGF). Green's functions play an important role in the description of many-body systems since they are connected to many quantities measured in experiment. We consider many-body systems represented by annihilation c_i and creation c_i^\dagger operators that obey the usual commutation relations

$$[c_i, c_j^\dagger]_\epsilon = \delta_{ij}, \quad [c_i, c_j]_\epsilon = [c_i^\dagger, c_j^\dagger]_\epsilon = 0, \quad (1.8)$$

where $\epsilon = \mp 1$ for bosons and fermions respectively. The real-time NEGF can be obtained from the contour Green's function

$$G_{ij}(z, z') = -i \langle \mathcal{T}_C c_{i, \mathcal{H}}(z) c_{j, \mathcal{H}}^\dagger(z') \rangle = -i \frac{\text{Tr} \left[\mathcal{T}_C \mathcal{S}_{\mathcal{H}} c_i(z) c_j^\dagger(z') \right]}{\text{Tr} \left[\mathcal{T}_C \mathcal{S}_{\mathcal{H}} \right]}. \quad (1.9)$$

The time arguments of field-operators on the right-hand side ensure the correct ordering along the contour. The reason for introducing the contour Green's function is that it possesses a diagrammatic expansion with the same structure as diagrammatic expansions in equilibrium systems. In the definition of correlation functions the time-ordering operator \mathcal{T}_C is differently defined compared to Eq. (1.6):

$$\mathcal{T}_C \{ \hat{A}(z) \hat{B}(z') \} = \theta(z, z') \hat{A}(z) \hat{B}(z') - \epsilon \theta(z', z) \hat{B}(z') \hat{A}(z), \quad (1.10)$$

This definition, known as Wick time-ordering, corresponds to the usual definition for time-ordering of fermion and boson operators. Wick time-ordering is required in order to obtain the usual equations of motion for the many-body Green's functions $-dG(z, z')/dz \sim i\delta(z, z')$. For bosonic systems both Wick and Dyson time-ordering are identical while the situation is more complicated for fermionic systems. For the latter we can replace Dyson time-ordering by Wick time-ordering in the definition of the time evolution operator (1.4) only if the Hamiltonian $\mathcal{H}(t)$ is even in fermion operators. Such a Hamiltonian commutes with all other operators under Wick time-ordering. Physical fermionic systems are always represented by Hamiltonians even in

fermionic operators. For convenience we introduce the notation

$$G_{ij}(z, z') \equiv G(1; 1') = -i \left\langle \mathcal{T}_C c_{\mathcal{H}}(1) c_{\mathcal{H}}^{\dagger}(1') \right\rangle \quad (1.11)$$

where the multi index $1 = \{i, z\}$ represents both, a time variable on the contour and an index in Hilbert space.

1.3 Perturbation theory

The full many-body Hamiltonian $\mathcal{H} = H_0 + H_{\text{int}}$ contains an easy quadratic Hamiltonian H_0 and a hard to deal with interaction Hamiltonian H_{int} . We want to establish a perturbation expansion of the contour ordered Green's function (1.9) in terms of the interaction H_{int} . Under contour ordering \mathcal{T}_C the free Hamiltonian H_0 and the interaction Hamiltonian H_{int} commute and the full \mathcal{S} -operator $\mathcal{S}_{\mathcal{H}}$ factorizes into an interacting $\mathcal{S}_{H_{\text{int}}}$ and a free contribution \mathcal{S}_{H_0} . Using these properties we can express the Green's function as

$$G(a; b) = -i \frac{\text{Tr} \left[\mathcal{T}_C \left\{ \mathcal{S}_{H_0} \mathcal{S}_{H_{\text{int}}} c(a) c^{\dagger}(b) \right\} \right]}{\text{Tr} \left[\mathcal{T}_C \left\{ \mathcal{S}_{H_0} \mathcal{S}_{H_{\text{int}}} \right\} \right]} \equiv -i \frac{\left\langle \mathcal{T}_C \mathcal{S}_{H_{\text{int}}} c(a) c^{\dagger}(b) \right\rangle_0}{\left\langle \mathcal{T}_C \mathcal{S}_{H_{\text{int}}} \right\rangle_0}, \quad (1.12)$$

where we introduced the non-interacting average $\langle \mathcal{T}_C \{ \dots \} \rangle_0 = \text{Tr}[\mathcal{T}_C \{ \mathcal{S}_{H_0} \dots \}]$ [46]. Expanding the interaction $\mathcal{S}_{H_{\text{int}}}$ operator in powers of H_{int} yields the expansion series for the Green's function:

$$G(a, b) = -i \frac{\sum_n \frac{(-i)^n}{n!} \int dz_1 \dots dz_n \left\langle \mathcal{T}_C \{ H_{\text{int}}(z_1) \dots H_{\text{int}}(z_n) c(a) c^{\dagger}(b) \} \right\rangle_0}{\sum_n \frac{(-i)^n}{n!} \int dz_1 \dots dz_n \left\langle \mathcal{T}_C \{ H_{\text{int}}(z_1) \dots H_{\text{int}}(z_n) \} \right\rangle_0} \quad (1.13)$$

Since all averages are taken with respect to a non-interacting density matrix we can use the statistical Wick's theorem to obtain a diagrammatic expansion of the contour Green's function in terms of the non-interaction Green's function $G_0(z, z')$ [47, 48]. The only formal difference between the diagrammatic expansion of the contour Green's function compared to usual equilibrium diagrammatics is that time integrations are along the contour C instead of integration along the real axes.

1.3.1 Dyson equation

Expanding the Green's function Eq. (1.12) in powers of the interaction $H_{\text{int}}(z)$ and applying Wick's theorem to expression (1.13) yields an expansion of the full contour Green's function G in terms of the non-interacting function G_0 . From this expansion a Dyson equation for the contour Green's function can be derived just as in equilibrium.

Defining the self energy $\Sigma(z, z')$ as the sum of all irreducible diagrams the Dyson equation for the contour Green's function reads as

$$G(z, z') = G_0(z, z') + [G_0 \otimes \Sigma \otimes G](z, z'). \quad (1.14)$$

Here, $[a \otimes b](z, z') = \int d\bar{z} a(z, \bar{z}) b(\bar{z}, z')$ denotes a convolution of contour functions. From the integral-formulation of the Dyson equation a differential equation for the Green's function can be derived. We define the inverse free Green's function

$$G_0^{-1}(z, \bar{z}) = \delta(z, \bar{z}) \left(i \frac{d}{dz} - H_0(z) \right). \quad (1.15)$$

Acting with the inverse free Green's function from the left on the Dyson equation we obtain the integro-differential formulation of the Dyson equation

$$[(G_0^{-1} - \Sigma) \otimes G](z, z') = \delta(z, z'), \quad (1.16)$$

The boundary condition for this first order differential equation are known as Kubo-Martin-Schwinger (KMS) relations [48, 49]. They state the (anti-) periodicity of the (fermionic) bosonic Green's functions on the contour, i.e. $G(z_i, z') = \pm G(z_f, z')$. The non-interacting Green's function obeying the KMS relations is given by [46]

$$G_0(z, z') = \mathcal{T}_C \left\{ e^{-i \int_{t_{0,b}}^z d\bar{z} h_0(\bar{z})} \right\} \left[\theta(z, z') \bar{f}(h_0^M) - \theta(z', z) f(h_0^M) \right] \bar{\mathcal{T}}_C \left\{ e^{i \int_{t_{0,b}}^{z'} d\bar{z} h_0(\bar{z})} \right\} \quad (1.17)$$

with the (Fermi) Bose function

$$f(x) = \frac{1}{e^{\beta x} + \epsilon}, \quad \bar{f}(x) = 1 - \epsilon f(x). \quad (1.18)$$

1.3.2 Contour diagrammatics

With Wick's theorem we can expand the interacting Green's function in terms of free Green's functions G_0 . This expansion can be represented by Feynman diagrams similar to equilibrium theory. Feynman rules for contour functions are identical to the corresponding Feynman diagrams in equilibrium theory. For standard rules we refer to literature, e.g., [50, 51]. Just as in equilibrium only connected diagrams have to be considered. We will state the diagrammatic expansion rules for three types of interaction that we will encounter in this work: a scalar potential, two-fermion interaction, and fermion-boson coupling.

Scalar potential For coupling to an external potential $H_{\text{int}}(t) = \sum_i U_i(t) c_i^\dagger c_i$ the expansion Eq. (1.13) takes the form

$$G(a, b) = -i \frac{\sum_n \frac{(-i)^n}{n!} \int d1 \dots dn U(1) \dots U(n) \langle \mathcal{T}_C \{ c(a) c(1) \dots c(n) c^\dagger(1) \dots c(n)^\dagger c^\dagger(b) \} \rangle_0}{\sum_n \frac{(-i)^n}{n!} \int d1 \dots dn U(1) \dots U(n) \langle \mathcal{T}_C \{ c(1) \dots c(n) c^\dagger(1) \dots c(n)^\dagger \} \rangle_0},$$

where we used the short-hand notation $\int dz H_{\text{int}}(z) = \int d1 U(1) c(1)^\dagger c(1)$. Every potential term $U(z)$ couples to one annihilation operator corresponding to an incoming Green's function and to one creation operator that corresponds to an outgoing Green's function. This gives the simple diagrammatic expansion

where every single line between vertexes i and j represents a Green's function $iG_0(i; j)$, a cross denotes a potential term $U(i)$ and the double line represents the full Green's function $G(a; b)$. Every cross represent an internal time z_i and fermion index i . Integration $\int di$ over all internal indexes is implied. The first order term in the diagrammatic expansion is a convolution between a Green's function G_0 and the product of a Green's function with the scalar potential:

$$G^{(1)}(a; b) = \int d1 G_0(a; 1) U(1) G_0(1; b).$$

The higher order terms are obtained in a similar manner. We see, that the contour self-energy is $\Sigma(z, z') = \delta(z, z') U(z)$ contains only time local components. The Dyson equation for a scalar potential takes the simple form

$$\left(i \frac{d}{dz} - H_0(z) - U(z) \right) G(z, z') = \delta(z, z'). \quad (1.19)$$

Two-particle interaction We will encounter two-body interactions of the form $H_{\text{int}}(z) = \sum_i v_{ij}(z) c_i^\dagger(z) c_j^\dagger(z) c_j(z) c_i(z)$. Using the notation

$$\int dz H_{\text{int}}(z) = \int d1 d1' v(1; 1') c(1)^\dagger c(1')^\dagger c(1') c(1) \quad (1.20)$$

the diagrammatic expansion for the full Green's function takes the following form

Here, a dashed line represents an interaction $v(1; 1') = \delta(z, z')v_{ij}(z)$. The two diagrams that correspond to the second order in the coupling correspond to

$$G^{(2,A)}(a; b) = i \int d1d1' G_0(a; 1)[G_0(1; 1')v(1; 1')]G_0(1'; b) \quad (1.21)$$

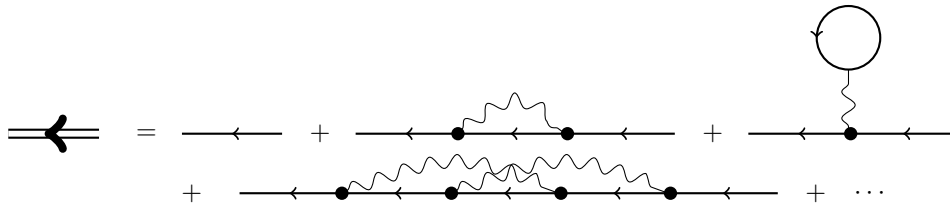
$$G^{(2,B)}(a; b) = -i \int d1d1' G_0(a; 1)G_0(1; b)[v(1; 1')G_0(1'; 1')]. \quad (1.22)$$

The minus sign in the second diagram stems from the fermion loop. The Green's function closed on itself is understood in the limit $G_0(z, z) = G_0(z, z^+)$, i.e. the creation operator in an interaction vertex is infinitesimally later than the annihilation operator. With this convention in mind we redefine a horizontal line as representing the Green's function $iG_0(1; 1'^+)$ in the sense, that for equal times the second argument is always later than the first.

Fermion-Boson coupling Later, we will discuss dephasing of a quantum simulator due to bosonic noise. There, we will find that we can map this process onto a fermion-boson coupling of the form

$$H_{\text{int}}(z) = \sum_i c_i^\dagger(z)c_i(z)\phi_i(z) \quad (1.23)$$

where $\phi_i(z) = \sum_s g_{is}(a_{i,s}(z) + a_{i,s}^\dagger(z))$ is the displacement of a bosonic field. For the fermion-boson coupling the diagrammatic expansion of the fermionic Green's function takes the form



where a wiggly line represents a free bosonic Greens function $i\mathcal{D}_0(1; 1') = \langle \mathcal{T}_C \phi(1)\phi(1') \rangle_0$ of a real bosonic field. It is connected to the contour Green's function D_0 of a the complex field we discussed so far as

$$\mathcal{D}_0(1; 1') = g(1)g(1')[D_0(1; 1') + D_0(1'; 1)]. \quad (1.24)$$

Here $D_0(1; 1') = \langle a(1)a(1')^\dagger \rangle$ is the bosonic many-body contour Green's function and $g(1) = g_{is}$ is the coupling strength. The two diagrams that correspond to the second

order in the coupling correspond to

$$G^{(2,A)}(a; b) = i \int d1d1' G_0(a; 1) [G_0(1; 1') \mathcal{D}(1; 1')] G_0(1'; b) \quad (1.25)$$

$$G^{(2,B)}(a; b) = -i \int d1d1' G_0(a; 1) G_0(1; b) [\mathcal{D}(1; 1') G_0(1'; 1'^+)]. \quad (1.26)$$

1.4 Continuation to real times

Since the Feynman diagrams for the contour Green's function have the same structure as Feynman diagrams in equilibrium, the contour formalism is a very compact representation of non-equilibrium many-body systems. However, measurable quantities are connected to real-time NEGF. Furthermore, in order to carry out integrations and differential calculations of contour functions we have to switch to a representation with real variables.

The contour Green's function is related to different types of real-time Green's functions depending on the position of the contour variables z and z' on the contour. If both arguments are on one of the horizontal branches the contour Green's function can be mapped to the four real time Green's functions

$$G(z, z') = \begin{cases} G^{\mathcal{T}}(t, t'), & z, z' \in C_+ \\ G^<(t, t'), & z \in C_+ \text{ and } z' \in C_- \\ G^>(t, t'), & z \in C_- \text{ and } z' \in C_+ \\ G^{\bar{\mathcal{T}}}(t, t'), & z, z' \in C_- \end{cases} \quad (1.27)$$

The greater and lesser Green's functions are defined as

$$G^>(t, t') = -i \langle \mathbf{c}_{\mathcal{H}}(t) \mathbf{c}_{\mathcal{H}}^\dagger(t') \rangle \quad (1.28)$$

$$G^<(t, t') = \epsilon i \langle \mathbf{c}_{\mathcal{H}}^\dagger(t') \mathbf{c}_{\mathcal{H}}(t) \rangle. \quad (1.29)$$

The time-ordered $G^{\mathcal{T}}$ and anti time-ordered Green's function $G^{\bar{\mathcal{T}}}$ can be expressed in terms of the greater and lesser function as

$$G^{\mathcal{T}}(t, t') = -i \langle \mathcal{T} \mathbf{c}_{\mathcal{H}}(t) \mathbf{c}_{\mathcal{H}}^\dagger(t') \rangle = \theta(t - t') G^>(t, t') + \theta(t' - t) G^<(t, t') \quad (1.30)$$

$$G^{\bar{\mathcal{T}}}(t, t') = -i \langle \bar{\mathcal{T}} \mathbf{c}_{\mathcal{H}}(t) \mathbf{c}_{\mathcal{H}}^\dagger(t') \rangle = \theta(t' - t) G^>(t, t') + \theta(t - t') G^<(t, t'). \quad (1.31)$$

In addition to the real-time Green's functions the definition of the contour Green's function allows for Green's functions with one or two arguments on the imaginary time axis. With two arguments on the imaginary branch the contour Green's function

Table 1.1: Langreth rules according to [46, 52]

$c(z, z') = \int_C d\bar{z} a(z, \bar{z})b(\bar{z}, z')$	$d(z, z') = a(z, z')b(z, z')$	$d(z, z') = a(z, z')b(z', z)$
$c^> = a^> \circ b^A - a^R \circ b^>$ $c^< = a^< \circ b^A - a^R \circ b^<$ $c^R = a^R \circ b^R$ $c^A = a^A \circ b^A$ $c^K = a^K \circ b^A + a^R \circ b^K$ $c^M = a^M \star b^M$	$d^> = a^> b^>$ $d^< = a^< b^<$ $d^R = \frac{1}{2}[a^K b^R + a^R b^K]$ $d^A = \frac{1}{2}[a^K b^A + a^A b^K]$ $d^K = \frac{1}{2}[a^K b^K + (a^R - a^A)(b^R - b^A)]$ $d^M = a^M b^M$	$d^> = a^> b^<$ $d^< = a^< b^>$ $d^R = \frac{1}{2}[a^K b^A + a^R b^K]$ $d^A = \frac{1}{2}[a^K b^R + a^A b^K]$ $d^K = \frac{1}{2}[a^K b^K - (a^R - a^A)(b^R - b^A)]$ $d^M = a^M b^M$

corresponds to the Matsubara Green's function. During this work we won't encounter Green's functions with arguments on the imaginary axes. Hence, we restrict our discussion to the real-time Green's functions. We complete the zoo of NEGF with the retarded G^R and advanced G^A Green's function

$$G^{R/A}(t, t') = \pm\theta(\pm(t - t'))[G^>(t, t') - G^<(t, t')] \quad (1.32)$$

and the kinetic Green's function

$$G^K(t, t') = G^>(t, t') + G^<(t, t'). \quad (1.33)$$

The full set of NEGF is not linearly independent. Indeed, only four components out of the entire zoo of NEGF form a linearly independent set where two of them are real-time functions. Depending on the initial conditions one has to choose a convenient set out of the zoo of functions.

For example, for non-interacting initial states a subset formed by G^R , G^A and G^K is very convenient while a linearly independent subset of real-time NEGF well suited for numerical calculations is given by the greater and lesser Green's function. The contour Green's function is continuous which leads to the boundary conditions

$$G^<(t_0, t_0) = G^M(0, 0^+), \quad G^<(t_0, t_0) = G^M(0^+, 0), \quad (1.34)$$

where G^M is the Matsubara Green's function obtained for z and z' imaginary times.

In order to work with contour Green's functions we need to calculate convolutions and products of contour functions. In order to calculate these quantities we need to convert the operations along the contour into operations with real valued variables. The transformations from contour to real time calculations are known as Langreth rules [52].

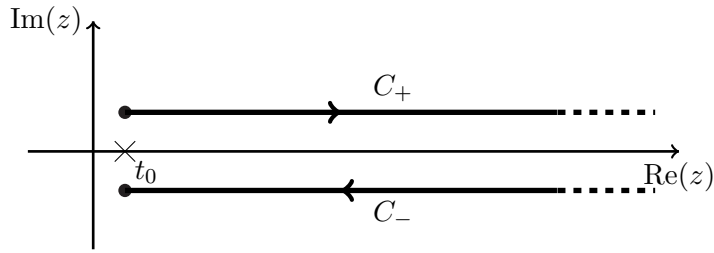


Figure 1.3: Contour $C_0 = C_+ \oplus C_-$ used for non-interacting initial states.

We summarize the Langreth rules in table 1.1. There, we use the definitions

$$a \circ b = \int_{t_0}^{\infty} d\bar{t} a(x, \bar{t}) b(\bar{t}, y) \quad \text{and} \quad a \star b = -i \int_0^{\beta} d\bar{\tau} a(x, \bar{\tau}) b(\bar{\tau}, y). \quad (1.35)$$

1.4.1 Kadanoff-Baym equations

Applying the Langreth relations to the Dyson equation (1.16) yields the Dyson equation for the real-time Green's functions.

For a system prepared in a non-interacting density matrix $\rho_0 = \exp(-\beta H_0^M)/Z_0$ there are no interactions along imaginary times and we can truncate the contour to the real-time branches as shown in Fig. 1.3. Consequently, we can restrict the contour Green's function to the real time Keldysh components and define the map

$$G(z, z') \mapsto \tilde{G}(t, t') = \begin{pmatrix} G^{\mathcal{T}}(t, t') & G^{<}(t, t') \\ G^{>}(t, t') & G^{\bar{\mathcal{T}}}(t, t') \end{pmatrix} \quad (1.36)$$

The four real time Green's functions are not linearly independent but obey the relation $G^{\mathcal{T}} + G^{\bar{\mathcal{T}}} = G^{<} + G^{>}$. We can dispose a part of this redundancy by a linear transformation in Keldysh space introduced by Larkin and Ovchinnikov [53]. Adopting the notation of [45] we define the linear transformation

$$\hat{G} = \frac{1}{\sqrt{2}}(\tau_0 - i\tau_2) \tau_3 \tilde{G} \frac{1}{\sqrt{2}}(\tau_0 + i\tau_2) = \begin{pmatrix} G^R(t, t') & G^K(t, t') \\ 0 & G^A(t, t') \end{pmatrix} \quad (1.37)$$

where τ_i are Pauli matrices acting in Keldysh space. When dealing with the Larkin-Ovchinnikov representation we will use the convention and call a matrix in this representation simply a matrix in Keldysh space. The Dyson equation for this matrix of real time functions takes the simple form

$$[(\hat{G}_0^{-1} - \hat{\Sigma}) \circ \hat{G}](t, t') = \delta(t - t') \tau_0 \quad (1.38)$$

where the convolution $\widehat{\Sigma} \circ \widehat{G}$ involves a matrix multiplication in Keldysh space. The inverse non-interacting Green's function in Keldysh space reads as

$$\widehat{G}_0^{-1}(t, t') = \delta(t - t') \begin{pmatrix} i\frac{d}{dt} - h_0(t) + i\eta & \\ & i\frac{d}{dt} - h_0(t) - i\eta \end{pmatrix} \quad (1.39)$$

where η is a small regularization that ensures the correct analytic behavior of $G_0^{R/A}$ [54]. The kinetic component of the inverse non-interacting Green's function is a pure regularization $\sim i\eta$ which can be omitted for interacting systems.

The advantage of the Larkin-Ovchinnikov representation is that the retarded and advanced function decouple from the kinetic component. Component-wise the Dyson equation becomes

$$\left[\left(G_0^{R/A} \right)^{-1} - \Sigma^{R/A} \right] \circ G^{R/A}(t, t') = \delta(t - t') \quad (1.40)$$

$$\left[\left(G_0^R \right)^{-1} \circ G^K \right](t, t') = \left[\Sigma^R \circ G^K + \Sigma^K \circ G^A \right](t, t'). \quad (1.41)$$

The Keldysh Green's function fulfills the boundary condition

$$G^K(t_0, t_0) = G^>(t_0, t_0) + G^<(t_0, t_0) = 1 - 2f(H_0^M) \equiv F(H_0^M) \quad (1.42)$$

and carries information about the occupation of states [45]. This can be illustrated by the equal time kinetic function which can be expressed in terms of the distribution,

$$G^K(t, t) = -i \langle \hat{U}_{\mathcal{H}}(t, t_0) F(H_0^M) \hat{U}(t_0, t) \rangle_0 \equiv i \langle F(t, H_0^M) \rangle_0. \quad (1.43)$$

Thus, $G^K(t, t)$ is the expectation value of the time dependent distribution function $F(t) = \hat{U}(t, t_0) F(H_0^M) \hat{U}(t_0, t)$. In equilibrium or for a steady state with $[H_0^M, \mathcal{H}] = 0$ the distribution function does not change in time but remains constant at its stationary value $F(t, H_0^M) = F(H_0^M)$. The retarded and advanced function carry no information about state occupation but only characterize the states [45]. The Dyson equations for the different real-time components are also known as Kadanoff-Baym equations.

Adiabatic approach

Based on the adiabatic assumption the interacting density matrix can be obtained from the non-interacting one by adiabatic switching of the interaction

$$H_{\text{int}}^M \rightarrow H_{\text{int}, \eta}^M = H_{\text{int}}^M e^{-\eta|t-t_0|} \quad (1.44)$$

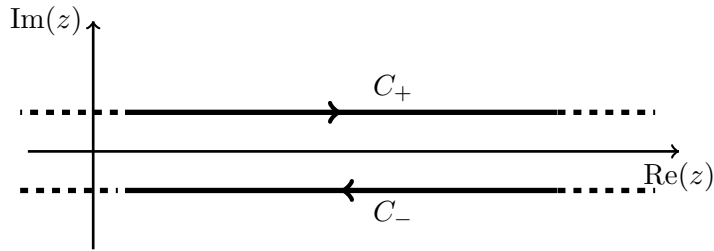


Figure 1.4: Contour $C_0 = C_+ \oplus C_-$ used in the adiabatic (Schwinger-Keldysh) approach.

where η is an infinitesimal positive constant. The interacting density matrix is obtained from the non-interacting density matrix via [55]

$$\rho = \hat{U}_{H_{\text{int}},\eta}^M(t_0, -\infty)\rho_0\hat{U}_{H_{\text{int}},\eta}^M(-\infty, t_0). \quad (1.45)$$

Just as in the previous section the interaction on the vertical branch vanishes. Consequently, we can employ the technique presented for non-interacting initial states on the adiabatic (or Schwinger-Keldysh) contour depicted in Fig. 1.4. The system evolves with the adiabatic Hamiltonian from $t = -\infty$ to $t = 0$. During this evolution correlations built up and the system has reached the interacting state at $t = 0$ when we switch on a time dependent perturbation. The Hamiltonian along the contour is defined as

$$\mathcal{H}(t) = \begin{cases} H_0^M + H_{\text{int},\eta}^M(t), & t < 0 \\ H_0(t) + H_{\text{int}}, & t \geq 0 \end{cases} \quad (1.46)$$

If the Green's functions fall off fast enough with the difference of their time arguments, neglecting the vertical part of the contour corresponds to neglecting initial correlations [56, 57]. Since initial correlations are not important we can assume that in the distant past the system was in equilibrium, $H_0^M = H_0 - \mu\hat{N}$. This is the approach originally used by Keldysh [58] and forms the basis of non-equilibrium field theoretical methods [51, 54].

Recovering equilibrium

In thermal equilibrium, $\mathcal{H} = H_0 + H_{\text{int}}$ and $\mathcal{H}^M = \mathcal{H} - \mu\hat{N}$ the Green's functions only depend on the difference of their time arguments and we can Fourier transform the Green's function according to $G(\omega) = \int dt e^{-i\omega t} G(t)$. In equilibrium the real-time Green's function decouple from imaginary time components. Similar to the non-interacting initial state we can restrict our discussions to the Keldysh matrix in the Larkin-Ovchinnikov representation. After Fourier transformation the Dyson equation

(1.38) for the Keldysh matrix reads as

$$\widehat{G}(\omega) = [(\omega - H_0)\tau_0 - \widehat{\Sigma}]^{-1} \quad (1.47)$$

where τ_0 is the identity matrix in Keldysh space. The Hamiltonian H_0 is diagonal in Keldysh space because the kinetic component of the self energy, Σ^K , has no time-local contribution. Explicitly, the Dyson equations for the individual Keldysh components read as

$$G^{R/A}(\omega) = [\omega - H_0 - \Sigma^{R/A}(\omega)]^{-1} \quad (1.48)$$

$$G^K(\omega) = G^R(\omega)\Sigma^K(\omega)G^A(\omega). \quad (1.49)$$

We define the spectral function $\mathcal{A}(\omega)$, the rate function $\widehat{\Gamma}(\omega)$ and the energy-shift $\widehat{\Delta}(\omega)$:

$$\mathcal{A}(\omega) = i[G^R(\omega) - G^A(\omega)] = -2 \operatorname{Im}[G^R(\omega)] \quad (1.50)$$

$$\widehat{\Gamma}(\omega) = i[\Sigma^R(\omega) - \Sigma^A(\omega)] = -2 \operatorname{Im}[\Sigma^R(\omega)] \quad (1.51)$$

$$\Delta(\omega) = [\Sigma^R(\omega) + \Sigma^A(\omega)]/2 = \operatorname{Re}[\Sigma^R(\omega)]. \quad (1.52)$$

The rate function determines the broadening of the Green's functions due to interactions while the energy-shift, well, shifts the energy. In equilibrium the fluctuation-dissipation theorem connects the kinetic Green's function G^K with the spectral function and the kinetic self energy with the rate function,

$$G^K = -iF_\epsilon(\omega)\mathcal{A}(\omega) \quad (1.53)$$

$$\Sigma^K = -iF_\epsilon(\omega)\widehat{\Gamma}(\omega). \quad (1.54)$$

Here, $F_\epsilon = 1 - 2\epsilon f_\epsilon$ is the distribution function.

1.5 From Keldysh to master equation

Small quantum mechanical systems couple to their environment which induces incoherent time evolution. We treat such *open quantum systems* with a system-bath approach. The Hamiltonian \mathcal{H} of the entire system is the sum of the uncoupled quantum system Hamiltonian H_{qs} , the environment Hamiltonian H_{B} and the coupling Hamiltonian V between system and environment:

$$\mathcal{H} = H_{\text{qs}} + H_{\text{B}} + V. \quad (1.55)$$

We describe the dynamics of the open quantum system in terms of its reduced density matrix $\rho(t)$. The reduced density matrix can be obtained from the full density matrix $\chi(t)$ of the coupled system by tracing out the environment

$$\rho(t) = \text{Tr}_B[\chi(t)]. \quad (1.56)$$

Here, $\text{Tr}_B[\dots]$ is the partial trace over the Hilbert space of the environment. Starting from the Von-Neumann equation $\dot{\chi}(t) = -i[\mathcal{H}, \chi(t)]_-$ for the full density matrix we derive a diagrammatic expansion of the reduced density matrix. We expand the reduced density matrix in a basis of the quantum system

$$\rho = \sum_{ss'} |s\rangle\langle s|\rho|s'\rangle\langle s'| = \sum_{ss'} \rho_{ss'} \hat{P}_{s's}. \quad (1.57)$$

with $\hat{P}_{ss'} = |s'\rangle\langle s|$. The time evolution of the matrix elements $\rho_{ss'}$ can be expressed in terms of expectation values of the projection operators as

$$\rho_{ss'}(t) = \text{Tr}_{\text{qs}}[\chi(t)\hat{P}_{ss'}] = \text{Tr}[\chi(t_0)\hat{P}_{ss',\mathcal{H}}(t)] = \langle \hat{P}_{ss'}(t) \rangle \quad (1.58)$$

$\hat{\mathcal{O}}_{\mathcal{H}}(t)$ denotes an operator in the Heisenberg picture with respect to the full Hamiltonian \mathcal{H} . This expression for density matrix elements corresponds to an expectation value of the form discussed in section 1.1. According to Eq. (1.7) we expand the expectation value on the closed time contour Fig. 1.1 without the vertical branch. Neglecting initial correlations we assume that the initial density matrix factorizes into a system component and a bath component according to $\chi(t_0) = \rho(t_0) \otimes \rho_B(t_0)$. Separating free time evolution and interaction as we did in order to derive a perturbation expansion for the Green's function we find

$$\rho_{ss'}(t) = \sum_{qq'} \rho_{qq'}(t_0) \langle q' | \text{Tr}_B\{\rho_B(t_0)\mathcal{T}_C\{\mathcal{S}_{H_0}\mathcal{S}_V\hat{P}_{ss'}(t_{\pm})\}|q\rangle \quad (1.59)$$

where $H_0 = H_{\text{qs}} + H_B$. As the time t marks the end of the contour we can place the projection operator \hat{P} either on the upper or lower branch of the contour, both choices yield the correct result. We choose to split the projection operator and place $|s'\rangle$ on the upper and $\langle s|$ on the lower branch. This choice will turn out to be convenient when introducing a diagrammatic expansion of the evolution operator. Eq. (1.59) resembles a master equation for the density matrix with time dependent scattering rates between matrix elements. The scattering from state qq' at time t_0 to ss' at time t is governed by the time evolution superoperator $\Pi_{qq' \rightarrow ss'}(t, t') = \langle q' | \text{Tr}_B\{\rho_B(t_0)\mathcal{T}_C\{\mathcal{S}_{H_0}\mathcal{S}_V\hat{P}_{ss'}(t_{\pm})\}|q\rangle$.

We expand the time evolution superoperator in powers of the interaction V and use

the relation

$$\mathcal{T}_C\{\mathcal{S}_{H_0}V(z_1)\dots V(z_n)\} = \mathcal{T}_C\{V_{H_0}(z_1)\dots V_{H_0}(z_n)\}$$

for an operator $\hat{O}_{H_0} = \hat{U}_{H_0}(z, z_i)\hat{O}\hat{U}_{H_0}(z_i, z)$ in the interaction picture. For a coupling between bath and system of the form $V = \hat{A}\hat{X}$ where \hat{X} is a bath operator and \hat{A} acts on the system we find the time evolution operator

$$\begin{aligned} \Pi_{qq' \rightarrow ss'}(t, t_0) &= \sum_n \frac{(-i)^n}{n!} \int dz_1 \dots dz_n \langle \mathcal{T}_C \hat{X}_{H_B}(z_1) \dots \hat{X}_{H_B}(z_n) \rangle_0 \\ &\times \langle q' | \mathcal{T}_C \{ \hat{A}_{H_{qs}}(z_1) \dots \hat{A}_{H_{qs}}(z_n) \hat{U}_{H_{qs}}(z_i, t_+) | s' \rangle \langle s | \hat{U}_{H_{qs}}(t_-, z_i) | q \rangle. \end{aligned} \quad (1.60)$$

For a bosonic or fermionic bath initially in equilibrium Wick's theorem applies to bath correlation functions $iD_n(z_1, \dots, z_n) = \langle \mathcal{T}_C \hat{X}_{H_B}(z_1) \dots \hat{X}_{H_B}(z_n) \rangle_0$. For such reservoirs the bath correlation function collapses into two-time correlation functions. Contrary to fermionic/ bosonic many body theory we cannot separate system correlations that appear in the second line of the expansion for arbitrary quantum systems H_{qs} . It turns out to be convenient to use a real time representation for integrations along the contour and keep track of the contour ordering explicitly. Changing from contour to real time integration yields

$$\begin{aligned} \Pi_{qq' \rightarrow ss'}(t, t_0) &= \sum_n (-i)^n \int_{t_0}^t dt_n \dots \int_{t_0}^{t_2} dt_1 \langle \mathcal{T}_C \hat{X}_{H_B}(t_1) \dots \hat{X}_{H_B}(t_n) \rangle_0 \\ &\times \langle q' | \tilde{\mathcal{T}}_C \{ \hat{A}_{H_{qs}}(t_1) \dots \hat{A}_{H_{qs}}(t_n) \hat{U}_{H_{qs}}(t_i, t_+) | s' \rangle \langle s | \hat{U}_{H_{qs}}(t_-, t_0) | q \rangle, \end{aligned} \quad (1.61)$$

where all possible ways to sort the times on the contour have to be taken into account and $\tilde{\mathcal{T}}_C$ introduces an additional minus sign for operators on the backward contour to account for the different orientations of the contours.

We insert a representation of unity $\mathbb{I} = \sum_{q_i} |q_i\rangle\langle q_i|$ between system operators $\hat{A}_{H_{qs}}(t_1)$ and apply Wick's theorem to bath correlation functions in order to represent the time evolution operator in a diagrammatic expansion as shown in Fig. 1.5 for a bosonic bath. A filled circle denotes an interaction vertex $\langle q_1 | \hat{A}(z') | q'_1 \rangle \hat{X}(z')$ with an incoming system state q_1 and an outgoing state q'_1 , a straight line between two vertexes denotes a free time evolution of the system $\langle q'_2 | \hat{U}_{H_{qs}}(z_1, z_2) | q_1 \rangle$, and a dashed line represents a contraction

$$C(1; 2) = iD(1; 2) \langle q_1 | \hat{A}(z_1) | q'_1 \rangle \langle q_2 | \hat{A}(z_2) | q'_2 \rangle.$$

Here, $D(1; 2)$ is the bosonic contour Green's function. For coupling to a fermionic reservoir of the form $\hat{X} = \sum_{kk'} t_{kk'} c_k^\dagger c_{k'}$ every interaction vertex has an incoming and an outgoing fermionic Green's function and the diagrammatic expansion for coupling

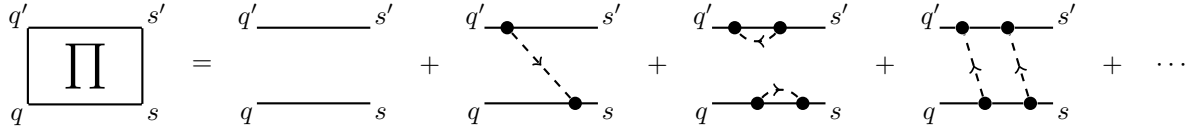


Figure 1.5: The time evolution superoperator $\Pi(t, t_0)$ for coupling to bosonic reservoirs. Dots represent interaction vertices, solid lines represent time evolution of the system and dashed lines represent bosonic correlations functions.

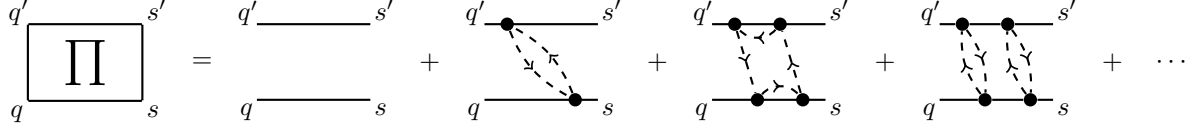


Figure 1.6: The time evolution superoperator $\Pi(t, t_0)$ for coupling to fermionic reservoirs. Contrary to a bosonic bath every vertex has an incoming and an outgoing fermionic correlation function. Diagrams as the second and fourth diagram containing only two-vertex fermionic loops yield an effective bosonic bath. We will neglect diagrams like the third diagram containing higher order fermionic loops.

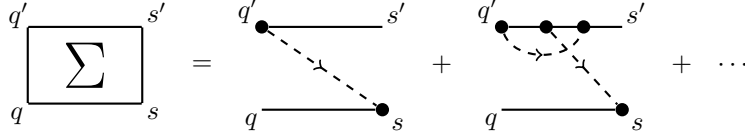


Figure 1.7: Self energy diagrams $\Sigma(t, t')$ for a bosonic reservoir. In Makrov approximation only second-order diagrams like the first diagram contribute.

to fermionic reservoirs takes the form shown in Fig. 1.6. Just as in the many-body theory we define a self-energy Σ as the sum of all irreducible diagrams shown in Fig. 1.7. The time evolution superoperator obeys a Dyson equation with the free evolution Π_0 which corresponds to the system without coupling to the bath:

$$\boxed{\Pi} = \boxed{\Pi_0} + \boxed{\Pi_0} \boxed{\Sigma} \boxed{\Pi}$$

The reduced density matrix is obtained from $\rho(t) = \Pi(t, t_0)\rho(t_0)$. Time derivation of this equation yields the quantum master equation for the reduced density matrix

$$\dot{\rho}(t) = -i[H_{\text{qs}}, \rho(t)] + \int_{t_0}^t \Sigma(t, t')\rho(t') \quad (1.62)$$

Through the self-energy the density matrix at time t depends on the entire history of the density matrix. For a memoryless bath the kernel Σ decays fast with increasing time difference $t - t'$ compared to typical time scales of the system and we can replace $\rho(t')$ with $\rho(t)$ under the integral. Additionally, we can take the limit $t_0 \rightarrow -\infty$. This yields the master equation in Markov approximation which forms the basis for many

calculations concerning open quantum systems

$$\dot{\rho}(t) \approx -i[H_{\text{qs}}, \rho(t)] + \hat{\Gamma}\rho(t). \quad (1.63)$$

The rate superoperator defines the transition rates

$$\hat{\Gamma}_{qq' \rightarrow ss'} = \int_{-\infty}^t \Sigma_{qq' \rightarrow ss'}(t, t') \quad (1.64)$$

between matrix elements of the density matrix of the system. We will compare results from many-body Keldysh calculations with results from master equation in Markov approximation in chapter 2.

2 Chapter 2

Analyzing a perturbed quantum simulator using many-body theory

2.1 Introduction

In principle, large quantum systems like interacting fermions could be simulated using a universal quantum simulator based on the application of discrete qubit gates [12, 15, 31, 59]. Unfortunately, a universal quantum simulator with implemented quantum error correction requires huge amounts of qubits with good coherence times. Due to limitations of the available quantum hardware universal quantum simulation will not be feasible in the near future [60]. Analog quantum simulation on systems restricted to solving specific classes of problems offers an alternative for the near future. An analog quantum simulator is an artificial system of qubits designed in such a way that its Hamiltonian maps to that of the simulated system. Performing measurements on this artificial system yields properties of the simulated system. Analog quantum simulation of the one-dimensional Fermi-Hubbard Model has been proposed with a bilinear chain of superconducting qubits [61] while the Holstein-Polaron Model can be realized using a combination of qubits and harmonic oscillators [62]. Many more systems have been proposed or have already been simulated on various physical realizations of quantum simulators [29, 63–65]

Unfortunately, analog quantum simulators are prone to imperfections such as noise from interaction with the environment or disorder arising from imprecise fabrication processes. Consequently, quantum simulators do not return properties of the simulated system but properties describing some disturbed system influenced by these imperfections. In addition analog quantum simulators are continuous systems that do not allow for quantum error correction. This raises questions on the reliability of analog quantum simulators [32]. At present, different methods of determining the reliability of analog quantum simulators are discussed with ideas ranging from cross-

validation using different physical realizations to numerical validation in parameter regimes solvable on classical computers. Another possible way to quantify the error of a quantum simulation is to connect the disturbed result to the ideal result using system-bath approaches [VI]. Small qubit systems coupled to the environment are commonly analyzed using quantum master equations [66]. For larger systems these methods become numerically expansive and quickly reach their limits.

We suggest an alternative way to analyze decoherence in a large quantum simulator. The basic idea is to map the noisy qubit system onto a fermionic system and apply non-equilibrium many-body methods to disturbed analog quantum simulators. Initially developed for many-body systems these methods are capable of handling even large quantum simulators. In this chapter, we focus on quantum simulators that can be used to simulate fermionic systems. An important quantity that can be extracted from such an analog quantum simulator is the spectral function of the simulated system [67–69]. The spectral function can also be formulated in terms of non-equilibrium Green’s functions as $\mathcal{A}(\omega) = -i(G^R(\omega) - G^A(\omega))$. Using many-body perturbation theory we relate the Green’s functions obtained from a perturbed quantum simulator to the Green’s function of the ideal quantum simulator. We analyze how single-qubit decoherence affects the spectral function of a multi-qubit system in and out of equilibrium. Intuitively, we expect that the spectral resolution of a quantum simulator is limited by the coherence of the individual qubits. The topics presented in this part of the thesis led to the publication [V] and are closely related to the publications [VI, VII].

In the first section we motivate our idea. Subsequently, we illustrate the failure of conventional many-body perturbation theory for spin systems and discuss the Jordan-Wigner transformation of a one-dimensional spin system onto a fermionic model. We show, that the Jordan-Wigner transformation of general qubit systems induces complicated many-particle interactions and fermionic source terms. Hence, we will restrict our discussion to a quantum simulator with nearest-neighbor qubit exchange terms coupled to different types of noise. We note, however, that our method can be applied to any quantum simulator that is obtained from mapping a fermionic system via the Jordan-Wigner transformation onto the qubit system. In the next step, we discuss the mapping of different types of noise, namely dephasing, relaxation and disorder, onto fermionic systems. We analyze the properties of the effective fermionic Hamiltonian that results from mapping of these different types of noise. To illustrate our method and the influence of disorder on analog quantum simulators we discuss dephasing due to a bosonic environment, relaxation due to a fermionic environment and disorder in the subsequent sections.

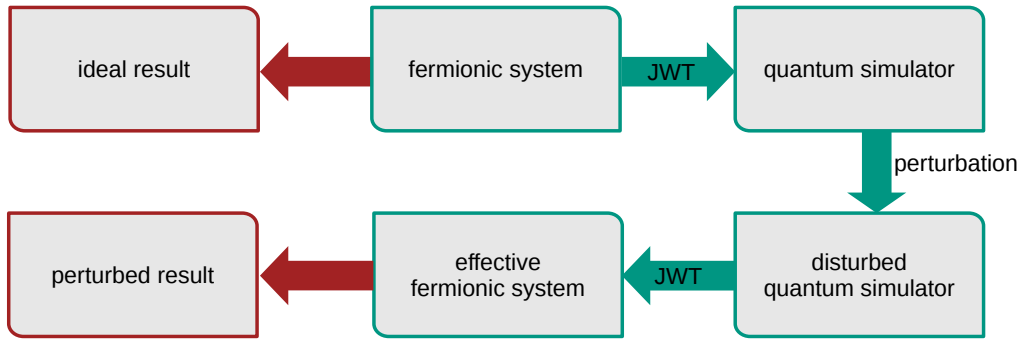


Figure 2.1: Schematics of the idea behind our approach. The fermionic system that shall be simulated is mapped to the quantum simulator via Jordan-Wigner transformation. Perturbations couple to the quantum simulator. Backwards Jordan-Wigner transformation yields the effective fermionic system simulated by the quantum simulator.

2.2 Motivation of the idea

Generally quantum simulators are created by using systems of coupled qubits. In order to simulate a fermionic system it is therefore necessary to map the fermionic system onto a qubit Hamiltonian. This can be achieved, for example, with the Jordan-Wigner transformation which we discuss in section 2.3.2. While this transformation can lead to rather complicated coupling terms between the individual qubits, it has the advantage that each qubit directly corresponds to a fermionic orbital. We use the fact that each qubit has such a simple fermionic representation, as we consider additional perturbations acting on the quantum simulator.

In order to qualitatively understand their influence we transform the additional perturbations using the same Jordan Wigner transformation used in the definition of the quantum simulator. Perturbations arising from the coupling to an environment map to effective perturbations of the fermionic system which can be analyzed using diagrammatic many-body perturbation theory. We will map different types of noise that can arise in a quantum simulator, i.e., dephasing, relaxation and disorder, onto fermionic systems. In Fig. 2.1 we show a schematic representation of the general idea behind our approach.

The effective perturbations in the fermionic system that arise from mapping of these different types of noise do not depend on the specific form of the quantum simulator Hamiltonian. Consequently, the effective perturbations in fermionic language and the resulting diagrammatic expansions can be applied to quantum simulators that represent various physical fermionic systems.

To test our approach we compare numerical master equation calculations, with results derived using our fermionic mapping combined with diagrammatic many-body

perturbation theory. In all regimes where the master equation approach is valid, the results match exactly.

2.3 Decoherence in a quantum simulator - general discussion

An analog quantum simulator is based on coupled qubits represented by spin-1/2 operators $\vec{\sigma}_i$. As discussed in more detail in chapter 3 the environment couples to the qubits, disturbs the quantum simulator and eventually leads to decoherence. The environment of a quantum simulator consists of external perturbations like electronic control-devices at finite temperature and of internal perturbations such as fluctuating charged or magnetic two-level systems.

We describe a noisy quantum simulator within a system bath approach where the full Hamiltonian $\mathcal{H} = H_{\text{qs}} + H_{\text{B}} + V$ is the sum of the quantum simulator Hamiltonian H_{qs} , the uncoupled bath or reservoir Hamiltonian H_{B} representing the environment and the coupling V between environment and quantum simulator. The coupling to the environment reads as

$$V = \sum_i \sum_{\alpha=x,z} \sigma_i^\alpha \hat{X}_i^\alpha, \quad (2.1)$$

where \hat{X}_i^α are bath operators describing the coupling of qubit i to its respective bath. Longitudinal coupling $\propto \sigma_i^z$ induces random fluctuations of the energy splittings of qubits. Thus, it destroys the phase coherence and leads to dephasing, while transversal coupling $\propto \sigma_i^x$ induces relaxation to a stationary state dictated by the environment.

The dynamics of the bath operators are governed by the bath Hamiltonian H_{B} . We assume that each qubit couples to an individual bath which is uncorrelated with the baths of the other qubits such that

$$\langle \mathcal{T}_C \hat{X}_i^\alpha(z) \hat{X}_j^\beta(z') \rangle_0 = \delta_{ij} \delta_{\alpha\beta} \langle \mathcal{T}_C \hat{X}_i^\alpha(z) \hat{X}_i^\alpha(z') \rangle_0 \quad (2.2)$$

holds for bath correlation functions. Here, $\langle \dots \rangle_0$ denotes the expectation value with respect to the equilibrium density matrix of the environment.

For small systems we usually employ quantum master equations in order to describe the disturbed quantum simulator [66]. However, as mentioned before these methods quickly reach their limits for systems comprising more than around 20 qubits. For larger systems the many-body methods discussed in chapter 1 seem to be an adequate tool in order to analyze decoherence.

Unfortunately, these many-body methods do not directly apply to spin systems due to the non-Abelian group properties of spin-1/2 systems [51, 70]. These properties reflect into the commutation relations of spin operators $\hat{\sigma}_\pm$. While fermionic operators always anti-commute and bosonic operators always commute, spin operators obey

mixed bosonic-fermionic commutation relations. Operators of different sites behave like bosons and commute while operators anti-commute on the same site:

$$[\sigma_i^-, \sigma_j^+]_- = [\sigma_i^-, \sigma_j^-]_- = [\sigma_i^+, \sigma_j^+]_- = 0, \quad i \neq j, \quad (2.3)$$

$$[\sigma_i^-, \sigma_i^+]_+ = 1, \quad [\sigma_i^-, \sigma_i^-]_+ = [\sigma_i^+, \sigma_i^+]_+ = 0. \quad (2.4)$$

Consequently, Wick's theorem is not valid for spin operators. We illustrate this in the following section.

2.3.1 Wick's theorem and spin operators

The time evolution of a quantum system is governed by the time evolution operator $\hat{U}(z, z') = \mathcal{T}_D \exp(-i \int_C H(z') dz')$, where \mathcal{T}_D is the Dyson contour-ordering operator. A Dyson-ordered product of operators is defined as

$$\mathcal{T}_D\{\hat{A}(z)\hat{B}(z')\} = \theta(z, z')\hat{A}(z)\hat{B}(z') + \theta(z', z)\hat{B}(z')\hat{A}(z). \quad (2.5)$$

In chapter 1 we discussed many-body perturbation theory for fermionic and bosonic systems. For these systems we substituted Dyson ordering by Wick ordering \mathcal{T}_C which is defined by its action on two fermionic/ bosonic operators on the time contour:

$$\mathcal{T}_C\{\hat{A}(z)\hat{B}(z')\} = \theta(z, z')\hat{A}(z)\hat{B}(z') \pm \theta(z', z)\hat{B}(z')\hat{A}(z). \quad (2.6)$$

The upper/ lower sign is valid for bosonic/ fermionic operators. We note that for bosonic operators Wick and Dyson time-ordering coincide. In chapter 1 we used that for Wick-ordered averages of bosonic or fermionic operators Wick's theorem applies and many-particle Green's functions factorize into two-particle non-interacting Green's functions. This factorization forms the basis of the many-body perturbation theory.

Suppose we want to apply many-body methods to calculate qubit-qubit correlation functions of the form $C_{ij} = \langle \mathcal{T}_C\{\sigma_i^-(z)\sigma_j^+(z')\} \rangle$. In order to use Wick's theorem we need to define a Wick ordering for spin operators which accounts for the spin commutation relations. Spin operators that belong to the same site anti-commute and require a fermionic time ordering while operators of different sites require a bosonic time ordering. Thus, the Wick time-ordering for spin-operators has to distinguish between operators on the same site and operators on different sites.

Such a Wick time-ordering cannot substitute Dyson time-ordering in the time evolution operator. In particular, the fermionic nature of on-site operators hinders the substitution of Dyson with Wick ordering. To illustrate this we take a look at the

action of Wick ordering on a single qubit Hamiltonian $H_i = E_i \sigma_i^z / 2$:

$$\mathcal{T}_C\{H_i(z)H_i(z')\} = \theta(z - z')H_i(z)H_i(z') - \theta(z' - z)H_i(z). \quad (2.7)$$

Due to the fermionic nature of the single qubit operator a minus sign appears in front of the second term on the r.h.s. which is not present under Dyson time-ordering. For systems of physical fermions this problem does not arise because fermionic operators always appear in even combinations in a physical Hamiltonian. For spin operators no such rule applies and the substitution Dyson \mapsto Wick is not valid. As a consequence Wick's theorem does not apply and no simple expansion of correlation functions in terms of two-operator correlation functions exists. Some exotic methods to find a diagrammatic expansion of spin-spin correlation functions have been proposed [71, 72]. However, these methods are not versatile in their applicability and do not follow standard diagrammatic rules.

In order to overcome these problems we map the qubit system to a fermionic system using the Jordan-Wigner transformation.

2.3.2 Mapping qubits onto fermions - the Jordan-Wigner transformation

Different mappings between fermionic and spin systems that preserve the correct commutation relations exist. Among these mappings are the Jordan-Wigner transformation [73], slave fermion representations [74, 75], mapping to Majorana fermions [70, 76] or the Bravyi-Kitaev transformation [77]. Unfortunately, each mapping mentioned above introduces new problems. For example, the Jordan-Wigner and Bravyi-Kitaev transformation induce non-local many-particle interactions while they preserve the dimensionality of the Hilbert space. Mapping to Majorana fermions and slave fermion representations on the other hand increase the dimensionality of the Hilbert space. Slave fermion representations introduce unphysical states which have to be traced out after calculations.

In this work we use the one dimensional *Jordan-Wigner transformation* to map qubits onto fermions [73]. For an ordered one-dimensional set of N qubits we define the operators

$$c_i = \prod_{j < i} (-\sigma_j^z) \sigma_i^- = e^{i\phi_i} \sigma_i^-. \quad (2.8)$$

One easily shows that the operators c_i and the conjugate operators c_j^\dagger obey fermionic commutation relations. This transformation from spin to fermion operators not only produces the correct fermionic anti-commutation relations but also preserves the dimensionality of the Hilbert space. The phase $\phi_i = \pi \sum_{j=1}^{i-1} \hat{n}_j$ counts the occupation of all qubits ordered earlier than qubit i . This accounts for the parity factor $(-1)^p = e^{i\phi_i}$

that comes along with the definition of fermionic operators in second quantization

$$c_i |n_1 n_2 \dots n_i \dots n_N\rangle = (-1)^p |n_1 n_2 \dots n_i - 1 \dots n_N\rangle. \quad (2.9)$$

In order to apply the Jordan-Wigner transformation fermions as well as qubits have to be ordered along a one dimensional chain. The necessary ordering along one dimension limits the applicability of the transformation in higher dimensions. Mapping single qubit operators with the Jordan-Wigner transformation yields

$$\sigma_i^- \mapsto e^{-i\phi_i} c_i, \quad (2.10)$$

$$\sigma_i^z = 2\sigma_i^+ \sigma_i - 1 \mapsto 2c_i^\dagger c_i - 1. \quad (2.11)$$

While the longitudinal operator σ^z maps to a fermionic term similar to a chemical potential, i.e. bilinear and local in fermionic operators the transverse operators σ^\pm map to complicated operators. Through the phase $\phi_i = \sum_{j<i} \hat{n}_j$ the transformed operators correspond to an interaction between the fermion on site i and all fermions on sites located earlier in the chain. Additionally, the mapping of σ^\pm induces fermionic source and sink terms respectively which account for the change of qubit populations. It follows that a quantum simulator containing transversal single qubit operators maps to a fermionic Hamiltonian that contains terms odd in fermionic operators. For such a system Wick's theorem does not apply. Consequently, we cannot deal with quantum simulators with transversal single qubit terms using the Jordan-Wigner transformation and restrict our considerations to simulators without such terms.

Now, we take a look at the mapping of qubit-qubit couplings. Applying the Jordan-Wigner transformation to qubit exchange terms we find

$$\sigma_i^+ \sigma_j^- \mapsto c_i^\dagger e^{i(\phi_i - \phi_j)} c_j = c_i^\dagger e^{i \sum_{k<i} \sum_{l<j} (\hat{n}_k - \hat{n}_l)} c_j. \quad (2.12)$$

Similar to the mapping of transverse single qubit operators (2.10)-(2.11) the Jordan-Wigner transformation induces exotic many-particle interactions. In contrast to the mapping of a single qubit all operators obtained from the mapping of exchange terms are even in fermionic operators and can in principle be tackled by standard many-body theory. However, dealing with interactions beyond two-particles is beyond the scope of standard many-body methods and we will restrict our discussion to systems without exotic interactions.

Despite the drawbacks we have encountered so far the Jordan-Wigner transformation can be used to analyze specific qubit systems. For a nearest-neighbor exchange term

the mapping reduces to a fermionic hopping term

$$\sigma_i^+ \sigma_{i+1}^- \mapsto c_i^\dagger c_{i+1}, \quad (2.13)$$

while a longitudinal qubit-qubit coupling induces a fermionic interaction of the form

$$\sigma_i^z \sigma_j^z \mapsto (2c_i^\dagger c_i - 1)(2c_j^\dagger c_j - 1). \quad (2.14)$$

Consequently, we restrict our discussion to an analog quantum simulator with nearest-neighbor exchange coupling J_{ij}^x and longitudinal interaction J_{ij}^z between qubits. In rotating-wave approximation the Hamiltonian of such a quantum simulator reads as

$$H_{\text{qs}} = \sum_i h_i \sigma_i^z + \sum_i J_i^x (\sigma_i^+ \sigma_{i+1}^- + \sigma_{i+1}^+ \sigma_i^-) + \sum_{i \neq j} J_{ij}^z \sigma_i^j \sigma_j^z. \quad (2.15)$$

An interesting system that can be mapped onto such an analog quantum simulator is the one dimensional Fermi-Hubbard model with nearest-neighbor hopping [61]. The Hamiltonian of the Fermi-Hubbard model reads as

$$H_{\text{F}} = \sum_i [g_i (c_i^\dagger c_{i+1} + c_{i+1}^\dagger c_i) + \varepsilon_i c_i^\dagger c_i] + \sum_{i \neq j} U_{ij} c_i^\dagger c_i c_j^\dagger c_j + E_0. \quad (2.16)$$

The parameters of the fermionic model and the qubit system are related by $U_{ij} = 2J_{ij}$ and $\varepsilon_i = -\sum_j (J_{ij} + J_{ji})/2 + 2h_i$. E_0 is a constant energy shift. In this thesis, we focus on the description of decoherence in the fermionic picture. We assume that $J_{ij}^z = 0$ and thus $U_{ij} = 0$.

In order to quantify the influence of the environment on the results of the simulation we map the system-bath interaction V onto the fermionic system as well. We discuss the mapping of the different contributions to V separately in the following paragraphs.

2.3.3 Dephasing

Applying the Jordan-Wigner transformation to longitudinal noise, the interaction between the quantum simulator and the environment takes the form

$$V_z = \sum_i \sigma_i^z \hat{X}_i^z \mapsto V_{z,f} = \sum_i 2c_i^\dagger c_i \hat{X}_i^z. \quad (2.17)$$

We absorbed an additional shift $\delta H_{\text{B}} = -\sum_i \hat{X}_i^z$ into the bath Hamiltonian.

We note that in the fermionic language pure dephasing corresponds to an interaction between the local density $\hat{n}_i = c_i^\dagger c_i$ and the environment represented by \hat{X}^z and induces fluctuations of the chemical potential. Consequently, mapping dephasing onto

a fermionic system always leads to physical Hamiltonians and is unproblematic in terms of many-body perturbation theory.

2.3.4 Relaxation

With Eq. (2.10) follows the mapping of transversal noise onto the fermionic system:

$$V_x = \sum_i \sigma_i^x \hat{X}_i^x \mapsto \sum_i \prod_{j<i} (1 - 2\hat{n}_j) (c_i^\dagger + c_i) \hat{X}_i^x. \quad (2.18)$$

Due to the linear source term $J_i = (c_i + c_i^\dagger)$, fermion number conservation is violated and Wick's theorem does not apply. This problem can be avoided if the bath operator \hat{X}_i^x is odd in fermionic operators. For such an interaction the Hamiltonian is even in fermionic creation and annihilation operators and Wick time ordering can be defined in the usual way. As an example for transversal noise we will discuss relaxation due to an ensemble of two-level systems at zero temperature which corresponds to a fermionic reservoir and meets the aforementioned requirements.

2.3.5 Disorder

So far we were concerned with the influence of fast fluctuating noise, i.e., noise on time scales shorter than the time required for a single run of the quantum simulator. These fast fluctuations lead to changes in the Hamiltonian during a single run and are responsible for decoherence of qubits. Another type of perturbation arises from quasi-static fluctuations that occur on time scales comparable to or longer than single-run times of the quantum simulator.

Thus, quasi-static fluctuations are frozen in a certain configuration during a single measurement and can be described in terms of quenched disorder. For a quantum simulator with Hamiltonian given in Eq. (2.15) disorder in on-site energies h_i and qubit-qubit couplings $J_{ij}^{x,z}$ can be represented as

$$h_i \rightarrow h_i + \delta h_i \quad (2.19)$$

$$J_{ij}^{x,z} \rightarrow J_{ij}^{x,z} + \delta J_{ij}^{x,z}, \quad (2.20)$$

with independent random variables δh_i and $\delta J_{ij}^{x,z}$. Typically, one assumes that these random variables are Gaussian distributed and hence characterized by their first and second moment [54],

$$\langle \delta a \rangle_{\text{dis}} = \mu_a \quad (2.21)$$

$$\langle \delta a \delta b \rangle_{\text{dis}} = w_a^2 \delta_{a,b}. \quad (2.22)$$

Here, μ_a is the mean value and w_a the width of the Gaussian distribution. Systematic shifts can be absorbed into a redefinition of parameters and we restrict our discussion to random fluctuations with vanishing mean value. The width w_a determines the disorder strength due to random variables. For a Gaussian distribution all higher order moments factorize into products of second moments (i.e., Wick's theorem).

Mapping the quantum simulator of the Fermi-Hubbard model subject to quenched disorder to fermions using the Jordan-Wigner transformation we find

$$H_F = \sum_i [(g_i + \delta g_i)(c_i^\dagger c_{i+1} + c_{i+1}^\dagger c_i) + (\varepsilon_i + \delta \varepsilon_i)c_i^\dagger c_i] + \sum_{i \neq j} (U_{ij} + \delta U_{ij})c_i^\dagger c_i c_j^\dagger c_j + E_0[\{\delta a\}], \quad (2.23)$$

where $\langle ij \rangle$ denotes a sum over nearest-neighbors. The relations between the random variables in the fermionic Hamiltonian and the random variables δJ and δh of the quantum simulator are described by $\delta g_i = \delta J_{i,i+1}^x$, $\delta \varepsilon_i = 2\delta h_i - \sum_j (\delta J_{ij}^z + \delta J_{ji}^z)$, and $\delta U_{ij} = 2\delta J_{ij}^z$. Using the second moments of the physical parameters given in Eq. (2.22) we find the second moments of the fermionic parameters

$$\langle \varepsilon_i \varepsilon_j \rangle = \delta_{ij} [(2w_{h_i})^2 + \sum_l (2w_{J_{il}^z})^2] + (2w_{J_{ij}})^2 \quad (2.24)$$

$$\langle g_i g_j \rangle = \delta_{ij} w_{J_{i,i+1}^+}^2 \quad (2.25)$$

$$\langle \delta U_{ij} \delta U_{kl} \rangle = [\delta_{ik} \delta_{jl} + \delta_{il} \delta_{jk}] (2w_{J_{ij}^z})^2 \quad (2.26)$$

$$\langle \delta \varepsilon_i \delta U_{kl} \rangle = \sum_j \langle \delta U_{ij} \delta U_{kl} \rangle = \delta_{ik} (2w_{J_{il}^z})^2 + \delta_{il} (2w_{J_{ik}^z})^2. \quad (2.27)$$

We note that fluctuations in J^z lead to fluctuations in both on-site energies and the interaction term. Thus, $\delta \varepsilon$ and δU are correlated random variables.

In order to obtain statistical significance a measurement on the quantum simulator is repeated many times. During each run a different realization of the set of random variables is realized and averaging over many runs corresponds to an average over the quenched disorder. The disorder average of an observable \hat{O} obtained from N_{meas} measurements is defined as

$$\langle \hat{O} \rangle_{dis} = \frac{1}{N_{\text{meas}}} \sum_{n=1}^{N_{\text{meas}}} \langle \hat{O}(\{\delta a\}_n) \rangle \xrightarrow{N_{\text{meas}} \rightarrow \infty} \int \prod_\nu d\delta a_\nu P(\delta a_\nu) \langle \hat{O}(\{\delta a_\nu\}) \rangle \quad (2.28)$$

where $\langle O(\{\delta a\}) \rangle$ is the measured result obtained for a certain realization of the set of random variables $\{\delta a\}$. $P(\delta a_\nu) d\delta a = e^{-(\delta a - \mu_a)^2 / 2w_a^2} / \sqrt{2\pi w_a^2} d\delta a$ is the Gaussian distribution function characterizing the random variable δa .

2.3.6 Summary

We conclude this section with a short summary. Mapping a qubit system onto fermions using the Jordan-Wigner transformation induces non-local many-particle interactions between fermions. In particular, local transversal operators σ_i^\pm and transverse couplings between qubits further apart than nearest-neighbor are affected from these complicated interactions. Consequently, we restrict our discussion to quantum simulators with nearest-neighbor qubit exchange terms and longitudinal single qubit terms $\propto \sigma^z$. However, as mentioned before, for a quantum simulator designed to map to a fermionic system via the Jordan-Wigner transformation these problems do not occur and the Hamiltonian after mapping corresponds to the initial fermionic Hamiltonian.

Mapping qubit interactions with the environment onto fermions leads to similar problems. While longitudinal coupling, i.e., dephasing, maps to fluctuations of fermionic on-site energies in the effective Hamiltonian, mapping transverse coupling to fermions induces fermionic source terms which violate fermion number conservation. Noting that transverse coupling to a fermionic environment prevents these issues we restrict our discussion to relaxation due to such systems.

2.4 Model

The bulk of the remaining chapter will be concerned with decoherence in the interaction-free form of the quantum simulator defined in Eq. (2.15),

$$H_{\text{qs}} = \sum_i [h_i \sigma_i^z + J_i^x (\sigma_i^+ \sigma_{i+1}^- + \sigma_{i+1}^+ \sigma_i^-)]. \quad (2.29)$$

In the following we will separately discuss a quantum simulator subject to dephasing due to a bosonic bath, relaxation due an ensemble of TLS and finally subject to disorder and dephasing.

Measurements on the analog quantum simulator yield qubit-qubit correlation functions $C_{\text{qq}}(t, t')$ which after Jordan-Wigner transformation correspond to specific but complicated fermionic Green's functions. Here, we assume that the quantum simulator is actually used to calculate fermionic Green's functions. Thus, the ideal quantum simulator would return the qubit-qubit correlation function

$$\begin{aligned} C_{\text{qq}}^{ij}(z, z') &= \langle \mathcal{T}_C \sigma_i^-(z) e^{-i(\Phi_i(z) - \Phi_j(z'))} \sigma_i^+(z') \rangle_0 \\ &= \langle \mathcal{T}_C c_i(z) c_j^\dagger(z') \rangle_0 = iG_{0,ij}(z, z'). \end{aligned} \quad (2.30)$$

Due to coupling with the environment the noisy quantum simulator, however, returns a disturbed Green's function \mathcal{G} . As discussed the mapping of the Hamiltonian H_{qs} onto

fermions using the Jordan-Wigner transformation yields the fermionic representation of the noisy quantum simulator. The ideal quantum simulator maps to the fermionic system

$$H_0 = \sum_i [g_i(c_i^\dagger c_{i+1} + c_{i+1}^\dagger c_i) + \varepsilon_i c_i^\dagger c_i] = \sum_{ij} c_i^\dagger A_{ij} c_j. \quad (2.31)$$

We chose this model because the unperturbed Hamiltonian of the quantum simulator can be solved exactly by diagonalizing the hermitian matrix A . Knowledge of an exact solution allows a good estimate of the errors arising from imperfections. The eigenmodes of the system are obtained from $a_k = \sum U_{ki} c_i$ where U is the unitary matrix that diagonalizes A . For constant on-site energy $\varepsilon_i = \varepsilon$ and constant hopping $g_i = g$ the eigenenergies are $\epsilon_k = \varepsilon_i + 2 \cos k$ with $k = 2\pi n/N$. Using the fermionic Hamiltonian we calculate the perturbed Green's function in the framework of non-equilibrium Green's functions presented in chapter 1. In the fermionic picture the disturbed output \mathcal{G} is connected to the ideal output G_0 by the Dyson equation (1.14)

$$\mathcal{G}(z, z') = G_0(z, z') + \iint_C dz_1 dz_2 G_0(z, z_1) \Sigma[H_{\text{int}}, V](z_1, z_2) \mathcal{G}(z_2, z'). \quad (2.32)$$

Here, the self-energy Σ describes the influence of the environment on the result returned from the disturbed quantum simulator. The double-convolution on the right-hand side of the Dyson equation determines the deviation of the simulated result from the ideal result. Broadening of features are related to the rate function $\Gamma = i(\Sigma^R - \Sigma^A)$ and energy shifts to the function $\Delta = (\Sigma^R + \Sigma^A)/2$. In the following sections we will separately analyze dephasing, relaxation and disorder for this model using the methods presented in chapter 1. In particular, we will compare the spectral function $\mathcal{A}_0 = i[G_0^R - G_0^A]$ of the ideal with the spectral function $\mathcal{A} = i[\mathcal{G}^R - \mathcal{G}^A]$ of the perturbed quantum simulator and we will compare our method to master equation calculations.

Outlook We note that with the Dyson equation one can, in principal, find a relation connecting the perturbed results measured on the real-world quantum simulator to the ideal results for interacting systems, too. For an interacting systems such a relation is difficult to establish and needs further investigation. In Sec. 2.8 we give a short motivation and outlook on how such a relation could be established.

Initial state and choice of contour We will discuss decoherence of a quantum simulator for two special cases. Firstly, for a quantum simulator with time-independent Hamiltonian using the adiabatic approach discussed in section 1.4.1 on the Schwinger-Keldysh contour shown in Fig. 1.4. For a time-independent Hamiltonian this analysis yields equilibrium properties such as the spectral function or dephasing rates.

Secondly, we analyze a time dependent problem for a quantum simulator prepared in an initial state represented by a density matrix $\rho(t_0)$ characterized by an interaction-free Hamiltonian H_0^M as discussed in section 1.4.1. A non-interacting initial state describes, for example, a situation where all qubits are in their respective ground state. A possible application for such an initial state could be adiabatic quantum simulation where the quantum simulator is prepared in the ground state of a simple Hamiltonian and evolves quasi-adiabatically into the ground state of a more complex Hamiltonian.

We always assume that the initial density matrix factorizes into system and bath according to $\rho_0 = \rho_S \otimes \rho_B$ and that the bath is in thermal equilibrium at temperature T .

2.5 Dephasing due to a bosonic bath

In this section we use the adiabatic approach in order to analyze dephasing from a bath of harmonic oscillators. Each qubit couples to the position operators of a set of oscillators

$$\hat{X}_i^z = \sum_s g_{is} (a_{is} + a_{is}^\dagger). \quad (2.33)$$

This model describes, e.g., decoherence due to a resistive environment, phonons, or the radiation field [78]. The bath of oscillators is in equilibrium and characterized by its power spectrum [79]

$$S_i(\omega) = \int \frac{dt}{2\pi} \left\langle \left\{ \hat{X}_i^z(t), \hat{X}_i^z(t') \right\} \right\rangle_0 e^{i\omega t} = J_i(\omega) \coth \frac{\beta\omega}{2}. \quad (2.34)$$

$J_i(\omega) = \sum_s g_{is}^2 [\delta(\omega - \omega_{is}) - \delta(\omega + \omega_{is})]$ is the spectral density and $\langle \dots \rangle_0$ denotes an average with respect to the thermal density matrix ρ_B .

Because the qubits couple to a real field, $\hat{X}_i^z \propto a + a^\dagger$, the spectral density is antisymmetric, $J(\omega) = -J(-\omega)$. The power spectrum is related to the kinetic Green's function of the bath according to

$$D_{0,i}^K(\omega) = \sum_s [D_{0,is}^>(\omega) + D_{0,is}^<(\omega)] = -iS_i(\omega). \quad (2.35)$$

Similarly, we find the retarded and advanced components of the bath

$$D_{0,i}^{R/A}(\omega) = \int \frac{d\nu}{2\pi} \frac{J_i(\nu)}{\omega - \nu \pm i0}. \quad (2.36)$$

In the following section we use a diagrammatic expansion of the perturbed Green's function in order to calculate the broadening $\Gamma(\omega)$ and energy shifts $\Delta(\omega)$ charac-

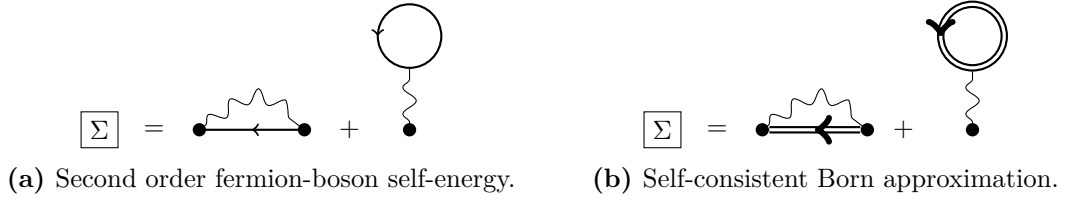


Figure 2.2: Self-energy for dephasing due to a bosonic bath in second order as well as self-consistent Born approximation.

terizing the influence of the bosonic bath on the quantum simulator. Subsequently, we use the frequency dependent rate function $\Gamma(\omega)$ obtained from the diagrammatic expansion to calculate the dephasing rate of a single qubit. For a Markovian bath we compare this rate to the usual golden-rule dephasing rate. Then, we analyze the behavior of the rate function for ohmic, sub-ohmic and super-ohmic environments in order to determine parameter regimes where Born-Markov approximations and master equation calculations are valid. Finally, we compare the spectral function of the perturbed quantum simulator obtained from many-body theory with the spectral function obtained from master equation calculations in the parameter regimes determined before.

2.5.1 Dephasing rate-function from a diagrammatic expansion

We calculate the self-energy characterizing the influence of the bosonic bath in second order in the coupling between qubits and environment. In this order two distinct diagrams contribute to the self-energy which we show in Fig. 2.2a. The first and second diagram respectively represent the Fock and the Hartree contribution. Calculating the Fock diagram we find $\Sigma_{\text{F},ij}(z, z') = i\delta_{ij}G_{0,ii}(z, z')D_{0,i}(z, z')$. Here, we used that bath operators of different qubits are uncorrelated according to assumption (2.2). Consequently, the Green's functions of the bath are diagonal in qubit space, $D_{0,ij} = D_{0,i}\delta_{ij}$. Using the Langreth rules for analytical continuation summarized in table 1.1 we find

$$\Sigma_{\text{F},ij}^{R/A}(t, t') = \delta_{ij} \frac{i}{2} [G_{0,ii}^{R/A}(t, t')D_{0,i}^K(t, t') + G_{0,ii}^K(t, t')D_{0,i}^{R/A}(t, t')] \quad (2.37)$$

$$\Sigma_{\text{F},ij}^K(t, t') = \delta_{ij} \frac{i}{2} [G_{0,ii}^K D_{0,i}^K + (G_{0,ii}^R - G_{0,ii}^A)(D_{0,i}^R - D_{0,i}^A)]. \quad (2.38)$$

The Fock self-energy for dephasing due to a bosonic bath is similar to the self-energy describing electron-phonon interaction as discussed, for example, by Rammer and

Smith [45]. In Fourier space the diagonal elements of the Fock self-energy read as

$$\begin{aligned} \Sigma_{ii}^{R/A}(\omega) = & -\frac{1}{2} \int \frac{d\nu}{2\pi} \left[G_{0,ii}^{R/A}(\omega - \nu) J_i(\nu) \coth \frac{\nu}{2T} \right. \\ & \left. + i \int \frac{d\nu'}{2\pi} G_{0,ii}^K(\omega - \nu) \frac{J_i(\nu')}{\nu - \nu' \pm i0} \right] \end{aligned} \quad (2.39)$$

$$\begin{aligned} \Sigma_{ii}^K(\omega) = & -\frac{1}{2} \int \frac{d\nu}{2\pi} J_i(\nu) (G_{0,ii}^R(\omega - \nu) - G_{0,ii}^A(\omega - \nu)) \\ & \times \left[\tanh \frac{(\omega - \nu)}{2} \coth \frac{\nu}{2T} + 1 \right]. \end{aligned} \quad (2.40)$$

The second diagram yields the Hartree self-energy $\Sigma_{H,ij}(z, z') = -i\delta_{ij}\delta(z, z') \int d\bar{z} \times D_{0,i}(z, \bar{z})G_{0,ii}(\bar{z}, z^+)$. The equal-time fermionic Green's function corresponds to the occupation number, $G_{0,ii}(z, z^+) = -in_i$. We evaluate the contour integral and transform the self-energy into Fourier-space. Since D_0 is the Green's function of a real field with $J(0) = 0$ the Hartree self-energy is purely real and induces an energy shift but no broadening. Additionally, the Hartree contribution is time-local and the energy shift is constant in Fourier space:

$$\Sigma_{H,ii}^{R/A}(\omega) = n_i \int_{-\infty}^{\infty} \frac{d\nu}{2\pi} P \left[\frac{J_i(\nu)}{\nu} \right], \quad (2.41)$$

where P denotes the Cauchy principal value. Adding the Hartree and the Fock contribution yields the self-energy in lowest order in the coupling between qubits and environment. From the self-energy the rate function $\hat{\Gamma} = i(\Sigma^R - \Sigma^A)$ and the energy shift $\hat{\Delta} = (\Sigma^R + \Sigma^A)/2$ in second order approximation follow as

$$\hat{\Gamma}(\omega) = -\frac{1}{2} \int \frac{d\nu}{2\pi} \mathcal{A}_0(\omega - \nu) \odot \mathcal{J}(\nu) \left[\tanh \frac{(\omega - \nu)}{2} + \coth \frac{\nu}{2T} \right] \quad (2.42)$$

$$\begin{aligned} \hat{\Delta}(\omega) = & -\frac{1}{2} \int \frac{d\nu}{2\pi} \left[\text{Re}[G_0^R(\omega - \nu)] \odot \mathcal{J}(\nu) \coth \frac{\beta\nu}{2} \right. \\ & \left. + iG_0^K(\omega - \nu) \odot \text{Re}[D_0^R(\nu) - D_0^R(0)] \right] - \text{Re}[D_0^R(0)]. \end{aligned} \quad (2.43)$$

Here, \odot denotes element wise multiplication in qubit Hilbert space. \mathcal{J} is a diagonal matrix with entries $[\mathcal{J}(\omega)]_{ii} = J_i(\omega)$ and $\mathcal{A}_0(\omega) = i[G_0^R(\omega) - G_0^A(\omega)]$ is the spectral function of the ideal quantum simulator.

Rate function and energy shift are diagonal operators in qubit space. In order to derive the expression for the energy shift $\hat{\Delta}(\omega)$ we used the relations $n_i = \frac{1}{2}(1 - iG^K(t, t))$ and $\text{Re}[D^R(\omega)] = \int \frac{d\nu}{2\pi} \frac{J(\nu)}{\omega - \nu}$. The Green's functions of the perturbed system

can be expressed in terms of the rate function and energy shift as

$$\mathcal{G}^{R/A}(\omega) = \frac{1}{\omega - [H_0 + \hat{\Delta}(\omega)] \pm \frac{i}{2}\hat{\Gamma}(\omega)} \quad (2.44)$$

$$\mathcal{G}^K(\omega) = -i\mathcal{G}^R(\omega)\hat{\Gamma}(\omega) \tanh \frac{\beta\omega}{2} \mathcal{G}^A(\omega). \quad (2.45)$$

The function $\hat{\Delta}$ induces shifts of the eigenenergies of the system while the rate function describes a broadening of the corresponding peaks in the spectral function.

Single qubit dephasing For a single qubit coupled to an environment characterized by a flat power spectrum the dephasing rate usually is calculated using Fermi's golden-rule. For such an environment our method should certainly yield the same result.

Using Eq.(2.42) the rate function and energy shift function of a single qubit with energy splitting ε in second order approximation read as

$$\hat{\Gamma}(\omega) = \frac{1}{2}J(\omega - \varepsilon) \left[\tanh \frac{\beta\varepsilon}{2} + \coth \frac{\beta(\omega - \varepsilon)}{2} \right] \quad (2.46)$$

$$\begin{aligned} \hat{\Delta}(\omega) = & - \int \frac{d\nu}{2\pi} \frac{\omega - \nu - \varepsilon_i}{(\omega - \nu - \varepsilon_i)^2 + \eta^2} J(\nu) \coth \frac{\beta\nu}{2} \\ & - \tanh \frac{\beta\varepsilon}{2} \operatorname{Re}[D_0^R(\omega - \varepsilon) - D_0^R(0)]. \end{aligned} \quad (2.47)$$

The Green's functions of the single qubit are peaked at the qubit energy splitting ε and the rate function is mainly evaluated at that energy. Due to the environment a peak at energy ε obtains a finite width $\propto \hat{\Gamma}(\varepsilon)$. If the power spectrum is flat close to the peak, i.e., $S(\omega) \approx \text{const.}$ for $|\omega - \varepsilon| \lesssim \hat{\Gamma}(\varepsilon)$, we can substitute $\omega \rightarrow \varepsilon$ in the rate function of the qubit. This yields the single qubit dephasing rate Γ_{2^*} and shift Δ_{2^*}

$$\Gamma_{2^*} = \lim_{\omega \rightarrow 0} J_i(\omega) \coth \frac{\beta\omega}{2} = S_i(0) \quad (2.48)$$

$$\Delta_{2^*} = \frac{1}{2} \int \frac{d\nu}{2\pi} \frac{J(\nu)\nu}{\nu^2 + \eta^2} \left[\coth \frac{\beta\nu}{2} + 1 \right]. \quad (2.49)$$

These results correspond to the usual golden-rule results for single qubit dephasing. The validity of the assumption of a flat power spectrum has to be checked self-consistently with the obtained rate Γ_{2^*} .

Two conditions must be fulfilled so that the approximation is valid. Firstly, bath correlation functions have to decay on short time scales compared to the lifetime of qubit excitations, i.e., $D(t - t') \propto e^{-\gamma|t-t'|}$ with rate $\gamma \gg \Gamma_{2^*}$. This corresponds to a memoryless bath where the Markov approximation is valid. Secondly, the coupling strength between bath and system has to be weak in the following sense: The broadening of the peaks in the Green's functions remains so small that the substitution

$\omega \rightarrow \varepsilon$ in the rate function is still valid. This corresponds to the validity of the Born approximation. For stronger coupling the broadening increases and the peaks cover a wider range of frequencies. Even for a relatively flat power spectrum the frequency dependence of the rate function can no longer be neglected. For large system-bath coupling a self-consistent Born approximation is better suited than the second-order approximation as it takes into account higher order terms in the interaction.

We conclude that for a system-bath interaction for which the Born-Markov approximation applies we recover the golden-rule results for single qubit dephasing.

Self-consistent Born approximation A better approximation for the self-energy can be obtained by replacing all free fermionic Green's functions with full Green's functions in the self-energy. This corresponds to the diagrams depicted in Fig. 2.2b. We assume that the bath reservoirs are large and are not affected by the coupling with the quantum simulator. The full bath Green's functions are thus identical to the free Green's functions $D(\omega) = D_0(\omega)$. The substitution $G_0 \rightarrow \mathcal{G}$ yields the self-consistent set of equations

$$\hat{\Gamma}^{\text{sc}}(\omega) = -\frac{1}{2} \int \frac{d\nu}{2\pi} \mathcal{A}(\omega - \nu) \odot \mathcal{J}(\nu) \left[\tanh \frac{\beta(\omega - \nu)}{2} + \coth \frac{\nu}{2T} \right] \quad (2.50)$$

$$\begin{aligned} \hat{\Delta}^{\text{sc}}(\omega) = & -\frac{1}{2} \int \frac{d\nu}{2\pi} \left[\text{Re}[\mathcal{G}^R(\omega - \nu)] \odot \mathcal{J}(\nu) \coth \frac{\beta\nu}{2} \right. \\ & \left. + i\mathcal{G}^K(\omega - \nu) \odot \text{Re}[D_0^R(\nu) - D_0^R(0)] \right] \end{aligned} \quad (2.51)$$

$$\mathcal{A}(\omega) = \mathcal{G}^R(\omega) \hat{\Gamma}^{\text{sc}}(\omega) \mathcal{G}^A(\omega). \quad (2.52)$$

Full quantum simulator Now, we use the second order rate function (2.42) in order to calculate dephasing rates of the coupled qubit system. The fermionic representation Eq. (2.31) of the quantum simulator can be diagonalized by the transformation

$$c_i \rightarrow U_{ik} a_k \quad (2.53)$$

where U is a unitary transformation matrix. The non-interacting Hamiltonian is diagonal in the new basis with eigenenergies ε_k . Expressing the Green's functions of the quantum simulator in terms of the Green's function $\hat{G}_{kk'}$ in the diagonal basis we find

$$\hat{\mathcal{G}}_{ij} = \sum_{kk'} U_{ik} \hat{\mathcal{G}}_{kk'} U_{k'j}^\dagger. \quad (2.54)$$

In the eigenbasis the non-interacting Green's functions read as $G_{0,kk'}^{R/A}(\omega) = \delta_{kk'} (\omega - \varepsilon_k \pm i\eta)^{-1}$ and $G_{0,kk'}^K(\omega) = -2\pi i \delta_{kk'} \delta(\omega - \varepsilon_k)$. The matrix elements $\hat{\Gamma}_{ii}$ of the rate function can be expressed in terms of the transformation matrix U and the eigenenergies of the

system,

$$\hat{\Gamma}_{ii}(\omega) = \frac{1}{2} \sum_k |U_{ik}|^2 J_i(\omega - \varepsilon_k) \left[\tanh \frac{\beta \varepsilon_k}{2} + \coth \frac{\beta(\omega - \varepsilon_k)}{2} \right]. \quad (2.55)$$

Similar to the single qubit Green's functions the Green's functions $\mathcal{G}_{ij}(\omega)$ of the coupled system are peaked around the system energies $\omega \approx \varepsilon_k$ with width $\propto \hat{\Gamma}(\varepsilon_k)$. For a flat power spectrum the broadening of a peak at energy ε_k is approximately given by the constant rate

$$\Gamma_{2^*,i,k} = \frac{1}{2} \sum_{k'} |U_{ik'}|^2 J_i(\varepsilon_k - \varepsilon_{k'}) \left[\tanh \frac{\beta \varepsilon_{k'}}{2} + \coth \frac{\beta(\varepsilon_k - \varepsilon_{k'})}{2} \right]. \quad (2.56)$$

The rate function of the coupled system Eq. (2.55) and the corresponding golden-rule approximation (2.56) depend on the differences of eigenenergies of the system $\varepsilon_k - \varepsilon_{k'}$. We distinguish three situations. Firstly, for a power spectrum that is flat over the entire energy range covered by the system the dephasing rates of the coupled system correspond to the single qubit dephasing rates. Here, we expect that a Lindblad master equation with single qubit rates can be used to simulate the quantum simulator. Secondly, the power spectrum is flat on a frequency range $\propto \hat{\Gamma}(\varepsilon_k)$ but varies over the range covered by the system. In this situation the disturbed quantum simulator can still be characterized by constant rates but the rates differ from the single qubit rates. Here, a Bloch-Redfield master equation which evaluates the power spectrum at the system energies yields reliable results. Thirdly, if the power spectrum is not flat at all constant-rate master equations cannot accurately simulate the system.

2.5.2 Analysis for environments characterized by a power-law spectral density

In this section we analyze dephasing of single qubits and a chain of qubits due to an environment characterized by a power-law spectral density using second-order and self-consistent Born approximations for the self-energy. From this analysis we extract parameter regimes where dephasing can be characterized by constant rates in order to compare with master equation calculations.

We will compare the results obtained with the fermionic theory with master equation calculations for a linear chain of N qubits with equal on-site energies $h_i = \varepsilon$ and constant nearest-neighbor hopping $t_{i,i+1} = g$ in the next section. The chain is represented by the fermionic Hamiltonian

$$H_0 = \sum_i \varepsilon c_i^\dagger c_i + \frac{g}{2} (c_{i+1}^\dagger c_i + c_i^\dagger c_{i+1}) \quad (2.57)$$

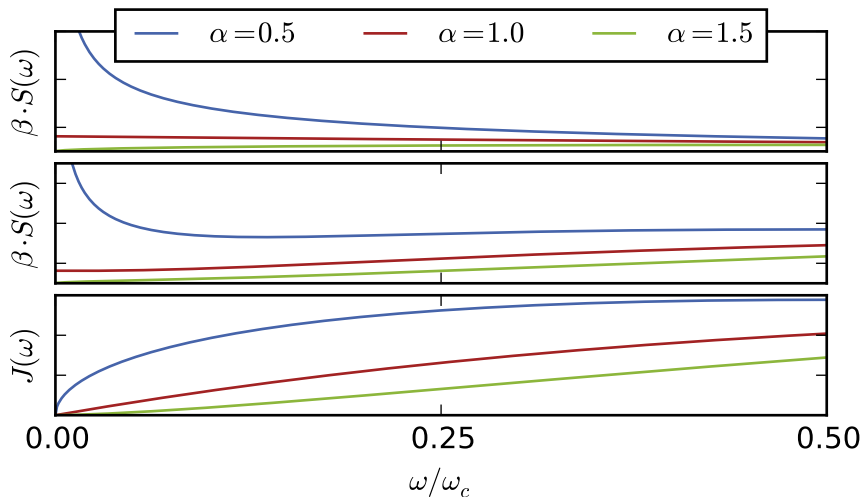


Figure 2.3: The spectral density $J(\omega)$ defined in Eq. (2.59) (*bottom*) and the power spectrum $S(\omega) = J(\omega) \coth(\beta\omega/2)$ for large temperature $\beta \ll \omega_c$ (*top*) and small temperature $\beta \gg \omega_c$ (*middle*).

with eigenenergies $\varepsilon_k = \varepsilon + g \cos k$ with $k = 2\pi n/N$.

The bath is characterized by its spectral density. In order to realize different situations with flat power spectrum and frequency dependent power spectrum as well as weak and strong effective coupling we assume a power-law form of the spectral density,

$$J_i(\omega) = \text{sign}(\omega) \frac{\pi}{2} \lambda_i \omega_c \left| \frac{\omega}{\omega_c} \right|^\alpha e^{-|\omega/\omega_c|}. \quad (2.58)$$

Here, ω_c is a characteristic frequency of the bath and λ_i is a dimensionless coupling constant. The exponent α determines the nature of the environment: sub-ohmic for $0 < \alpha < 1$, ohmic for $\alpha = 1$ and super-ohmic for $\alpha > 1$. We plot the spectral-density and the corresponding power spectrum for the three different types of noise in Fig. 2.3.

With Eq. (2.48) and using the series expansion $\coth(x) = 1/x + \mathcal{O}(x)$ we find the single qubit golden-rule dephasing rate

$$\Gamma_{2^*} = \lim_{\omega \rightarrow 0^+} J(\omega) \coth \frac{\beta\omega}{2} = \frac{\pi \lambda_i}{\beta} \lim_{\omega \rightarrow 0^+} \left(\frac{\omega}{\omega_c} \right)^{\alpha-1}. \quad (2.59)$$

We note that the effective coupling strength between bath and system scales with the temperature according to $\lambda_i^{\text{eff}} = \lambda_i/\beta$. In order to obtain comparable results for different temperatures we scale the coupling constant with the inverse temperature in all subsequent calculations.

Furthermore, the golden-rule rate only is defined for an ohmic bath. For a sub-ohmic bath the power-spectral density diverges for small frequencies while it vanishes for a

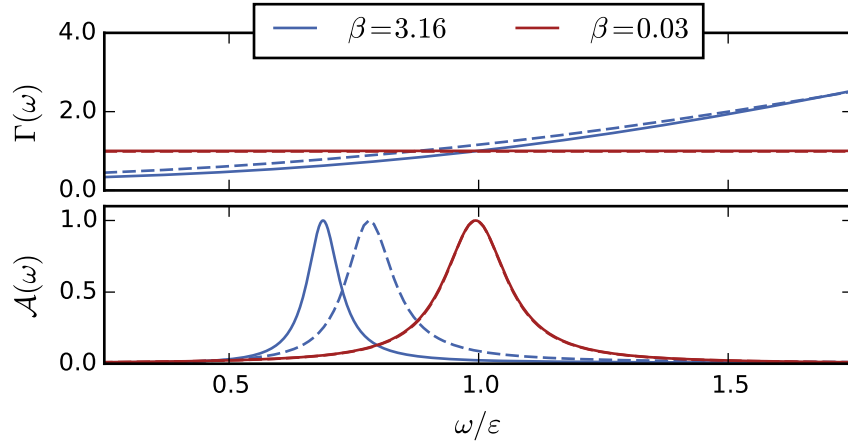


Figure 2.4: Single qubit coupled to an ohmic environment at low temperature, $\beta = 3.16/\varepsilon$ and high temperature, $\beta = 0.03/\varepsilon$. Solid lines correspond to second-order results and dashed lines to self-consistently obtained solutions. For comparability, the coupling constants are scaled with the inverse temperature, $\lambda \rightarrow \beta\lambda$. *Top:* Rate function normalized to the golden-rule rate, $\Gamma(\omega)/\Gamma_{2^*}$. For high temperatures the full rate function is constant and coincides with the golden-rule rate. For small temperatures the rate function becomes frequency dependent. Due to the relatively small coupling to the environment the effect of self-consistency on the rate is small. *Bottom:* Normalized qubit spectral function $\mathcal{A}(\omega)$. Coupling to the environment induces broadening $\propto \Gamma(\omega)$ of the peaks and an energy shift $\propto \Delta(\omega)$.

super-ohmic bath. The self-consistent approximation for the self-energy yields finite rates for both sub-ohmic and super-ohmic environment.

For an ohmic bath, the condition of a flat power spectrum is met for high temperatures $\beta^{-1} = k_B T \gg \Gamma_{2^*}$. For high temperatures and an ohmic bath we find the single qubit dephasing rate

$$\Gamma_{2^*,\text{ohmic}} = \frac{\pi\lambda_i}{\beta} = \pi\lambda_i^{\text{eff}}. \quad (2.60)$$

For small temperatures the frequency dependence of $\Gamma(\omega)$ cannot be neglected. In Fig. 2.4 we plot the normalized rate function $\Gamma(\omega)/\Gamma_{2^*,\text{ohmic}}$ and the spectral function of the qubit $\mathcal{A}(\omega)$ for a single qubit coupled to an ohmic environment at different temperatures. As expected, the golden-rule approximation and the full rate function coincide for high temperatures while the rate depends on the frequency for lower temperatures. Additionally, coupling to an ohmic bath at small temperatures induces an energy shift to smaller energies. Hence, the rate function is evaluated at a smaller frequency $\omega < \varepsilon$. We can improve the golden-rule results by taking the energy shift into account in the golden-rule rate according to $\Gamma_{2^*} \approx \hat{\Gamma}(\varepsilon + \Delta_{2^*})$. For an ohmic bath the power spectrum remains relatively flat on the scale determined by the rate Γ_{2^*} and the golden-rule-approximation with energy shift yields reasonably good results.

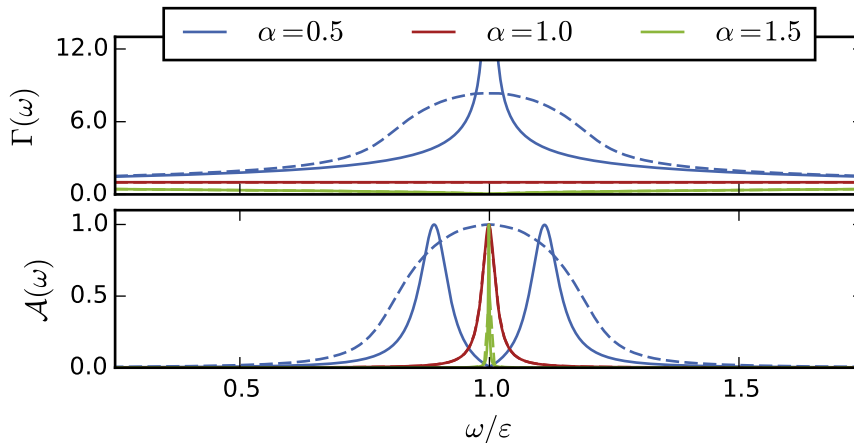


Figure 2.5: Single qubit coupled to environments characterized by the exponent α and the inverse temperature $\beta = 0.03/\varepsilon$. Solid lines correspond to second-order results and dashed lines to self-consistently obtained solutions. *Top:* Dephasing rate function $\Gamma(\omega)/\Gamma_{2^*,\text{ohmic}}$. Here, $\Gamma_{2^*,\text{ohmic}}$ is the golden-rule rate due to interaction with an ohmic bath. For a sub-ohmic environment ($\alpha = 0.5$) the rate function in second order approximation diverges at the qubit energy. In self-consistent Born approximation the divergence is smoothed and a finite rate is obtained. A super-ohmic bath weakly contributes to dephasing due to the vanishing power spectrum for small frequencies. *Bottom:* Normalized spectral function $\mathcal{A}(\omega)$ of the qubit. Due to the divergent rate function only the self-consistent Born approximation yields reliable results for a sub-ohmic environment.

Self-consistent Born does not significantly change the rate function due to an ohmic bath.

To demonstrate the influence of the exponent α of the spectral density on the dephasing behavior we compare $\Gamma(\omega)$ for a single qubit coupled to a sub-ohmic, ohmic, and super-ohmic environment. In Fig. 2.5 we plot the corresponding rate functions normalized to the golden-rule rate of the ohmic environment, $\Gamma(\omega)/\Gamma_{2^*,\text{ohmic}}$. For the ohmic environment the rate function is well characterized by the constant rate Γ_{2^*} . Contrary, for the sub-ohmic environment the rate function in second order approximation diverges for $\omega \rightarrow \varepsilon$. Thus, we use the self-consistent Born approximation which smooths the divergence and yields a finite rate function. In chapter 4 we show that the spectral density characterizing superconducting quasiparticles diverges for small frequencies. Using a similar approach Catelani et al. obtained a self-consistent qubit dephasing rate due to quasiparticle tunneling [80]. A super-ohmic environment weakly contributes to dephasing because the rate function vanishes for $\omega \rightarrow \varepsilon$.

From our considerations for a single qubit we conclude that for an environment characterized by a power-law spectral density results of Born-Markov master equations can compare to our method only for an ohmic bath.

After discussing single qubit dephasing due to the different environments we turn to the full simulator and analyze the influence of decoherence on the coupled chain

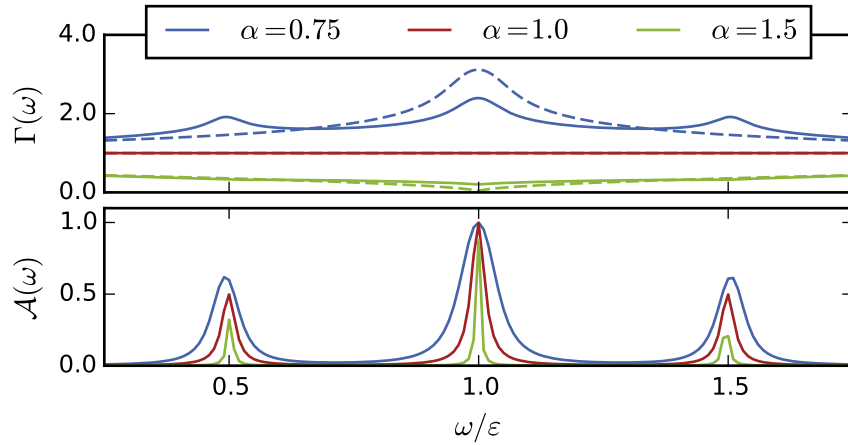


Figure 2.6: Numerical simulation of a chain comprising four qubits with nearest-neighbor hopping $g = 0.5\varepsilon$ and on-site energies $h_i = \varepsilon$. The chain couples to baths characterized by the exponent α . The inverse temperature is $\beta = 3.16/\varepsilon$. *Top:* Self-consistently obtained rate function of the first qubit, $\Gamma_{11}^{\text{sc}}(\omega)/\Gamma_{2^*,\text{ohmic}}$, normalized to the single qubit golden-rule rate due to an ohmic bath (solid lines). Dashed lines show the corresponding single qubit rate function $\Gamma_{\text{sq},1}^{\text{sc}}(\omega)/\Gamma_{2^*,\text{ohmic}}$. For the ohmic environment the single qubit rate function is identical to the multi-qubit function. For the strongly frequency dependent sub-ohmic bath the rates of the multi-qubit system and the single qubit differ. *Bottom:* Normalized spectral function $\mathcal{A}_{11}(\omega)$ of qubit 1 with peaks at the system's eigenenergies.

of qubits. The spectral density of the unperturbed system is peaked at the energies $\varepsilon_k = \varepsilon + g \cos k$. For a flat spectral density the rate function of the coupled qubit-system defined in Eq. (2.55) is almost constant in the relevant energy range. If these assumptions are fulfilled each peak in the diagonal components of the spectral density $\mathcal{A}_{ii}(\omega)$ can be characterized by the single qubit dephasing rate $\Gamma_{2^*,i}$. For a frequency dependent rate function the width of each peak has a different width which depends on the system energies ε_k as well as the matrix elements $|U_{ik}|$.

Consequently, we expect that for an ohmic bath at high temperature the single qubit dephasing rates suffice to describe the perturbed many-qubit system. Contrary, for a sub-ohmic bath or an ohmic environment at low temperatures we expect deviations from the single qubit behavior. In Fig. 2.6 we show the spectral density $\mathcal{A}_{11}(\omega)$ corresponding to the first qubit for a chain comprising four qubits with hopping $g = 0.5\varepsilon$. The chain is coupled to different environments at a high temperature. Our numerical calculations confirm our expectation: dephasing due to an ohmic environment is well characterized by the single qubit rates while for sub-ohmic and super-ohmic environments we find strong deviations from single qubit behavior. Rates and spectral function are obtained self-consistently.

Even for small temperatures the ohmic environment provides a rather flat spectral density as shown in Fig. 2.7. Thus, dephasing due to the low-temperature ohmic bath

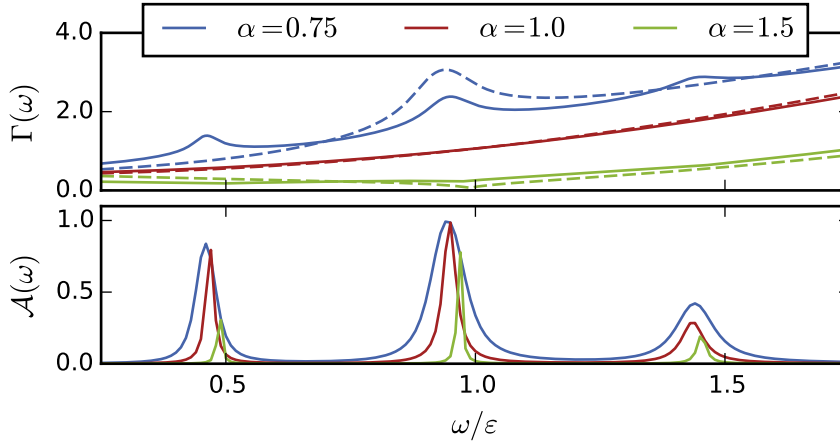


Figure 2.7: Same system as in Fig. 2.6 but the inverse temperature is $\beta = 3.16/\varepsilon$. *Top:* Self-consistent rate function $\Gamma_{11}^{\text{sc}}(\omega)/\Gamma_{2^*,\text{ohmic}}$ (solid lines). Dashed lines show the corresponding single qubit rate function $\Gamma_{\text{sq},1}^{\text{sc}}(\omega)/\Gamma_{2^*,\text{ohmic}}$. For the ohmic environment the single qubit rate function and the multi-qubit function are very similar. *Bottom:* Normalized spectral function $\mathcal{A}_{11}(\omega)$ of qubit 1.

can be described by the constant rates (2.56) of the full system.

2.5.3 Comparison with master equation

For small systems the time evolution of the noisy quantum simulator can be calculated with quantum master equations as discussed in section 1.5. Since quantum master equations are the standard method used to analyze decoherence in qubit systems we validate our method, i.e., mapping to fermionic system and expansion on the Keldysh contour, by comparing it with master equation calculations.

The chain of qubits is represented by the Hamiltonian

$$H_{\text{qs}} = \sum_i \frac{\varepsilon}{2} (\sigma_i^z + 1) + \frac{g}{2} (\sigma_{i+1}^+ \sigma_i^- + \sigma_i^+ \sigma_{i+1}^-). \quad (2.61)$$

The Lindblad form of the Markovian master equation Eq. (1.63) for the density matrix ρ of the quantum simulator reads as

$$\begin{aligned} \dot{\rho} = \mathcal{L} \rho = & -i[\rho, H_{\text{qs}}] + \sum_i \frac{\Gamma_{2^*,i}}{2} (\sigma_i^z \rho \sigma_i^z - \rho) \\ & + \frac{\Gamma_{1,i}}{2} (2\sigma_i^- \rho \sigma_i^+ - [\sigma_i^+ \sigma_i^-, \rho]_+). \end{aligned} \quad (2.62)$$

The rates correspond to the single qubit dephasing rate $\Gamma_{2^*,i}$ and the single qubit decay rate $\Gamma_{1,i}$. We formally integrate the master equation (2.62) to obtain $\rho(t) = e^{\mathcal{L}(t-t')} \rho(t')$. For a master equation in Markov approximation two-time correlation

functions can be calculated using the quantum regression theorem [66]. For $\tau \geq 0$ the theorem states

$$\langle \hat{A}(t + \tau) \hat{B}(t) \rangle = \text{tr}\{\hat{A}e^{\mathcal{L}\tau}[\hat{B}\rho(t)]\} \quad (2.63)$$

$$\langle \hat{A}(t) \hat{B}(t + \tau) \rangle = \text{tr}\{\hat{B}e^{\mathcal{L}\tau}[\rho(t)\hat{A}]\}. \quad (2.64)$$

We use the QuTip python package [81] to calculate the fermionic Green's functions with the quantum regression theorem. For example, the Green's function $\mathcal{G}^>$ is obtained from

$$\begin{aligned} \mathcal{G}_{ij}^>(\tau + t, t) &= -i\langle c_i(t + \tau)c_j^\dagger(t) \rangle \\ &= -i\left\langle \prod_{k < i} (-\sigma_k^z)\sigma_i^-(t + \tau) \prod_{l < j} (-\sigma_l^z)\sigma_j^-(t) \right\rangle. \end{aligned} \quad (2.65)$$

While the quantum regression theorem directly applies to time dependent problems we have to tweak it slightly in order to compare it with results obtained within the adiabatic approach of the fermionic method. This is, we have to define the correct initial state for the regression theorem. We realize this by assuming that our system was decoupled from the bath and in thermal equilibrium $\rho(0) = Z^{-1}e^{-\beta H_{\text{qs}}}$ in the distant past. Subsequently, we evolve the density matrix with the Lindblad operator \mathcal{L} for a time $t \gg \Gamma_0^{-1}$, where Γ_0^{-1} is a time scale defined by the smallest decoherence rate of the system. Correlations between bath and qubit system develop during the time evolution until the entire system eventually reaches a stationary state. We use the corresponding density matrix as initial state in the quantum regression theorem. Consequently, the correlation function only depends on the time difference τ . In order to compare the results from the master equation approach we calculate the Fourier transform with respect to τ . The Green's functions obtained by this calculation correspond to the Green's functions obtained with the adiabatic approach of the fermionic theory.

In Fig. 2.8 we compare master equation calculations with the results obtained from Keldysh-calculations. We compare results for an ohmic bath at two different temperatures $k_B T \gg \varepsilon + g$ and $k_B T \ll \varepsilon + g$.

From our considerations we expect that a quantum simulator in contact with an ohmic environment at a high temperature can be described with a Lindblad master equation. For the Lindblad master equation we use the single qubit dephasing rates Γ_{2^*} given in Eq. (2.60). As expected, the Lindblad and Keldysh calculations are identical for high temperatures (left-hand column, bottom). The description with single qubit dephasing rates fails for low temperatures (left-hand column, top).

However, as mentioned before dephasing due to a low-temperature ohmic bath can

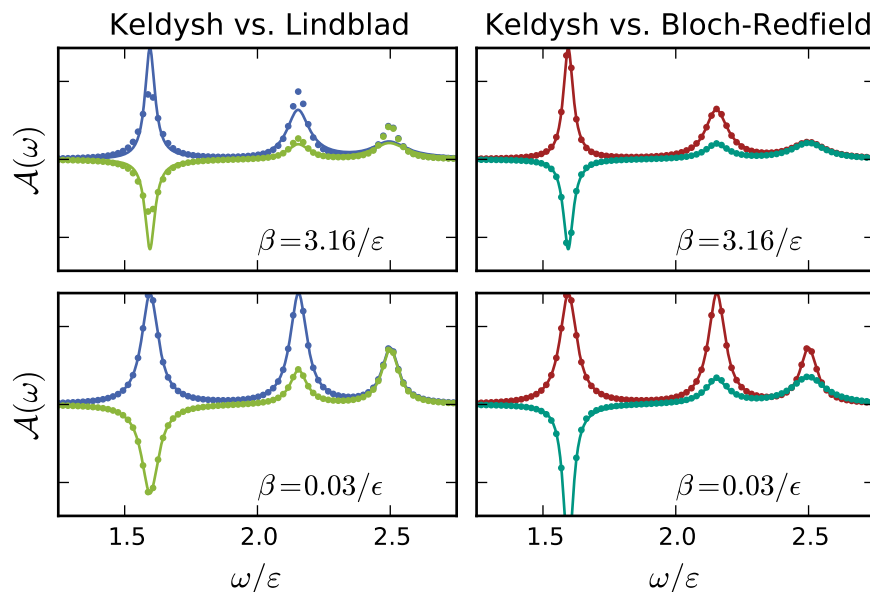


Figure 2.8: Numerical simulation of a tight binding chain with $N = 5$ sites with on-site energy $\varepsilon = 2$ and hopping $g = 0.5\varepsilon$ coupled to an ohmic environment at inverse temperature $\beta = 3.16/\varepsilon$ (top row) and $\beta = 0.03/\varepsilon$ (bottom row). We plot the components $\mathcal{A}_{11}(\omega)$ and $\mathcal{A}_{12}(\omega)$ of the spectral function obtained via Keldysh calculation (solid lines) and master equation calculations (dots). In the left column we show results obtained with a master equation in Lindblad form. We used single qubit dephasing-rates, Eq. (2.59), to define Lindblad collapse operators. The Lindblad master equation fails at small temperatures where the rate function depends on frequency. In the right-hand column we show results from a Bloch-Redfield master equation. Bloch-Redfield and Keldysh method are in perfect agreement.

be characterized by the single qubit rate function evaluated at the system's energies. For such a system we can use a Bloch-Redfield master equation to calculate the spectral function of the perturbed system. In a Bloch-Redfield approach the spectral density is evaluated at the system's excitation energies. Bloch-Redfield and Keldysh method are in good agreement for an ohmic bath as shown in the right-hand column of Fig. 2.8.

For a sub-ohmic environment one cannot define a dephasing-rate in golden-rule approximation. Consequently, we expect that both Bloch-Redfield and Lindblad master equation do not suffice to describe a system coupled to such an environment. We compare Bloch-Redfield and many-body results in Fig. 2.9 for a super-ohmic and a sub-ohmic environment with infrared cutoff $\omega_{ir} = 10^{-6}\varepsilon$.

We conclude, that the mapping of longitudinal noise to fermionic operators works as expected. In regimes where the Bloch-Redfield or Lindblad master equation approach are valid our method compares well to them. With the Keldysh-approach we can additionally handle situations where frequency-dependent spectral densities render simple master equation approaches inaccurate.

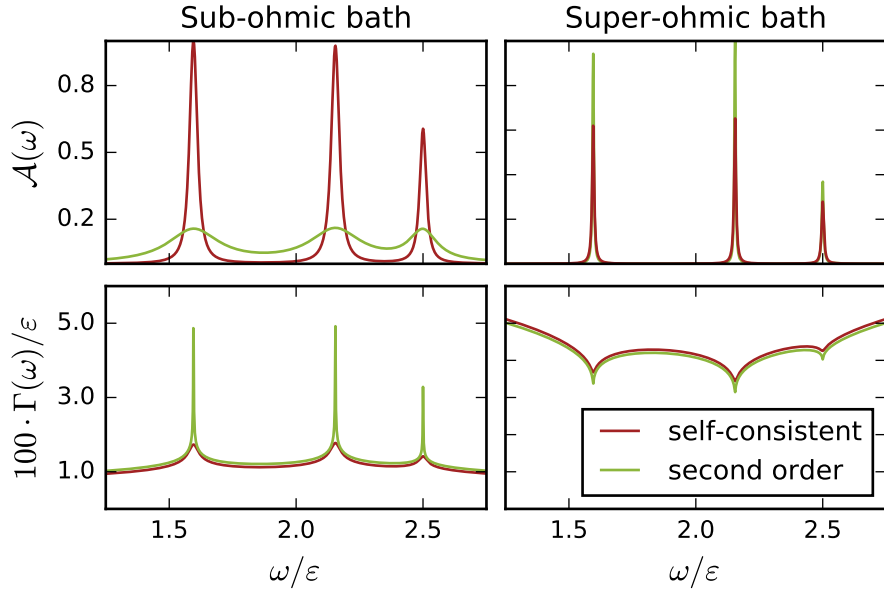


Figure 2.9: Numerical simulation of a tight binding chain with $N = 5$ sites with on-site energy $\varepsilon = 2$ and hopping $g = 0.5\varepsilon$ coupled to a sub-ohmic (*left column*) and super-ohmic (*right column*) environment. In the *top row* we plot the component $\mathcal{A}_{11}(\omega)$ of the spectral function obtained via self-consistent many-body calculation (red) and Bloch-Redfield master equation (green). In the *bottom row* we show the second-order rate function (green) which, evaluated at the system energies ε_k , corresponds to the Bloch-Redfield-rates and the self-consistent rate (red) used in the the many-body calculation. The super-ohmic rate is scaled by an additional factor of 10.

2.5.4 Effect of decoherence in large systems

In this section we analyze effects of decoherence on the spectral resolution of a large quantum simulator. The spectral-resolution $\delta\omega(\omega)$ determines the minimal distance of features in the spectral function that can be resolved by the quantum simulator at a given frequency ω . From our earlier considerations we know that due to the environment features in the spectral function obtain a finite width determined by the rate function $\hat{\Gamma}(\omega)$. From this the spectral-resolution can be estimated as $\delta\omega \gtrsim \hat{\Gamma}/2$ meaning that only features further apart than the width determined by the coupling to the environment can be resolved by the quantum simulator.

Another important quantity is the relative resolution which compares the spectral resolution of the quantum simulator with typical energy scales of the simulated system. We define the relative resolution as $\delta\omega/\delta\varepsilon$, where $\delta\varepsilon$ denotes a characteristic energy difference of the system. The relative resolution is a system specific measure of the resolution one can expect from a quantum simulation.

An interesting feature is the scaling of the relative resolution with the system size. Typically, eigenenergies of a system become more and more dense with increasing

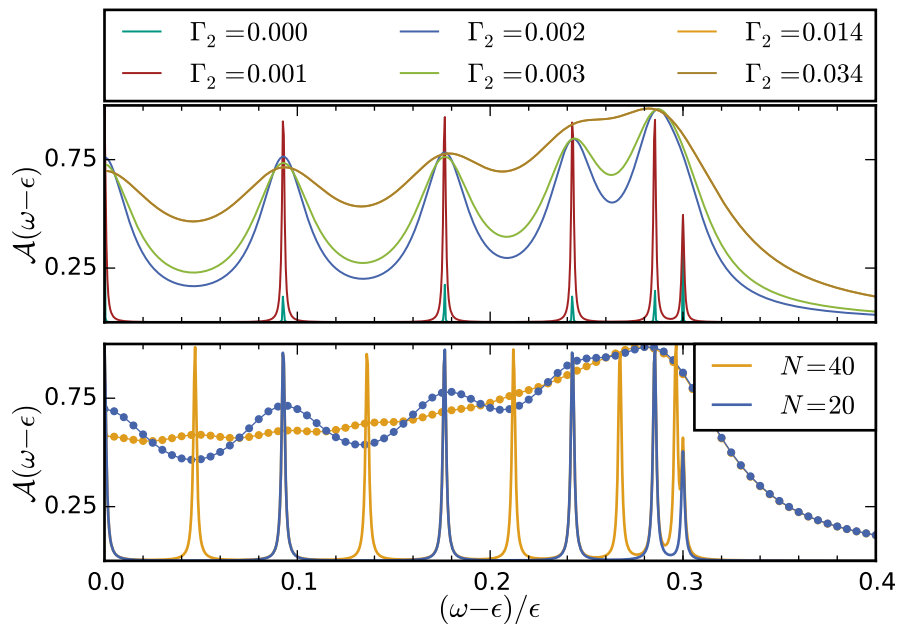


Figure 2.10: Numerical simulation of tight binding chains with hopping $g = \epsilon/2$ coupled to high temperature ohmic baths. *Top:* The spectral function \mathcal{A}_{00} for $N = 20$ sites and increasing dephasing strength. The dephasing strength is measured by the golden-rule rates Γ_2 that correspond to the ohmic environment used in the simulations. *Bottom:* For $N = 20$ and $N = 40$ sites we compare the spectral function returned from a noisy quantum simulator (dots) with the ideal one (solid lines). The corresponding golden-rule dephasing rate is $\Gamma_2 = 0.034$.

system size until they become continuous in the limit of an infinitely large system. Consequently, the relative resolution gets worse with increasing system size. For small relative resolutions individual features of the simulated system are lost and the simulated spectral function more and more resembles that of a continuous system.

For the linear chain of qubits with nearest-neighbor hopping g and on-site energy ϵ discussed in the previous section the energy difference between two neighboring energy levels scales with the number of qubits N as

$$\delta\epsilon = |\epsilon_{k_{n+1}} - \epsilon_{k_n}| \approx g \frac{2\pi}{N} |\sin k_n|.$$

The relative spectral resolution follows as $\delta\omega/\delta\epsilon \propto \Gamma(\epsilon_k) \cdot N$. This means that in order to distinguish individual features of the fermionic system the relation

$$\hat{\Gamma}(\omega) < \frac{2\pi g}{N} \sin \frac{2\pi}{N} \quad (2.66)$$

must hold. The relative resolution worsens proportional to the system size N and the rate function $\Gamma(\omega)$. For a general non-interacting system we can estimate the requirements on the quantum simulator. The hopping parameters t_{ij} of the fermionic

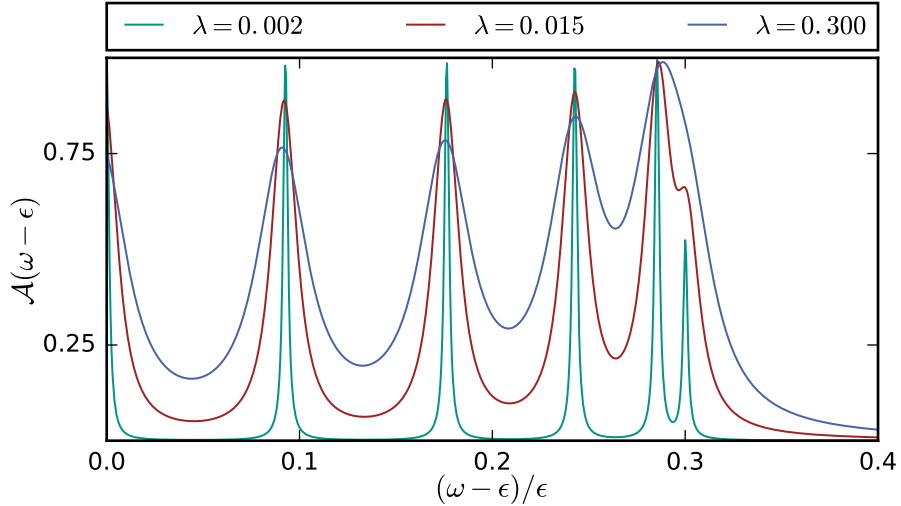


Figure 2.11: Numerical simulation of tight binding chain of 20 qubits coupled to a sub-ohmic environment. We show the spectral function \mathcal{A}_{00} obtained with a self-consistent self-energy for different couplings λ_i to the environment.

problem must be large compared to the relative resolution, i.e.,

$$t_{ij} \geq N \cdot \hat{\Gamma}(\omega). \quad (2.67)$$

To demonstrate these typical features of a disturbed quantum simulator we calculate the spectral function of a quantum simulator coupled to an ohmic environment for increasing dephasing strength and for different sizes of the system. We characterize the strength of dephasing due to a certain ohmic environment by the golden-rule dephasing rate Γ_2 of a single qubit obtained for this environment. We show the spectral function for increasing dephasing rates in the top graph of Fig. 2.10. The numerical simulation shows the expected behavior. For increasing dephasing rates the sharp peaks become more and more indistinguishable. The numerical simulation clearly shows that only features further apart than the dephasing rates can be resolved. In the bottom plot of Fig. 2.10 we plot the spectral functions of two perturbed quantum simulators with different system sizes (dots) together with the corresponding spectral functions of the unperturbed simulators (lines). While the smaller quantum simulator with $g/(n \cdot \Gamma_2) < 1$ is able to resolve most of the peaks present in the ideal spectral function, the spectral function returned from the quantum simulator comprising more qubits with $g/(n \cdot \Gamma_2) > 1$ is very inaccurate. Most features are lost and only a continuous spectral function remains.

2.6 Relaxation due to an ensemble of TLS

Mapping the transversal coupling of qubits to the environment onto a fermionic system we found that the resulting coupling Hamiltonian, Eq. (2.18), is odd in fermionic operators. We concluded that Wick's theorem and with it many-body perturbation theory applies only if the bath operators \hat{X}_i^x are odd fermionic operators as well.

In this section we analyze relaxation due to a microscopic realization of such an interaction, namely a bath of two-level systems at low temperature. As we describe in more detail in chapter 4, TLS are a major source of decoherence for superconducting qubits. The TLS couple via their dipole moment to the electrical fields of the qubits. In rotating wave approximation this induces a coupling between TLS and qubits of the form

$$V_x = \sum_{i,s} g_{i,s} (\sigma_i^+ \tau_{i,s}^- + h.c.). \quad (2.68)$$

Here, σ_i^\pm are qubit operators and $\tau_{i,s}^\pm$ are Pauli matrices acting in TLS space. In order to solve problems arising from odd fermionic terms we map both systems, qubits and TLS, onto fermionic operators. In order to apply the Jordan-Wigner transformation on both systems simultaneously we order the TLS and the qubits along a one-dimensional chain in the way depicted in Fig. 2.12.

The first qubit is labeled as qubit-fermion number one, $\sigma_1^- \mapsto c_1$. Subsequently follow all N_1 TLS that couple to the first qubit according to $\tau_{1,s}^- \mapsto a_{1,s}$ for $s = 1, \dots, N_1$. For clarity we denote qubit-fermions with c and TLS-fermions with a . Next, on site $1 + N_1 + 1$, follows the second qubit that maps to fermion c_2 . Subsequently, on sites $1 + N_1 + 2$ to $1 + N_1 + 1 + N_2$ follow all TLS that couple to the second qubit and so on. This yields the following map of different Pauli operators to the fermionic system:

$$\sigma_i^- \mapsto e^{-i\phi_i} c_i \quad (2.69)$$

$$\tau_{i,s}^- \mapsto e^{-i(\phi_i + \varphi_{s-1}^{(i)})} a_{i,s} \quad (2.70)$$

$$\varphi_s^{(i)} = \pi \sum_{r=1}^{s-1} a_{i,r}^\dagger a_{i,r} \quad (2.71)$$

$$\phi_{i+1} = \phi_i + \pi c_i^\dagger c_i + \varphi_{N_i}^{(i)}, \quad \phi_1 = 0. \quad (2.72)$$

Here, N_i is the number of TLS coupling to qubit i . With this ordering of operators the Jordan-Wigner transformation induces many-particle interactions into the qubit-qubit hopping as well as into coupling terms between qubits and TLS. For example, a

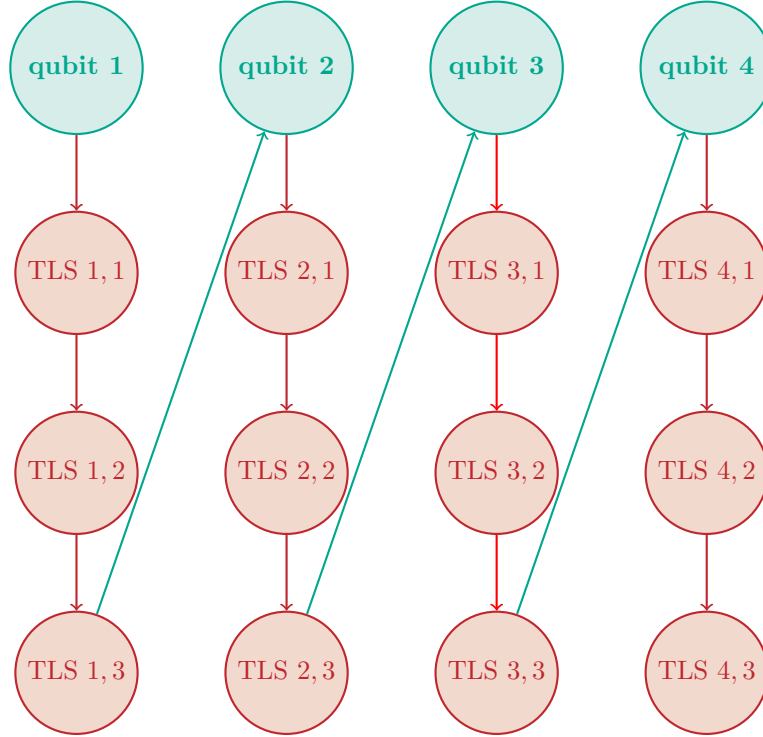


Figure 2.12: Graphical representation of the ordering of qubits and two-level systems on a single chain. Qubit i couples to TLS denoted with TLS i,s with $s \leq N_i$. The arrows indicate the ordering along a one-dimensional chain required for the Jordan-Wigner transformation.

nearest-neighbor qubit exchange term is given by

$$\sigma_i^+ \sigma_{i+1}^- \mapsto c_i^\dagger e^{i\varphi_{N_{i+1}}^{(i+1)}} c_{i+1}. \quad (2.73)$$

These interactions due to the Jordan-Wigner transformation render the full problem intractable. However, for a typical experimental situation the Hamiltonian significantly simplifies.

Relaxation induces an exchange of excitations between the bath of TLS and the qubits. In order to participate in this exchange a TLS needs to have an energy splitting close to typical qubit energies. These energies are large compared to the temperature in a typical quantum simulator. At such temperatures the TLS are in their ground-state and the TLS occupation number $\hat{n}_{i,s}$ is negligibly small. Furthermore, the ensemble of TLS is large and is not influenced by the quantum simulator. Thus, we substitute $\hat{n}_{i,s} = a_{i,s}^\dagger a_{i,s} \rightarrow 0$ in the Hamiltonian. The TLS induced phases $\varphi_s^{(i)}$ vanish and we recover the original Hamiltonian H_0 of the quantum simulator mapped to the qubit-fermions c_i . Furthermore, the coupling between quantum simulator and ensemble of

TLS in the limit $T \rightarrow 0$ takes the form

$$V_x \approx \sum_{i,s} g_{i,s} c_i^\dagger a_{i,s} + h.c. \equiv \mathbf{c}^\dagger \hat{V} \mathbf{a} + h.c. . \quad (2.74)$$

This coupling Hamiltonian corresponds to a tunneling Hamiltonian between the fermionic reservoirs respectively comprising qubit-fermions and TLS-fermions. In the last step we introduced vectors $\mathbf{c} = (c_1, \dots, c_N)^\top$ and $\mathbf{a} = (a_{1,1}, \dots, a_{N,N_N})^\top$ and the tunneling matrix \hat{V} .

In the following we extend our discussion to relaxation due to a fermionic bath at finite temperature coupling to the quantum simulator with the coupling given in Eq. (2.74). However, we keep in mind that the microscopic model describing the interaction between qubits and TLS only maps to H_0 and V_x at zero temperature.

Because the Hamiltonian representing quantum simulator and ensemble of TLS is quadratic in fermionic operators we can solve for the Green's functions exactly. The disturbed Green's function $\mathcal{G}(z, z')$ of the quantum simulator follows from the Dyson equation $\mathcal{G} = G_0 + G_0 \otimes \Sigma_{\text{tls}} \otimes \mathcal{G}$ with the exact self-energy $\Sigma_{\text{tls}} = \hat{V} G_{0,B} \hat{V}^\dagger$. Here, $G_{0,B}$ denotes the non-interacting Green's function of the TLS. This type of self-energy is well known as an embedding self-energy in the context of open quantum systems such as a quantum dot coupled to electronic leads [46]. Due to the assumption that each qubit couples to an individual bath that is uncorrelated with all other baths the self-energy is diagonal in the Hilbert space of the qubits. We find

$$\Sigma_{ij}^c = \delta_{ij} \sum_s |g_{is}|^2 G_{0,B, is}^c, \quad (2.75)$$

where $c = R, A, K$ denotes the different components in Keldysh-space.

2.6.1 Adiabatic approach

We calculate equilibrium properties such as the relaxation rate of the quantum simulator coupled to a fermionic reservoir using the adiabatic approach. The embedding self-energy Eq. (2.75) is characterized by the Green's functions of the two-level systems. As we show in chapter 4 the two-level systems are subject to decoherence which induces an intrinsic broadening γ_{is} into the Green's functions of TLS i,s . Thus the retarded and advanced Green's functions of a TLS with energy splitting ω_{is} are given by $G_{0,B, is}^{R/A}(\omega) = (\omega - \omega_{is} \pm i\gamma_{is})^{-1}$. From the Green's functions of the TLS follow the rate function $\hat{\Gamma}(\omega)$ and the shift $\hat{\Delta}(\omega)$ characterizing the broadening and energy shift

induced by the bath of TLS. We find

$$\hat{\Gamma}_{ij}(\omega) = \delta_{ij} \sum_s \frac{2|g_{is}|^2 \gamma_{is}}{(\omega - \omega_{is})^2 + \gamma_{is}^2} \quad (2.76)$$

$$\hat{\Delta}_{ij}(\omega) = \delta_{ij} \sum_s \frac{2|g_{is}|^2 (\omega - \omega_{is})}{(\omega - \omega_{is})^2 + \gamma_{is}^2}. \quad (2.77)$$

The retarded and advanced Green's functions of the disturbed quantum simulator follow as

$$[(\mathcal{G}^{R/A}(\omega))^{-1}]_{ij} = [(G_0^{R/A}(\omega))^{-1}]_{ij} - \delta_{ij} \hat{\Delta}_{ij}(\omega) \pm i \delta_{ij} \frac{1}{2} \hat{\Gamma}_{ij}(\omega)$$

For a small intrinsic broadening γ_{is} the Lorentz-function turns into a delta-function and the rate function is given by $\Gamma_i(\omega) \approx \frac{\pi}{2} J_i(\omega)$. Information about state occupation is carried by the kinetic component G^K . The Keldysh component of the self-energy follows from the fluctuation-dissipation relation

$$\Sigma^K = [\Sigma^R - \Sigma^A] F_{\text{tls}} = -i \hat{\Gamma}(\omega) F_{\text{tls}}(\omega) \quad (2.78)$$

with the TLS distribution function $F_{\text{tls}}(\omega) = \tanh(\beta\omega/2) \approx 1$. From this the kinetic component of the Green's function follows as

$$\mathcal{G}^K(\omega) = i \mathcal{G}^R(\omega) \hat{\Gamma}(\omega) G^A(\omega) F_{\text{tls}}(\omega). \quad (2.79)$$

This relation for the kinetic component states the fluctuation-dissipation relation $\mathcal{G}^K = (\mathcal{G}^R - \mathcal{G}^A)F$ for the system of qubits. Since bath and system are in equilibrium the distribution function $F(\omega) = 1 - 2f(\omega)$ of the quantum simulator is identical to the TLS distribution function F_{tls} .

For a single qubit with energy splitting ε we find the single qubit Green's function

$$\mathcal{G}_{\text{sq}}^{R/A}(\omega) = (\omega - \varepsilon \pm i \hat{\Gamma}(\omega)/2)^{-1} \approx (\omega - \varepsilon \pm i \Gamma_1)^{-1}. \quad (2.80)$$

In the last step we used that the Green's function is peaked at the qubit energy and approximated $\hat{\Gamma}_{\text{sq}}(\omega) \approx \hat{\Gamma}(\varepsilon) = \Gamma_{1,\text{sq}}$. Here, the rate

$$\Gamma_{1,\text{sq}} = \sum_s \frac{2|g_s|^2 \gamma_s}{(\varepsilon - \omega_s)^2 + \gamma_s^2} \quad (2.81)$$

corresponds to Fermi's golden-rule decay rate for a qubit coupled to a bath of TLS. We note that only TLS with energy splitting close to the qubit energy ε are able to exchange excitations with the qubit and participate in decay.

2.6.2 Time dependence

The adiabatic approach employed in the previous section is well suited to analyze equilibrium properties such as decoherence rates or the spectrum of the system. The approach does not reflect the experimentally relevant situation where the time evolution of some arbitrary initial state is simulated. In such an experiment the quantum simulator is prepared in a general initial state $\rho_0 = |\psi_0\rangle\langle\psi_0|$. For a general initial state the Green's functions of the system do not only depend on the time difference but individually on both time arguments $t - t_0$ and $t' - t_0$. Consequently, we cannot use a Fourier transform to solve the Dyson equation.

We assume that the simulator is prepared in a state where all qubits are decoupled from each other. This corresponds to an initial density matrix characterized by the non-interacting Hamiltonian $H_0^M = \sum_i \delta_i c_i^\dagger c_i$ where $\delta = -1$ for a qubit prepared in the excited and $\delta = 1$ for a qubit prepared in the ground state. The temperature β_{ini}^{-1} characterizing the initial state is zero, i.e. $\beta_{\text{ini}} \rightarrow \infty$. At the beginning of the simulation the interactions between qubits are turned on at time $t_0 = 0$ and the simulator evolves under the full Hamiltonian H_{qs} . We assume that no correlations between simulator and environment exist prior to the time t_0 .

With these assumptions we can use the Dyson equation Eq. (1.40) for a non-interacting initial state. For a quantum simulator coupled to a bath of non interacting fermions the self-energy, Eq. (2.75), reads as ($c = R, A, K$)

$$\Sigma_{ij}^c = \delta_{ij} \sum_s |g_{is}|^2 G_{B,0,is}^c. \quad (2.82)$$

Since $G_{B,0,is}$ are non-interacting Green's functions of the bath-fermions which were initially in thermal equilibrium we can Fourier transform the bath Green's functions. Hence, the self-energy can be expressed as

$$\Sigma^c(t, t') = \Sigma^c(t - t') = \int \frac{d\omega}{2\pi} \Sigma^c(\omega) e^{i\omega(t-t')}, \quad (2.83)$$

where $\Sigma^{R/A} = \hat{\Delta}(\omega) \pm i\hat{\Gamma}(\omega)/2$ and $\Sigma^K(\omega) = i\hat{\Gamma}(\omega)F_{\text{tfs}}(\omega)$ with $F_{\text{tfs}} = \tanh \beta\omega/2$. The rate function is defined as in Eq. (2.77). Numerical integration of the Dyson equation with this self-energy is straightforward.

The following calculation is closely related to a calculation on time-dependent transport in the book by Stefanucci and van Leeuwen [46]. In order to compare our method with master equation calculations and to get further analytical insight we will use the wide band approximation (WBA) for the ensemble of TLS. Assuming that the relevant energies of the quantum simulator lie well within the excitation spectrum of the dense ensemble of TLS the rate function is almost constant, $\hat{\Gamma}_{ii}(\omega) \approx \Gamma_{1,i} = \text{const.}$. Within

this approximation the bath of TLS is a source of white noise and the retarded and advanced self-energy become local in time,

$$\Sigma^{R/A}(t, t') \approx \mp i \frac{\hat{\Gamma}}{2} \delta(t - t'). \quad (2.84)$$

Here, $\hat{\Gamma}$ is a diagonal matrix of rates $\Gamma_{1,i}$ which coincide with the relaxation rates Eq.(2.81) $\Gamma_{1,i}$ used in a master equation approach. In the WBA the kinetic self-energy reads as

$$\Sigma^K(t, t') = i\hat{\Gamma} \int \frac{d\omega}{2\pi} F_{\text{tls}}(\omega) e^{i\omega(t-t')} = i\hat{\Gamma} F_{\text{tls}}(t - t'). \quad (2.85)$$

Here, we defined the time dependent distribution function $F_{\text{tls}}(t - t')$ as the inverse Fourier transform of $F_{\text{tls}}(\omega)$. Within the wide-band approximation we find the Dyson equation for the retarded, advanced and kinetic Green's functions of the perturbed quantum simulator

$$[i\partial_t - H_0(t) \pm i\hat{\Gamma}/2]\mathcal{G}^{R/A}(t, t') = \delta(t - t') \quad (2.86)$$

$$[i\partial_t - H_0(t) + i\hat{\Gamma}/2]\mathcal{G}^K(t, t') = [\Sigma^K \circ \mathcal{G}^A](t, t'). \quad (2.87)$$

For a time independent Hamiltonian $H_0(t) = H_0$ the retarded and advanced Dyson equation depend only on the the time difference. This reflects the fact that retarded and advanced component do not carry information of the state-occupations which are time-dependent for a non-stationary state. Thus, for a time independent Hamiltonian and in the WBA we can Fourier transform the retarded and advanced Dyson equation with respect to the time difference. We find

$$\mathcal{G}^{R/A}(t, t') = \int \frac{d\omega}{2\pi} \frac{1}{\omega - H_0 \pm i\hat{\Gamma}/2} e^{i\omega(t-t')}. \quad (2.88)$$

The kinetic Green's function can be obtained from

$$[i\partial_t - H_0(t) + i\hat{\Gamma}/2]\mathcal{G}^K(t, t') = i \int \frac{d\omega}{2\pi} e^{i\omega(t-t')} F_{\text{tls}}(\omega) \hat{\Gamma} \mathcal{G}^A(\omega). \quad (2.89)$$

We use the ansatz $G^K(t, t') = e^{-i(H_0 - i\hat{\Gamma}/2)t} g^K(t, t') e^{i(H_0 + i\hat{\Gamma}/2)t'}$ for G^K . The function g^K obeys the right-hand side and left-hand side equations of motion

$$\partial_t g^K(t, t') = \int \frac{d\omega}{2\pi} e^{i(\omega + h_0 - i\hat{\Gamma}/2)t} F_{\text{tls}}(\omega) \hat{\Gamma} \mathcal{G}^A(\omega) e^{-i(\omega + h_0 + i\hat{\Gamma}/2)t'}, \quad (2.90)$$

$$\partial_{t'} g^K(t, t') = \int \frac{d\omega}{2\pi} e^{i(\omega + h_0 - i\hat{\Gamma}/2)t} F_{\text{tls}}(\omega) \mathcal{G}^R(\omega) \hat{\Gamma} e^{-i(\omega + h_0 + i\hat{\Gamma}/2)t'}. \quad (2.91)$$

It fulfills the initial condition $g^K(0, 0) = -i[1 - 2f(H_0^M)] = -iF(H_0^M)$ where $f(H_0^M) = 1/[1 + \exp(\beta_{\text{ini}}H_0^M)]$. The decay of a qubit from its excited state to the ground state corresponds to the loss of one excitation of the quantum simulator. Thus, concerning relaxation we focus on the populations $n_i(t)$. The populations are related to the equal-time kinetic Green's function according to the relation $G_{ii}^K(t, t) = 2n_i(t) - i$. The function $g^K(t, t)$ at equal times obeys the equation of motion

$$\partial_t g^K(t, t) = \int \frac{d\omega}{2\pi} F_{\text{tls}}(\omega) e^{i(H_0 - i\hat{\Gamma}/2)t} [\mathcal{G}^R(\omega)\hat{\Gamma} - \hat{\Gamma}\mathcal{G}^A(\omega)\hat{\Gamma}] e^{-i(H_0 + i\hat{\Gamma}/2)t}. \quad (2.92)$$

The operators in the left-hand side and right-hand side exponent correspond to the denominator in the retarded and advanced Green's function. Owing to that we can integrate the differential equation for g^K . With the spectral function $\mathcal{A} = i(\mathcal{G}^R - \mathcal{G}^A) = \mathcal{G}^R\hat{\Gamma}\mathcal{G}^A$ we find the equal time kinetic function

$$\mathcal{G}^K(t, t) = -i \int \frac{d\omega}{2\pi} \left\{ \mathcal{A}(\omega) F_{\text{tls}}(\omega) - e^{-iH_0t - \hat{\Gamma}/2t} \left[\mathcal{A}(\omega) F_{\text{tls}}(\omega) - \delta(\omega - H_0^M) F(\omega) \right] e^{iH_0t - \hat{\Gamma}/2t} \right\}. \quad (2.93)$$

At $t = 0$ system and bath are decoupled and the system is prepared into its initial state with distribution $F(H_0^M) = 1 - 2f(H_0^M)$. The corresponding occupation number is given by $n_i(t) = f(H_0^M)$. Subsequently, the system evolves with the effective Hamiltonian $H_{\text{eff}} = H_0 - i\hat{\Gamma}/2$. The rate $\hat{\Gamma}$ accounts for the interaction with the environment and leads to a decay of the initial distribution. For long times $t \gg \min \Gamma^{-1}$ the time dependent term decays and the system reaches a steady state $\mathcal{G}_{\text{ste}}^K(t, t) = -i \int d\omega \mathcal{A}(\omega) F_{\text{tls}}(\omega)$. At this time the simulator is in equilibrium with the fermionic reservoirs at the temperature $(k_B\beta)^{-1}$. We note that the fluctuation dissipation theorem $\mathcal{G}^K(\omega) = (\mathcal{G}^R - \mathcal{G}^A)F_{\text{tls}}$ holds for the stationary state kinetic function.

For $t \geq t'$ and the special case $[H_0, \hat{\Gamma}] = 0$ and at zero temperature we find the analytical solution for the kinetic component,

$$\mathcal{G}^K(t, t') = -ie^{-iH_0t - \frac{\hat{\Gamma}}{2}t} \left[e^{\hat{\Gamma}t'} - 2f(H_0^M) \right] e^{iH_0t' - \frac{\hat{\Gamma}}{2}t'}. \quad (2.94)$$

If both time arguments are large compared to the smallest decay rate, $t, t' \gg \Gamma_{\text{min}}^{-1}$ the information about the initial state has decayed and only the first term in the square brackets survives. The corresponding stationary-state solution $\mathcal{G}^K = -i \exp\{(-iH_0 - \hat{\Gamma}/2)(t - t')\}$ only depends on the time difference. It corresponds to a system in equilibrium at temperature $T = 0$. This reflects the typical behavior of a system exchanging excitations with the environment. The information about the initial state dissipates into the environment. During this dissipation the Green's function depends

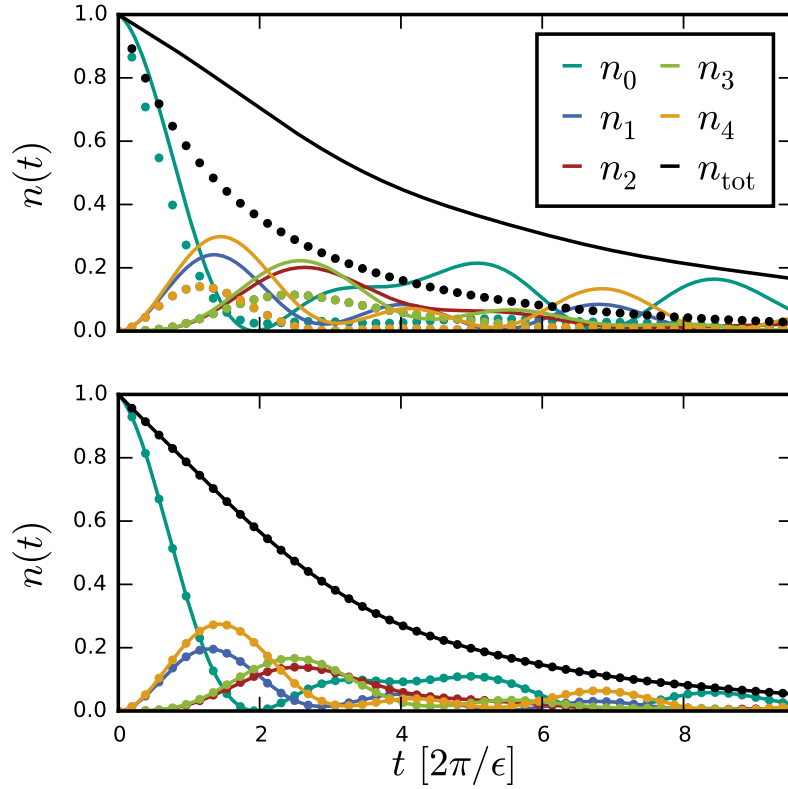


Figure 2.13: Numerical simulation of a tight binding chain with $N = 5$ sites coupled to bath of TLS in the wide band approximation (bottom) and for decay due to a bath of 10 TLS per qubit (top). We plot the occupation $n_i(t) = \langle c_i^\dagger(t)c_i(t) \rangle$ as well as the total number of particles $n_{\text{tot}}(t) = \sum_i n_i(t)$ in the system. Initially, qubit $i = 0$ was in the excited state, all other qubits in the ground state. Solid lines are obtained via fermionic Keldysh theory and dots via Bloch-Redfield master equation.

on both time arguments separately. After the information about the initial state has decayed the system reaches equilibrium with the environment and the Green's function only depends on the difference between its time arguments.

2.6.3 Comparison with master equation

We compare our method to master equation calculations for a linear chain of five qubits coupled to a bath of TLS, i.e., a fermionic environment at zero temperature. Initially, the first qubit is prepared in the excited state while the other qubits remain in their ground-state. This is achieved with the preparation-Hamiltonian $H_0^M = -c_0^\dagger c_0 + \sum_{i=1}^{N-1} c_i^\dagger c_i$ and $\beta^M \rightarrow \infty$. We use the Bloch-Redfield master equation implemented in the QuTip python package in order to obtain results for the master equation.

In Fig. 2.13 we show the time dependent occupation numbers $n_i(t) = \frac{1}{2}[\mathcal{G}_{ii}^K(t, t) + i]$ and the total number of particles $n_{\text{tot}}(t) = \sum_i n_i(t)$ in the system obtained with many-

body methods (solid lines) and with the Bloch-Redfield master equation (dots). The bottom plot corresponds to the WBA. The total number of particles in the system decays exponentially. At each time the decay is dominated by the decay rate Γ_i of the most populated qubit. In the wide-band limit, where the self-energy is local in time and the Born-Markov approximation is valid, master equation and KBE yield identical results.

In the top plot we show results for a linear chain of qubits coupled to a non-averaging ensemble of TLS. Each qubit couples to ten individual TLS. The spectral density of the TLS is obtained from the discrete sum over individual TLS. Unless the internal decoherence rates are large the spectral density depends on frequency and cannot be described within the WBA. Consequently, the rate function $\Gamma_i(\omega) = 2\pi \sum_s g_{is}^2 \gamma_{is} / ((\omega - \omega_{is})^2 + \gamma_{is}^2)$ is frequency dependent. We expect that for such a system master equation and Keldysh method disagree. Solving the KBE numerically and comparing it to results obtained with a Bloch-Redfield master equation we confirm the expected disagreement between Keldysh method and master equation.

2.7 Disorder

In section 2.3.5 discussed the influence of slow fluctuations occurring on time scales that are large compared to single measurement times of the quantum simulator. We showed that such a type of noise can be described in terms of quenched disorder of parameters of the quantum simulator. In order to describe disorder quantitatively we employ fermionic many-body theory. Throughout this section we denote the width of a random variable a with σ_a . Mapping the disordered quantum simulator onto fermions using the Jordan-Wigner transformation we found the Hamiltonian

$$\mathcal{H} = \sum_i (\varepsilon_i + \delta\varepsilon_i) c_i^\dagger c_i + \sum_{\langle ij \rangle} (g_i + \delta g_i) c_i^\dagger c_j + \sum_{ij} \delta U_{ij} c_i^\dagger c_j^\dagger c_j c_i, \quad (2.95)$$

where $\langle ij \rangle$ denotes a sum over nearest-neighbors. Although the simulated system is non-interacting imperfections such as gate errors or fluctuating fields induce fluctuations of qubit-qubit couplings which lead to undesired interactions δU_{ij} in the fermionic representation of the quantum simulator.

Due to disorder the Green's function obtained in every experimental run will depend on the current set $\{\delta a\}$ of the disordered parameters. The experimentally measured Green's function after N_{meas} runs of the simulator is the disorder averaged Green's function

$$G_{N_{\text{meas}}} = \frac{1}{N_{\text{meas}}} \sum_{n=1}^{N_{\text{meas}}} G[\{\delta a\}_n] \xrightarrow{N_{\text{meas}} \rightarrow \infty} \langle G \rangle_{\text{dis}}, \quad (2.96)$$

where $\{\delta a\}_n$ is the set of parameters characterizing the system during the n^{th} run. The disorder averaged Green's function is defined as

$$\langle G \rangle_{\text{dis}} = \prod_{\nu} \int d\delta a_{\nu} G[\{\delta a\}] P(\delta a_{\nu}). \quad (2.97)$$

The general idea we employ in order to calculate the disorder averaged Green's function is as follows: Firstly, we expand the Green's function in the fluctuating parameters δa and subsequently average this expansion over the quenched disorder. Since the disorder distributions are Gaussian all higher order disorder averages factorize into products of the second moments (2.22). This corresponds to a Wick theorem for the random variables δa which we use to calculate disorder averages. With this we can define a disorder self-energy and find a Dyson equation for the disorder averaged Green's function.

Besides disorder the system is still subject to decoherence due to fast fluctuations. Owing to the different time scales of slow fluctuations causing disorder and dynamical noise inducing decoherence the disorder self-energy and decoherence self-energy separate and we find the Dyson equation for the disorder averaged Green's function

$$\langle G \rangle_{\text{dis}}^{-1} = \mathcal{G}^{-1} - \Sigma_{\text{dis}}. \quad (2.98)$$

Here, $\mathcal{G} = [G_0^{-1} - \Sigma_{\text{dec}}]^{-1}$ is the Green's function including with decoherence while $\Sigma_{\text{dis}} = \Sigma_{\text{dis}}[\mathcal{G}]$ characterizes the influence of disorder.

In the following section we discuss disorder due to fluctuations in on-site qubit energies and transversal qubit-qubit couplings. In the section after next we give an outlook on our ongoing work on disorder in longitudinal qubit-qubit couplings.

2.7.1 Disorder in on-site energies and transversal qubit couplings

Fluctuations of the local field h_i and the transversal qubit-qubit coupling J_{ij}^x lead to disorder in the on-site energies ε_i as well as in the hopping amplitudes g_i . Both terms are bi-linear in fermionic operators such that disorder in these parameters induces an effective disorder potential

$$U_{\text{dis}} = \sum_{i,j} (\delta_{ij} \delta \varepsilon_i + \delta_{j,i+1} \delta g_i + \delta_{i,j+1} \delta g_j) c_i^{\dagger} c_{i+1} = \sum_{ij} u_{ij} c_i^{\dagger} c_j \quad (2.99)$$

into the Hamiltonian, i.e., $H_{\text{qs}} \rightarrow H_{\text{qs}} + U_{\text{dis}}$. As outlined before we expand the Green's function in powers of the random potential U_{dis} . Since the disorder potential is a scalar potential this leads to the diagrammatic expansion of the many-body Green's function due to coupling with a classical field presented in section 1.3.2,



Figure 2.14: The disorder self-energy Σ_{dis}

$$\text{Thick line} = \text{Thin line} + \text{Thin line with 1 cross} + \text{Thin line with 2 crosses} + \dots$$

Here, every cross represents a disorder potential U_{dis} and the thick line represents the disorder averaged Green's function $\langle G \rangle_{\text{dis}}$. The quantum simulator is still subject to decoherence due to faster fluctuations of the environment. Thus, contrary to the diagrammatic expansion for coupling to a classical potential where a thin line represents a free fermionic Green's function, a thin line corresponds to the full Green's function \mathcal{G} in the diagrammatic expansion for disorder.

In the next step we average the diagrammatic expansion over disorder. In order to carry out that averaging we need to calculate disorder averages of the form $\langle U_{\text{dis}}(1)U_{\text{dis}}(2)\dots U_{\text{dis}}(n) \rangle_{\text{dis}}$. These averages correspond to certain moments of the disorder distribution functions. Since the fluctuations are represented by Gaussian random variables with zero mean all odd moments vanish while even moments can be expressed as products of the second order moments [54].

This corresponds to a Wick theorem for the disorder potential. Thus, the disorder averaged Green's function is obtained by pairing disorder-crosses in all possible ways. Each connected pair contributes the Gaussian average

$$\langle U_{\text{dis}}(1)U_{\text{dis}}(1') \rangle_{\text{dis}} \equiv D_{\text{dis}}(1; 1'). \quad (2.100)$$

After averaging the diagrammatic expansion in terms of the Gaussian disorder takes the form

$$\text{Thick line} = \text{Thin line} + \text{Thin line with 2 crosses connected by dashed line} + \dots$$

We define the disorder self-energy as the sum of all irreducible disorder diagrams. In lowest order the disorder self-energy shown in Fig. 2.14a reads as

$$\left(\Sigma_{\text{dis}}(z, z') \right)_{ij} = \sum_{kl} \mathcal{G}_{kl}(z, z') \langle u_{ki} u_{jl} \rangle_{\text{dis}}. \quad (2.101)$$

Usually, low-order approximations of the disorder self-energy are unreliable [54]. Especially in one-dimensional systems they very often fail to capture important features

arising from disorder such as localization. For weak disorder the inherent broadening of the Green's functions due to decoherence improves the accuracy of such a low-order approximation but in general one needs to take into account higher order terms in the self-energy. One way to systematically improve the diagrammatic expansion for strong disorder is a self-consistent ansatz for the disorder self-energy. This is achieved by replacing the full Green's function \mathcal{G} with the full disorder averaged Green's function $\langle G \rangle_{\text{dis}}$ in all diagrams. With the self-consistent ansatz the lowest order self-energy becomes

$$\left(\Sigma_{\text{dis}}^{\text{sc}}(z, z') \right)_{ij} = \sum_{kl} \langle G \rangle_{\text{dis},kl}(z, z') \langle u_{ki} u_{jl} \rangle_{\text{dis}}. \quad (2.102)$$

Disorder for a single qubit We demonstrate the quality of the different approximations for a single qubit subject to both disorder and decoherence. We compare the accuracy of the approximations with the exact disorder-averaged Green's function of the qubit for different ratios between disorder and decoherence.

We analyze a single qubit with energy splitting ε which is subject to decoherence. The disorder-free retarded Green's function of this qubit in the frequency domain reads as

$$G^R(\omega) = \frac{1}{\omega - \varepsilon + i\Gamma}, \quad (2.103)$$

where Γ is the decoherence rate. For a fluctuating energy splitting $\varepsilon \rightarrow \varepsilon + \delta\varepsilon$ characterized by a Gaussian distribution with width σ the disorder averaged Green's function can be calculated exactly.

From Eq. (2.97) the exact disorder averaged Green's function follows as

$$\langle G \rangle_{\text{dis}}^R = \int \frac{d\delta\varepsilon}{\sqrt{2\pi\sigma^2}} \frac{e^{-\frac{\delta\varepsilon^2}{2\sigma^2}}}{\omega - \varepsilon - \delta\varepsilon + i\Gamma} \quad (2.104)$$

$$= -i \sqrt{\frac{\pi}{2\sigma^2}} e^{-\frac{1}{2} \left(\frac{\omega - \varepsilon + i\Gamma}{\sigma} \right)^2} \text{Erfc} \left[-i \frac{1}{\sqrt{2}} \frac{\omega - \varepsilon + i\Gamma}{\sigma} \right], \quad (2.105)$$

where $\text{Erfc} = 1 - \text{Erf}$ is the complementary error function. We can benchmark the approximations for the disorder self-energy with this exact relation.

The lowest-order disorder self-energy (2.101) for the single qubit becomes $\Sigma_{\text{dis}}^R = \sigma^2 / (\omega - \varepsilon + i\Gamma_{\text{dec}})$. With this approximation for the self-energy the disorder averaged Green's function reads as

$$\langle G \rangle_{\text{dis}}^R = \frac{\omega - \varepsilon + i\Gamma}{(\omega - \varepsilon + i\Gamma)^2 + \sigma^2} \approx \frac{1}{\omega - \varepsilon + i\Gamma(1 + \sigma^2/\Gamma^2)}. \quad (2.106)$$

The exact disorder averaged Green's function and the Green's function obtained in second order coincide only for very weak disorder compared to the decoherence rate, $\sigma \ll \Gamma$. As soon as the disorder strength becomes comparable to the decoherence rate,

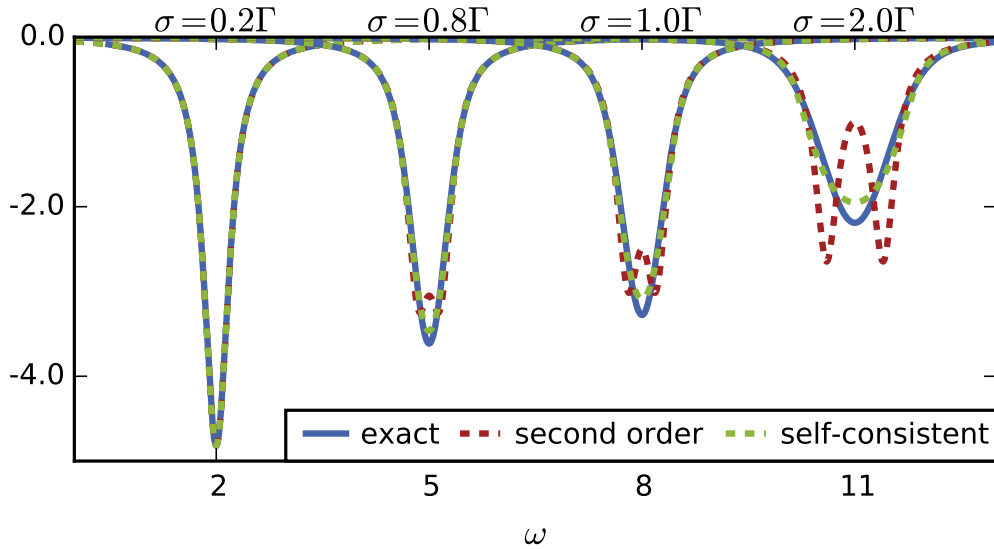


Figure 2.15: Disorder-averaged retarded Green's function of a single qubit. The qubit is subject to disorder with disorder strength σ and to decoherence with constant decoherence rate Γ . We compare the Green's function for increasing disorder strength obtained with different approximations: Exact solution (2.105) in blue, self-consistent solution with self-energy (2.107) in green, and second order self-energy (2.101) in red. For visual clarity the Green's functions are shifted along the ω -axes.

the simple approximation quickly becomes inaccurate. In the limit $\sigma \gg \Gamma$ the exact disorder averaged Green's function takes a Gaussian shape with width σ ,

$$\lim_{\Gamma_{\text{dec}} \rightarrow 0} \bar{G}^R \propto -i \exp(-(\omega - \varepsilon)^2 / 2\sigma^2).$$

Contrary, the lowest-order self-energy defined above yields a Lorentzian shape of the Green's function. For disorder strength $\sigma > \Gamma_{\text{dec}}$ the lowest order approximation even predicts a separation of a single peak into two distinct peaks with width Γ_{dec} , a feature is not present in the exact solution. With the self-consistent ansatz Eq. (2.102) the retarded self-energy reads as

$$\Sigma_{\text{dis}}^{R,sc}(\omega) = \frac{\omega - \varepsilon + i\Gamma_{\text{dec}}}{2} + \text{sign}(\omega - \varepsilon) \sqrt{\left(\frac{\omega - \varepsilon + i\Gamma}{2}\right)^2 - \sigma^2}. \quad (2.107)$$

We compare the exact disorder averaged Green's function with the Green's functions obtained in second-order and self-consistently in Fig. 2.15. The self-consistent disorder average Green's function compares well with the exact solution even for strong disorder while the second order approximation quickly fails for increasing disorder strength.

Numerical calculation for a chain of qubits We use the different approximations to calculate the disorder averaged Green's function for a linear chain of qubits with nearest-neighbor hopping. The quantum simulator is represented by the fermionic Hamiltonian given in Eq. (2.23). Each qubit longitudinally couples to a bath of oscillators as described in section 2.5. The coupling to the oscillators induces a broadening $\Gamma_{\text{dec}}(\omega) = i(\Sigma_{\text{dec}}^R(\omega) - \Sigma_{\text{dec}}^A(\omega))$. The rate function is given in Eq.(2.42). With the rate function and neglecting energy shifts the disorder free Green's functions for the system of qubits coupled to the bath are, see Eq. (2.44),

$$\mathcal{G}^{R/A}(\omega) = [G_0^{-1}(\omega) \pm i\Gamma_{\text{dec}}(\omega)]^{-1} \quad (2.108)$$

In order to calculate the disorder self-energy we need the second moments of the disorder potential. Using the relations connecting fermionic with qubit parameters, Eq. (2.24)-(2.27), we calculate the second moments $\langle u_{ik}u_{lj} \rangle$. With that we find the disorder self-energy in lowest order

$$\begin{aligned} \Sigma_{ij}(\omega) = & \delta_{ij}[\mathcal{G}_{ii}(\omega)\sigma_{h_i}^2 + \mathcal{G}_{i-1,i-1}(\omega)\sigma_{J_{i-1,i}^x}^2 + \mathcal{G}_{i+1,i+1}(\omega)\sigma_{J_{i,i+1}^x}^2] \\ & + \delta_{i-1,j}\mathcal{G}_{i-1,i}(\omega)\sigma_{J_{i-1,i}^x}^2 + \delta_{i+1,j}\mathcal{G}_{i+1,i}(\omega)\sigma_{J_{i,i+1}^x}^2. \end{aligned} \quad (2.109)$$

The self-consistent self-energy is obtained with the substitution $\mathcal{G} \rightarrow \langle G \rangle_{\text{dis}}$. We numerically calculate the disorder averaged Green's function in second-order approximation and self-consistently and compare the results with Green's functions obtained via Monte Carlo calculations. With Monte Carlo simulation we mean a simulation of the experimentally obtained results. A random realization of parameters is chosen and the Green's function calculated for this specific set of random variables. This is repeated N_{meas} times. From this we obtain an approximation of the disorder-averaged Green's function which corresponds to the experimentally obtained result. For $N_{\text{meas}} \rightarrow \infty$ the Monte Carlo calculation yields the exact disorder averaged Green's function.

In Fig. 2.16 we compare results obtained with the different approximations for a chain of four qubits. The self-consistently obtained disorder averaged Green's function is in good agreement with the Monte-Carlo simulation while the second-order approximation of the disorder self-energy strongly differs from the Monte Carlo simulation. We conclude that disorder in the hopping of a non-interacting quantum simulator is well described by the self-consistently obtained Green's function.

In the bottom plot we show the influence of strong disorder and dephasing on the chain of qubits. The discrete features blur out and the spectral function becomes continuous.

In Fig. 2.17 we show the influence of increasing disorder strength σ on the spectral density of a simulator comprising ten qubits. Contrary to dephasing, disorder

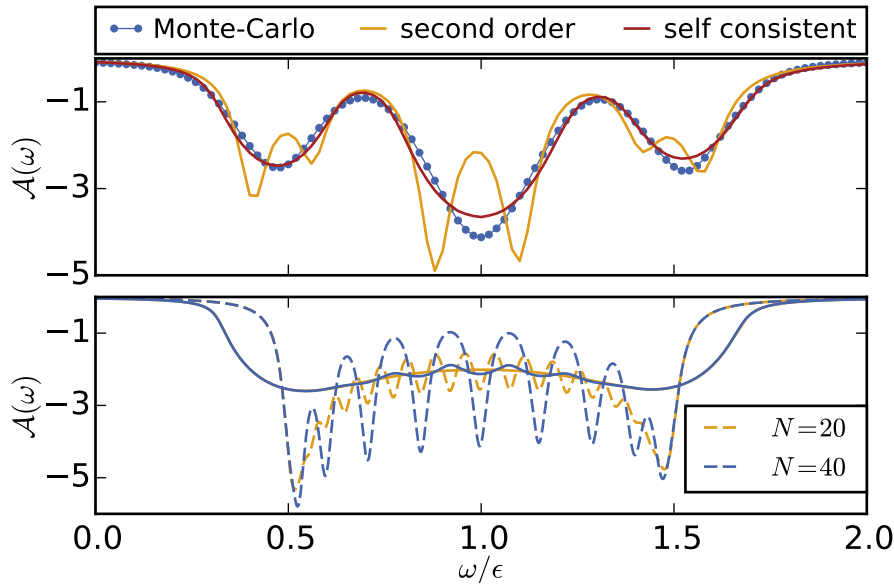


Figure 2.16: Influence of disorder in hopping-parameters and on-site energies on the spectral function $\mathcal{A}(\omega)$. In the *top* plot we show the spectral density for a chain of 4 qubits with hopping $g = \varepsilon/2$ subject to dephasing due to an ohmic bath and disorder in hopping and on-site energy. Dephasing is characterized by the rate function $\Gamma(\omega)$. The width of the random fluctuations is $\sigma_\varepsilon = \sigma_g = 0.8\hat{\Gamma}(0)$. We compare a Monte-Carlo simulation with the self-consistent and second-order disorder averaged Green's function. In the *bottom* plot we show the spectral density of a quantum simulator comprising $N = 20$ and $N = 40$ qubits (solid) with the disorder-free simulator (dashed).

changes the shape of features in the spectral density. The Lorentz-peaks transform into Gaussian peaks due to disorder.

2.7.2 Outlook I: Disorder in the interaction

In the previous section we analyzed disorder in the bi-linear terms of the fermionic Hamiltonian. These stem from fluctuations of transversal qubit-qubit couplings J_{ij}^x and local fields h_i . Here, we give an outlook on effects of disorder in longitudinal qubit-qubit couplings.

Quasi-static fluctuations of longitudinal qubit-qubit couplings cause a random two-particle fermionic interaction of the form

$$U_{\text{dis}} = \sum_{ij} \delta U_{ij} c_i^\dagger c_j^\dagger c_j c_i. \quad (2.110)$$

The random interaction is proportional to the disorder in the transverse coupling, $\delta U_{ij} = 2\delta J_{ij}^z$. Additionally to the random interaction, fluctuations in J_{ij}^z induce fluctuations of on-site energies according to $\delta\varepsilon_i = \sum_j (\delta J_{ij}^z + \delta J_{ji}^z)$. The fluctuations in $\delta\varepsilon$

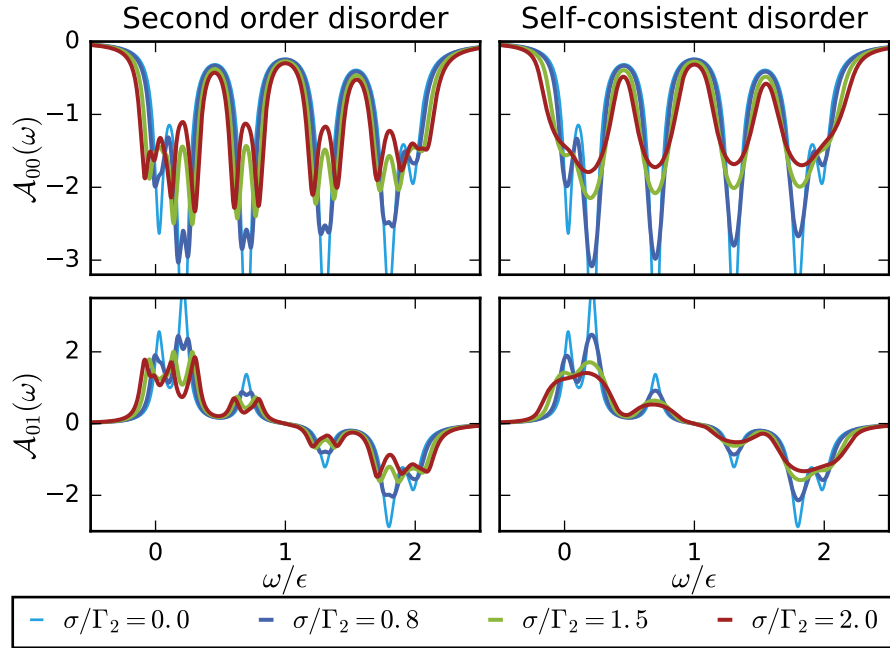
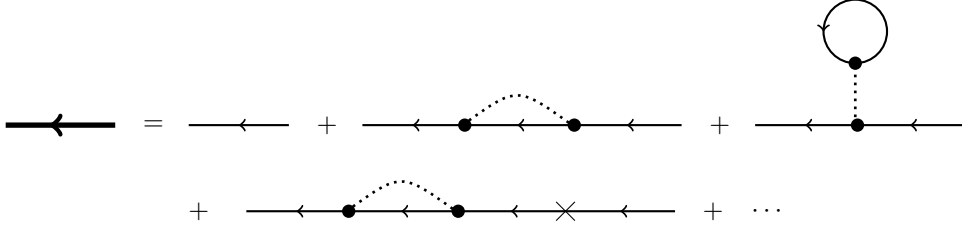


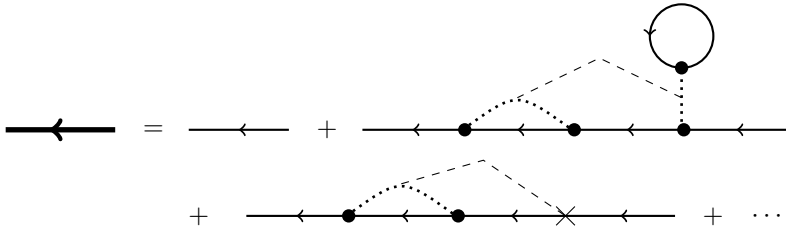
Figure 2.17: Influence of disorder in hopping-parameters and on-site energies on the spectral function $\mathcal{A}(\omega)$ for increasing disorder strength σ from weak disorder (blue) to strong disorder (red). In the *top* row we show the component \mathcal{A}_{00} and in the bottom row the component $\mathcal{A}_{01}(\omega)$ for a chain of 10 qubits with hopping $g = \varepsilon/2$. The *left* column shows second-order results, the *right* column self-consistent solutions. The chain is subject to dephasing due to an ohmic bath and disorder in hopping and on-site energy. Dephasing is characterized by the rate Γ_2 .

are described by a random potential as discussed in the previous section. According to Eq. (2.27) the fluctuations of on-site energies due to δJ_{ij}^z and the interaction-disorder δU_{ij} are correlated.

In order to analyze the effects of such a disorder, we proceed as we did in the previous section. Firstly, we expand the Green's function in powers of the disorder and subsequently average over disorder. We define the disorder-interaction $\delta U(1; 2) = \delta U_{i_1, i_2}(z_1) \delta(z_1 - z_2)$ on the contour. With this definition the expansion of the Green's function in the disordered interaction is identical to the diagrammatic expansion for interacting fermions presented in section 1.3.2. Together with the random potential representing the fluctuations in the on-site energies the diagrammatic expansion of the Green's function before averaging over disorder takes the form



Here, every dotted line represents a disorder-interaction, a cross represents a disorder potential (i.e., $\delta\varepsilon$), and a thin line a Green's function \mathcal{G} . Now, we average the expansion over disorder. This corresponds to contracting either two interaction lines, two potential crosses, or a cross with a potential line. Representing a disorder-contraction with a dashed line the diagrammatic expansion of the disorder-averaged Green's function takes the form



For example, the contributions of the second and third diagram to the self-energy read as

$$\Sigma_{\text{dis},ij}^{(2)}(z, z') = \frac{1}{2} \int_C dz_1 \delta(z - z_1) \langle \delta U_{ik} \delta U_{jl} \rangle_{\text{dis}} G_{kk}(z, z_1) G_{ll}(z', z_1^+) G_{ij}(z_1, z') \quad (2.111)$$

$$\Sigma_{\text{dis},ij}^{(3)}(z, z') = -\frac{1}{2} \int_C dz_1 \delta(z - z_1) \langle \delta U_{ik} \delta \varepsilon_j \rangle_{\text{dis}} G_{kk}(z, z_1) G_{ij}(z_1, z') \quad (2.112)$$

The diagrammatic expansion in random fermion-fermion interactions and a random potential together with contractions between the different terms need to be analyzed in more detail in the future. The structure of the diagrams with correlated potential and interaction terms promises interesting properties of such an expansion.

2.8 Outlook II: Decoherence in interacting systems

The Dyson equation for the disturbed Green's function, Eq. (2.32), relates the non-interacting Green's function G_0 with the result of the perturbed simulator \mathcal{G} . For the simulators considered in this work the non-interacting Green's function coincides with the ideal result and the Dyson equation yields the looked-for connection between the disturbed and the ideal result.

For a general quantum simulator with interacting terms the ideal result is given by the Green's function G of the interacting system without coupling to the environment.



Figure 2.18: Self-energy diagrams of a quantum simulator subject to dephasing due to a bosonic bath. A circle represents an interaction with the environment while a square represents a fermionic interaction from H_{int} . A dashed line is a bosonic bath correlation function and solid lines are non-interacting fermionic Green's functions. Diagram (a) contains no crossing between bath-interactions and system interactions while diagram (b) contains a single crossing.

The ideal Green's function G can be obtained from the Dyson equation,

$$G(z, z') = G_0(z, z') + \iint_C dz_1 dz_2 G_0(z, z_1) \Sigma_{\text{qs}}(z_1, z_2) G(z_2, z'), \quad (2.113)$$

where the quantum simulator self-energy Σ_{qs} describes internal interactions of the simulator.

In order to establish a connection between the ideal result G and the perturbed result \mathcal{G} a more detailed analysis of the diagrammatic expansion of the decoherence-self-energy is necessary. Here, we give an idea on how such a connection could be found.

Therefore, we take a look at the diagrammatic expansion of the self-energy Σ of the disturbed simulator. Such a self-energy contains free Green's function G_0 , bath correlation functions D as well as contributions from the internal-interaction H_{int} and the coupling V to the bath. These contributions can be connected in arbitrarily complicated ways. However, the coupling to the environment should be small compared to the energy scales of the simulated systems. Consequently, we consider only low-order approximations of the self-energy in the coupling V to the environment. If the bath additionally is Markovian, i.e., memoryless, diagrams with crossing between bath Green's functions and system internal-interactions can be neglected.

Additionally, from phase space arguments it follows that diagrams that contain a crossing between fermionic interactions and bath interactions are suppressed by at least a factor $1/N$ as compared to diagrams of the same order without crossing where N is the system size. To illustrate this we take a quantum simulator subject to dephasing due to a bosonic bath and look at the diagrams depicted in Fig. 2.18. Here, a circle represents an interaction with the environment while a square represents a fermionic interaction from H_{int} . A dashed line is a bosonic bath correlation function and solid lines are non-interacting fermionic Green's functions. Diagram (a) contains no crossings between interactions while diagram (b) contains one crossing. Every circle contains in principle two free system indexes while every square contains four

indexes. With index we mean a fermionic mode. As we have shown before dephasing is local in fermionic operators and all four internal indexes of two connected dephasing vertexes reduce to a single index according to $V_{ij}D_{jk}V_{kl} \propto \delta_{ij}\delta_{jk}\delta_{kl}$. Assuming that system Green's functions are diagonal, the diagram depicted in Fig. 2.18a has four free internal indexes while the diagram depicted in Fig. 2.18b only contains three free indexes. Every sum over an internal index yields a factor N . Consequently, diagram (b) is smaller than diagram (a) by a factor $\propto 1/N$.

If these assumptions hold we can substitute the non-interacting Green's function appearing in the Dyson equation (2.32) with the ideal Green's function G and the Dyson equation only depends on the ideal Green's function, the coupling to the environment and the self-energy $\Sigma[V]$ characterizing the influence of the environment:

$$\mathcal{G}(z, z') = G(z, z') + \iint_C dz_1 dz_2 G(z, z_1) \Sigma[V](z_1, z_2) \mathcal{G}(z_2, z'). \quad (2.114)$$

For dephasing due to a bosonic environment as discussed in Sec. 2.5 the procedure described above corresponds to substituting the non-interacting Green's function in the second-order self energy with the ideal Green's function G and the self-energy reads as

$$\Sigma = i\delta_{ij}G_{ii}(z, z')D_{0,i}(z, z') - i\delta_{ij}\delta(z, z') \int d\bar{z} D_{0,i}(z, \bar{z})G_{ii}(\bar{z}, \bar{z}^+). \quad (2.115)$$

This self-energy is an example for a self-energy that directly relates the result \mathcal{G} of a perturbed quantum simulator with the ideal result G .

Part II

Decoherence of microscopic two-level systems

3

Chapter 3

Theoretical background II: Dynamics of two-level systems

Qubits as well as microscopic two-level systems play an important role in this work. In this chapter we summarize important characteristics of the dynamics of isolated TLS and TLS coupled to environmental degrees of freedom.

In the first part we shortly discuss basic concepts of the dynamics of two-level systems. In the following section we give an overview over the description of decoherence in two-level systems. Finally, in the last section we use the methods developed in chapter 1 in order to analyze refocusing techniques.

3.1 Isolated TLS

A quantum mechanical two-level system characterized by its ground $|g\rangle$ and excited state $|e\rangle$ and Hamiltonian $H_{\text{tls}} = E_g|g\rangle\langle g| + E_e|e\rangle\langle e|$ can be represented in terms of the Pauli matrices

$$\tau^x = \begin{pmatrix} 0 & 1 \\ 1 & 0 \end{pmatrix} \quad \tau^y = \begin{pmatrix} 0 & -i \\ i & 0 \end{pmatrix} \quad \tau^z = \begin{pmatrix} 1 & 0 \\ 0 & -1 \end{pmatrix}, \quad (3.1)$$

which obey the spin commutation relations

$$\tau^i \tau^j = \delta_{ij} + i\epsilon_{ijk} \tau^k \quad [\tau^i, \tau^j]_- = 2i\epsilon_{ijk} \tau^k \quad [\tau^i, \tau^j]_+ = 2\delta_{ij}. \quad (3.2)$$

Throughout this work we use the convention to denote Pauli matrices in the energy basis with τ^α and Pauli matrices in some physical basis with σ^α . We define $\tau^z = |e\rangle\langle e| - |g\rangle\langle g|$ and the spin raising $\tau^+ = |e\rangle\langle g|$ and lowering $\tau^- = |g\rangle\langle e|$ operators which can be expressed in terms of the Pauli matrices as $\tau^\pm = (\tau^x \pm i\tau^y)/2$. Measuring

energy relative to the mean energy $2E_0 = E_g + E_e$ the Hamiltonian takes the form

$$H_{\text{tls}} = -\frac{E_{\text{tls}}}{2} \tau^z, \quad (3.3)$$

with the TLS energy splitting $E_{\text{tls}} = E_b - E_a$. The dynamics of a two-level system can be formulated in terms of its density matrix $\rho(t) = |\psi(t)\rangle\langle\psi(t)|$. Using the eigenstates $|0\rangle$ and $|1\rangle$ of τ^z as basis for the TLS Hilbert space the matrix elements $\rho_{ij} = \langle i|\rho|j\rangle$ can be expressed in terms of the Pauli operators τ^z and $\tau^{x/y}$. The expectation values of these operators are connected to the population difference

$$\rho_{11} - \rho_{00} = \langle \tau^z \rangle = \text{Tr}\{\rho\tau^z\} \quad (3.4)$$

between the TLS eigenstates and the coherences

$$\rho_{01} = \langle \tau^+ \rangle = \langle \tau^x + i\tau^y \rangle / 2 \quad \text{and} \quad \rho_{10} = \langle \tau^- \rangle = \langle \tau^x - i\tau^y \rangle / 2. \quad (3.5)$$

The standard representation $\rho = \frac{1}{2}[\tau^0 + \langle \tau^z \rangle \tau^z + \langle \tau^x \rangle \tau^x + \langle \tau^y \rangle \tau^y]$ can be mapped to a real three dimensional vector $\vec{\psi} = (\langle \tau^x \rangle, \langle \tau^y \rangle, \langle \tau^z \rangle)^T$ with length $|\vec{\psi}| \leq 1$. Thus, the vectors representing the state of the TLS lie within the three dimensional unit sphere, the so-called Bloch sphere. For pure states $|\psi\rangle_{\text{pure}} = \cos\frac{\vartheta}{2}|0\rangle + \sin\frac{\vartheta}{2}e^{i\varphi}|1\rangle$ with density matrix

$$\rho_{\text{pure}} = \frac{1}{2} \begin{pmatrix} 1 - \cos\vartheta & e^{i\varphi} \sin\vartheta \\ e^{-i\varphi} \sin\vartheta & 1 + \cos\vartheta \end{pmatrix} \quad (3.6)$$

the Bloch vector $\vec{\psi}_{\text{pure}} = (\sin\vartheta \cos\varphi, \sin\vartheta \sin\varphi, \cos\vartheta)^T$ has length one. Thus, pure states point on the surface of the Bloch sphere. Mixed states are represented by vectors with length $|\vec{\psi}_{\text{mixed}}| < 1$ that point at the interior of the Bloch sphere.

3.1.1 TLS coupled to the environment - decoherence

Quantum mechanical two-level systems couple to their environment. This interaction with the environment has strong influence on the time evolution of the TLS eventually destroying quantum coherence. The coupled TLS-environment system can be described within a system-bath approach. In this approach the Hamiltonian \mathcal{H} of the entire system is the sum of the uncoupled TLS Hamiltonian H_{tls} , the uncoupled environment Hamiltonian H_{B} and the coupling Hamiltonian V between TLS and environment:

$$\mathcal{H} = H_{\text{tls}} + H_{\text{B}} + V. \quad (3.7)$$

As we have seen in section 1.5 the time evolution of the TLS in the presence of the environment is best described with the help of its reduced density matrix. From the full density matrix $\chi(t)$ of the coupled system we can extract the reduced density matrix of the TLS by tracing out the environment

$$\rho(t) = \text{Tr}_B[\chi(t)] \quad (3.8)$$

Here, $\text{Tr}_B[\dots]$ denotes the trace with respect to bath states. The time evolution of the reduced density matrix follows as

$$\rho(t) = \hat{U}_{H_{\text{tls}}}(t, t_0) \text{Tr}_B \left[U_V(t, t_0) \chi(t_0) U_V(t_0, t) \right] \hat{U}_{H_{\text{tls}}}(t_0, t) \quad (3.9)$$

with evolution operator $\hat{U}_{H_{\text{tls}}}$ of the free TLS and the time evolution operator $\hat{U}_V(t, t_0)$ in the interaction picture

$$\hat{U}_V(t, t_0) = \mathcal{T} \exp \left[-i \int_{t_0}^t dt' V_{H_0}(t') \right]. \quad (3.10)$$

Here, $V_{H_0}(t) = \hat{U}_{H_0}(t_0, t) V(t) \hat{U}_{H_0}(t, t_0)$ is the coupling between TLS and environment in the interaction picture. $H_0 = H_{\text{tls}} + H_B$ is the Hamiltonian describing uncoupled bath and TLS.

The initial density matrix factorizes into environment and TLS part, $\chi(t_0) \equiv \rho(t_0) \otimes \rho_B(t_0)$. This corresponds to the assumption that initial correlations between TLS and environment are irrelevant on experimental time scales. The coupling between TLS and bath is of the form

$$V = g_x \hat{X}_x \tau^x + g_z \hat{X}_z \tau^z, \quad (3.11)$$

where \hat{X} is a bath operator. Transverse coupling proportional to τ_x induces real transitions between TLS states and eventually leads to the decay of the population difference $\langle \tau^z(t) \rangle$ to its stationary value. This effect is called relaxation. Longitudinal coupling proportional to τ^z induces random fluctuations of the TLS level spacing E_{tls} . The TLS wavefunction accumulates a random phase due to this random fluctuations. This induces a loss of phase coherence. Longitudinal coupling leads to pure dephasing. Due to dissipation the TLS eventually reaches its steady state $\rho_\infty = \tanh(\beta E_{\text{tls}}/2)$ where the temperature β^{-1} is determined by the environment. The dynamics of the reduced density matrix is governed by the quantum master equation (1.62),

$$\dot{\rho}(t) = -i[H_{\text{qs}}, \rho(t)] + \int_{t_0}^t \Sigma(t, t') \rho(t') dt'$$

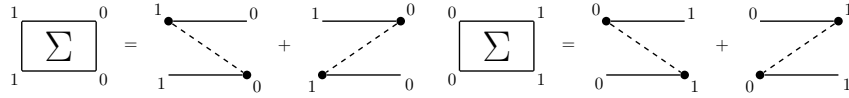


Figure 3.1: Decay (left) and excitation (right) inducing components of the self-energy in second order perturbation theory.

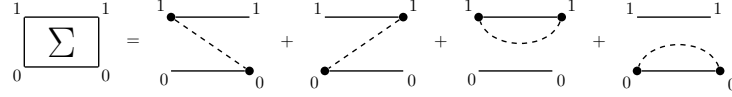


Figure 3.2: Pure dephasing diagrams in second order.

With Markov's approximation the master equation becomes time-local. In Lindblad form it reads as [66]

$$\dot{\rho} = -i[H_{\text{tls}}, \rho] + L_{\downarrow}\rho + L_{\uparrow}\rho + L_z\rho = -i[H_{\text{tls}}, \rho] + L\rho. \quad (3.12)$$

The Lindblad superoperator L is connected to the rate superoperator $\hat{\Gamma}$ defined in Eq. 1.64, $L_{qq' \rightarrow ss'} = \Gamma_{qq' \rightarrow ss'}$ and contains all effects of the environment. The Lindblad operator is defined by its action on the reduced density matrix according to

$$L_{\downarrow}\rho = \frac{\Gamma_{\downarrow}}{2} \{ \tau_- \rho \tau_+ - \tau_+ \tau_- \rho - \rho \tau_+ \tau_- \} \quad (3.13)$$

$$L_{\uparrow}\rho = \frac{\Gamma_{\uparrow}}{2} \{ \tau_+ \rho \tau_- - \tau_- \tau_+ \rho - \rho \tau_- \tau_+ \} \quad (3.14)$$

$$L_z\rho = \frac{\Gamma_{\phi}}{2} \{ \tau_z \rho \tau_z - \rho \} . \quad (3.15)$$

The relaxation rate Γ_{\downarrow} and excitation rate Γ_{\uparrow} describe the transition from excited state to ground state and vice versa while Γ_{ϕ} describes pure dephasing. From the equation of motion for the reduced density matrix the equations of motion for the population difference $\langle \tau^z(t) \rangle$ and the coherences $\langle \tau^{\pm}(t) \rangle$ can be derived. We find

$$\frac{d}{dt} \langle \tau^z(t) \rangle = -\Gamma_1 (\langle \tau^z(t) \rangle - \langle \tau_{\infty}^z \rangle) \quad (3.16)$$

$$\frac{d}{dt} \langle \tau^{\pm}(t) \rangle = (\pm \frac{i}{2} E_{\text{tls}} - \Gamma_2) \langle \tau^{\pm}(t) \rangle \quad (3.17)$$

Here, the relaxation rate $\Gamma_1 = \Gamma_{\uparrow} + \Gamma_{\downarrow}$ describes the decay of the population difference $\langle \tau^z \rangle$ to its stationary/ equilibrium value $\langle \tau_{\infty}^z \rangle = (\Gamma_{\downarrow} - \Gamma_{\uparrow})/\Gamma_1$. The decoherence rate $\Gamma_2 = \Gamma_1/2 + \Gamma_{\phi}$ describes the decay of coherences $\langle \tau^{\pm} \rangle$ to zero. The different processes relaxation, dephasing and decoherence can be visualized on the Bloch sphere, see Fig. 3.4. The decoherence rate Γ_2 describes the decay of the Bloch vector ψ onto the \hat{z} axis and the relaxation rate Γ_1 describes the decay of the \hat{z} value of the vector to its stationary value.

In lowest order perturbation theory the up and down rates follow from the self-energy diagrams depicted in Fig. 3.1. Pure dephasing rates follow from the diagrams in Fig. 3.2. This yields the up, down and dephasing rates

$$\Gamma_{\uparrow/\downarrow} = \frac{\pi}{2} g_x^2 S_{\hat{X}_x}(\mp E_{\text{tls}}) \quad (3.18)$$

$$\Gamma_2 = \pi g_z^2 S_{S, \lambda^z}(0). \quad (3.19)$$

The bath enters the golden rule rates only through the noise spectral density [82]

$$S_{\hat{X}}(\omega) = \int \frac{dt}{2\pi} \langle \hat{X}(t) \hat{X}(0) \rangle e^{-i\omega t}. \quad (3.20)$$

Since the effects of the bath on the TLS are characterized by its spectral density, calculating the spectral density for different sources of decoherence will be a main topic in this work.

The Markov approximation holds for a spectral density that is flat in vicinity of relevant frequencies. For relaxation the relevant energy scale is defined by the TLS energy splitting. In this frequency range the assumption of a flat spectral density often holds. Pure dephasing on the other hand is characterized by small frequencies $\omega \approx 0$. In this small frequency regime the spectral density strongly depends on frequency quite often. For some important sources of decoherence such as $1/f$ noise or superconducting quasiparticles the spectral density even diverges for small frequencies. and the Markov approximation fails to describe pure dephasing.

3.2 Dephasing and refocusing techniques

Transverse coupling proportional to τ^x induces energy exchange with the environment. Longitudinal coupling on the other hand is in principle a reversible process as excitations remain in the TLS system. Refocusing techniques to counter low frequency fluctuations have been developed in the field of nuclear magnetic resonance (NMR) and are nowadays used to improve qubit coherence as well. In this section we apply the non-equilibrium methods developed in chapter 1 in order to derive the governing equations describing refocusing techniques.

The idea behind these refocusing techniques is to apply a sequence of coherent pulses to counteract undesired phase shifts provoked by the environment. For example, static noise can be effectively canceled by the Hahn spin-echo protocol, where a single π -pulse is applied in the middle of the experimental time interval. Higher frequency components can be suppressed by periodic application of π -pulses [83, 84]. We assume that qubit/ TLS control pulses are ideal, i.e. instantaneous and error free. For example, a rotation around the \hat{y} -axis of the Bloch sphere can be represented by the rotation

matrix $Y_\phi = \exp(-i\phi \tau^y/2)$. A π -pulse, i.e. $\phi = \pi$, corresponds to the transformation $\tau^z \mapsto -\tau^z$. In a typical experiment the TLS is prepared in some initial state at time $t = 0$. Subsequently, the TLS evolves in time and its state is measured after the run time t . A refocusing sequence corresponds to the application of N π -pulses at times $t_k = \delta_k t$ with $0 < \delta_k < 1$ during the run time. Between pulses the TLS evolves freely. Every pulse induces a sign-change of τ^z while the transverse coupling proportional to τ^x remains unaffected. Thus, relaxation effects enter through the rate $\Gamma_1/2$ and induce exponential decay of coherences proportional to $\exp(-\Gamma_1 t/2)$.

The TLS Hamiltonian is piecewise constant $H_{\text{tls}} = \pm E_{\text{tls}} \tau^z$. The same holds for the longitudinal interaction between TLS and environment. The sign in front of τ^z depends on the current time interval between pulses. The longitudinal coupling between bath and TLS commutes with the TLS Hamiltonian during the entire experiment. Thus, the coupling takes the form $V_{H_0}(t) = \pm \tau^z \hat{X}_{H_B}(t)$ in the interaction picture. Taking into account that the Hamiltonian is piecewise constant expression (1.59) for the TLS' coherences simplifies to ($t_0 = 0$)

$$\rho_{s\bar{s}}(t) = \text{Tr}_B \left[\rho_B(0) \hat{U}_V^\dagger(t, s) \hat{U}_V(t, \bar{s}) \right] \langle s | \hat{U}_{H_{\text{tls}}}(t) | s \rangle \langle \bar{s} | \hat{U}_{H_{\text{tls}}}^\dagger(t) | \bar{s} \rangle \quad (3.21)$$

where \bar{s} denotes the opposite TLS state of s . The effective time evolution operator $\hat{U}_V(t, s)$ in the interaction picture is defined as

$$\hat{U}_V(t, s) = \mathcal{T} \exp \left[-i \sum_{j=0}^N (-1)^j s \int_{t_j}^{t_{j+1}} dt' \hat{X}_{H_B}(t') \right]. \quad (3.22)$$

With ordering along the closed time contour we find

$$\rho_{s\bar{s}}(t) = \left\langle \mathcal{T}_C \exp \left[i s \int_C dz \hat{X}_{H_B}^{\text{ef}}(z) \right] \right\rangle_B \langle s | \hat{U}_{H_{\text{tls}}}(t) | s \rangle \langle \bar{s} | \hat{U}_{H_{\text{tls}}}^\dagger(t) | \bar{s} \rangle. \quad (3.23)$$

The bath operator along the forward/ backward branch of the contour is defined as $\hat{X}_{H_B}^{\text{ef}}(t_\pm) = \pm (-1)^j \hat{X}_{H_B}(t)$ for $t_j < t \leq t_{j+1}$. For Gaussian bath operators the bath expectation value simplifies according to $\langle \exp(A) \exp(A) \rangle = \exp(\langle A^2 \rangle/2)$ and the TLS coherences take the form

$$\rho_{s\bar{s}}(t) = \exp \left[-\frac{1}{2} \int_C dz \int_C dz' \langle \mathcal{T}_C \hat{X}_{H_B}^{\text{ef}}(z) \hat{X}_{H_B}^{\text{ef}}(z') \rangle \right] \langle s | \hat{U}_{H_{\text{tls}}}(t) | s \rangle \langle \bar{s} | \hat{U}_{H_{\text{tls}}}^\dagger(t) | \bar{s} \rangle. \quad (3.24)$$

We transform the contour integrals to real-time integrals. This yields

$$\rho_{s\bar{s}}(t) = \exp \left\{ -2 \int_0^t dt_1 \int_0^{t_1} dt_2 \left\langle \left[\hat{X}_{H_B}^{\text{ef}}(t_1), \hat{X}_{H_B}^{\text{ef}}(t_2) \right]_+ \right\rangle \right\} \langle s | \hat{U}_{H_{\text{tls}}}(t) | s \rangle \langle \bar{s} | \hat{U}_{H_{\text{tls}}}^\dagger(t) | \bar{s} \rangle. \quad (3.25)$$

With the bath power spectral density $S(\omega) = \int dt e^{-i\omega t} \langle [\hat{X}(t), \hat{X}(0)]_+ \rangle$ we can write

$$\rho_{s\bar{s}}(t) = e^{-\Gamma_1 t/2 - x_N(t)} \langle s | \hat{U}_{H_{\text{tls}}}(t) | s \rangle \langle \bar{s} | \hat{U}_{H_{\text{tls}}}^\dagger(t) | \bar{s} \rangle. \quad (3.26)$$

with the dephasing function $x_N(t) = 2t^2 \int_0^\infty \frac{d\omega}{2\pi} S(\omega) g_N(\omega t)$. We reintroduced the contribution of relaxation to decoherence into the equation. The dimensionless function $g_N(\omega)$ can be viewed as a low-pass frequency filter. Similar to Götze and Uhrig [84] and Bylander et al. [83] we find the filter function

$$g_N(x) = \frac{1}{x^2} 2 \operatorname{Re} \left[\sum_{n=1}^{N+1} 1 - e^{ix(\delta_n - \delta_{n-1})} + \sum_{m=1}^{n-1} (-1)^{n+m} (e^{ix\delta_n} - e^{ix\delta_{n-1}})(e^{-ix\delta_m} - e^{-ix\delta_{m-1}}) \right] \quad (3.27)$$

with $\delta_0 = 0$ and $\delta_{N+1} = 1$.

During this work we will calculate the dephasing functions for Ramsey dephasing and spin-echo due to different sources of decoherence. The Ramsey protocol corresponds to the free time evolution of the TLS without any refocusing pulse, $N = 0$, while spin-echo is the simplest non-trivial sequence with a single π -pulse at $\delta_1 = 0.5$. Spin-echo and Ramsey protocol evaluate the bath spectral function at different frequencies. The Ramsey filter is strongly peaked at $\omega t = 0$ and is sensitive to quasi-static noise. Spin-echo filters quasi-static noise and evaluates the spectral function at slightly higher frequencies, $\omega t \approx 4.6$, see Fig. 3.3. Due to shifted weight of the filter function different protocols can be used to probe the frequency dependence of the noise spectral density [83]. Spin-echo and Ramsey protocol have been applied by J. Lisenfeld et al. to microscopic TLS inside a Josephson junction in order to obtain more information about their microscopic properties [III]. For those protocols the dephasing functions are given by

$$x_0(t) = \frac{t^2}{2} \int d\omega S(\omega) \operatorname{sinc}^2 \left(\frac{\omega t}{2} \right), \quad (3.28)$$

$$x_1(t) = \frac{t^2}{2} \int d\omega S(\omega) \sin^2 \left(\frac{\omega t}{4} \right) \operatorname{sinc}^2 \left(\frac{\omega t}{4} \right). \quad (3.29)$$

For a flat spectral density the filter functions become δ -like. Approximating the spectral density as a constant $S(\omega')$ with the frequency of the filter maximum ω' Ramsey and spin echo dephasing functions turn into the usual rate form

$$x_0(t) \approx \frac{\pi}{2} S(0) t = \Gamma_r t, \quad (3.30)$$

$$x_1(t) \approx \frac{\pi}{2} S(4.6/t) t = \Gamma_e t. \quad (3.31)$$

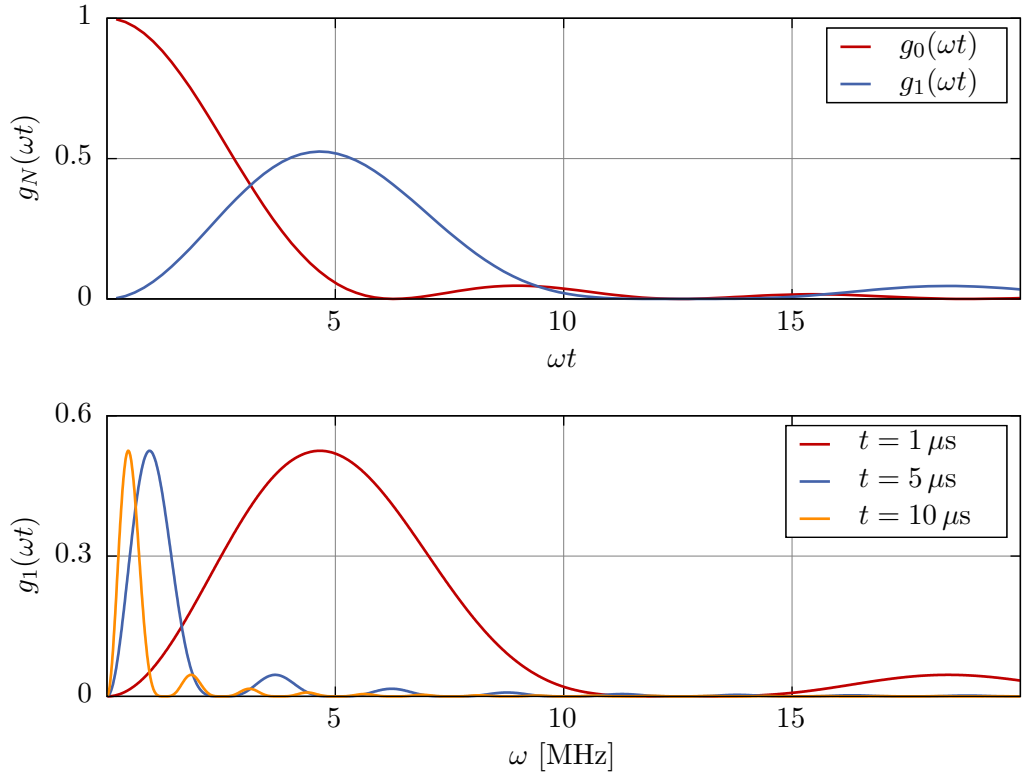


Figure 3.3: *Top:* Filter function g_N for Ramsey protocol (red) and spin-echo protocol (blue) as functions of the dimensionless variable ωt . While the Ramsey filter is peaked at $\omega t = 0$ the maximum of the spin-echo filter is shifted to higher values, $\omega t \approx 4.6$. *Bottom:* Spin-echo filter function for different measurement times t . Shorter times shift the maximum of the weight function $\omega' = 4.6/t$ to higher frequencies.

The effectiveness of spin-echo refocusing can be quantized by the ratio between Ramsey and spin echo rate which corresponds to the ratio between the spectral density evaluated at the different maximum frequencies. For spectral densities that vary on the bandwidth defined by the filter functions the linear approximation fails, and dephasing follows the non-linear decay given by the full dephasing functions. For such situations the ratio between Ramsey and spin-echo may be defined by taking the dephasing rate as the inverse of the time the measurement signal has decayed to $1/e$ of its original value.

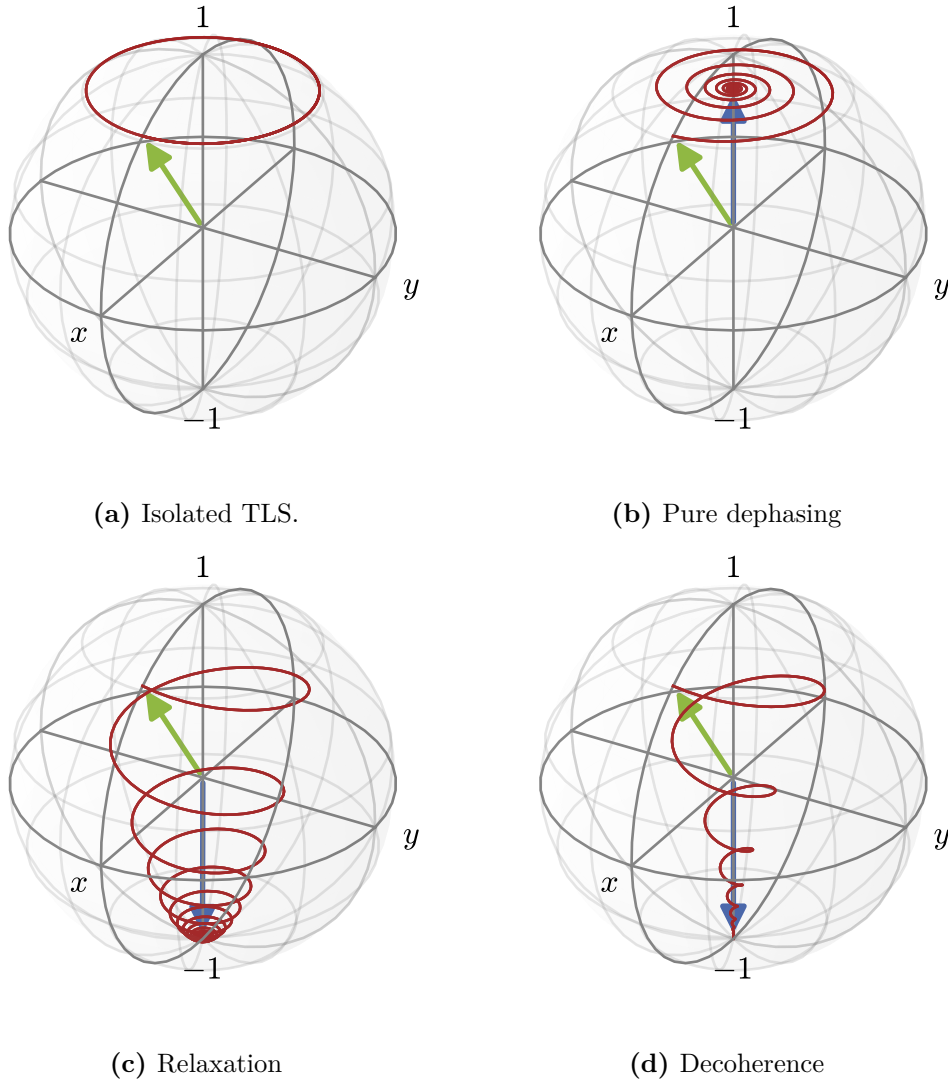


Figure 3.4: Dynamics of a TLS on the Bloch sphere for different couplings to the environment. The green vector represents the initial state, the blue vector the stationary state for $t \rightarrow \infty$ and the red line represents the time evolution of the vector. (a) For an isolated TLS the state remains pure and the vector $\vec{\psi}$ points on the surface of the Bloch sphere. (b) Pure longitudinal coupling $\propto \tau^z$ to the bath. The qubit state loses its phase information while the \hat{z} value remains constant, $\langle \tau^z(t) \rangle = \langle \tau^z(0) \rangle$. (c) Pure transversal coupling $\propto \tau^x$. This coupling induces relaxation to the stationary state, $\langle \tau_\infty^z \rangle = -1$, and loss of phase information $\propto \Gamma_1/2$. (d) Dephasing and relaxation inducing coupling. Decoherence happens at the rate Γ_2 .

4 Chapter 4

4 Decoherence of Two-Level Systems

4.1 Introduction

Research on two-level systems (TLS) in amorphous solids dates back to early experiments by Zeller and Pohl in 1971 [85]. In their experiments the authors found unexpected behavior of the thermal conductivity and specific heat of amorphous solids. For crystalline insulators the Debye model predicts that both specific heat and thermal conductivity vary with the temperature as $C \sim T^3$ and $\kappa \sim T^3$. In contrast, Zeller and Pohl found that the specific heat in amorphous materials varies almost linearly with temperature $C \sim T^{1.2}$ while the thermal conductivity is nearly quadratic in temperature, $\kappa \sim T^{1.8}$.

Independently from each other Phillips [35] and Anderson et al. [36] came up with an explanation of the “anomalous” behavior of amorphous materials based on two-level systems. Although their phenomenological tunneling model comes without microscopic theory, these two-level systems can be related to low energy bistable excitations residing in amorphous materials. A possible explanation for the appearance of these defects is as follows: Due to the random nature of amorphous solids single atoms or small groups of atoms can tunnel between two different configurations with similar energies. Other possible candidates for TLS are dangling bonds, trapped electrons or hydrogen defects. All microscopic models rely on the random structure of the host material and have two energetically similar low-energy configurations. At low temperatures the defects can be reduced to these two configurations yielding effective two-level systems. These two-level systems become evident for temperatures below approximately 20 K [86]. Due to the amorphous nature many different configurations supporting TLS can form yielding a wide range of characteristic TLS properties even in small samples.

Although the exact nature of TLS remains unclear the standard tunneling model (STM) has been used to describe many low temperature properties of amorphous solids

such as specific heat [87], heat release [88, 89] or acoustic properties [90, 91]. In the STM one assumes a homogeneously distributed set of TLS properties throughout the amorphous material [86]. Theoretical models for microscopic realizations can be used to determine parameters of the STM which allows direct comparison with experiments. However, those experiments provide only information about the ensemble of TLS. Thus, extracting information about microscopic properties of individual TLS is difficult to accomplish.

The interest in microscopic TLS has increased yet again since several experiments on superconducting circuits provided evidence that two-level systems induce strong decoherence effects in superconducting qubits [33, 34, 92] and superconducting resonators [93]. In superconducting devices TLS reside in dielectric substrates, disordered interfaces, surface oxides, inside the barriers of Josephson junctions, or in other amorphous materials in the devices [34].

Much effort has been put into understanding and minimizing various noise sources. Despite those efforts the microscopic origin of TLS remains unclear at present. While experiments were limited to indirect measurements of statistical properties of the TLS in the past, the advance in control and application of superconducting circuits enabled experiments on individual qubits [34, 41].

A better experimental as well as theoretical understanding of those TLS has been the focus of much recent work: using a superconducting phase qubit for TLS control and read-out strain dependent spectroscopy showed a parabolic energy dependence of TLS energy-splittings on the applied strain [42], Martinis et al. investigated the effect of TLS on qubit decoherence [92] while Gunnarsson et al. used superconducting qubits to characterize high frequency loss in dielectrics [37]. Different microscopic candidates for TLS have been suggested such as tunneling oxygen [38], impurity states in the junction [40] or tunneling hydrogen defects [39]. Models have been analyzed and tested experimentally using superconducting qubits [94, 95].

In this part of the thesis we analyze TLS decoherence due to coupling with different sources of noise such as phonons, quasiparticles, or other TLS. The work was motivated by several experiments on decoherence of TLS performed in the group of A. Ustinov. Two of these experiments are particularly interesting in context of this thesis.

In the first experiment strain dependent decoherence rates of TLS inside the amorphous tunneling barrier of a Josephson junction have been investigated by Lisenfeld et al. [III]. In the experiment decay rates as well as strain dependent Ramsey and spin-echo dephasing rates of TLS have been measured. Spin echo refocusing proved surprisingly effective with ratios between spin-echo and Ramsey dephasing rates up to $\Gamma_e/\Gamma_r \approx 22$. We discuss the experiment in section 4.2.2 and our theory in section 4.4.

In the second experiment the influence of quasiparticles on TLS coherence has been examined by A. Bilmes et al. [IV]. Non-equilibrium quasiparticles have been un-

der investigation as a source of decoherence inherent to superconducting qubits for a long time [I, 96–103]. In the experiment quasiparticle dependent decoherence rates of junction-TLS have been measured. The experiment clearly demonstrates the coupling between TLS and quasiparticles. This offers an additional experimental tool to test microscopic models for two-level systems. Earlier measurements of TLS life times showed an unexpected temperature dependence [43]. This can be explained by quasiparticles as well. We develop a theory of the interaction between TLS inside the junction and quasiparticles in section 4.3.

The chapter is structured as follows. In the first part we introduce the standard tunneling model following Phillips and Anderson [35, 36] and summarize important properties and parameters of the model. In the following part, we summarize the basic ideas used in the experiments by Lisenfeld and Bilmes. In particular, we describe how a superconducting phase qubit can be used as a read-out device for TLS. In section 4.3 we analyze decoherence of TLS due to quasiparticles. We give a short summary of the experiment by Bilmes [IV]. Subsequently, we introduce our model for the coupling between TLS and quasiparticle, and analyze quasiparticle dynamics in the system. Finally, we calculate decay, dephasing, and Rabi decay rates of TLS due to quasiparticles. In the last section, 4.4, we analyze decoherence of TLS due to coupling with different types of noise in order to explain the surprising results of the experiment by Lisenfeld [III].

4.2 Microscopic TLS - the standard tunneling model

A lot of research has been done to understand the nature of low energy excitations in amorphous solids. Nonetheless, the microscopic origin of TLS remains unclear with trapped electrons, dangling bonds, hydrogen defects and tunneling atoms among possible microscopic candidates for TLS. In Fig. 4.1 we show a sketch of a Josephson junction comprising of an amorphous aluminum oxide layer between two crystalline aluminum layers with several possible realizations of TLS. We use the phenomenological standard tunneling model (STM) to describe the TLS [35]. In the STM the microscopic system with its two stable configurations is represented by an effective particle with mass m and charge Q trapped in a double well potential, see Fig. 4.2a. The wells represent the two stable configurations of the microscopic system. For simplicity we assume that both wells are characterized by the same ground state energy ω_0 whereas the energy spectrum of the second well is shifted by the asymmetry Δ relative to the first well [86]. The energy spacing between first excited state and ground state of a single well is large compared to the asymmetry, $\omega_1 - \omega_0 \gg \Delta$. For small energies or respectively low temperatures $k_B T \ll \omega_1 - \omega_0$ no excitation to higher energy levels

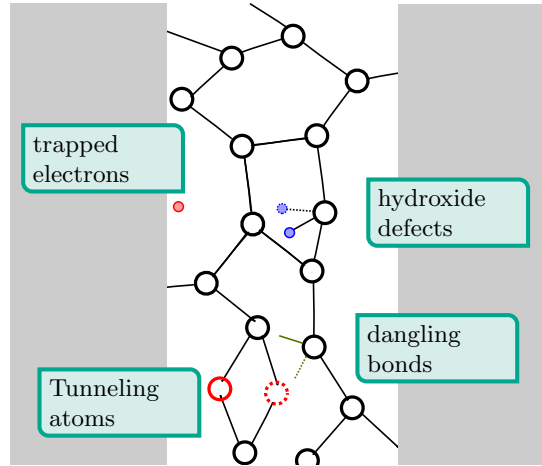


Figure 4.1: Two superconducting aluminum layers (left and right) with an amorphous aluminum oxide (AlO_x) layer in between. The AlO_x layer hosts microscopic TLS such as trapped electrons (top left), Hydrogen defects (top right), tunneling atoms (bottom left) or dangling bonds (bottom right).

in the wells occur. Consequently, we can truncate the Hilbert space of the trapped particle to the ground states of the wells. Assuming identical wells we can represent both ground states Φ_α by the same wavefunction Φ_0 . Consequently, only the space variable is shifted according to $\Phi_\alpha(\mathbf{R}) = \Phi_0(\mathbf{R} - \mathbf{R}_\alpha)$ where $\alpha = 1, 2$ for the first and second well respectively. Here, $\mathbf{R}_{1,2} = \mathbf{R}_0 \pm \mathbf{d}/2$. is the position of the well minimums and the vector \vec{d} connects both wells. We approximate the ground state wave function with the harmonic oscillator ground state

$$\Phi_0(\mathbf{R}) = \frac{1}{(r_0^2 \pi)^{\frac{1}{4}}} \exp\left(-\frac{R^2}{2r_0^2}\right) \quad (4.1)$$

with the width of the localized state $r_0 = 1/\sqrt{M\omega}$. For Hydrogen defects typical values of the parameters are $d \approx 0.85\text{\AA}$ and $r_0 \approx 0.14\text{\AA}$ while for larger systems typical values are $r_0 \sim 0.1 - 0.03\text{\AA}$ and $d \sim 0.15 - 0.5\text{\AA}$ [104, 105]. Thus, the TLS wave functions are well localized close to the well minimums. The effective particle can tunnel with amplitude Δ_0 from one well to the other mimicking tunneling between the stable configurations of the microscopic model. In the STM both tunneling amplitude and asymmetry are phenomenological parameters. The tunneling amplitude can be expressed in terms of the well energy ω_0 and the Gamow parameter λ as $\Delta_0 = \omega_0 e^{-\lambda}$. Using WKB approximation the Gamow parameter can be expressed in terms of the barrier height V , the barrier width d and the effective particle mass m as $\lambda = \sqrt{2mV}d^2$ [86]. In the basis spanned by the localized eigenstates $|1\rangle$ of the first and $|2\rangle$ of the

second well the TLS Hamiltonian takes the form

$$H_{\text{tls}} = \frac{\Delta}{2} (|1\rangle\langle 1| - |2\rangle\langle 2|) + \frac{\Delta_0}{2} (|1\rangle\langle 2| + |2\rangle\langle 1|) = \frac{\Delta}{2}\sigma^z + \frac{\Delta_0}{2}\sigma^x. \quad (4.2)$$

where $\sigma^z = |1\rangle\langle 1| - |2\rangle\langle 2|$ and $\sigma^x = |1\rangle\langle 2| + |2\rangle\langle 1|$ are Pauli matrices in the localized state basis. The eigenstates of the TLS are superpositions of the left and right eigenstate. Diagonalizing the Hamiltonian with the unitary transformation

$$U = \begin{pmatrix} \cos \phi/2 & \sin \phi/2 \\ -\sin \phi/2 & \cos \phi/2 \end{pmatrix}, \quad (4.3)$$

we find the energy splitting between ground and excited state $E_{\text{tls}} = \sqrt{\Delta^2 + \Delta_0^2}$. The mixing angle fulfills the condition $\tan \phi = -\Delta_0/\Delta$. With the Pauli-z matrix τ^z in the energy eigenbasis spanned by ground state $|g\rangle$ and excited state $|e\rangle$ the Hamiltonian can be expressed as

$$H_{\text{tls}} = \frac{E_{\text{tls}}}{2}\tau^z. \quad (4.4)$$

We will use the convention to denote Pauli operators in the physical left-right basis with σ^i and operators in the energy basis with τ^i . In the STM one assumes that the physical parameters λ and Δ are uniformly distributed parameters. Thus, the probability P_0 to find a TLS with parameters in the parameter space $\lambda, \lambda + d\lambda$ and $\Delta, \Delta + d\Delta$ is constant. This corresponds to the random distribution of TLS

$$P(\Delta, \lambda)d\lambda d\Delta = P_0 d\lambda d\Delta \quad (4.5)$$

with upper bounds λ_{max} and Δ_{max} . We can express the probability distribution in different sets of TLS parameters. Transforming the probability distribution to the most common pairs of parameters we find

$$P(\Delta, \Delta_0)d\Delta d\Delta_0 = \frac{P_0}{\Delta_0} d\Delta d\Delta_0 \quad (4.6)$$

$$P(\Delta, V)d\Delta dV = \frac{P_0}{\omega_0} d\Delta dV \quad (4.7)$$

$$P(E_{\text{tls}}, u)dE_{\text{tls}} du = \frac{P_0}{u\sqrt{1-u^2}} dE_{\text{tls}} du, \quad u = \frac{\Delta_0}{E}. \quad (4.8)$$

The standard tunneling model with uniform distributed Gamow parameter and asymmetry has been used successfully to explain low temperature specific heat $C \sim T^{1.2}$, thermal conductivity $\kappa \sim T^{1.8}$, and many more low-temperature properties of amorphous solids. We will use the STM with uniform distribution function to describe

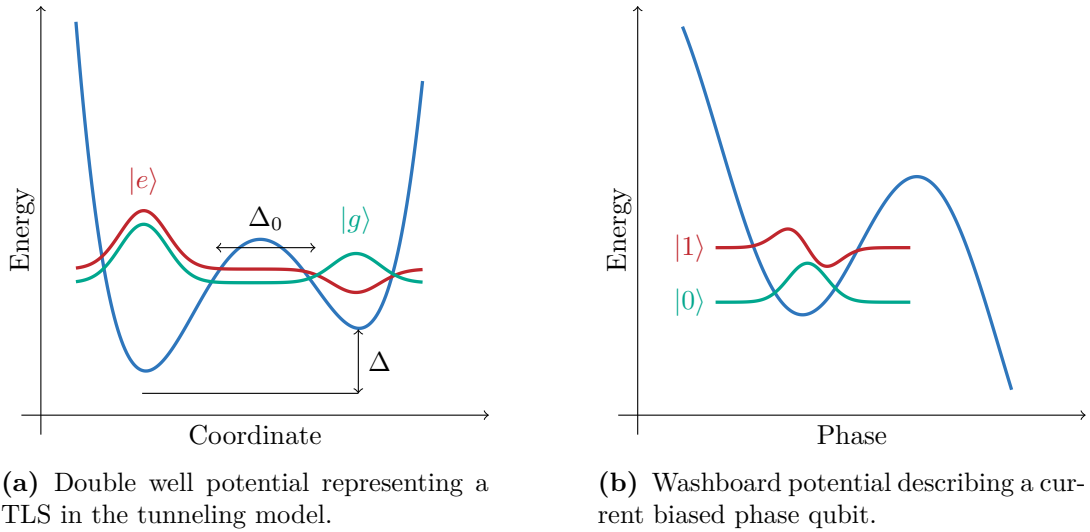


Figure 4.2: (a) Potential landscape for a TLS in the standard model. We show the ground state wavefunction (green) and first excited state wavefunction (red). The wells are shifted relative to each other by the asymmetry Δ . (b) Tilted washboard potential for an effective particle representing a phase qubit.

decoherence of a single TLS due to a bath of uncoupled TLS.

4.2.1 Artificial TLS - Current biased Phase Qubit

In the experiments by J. Lisenfeld et al. a current-biased single- Josephson-junction (JJ) phase qubit has been used to analyze TLS. The junction comprises two aluminum layers separated by a thin aluminum oxide barrier. TLS analyzed in these experiments reside inside the amorphous barrier of the junction itself. In terms of the phase difference φ of the superconducting condensate across the junction and its conjugate variable, the number of tunneled Cooper pairs \hat{n} , the Hamiltonian of the current biased phase qubit takes the form

$$H_{\text{qubit}} = E_C \hat{n}^2 + \frac{(\varphi - \phi_{\text{ext}})^2}{2E_L} - E_J \cos \varphi - I \frac{\dot{\varphi}}{\phi_0}. \quad (4.9)$$

The qubit is characterized by the Josephson energy E_J and the charging energy E_C . The Josephson energy is determined by the normal state resistance of the junction while the charging energy corresponds to the electrostatic energy accumulated on the superconducting pads. The phase qubit can be understood as an effective particle with space coordinate φ and momentum \hat{n} moving in an effective potential $U(\varphi)$, see Fig. 4.2b. The bias current I determines the overall slope of the tilted washboard potential. The non-linear inductance of the Josephson junction induces anharmonicity and a truncation of the Hilbert space to the two lowest energy levels is valid. The effective qubit Hamiltonian is identical to the Hamiltonian describing a microscopic

two-level system, $H_{\text{qubit}} = \frac{E_q}{2}\tau^z$ with the qubit resonance energy E_q . The resonance energy of the qubit can be tuned by applying an external flux ϕ_{ext} that couples to the linear junction-inductance E_L .

4.2.2 Experiments with TLS

In several recent experiments superconducting qubits have been used to analyze TLS in amorphous Aluminum oxide [III, IV, 42, 43]. The Josephson junction (JJ) of such a qubit consists of two superconducting aluminum layers separated by an approximately 2 nm thick insulating barrier where the barrier comprises aluminum oxide (AlO_x). The amorphous AlO_x layer hosts microscopic two-level systems, Fig. 4.1. These TLS couple to the JJ qubit either via their electrical dipole moment or they modify the junctions Josephson energy which also leads to an effective coupling between qubit and TLS [82]. In the latter case the coupling is of the form $H_{\text{q,tls}} = -E_j(j_x\sigma^x + j_z\sigma^z) \cos 2\pi\varphi/\phi_0$ with the Josephson energy E_j , the phase φ across the junction and the coupling constant \vec{j} . A charged TLS with dipole moment $\vec{p} = Q_{\text{tls}}\vec{d}\sigma^z$ couples to the electrical field $E \sim \dot{\varphi}$ across the Josephson junction. Here, Q_{tls} is the effective charge of the TLS and \vec{d} the spatial vector connecting left and right well, i.e. the spatial separation between wells is $|\vec{d}|$. The dipole coupling between qubit and TLS takes the form

$$H_{\text{q,tls}} = \vec{E} \cdot \vec{p} = \frac{p \cos \eta}{eW} E_C \sigma^z \hat{n}$$

where \hat{n} is the number operator of excess Cooper pairs on the junction capacity, $W \approx 2\text{nm}$ is the width of the junction, E_C the charging energy and η is the angle between TLS axis and the electrical field. Typical values for the dipole moment parallel to the electrical field are $p \cos \eta \sim 0.2 - 0.5 \text{ eÅ}$ [III].

Independent of the exact form of interaction the coupling between qubit and TLS can be used to manipulate and read-out TLS inside the junction barrier [42, 43]. The general idea is to use qubit spectroscopy to find TLS inside the JJ. A resonance between qubit and a TLS manifests as an avoided level crossing in the qubit spectrum [92]. From the avoided level crossing TLS level splitting and coupling strength between qubit and TLS can be extracted. Using these information TLS can be controlled using standard microwave pulses tuned to the TLS energy splitting. In order to read-out the TLS the qubit is tuned into resonance with the TLS. In resonance, qubit and TLS exchange excitations. Waiting for a time $t_{\text{swap}} \approx h/4g$ where g is the coupling strength between TLS and qubit the state can be swapped from TLS to the qubit. Tuning the qubit away from resonance and reading out the qubit yields a measurement on the TLS state. We take a closer look on two of those experiments in which decoherence of TLS has been analyzed.

In the first experiment strain dependent decay rates as well as Ramsey and spin-echo

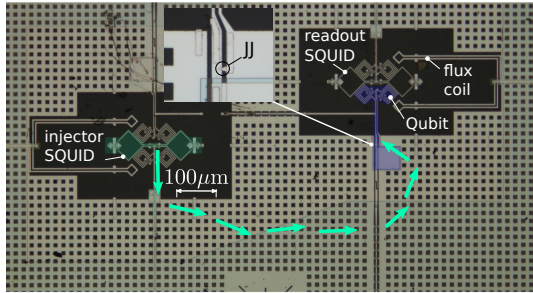


Figure 4.3: Image of the setup used in the experiments [III, IV]. The phase qubit with the Josephson junction (JJ) is located on the right-hand side (blue highlight). The qubit is connected to a readout SQUID and controlled by the flux coil. On the left-hand side the SQUID used to inject quasiparticles is emphasized in green. Quasiparticles diffuse from the injection site to the junction (green arrows). The distance from the injection site to the different electrodes comprising the junction is $700 \mu\text{m}$ and $1400 \mu\text{m}$ respectively. Image taken from [IV].

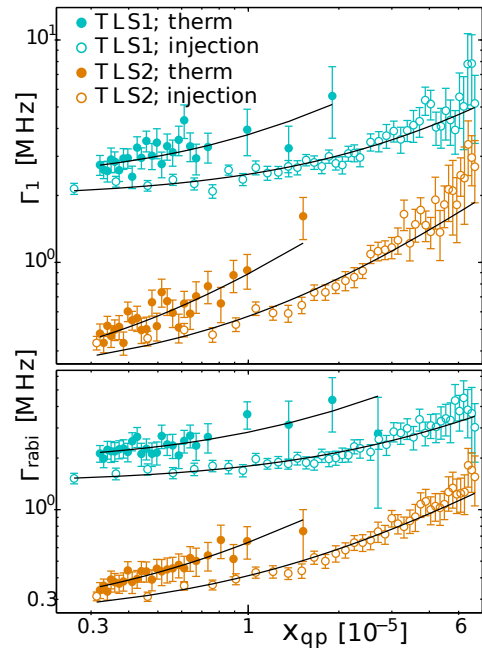


Figure 4.4: Quasiparticle induced relaxation rates (top) and Rabi decay rates (bottom) versus quasiparticle density in units of the Cooper pair density n_{cp} . Black lines are fits of our theory to the data. Both Rabi decay rate and relaxation rate are proportional to the quasiparticle density. Decoherence rates due to thermally created quasiparticles exceed decoherence rates due to injected quasiparticles. Graphs taken from [IV].

dephasing behavior of TLS have been investigated [III]. The analysis of the findings of this experiment are an important part of this thesis. We discuss several sources of decoherence in order to explain the experimental results in section 4.4.

In the second experiment the influence of quasiparticles on TLS coherence has been examined by A. Bilmes et al. [IV]. Quasiparticles have been under investigation as a source of decoherence inherent to superconducting qubits for long time [106, 107]. The experiment demonstrates the coupling between TLS and quasiparticles. This coupling can be used as an additional tool to test microscopic models for two-level systems. In section 4.3 we discuss our theory that explains quasiparticle-TLS interaction and resulting TLS decoherence.

Decoherence due to quasiparticles, Bilmes et al. [IV]

Experiments by Lisenfeld et al. showed unexpected temperature dependence of relaxation rates of TLS as shown in Fig. 4.5 [43].

The strong temperature dependence of the rates hints that superconducting quasiparticles couple to microscopic TLS inside the JJ and induce TLS decoherence similar to decoherence of qubits. These findings led to follow-up experiment by A. Bilmes. The goal of this experiment was the investigation of quasiparticle induced decoherence of TLS inside a Josephson junction [IV]. Control and measurements of the TLS were realized using microwave pulses and a JJ phase qubit [42, 43].

To analyze the dependence of decoherence rates on the amount of quasiparticles present in vicinity of the junction, quasiparticles were generated in two ways. Firstly, heating the sample led to an increase of the quasiparticle density according to $n_{qp} \propto \exp(-\Delta_{\text{bcs}}/k_B T)$, where $\Delta_{\text{bcs}} \approx k_B \cdot 2.1$ K is the superconducting gap of aluminum. The base temperature of the sample was increased from 30 mK up to 330 mK. These temperatures are well below TLS energy splitting avoiding unintentional excitations of the TLS. On the other hand the temperatures are high enough in order to significantly increase the amount of quasiparticles. Secondly, non-equilibrium quasiparticles were injected using a SQUID placed on the same chip. Applying an overcritical current to the SQUID injected quasiparticles into the system. Subsequently, the quasiparticles diffused through the superconducting layer to the junction where they increased the local quasiparticle density.

In the experiment the quasiparticle density at the junction was measured for each temperature and injection current using the frequency shift of the phase qubit. This frequency shift is proportional to the quasiparticle density at the junction, $\Delta f \propto n_{qp}$ [106]. Then TLS decoherence decay, dephasing and Rabi oscillation decay of the TLS were measured. All measurements were performed after the quasiparticles had reached a stationary state. This was ensured by time resolved measurements of the quasiparticle density. In Fig. 4.10 we show time dependent measurements of the quasiparticle density together with our simulations of the diffusion process. A photograph of the superconducting chip with SQUID, phase qubit and quasiparticle diffusion path is depicted in Fig- 4.3. The measured TLS relaxation and Rabi decay rates depend linearly on the measured quasiparticle density 4.4. In the figure, the quasiparticle density is normalized to the Cooper pair density, $x_{qp} = n_{qp}/n_{cp}$.

The experimental data display a surprising difference between decoherence rates due to thermally created quasiparticles and injected quasiparticles. In section 4.3 we develop a theory of quasiparticle induced TLS decoherence. Black lines in Fig. 4.4 are fits to this theory. With this theory and the diffusion and recombination processes of

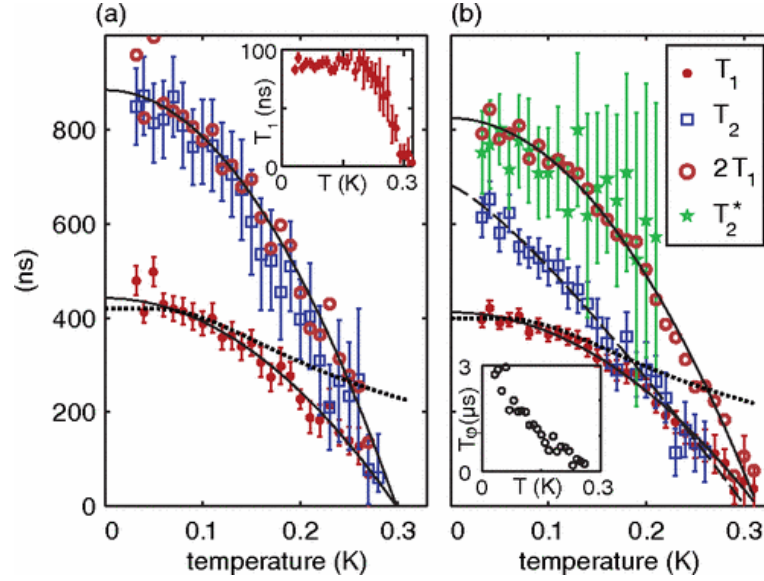


Figure 4.5: Temperature dependent coherence times of two TLS. Dotted lines correspond to decay through phonons $\propto \tanh \frac{\beta E_{\text{tls}}}{2}$ while solid lines are fits to a phenomenological power-law $T_1(T) = A - BT^2$. The strong decrease of the coherence times hints at quasiparticles as an additional source of decoherence. A combination of quasiparticle induced decay $\propto \exp(-\beta \Delta_{\text{bcs}})$ and phonon-induced decoherence fits the data. The inset shows the qubit decay time. Reprint with permission from [43], © American Physical Society, 2010

injected quasiparticles we can explain the differences between injected and thermally created quasiparticles.

Strain dependent TLS decoherence, Lisenfeld et al. [III]

A local strain field distorts the positions of atoms around a microscopic TLS. The asymmetry Δ of the TLS is susceptible to the distortion of surrounding atoms. Consequently, it changes with an applied mechanical strain ϵ_p according to $\Delta(\epsilon) = \gamma_p(\epsilon_p - \epsilon_0)$. Here, γ_p is the deformation potential [III]. The symmetry point ϵ_0 corresponds to the strain where the TLS is symmetric, i.e. $\Delta = 0$. Due to the linear change of the asymmetry with the applied strain, the TLS energy splitting is a parabolic function of the mechanical strain, $E_{\text{tls}} = \sqrt{\Delta_0^2 + \gamma_p^2(\epsilon_p - \epsilon_0)^2}$.

Strain dependent TLS spectroscopy has been performed in earlier experiments where the parabolic dispersion of TLS has been confirmed [42]. In a recent experiment Lisenfeld et al. measured the strain dependence of TLS decoherence rates for different measurement protocols: relaxation rates, Ramsey dephasing, spin-echo dephasing, and Rabi oscillations. For each strain the decoherence rates have been obtained from time dependent measurements as shown in Fig. 4.6. The plots are reprints from [III] and show the probability to find the TLS in the excited state after time t . From these

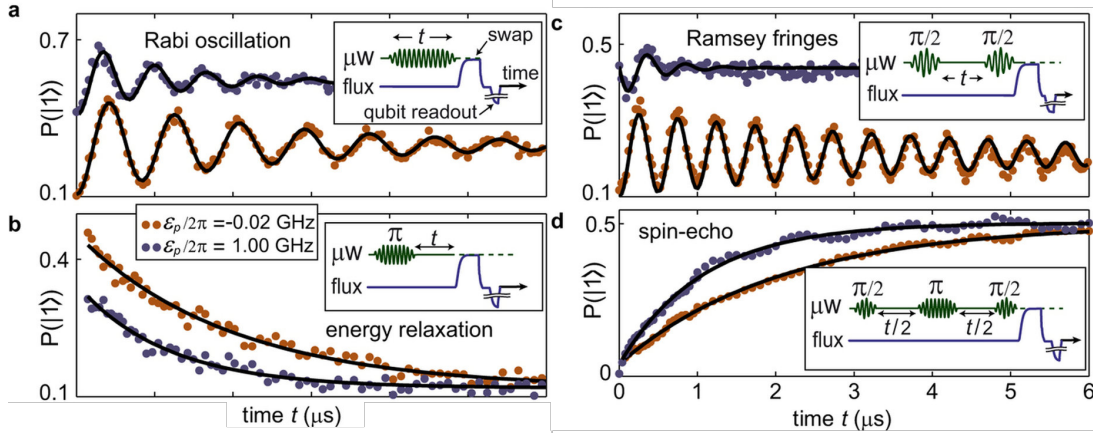


Figure 4.6: Reprint from [III] used under $\text{\textcircled{C}}$ $\text{\textcircled{I}}$. Time resolved measurements demonstrating coherent control and decoherence of TLS. Each panel shows a measurement on a microscopic TLS close to symmetry (brown) and further apart from symmetry, $\epsilon_p - \epsilon_0 = h \cdot 1$ GHz (blue). Insets show the applied pulse sequence to the qubit (flux) and TLS (microwave). The protocols used in the different panels are: **a** Rabi oscillations **b** decay time measurements **c** Ramsey dephasing **d** spin-echo dephasing. The panels show raw data, i.e. the probability of the qubit to be in the excited state.

measurements decoherence rates were obtained from fits to an exponential decay. Measuring TLS coherence for different applied strains the strain dependent decoherence rates shown in Fig. 4.7 were obtained, reprint from [III]. Each column corresponds to a certain microscopic TLS. The relaxation rates depicted in the first row show pronounced features that are symmetric in the applied strain. These features could stem from coupling to discrete phonon modes of the amorphous material. The dephasing rates in the fourth row of Fig. 4.7 show another interesting feature: the spin-echo rates are much smaller than Ramsey rates. The effect of spin-echo refocusing is surprisingly large. This raises the question due to which mechanisms the TLS dissipative information. For example, for dephasing due to $1/f$ noise the ratio is $\Gamma_r/\Gamma_e \approx 2$ while the experiment shows much higher ratios up to 22. Microscopic TLS seem to be prone to strong quasi-static noise that can be filtered effectively with the spin-echo protocol. Contrary to the relaxation rate the dephasing rates show a parabolic or linear dependence on the applied strain. Thus, dephasing and relaxation stem from different sources.

In Sec. 4.4 we analyze different sources of decoherence in order to explain the effectiveness of spin-echo refocusing as well as the strain dependence of relaxation rates. We find that only strong coupling to a single TLS can explain the huge ratios while relaxation is dominated by coupling to acoustic phonons.

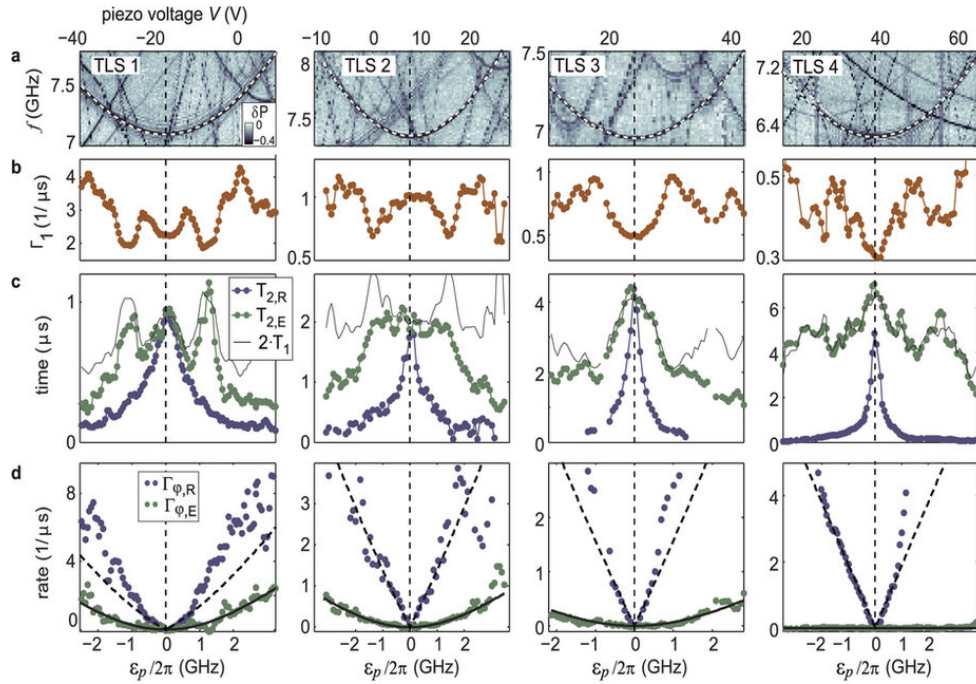


Figure 4.7: Reprint from [III] used under CC BY . Strain dependent measurements. The applied mechanical strain $\epsilon_p - \epsilon_0$ is plotted on the x-axis. **a** TLS spectroscopy. Dark lines represent resonances between qubit and TLS. Resonances manifest as reduced population probability of the qubit. Light dotted lines are fits to $E_{\text{tls}} = \sqrt{\gamma_p^2(\epsilon_p - \epsilon_0)^2 + \Delta_0^2}$. **b** Relaxation rate Γ_1 . The rates show pronounced features that are symmetric in strain. **c** Decoherence times obtained with Ramsey protocol (blue) and spin-echo protocol (green). Thin black lines represent $2T_1$. Except for TLS2 the spin-echo decoherence times are dominated by T_1 . **d** Pure dephasing rates.

4.3 Decoherence Due to Quasiparticles

In this section we analyze decoherence of charged TLS inside the amorphous layer of a Josephson junction [34, 42] due to scattering and tunneling of non-equilibrium quasiparticles in the superconducting leads. The work presented in this section led to the publications [I, II, IV].

In normal metallic glasses the interaction between conduction electrons and localized states have been analyzed theoretically by Kondo [108], Black [44, 109] and other authors [104]. They found relaxation rates of localized states similar to the Korringa relaxation rate of nuclear spins in metals [110]. Measurements of acoustic attenuation in metallic glasses confirmed the theoretical predictions [111]. At low temperatures the interaction with electrons can outweigh the coupling of TLS to the phonon bath and become the dominant damping mechanism [112]. Due to the surrounding cloud of conduction electrons the dressed tunneling amplitude for small temperatures $\tilde{\Delta}_0 \sim (\Delta_0/D)^K$ was found where K is the Kondo factor and D the band-width of conduction electrons [108]. The same effects lead to a divergence in the resistivity of a metallic glass $\sim \log[D/T]^2$ [113].

In a BCS superconductor all electrons are paired as Cooper pairs in the ground state. With increasing temperature Cooper pairs break leading to a finite amount of quasiparticles $n_{qp} \propto e^{-\Delta_{bc}/k_B T}$ in the superconductor. This leads to an exponentially suppressed effective interaction between superconducting quasiparticles and localized defects. Two-level systems in superconducting amorphous $\text{PD}_{30}\text{Zr}_{70}$ and hydrogen tunneling in niobium have been examined by Weiss and Golding et al. [114, 115]. They confirmed the expected exponential increase of the effective coupling with temperature. Nonetheless, experimentally it was found that the amount of quasiparticles present at temperatures well below the superconducting gap exceeds the number of quasiparticles predicted for a BCS superconductor in equilibrium [92, 100]. This leads to a finite coupling between TLS and quasiparticles even at temperatures far below the critical temperature of the superconductor. Excess quasiparticles present at low temperatures stem from non-equilibrium processes such as infrared radiation or heating from normal conducting electronic devices.

Scattering with quasiparticles provides an intrinsic source of decoherence for superconducting qubits [101, 107] or the dynamics of Andreev bound states [116]. Qubit dephasing and relaxation due to non-equilibrium quasiparticles has been analyzed by us [I] and other authors [34, 80] both experimentally and theoretically. Experiments by Lisenfeld et al. on TLS inside the amorphous layer of a Josephson junction showed strong temperature dependence of TLS decoherence [43]. This strong dependence on temperature could hint that quasiparticles provide a channel of decoherence to junction TLS. A. Bilmes analyzed effects of quasiparticles on TLS decoherence in an

experiment and indeed found that quasiparticles couple to junction TLS and induce decoherence [IV].

In this section we develop a theory of interaction between TLS and superconducting quasiparticles. We compute decoherence rates of charged TLS due to this coupling and apply our theory to the experimental data of [IV].

As the quasiparticle wavefunction decays exponentially in the junction barrier the coupling between TLS in the junction and quasiparticles decays fast for TLS further away from the junction edges. The decay of the interaction strength leads to different interaction strengths for quasiparticles which scatter back to their original superconducting electrode during a scatter process with a TLS and quasiparticles that tunnel through the junction during an interacting with the TLS. These differences as well as the strong dependence of the coupling strength on the position of TLS explain the differences between thermal and injected quasiparticles found in the experiment by Bilmes [IV].

We note that our results are not restricted to microscopic TLS but can be to decoherence of superconducting qubits as well [I].

The section is based on the experimental work by A. Bilmes which led to the publication [IV] and our related theoretical papers on TLS and qubit decoherence due to quasiparticles [I, II].

4.3.1 Model

We consider the scattering of superconducting quasiparticles from a two-level system located inside the amorphous barrier of an aluminum-oxide Josephson junction. The full Hamiltonian reads as

$$\mathcal{H} = H_{\text{tls}} + \sum_{l=L,R} H_{\text{bcs},l} + V, \quad (4.10)$$

where H_{tls} is the TLS Hamiltonian, $H_{\text{bcs},L/R}$ is respectively the free BCS Hamiltonians of the left and right electrode, and V is the coupling between TLS and quasiparticles. To describe the TLS we use the phenomenological TLS model introduced in Sec. 4.2. In the basis of states localized in the two wells the TLS Hamiltonian takes the form $H_{\text{tls}} = \frac{\Delta}{2}\sigma_z + \frac{\Delta_0}{2}\sigma_x$. In the energy basis it reads as $H_{\text{tls}} = \frac{1}{2}E_{\text{tls}}\tau_z$ with the TLS energy splitting $E_{\text{tls}} = \sqrt{\Delta_0^2 + \Delta^2}$. The aluminum layers of the sample can be described with standard BCS theory. The electronic Hamiltonian reads as

$$H_{\text{bcs},l} = \int d^3r \hat{\Psi}_l^\dagger(\mathbf{r}) \begin{pmatrix} h_l(\mathbf{r}) & \Delta_{\text{bcs},l}(\mathbf{r}) \\ \Delta_{\text{bcs},l}^*(\mathbf{r}) & h_l(\mathbf{r}) \end{pmatrix} \hat{\Psi}_l(\mathbf{r}).$$

Here, we introduced the Nambu spinors $\hat{\Psi}_l(\mathbf{r}) = (\hat{\Psi}_{l,\uparrow}(\mathbf{r}), \hat{\Psi}_{l,\downarrow}^*(\mathbf{r})^\dagger)^T$. The free electron Hamiltonian $h_l = -\frac{1}{2m}\nabla^2 - \mu_l + V(\vec{r})$ is diagonal in Nambu space while the superconducting gap $\Delta_{\text{bcs}}(\mathbf{r})$ describes phonon-mediated s-wave pairing between electrons of opposite spin and opposite momentum. We assume that the aluminum superconductor is homogeneous with constant gap $\Delta_{\text{bcs}}(\mathbf{r}) = \Delta_{\text{bcs}}$ in the entire superconducting region and that the gap drops immediately to zero in the insulating barrier of the Josephson junction. For simplicity we assume that electrons are free in the bulk superconductor while in the barrier a single electron potential $V_0 \gg \mu$ prevails. Thus, in the bulk region of the left and right electrode the eigenfunctions $\psi_{\mathbf{k}\sigma}(\mathbf{r})$ of the free electron Hamiltonian are plane waves $\psi_{\mathbf{k}\sigma} = \mathcal{V}^{-1/2}e^{i\mathbf{k}\cdot\mathbf{r}}$ with the sample volume \mathcal{V} . Expanding the field operators in the eigenbasis of h_l the BCS Hamiltonian reduces to

$$H_{\text{BCS},l} = \sum_{k\sigma} \xi_{l,k} c_{l,k\sigma}^\dagger c_{l,k\sigma} + \Delta_k c_{l,k\uparrow}^\dagger c_{l,-k\downarrow}^\dagger + \Delta_k^* c_{l,-k\downarrow} c_{l,k\uparrow} \quad (4.11)$$

with the single electron energies $\xi_{l,k}$ measured relatively to the chemical potential μ_l of lead l . We diagonalize the BCS Hamiltonian with a Bogoliubov transformation

$$\Upsilon_{l,k} = \begin{pmatrix} \gamma_{l,k\uparrow} \\ \gamma_{l,-k\downarrow}^\dagger \end{pmatrix} = \begin{pmatrix} u_k^* & -v_k \\ v_k^* & u_k \end{pmatrix} \begin{pmatrix} c_{l,k\uparrow} \\ c_{l,-k\downarrow}^\dagger \end{pmatrix} \quad (4.12)$$

with $|u_k|^2 + |v_k|^2 = 1$. The particle u_k and hole amplitude v_k are defined as

$$u_k = \sqrt{\frac{1}{2} \left(1 + \frac{\xi_k}{E_k} \right)}, \quad v_k = e^{i\varphi} \sqrt{\frac{1}{2} \left(1 - \frac{\xi_k}{E_k} \right)}. \quad (4.13)$$

Here, φ is the phase of the BCS order parameter Δ_{bcs} and $E_k = \sqrt{\xi_k^2 + |\Delta_{\text{bcs}}|^2}$ is the quasiparticle excitation energy. In terms of Bogoliubov quasiparticles the BCS Hamiltonian reduces to a free fermionic Hamiltonian, $H_{\text{bcs}} = E_0 + \sum_{k\sigma} E_k \gamma_{k\sigma}^\dagger \gamma_{k\sigma}$. In order to describe the coupling between electrons and TLS we note that conduction electrons close to the barrier feel the charge of the TLS. This induces an effective coupling potential $\hat{V}(\mathbf{r})$. Expanding in the localized TLS basis the interaction between a TLS and an electron takes the form

$$V = \sum_{l'l'} \int d^3r \hat{\Psi}_l^\dagger(\mathbf{r}) \hat{V}(\mathbf{r}) \hat{\Psi}_{l'}(\mathbf{r}) = \sum_{l',\alpha\beta} |\alpha\rangle \left(\int d^3r \hat{\Psi}_l^\dagger(\mathbf{r}) \langle\alpha| \hat{V}(\mathbf{r}) |\beta\rangle \hat{\Psi}_{l'}(\mathbf{r}) \right) \langle\beta|. \quad (4.14)$$

where $|\alpha/\beta\rangle$ are localized TLS states. Expanding the electronic field operators in the eigenbasis $\psi_k(\mathbf{r})$ we find for a non-magnetic TLS

$$\hat{V} = \sum_{l',\alpha\beta} |\alpha\rangle V_{lk,l'k'}^{\alpha\beta} \langle\beta| c_{l,k\sigma}^\dagger c_{l',k'\sigma}. \quad (4.15)$$

If the TLS possesses a magnetic moment an additional spin flip can occur for an electron scattering with the TLS. We assume that the TLS in our sample are non-magnetic and $\sigma = \sigma'$. Assuming that the interaction between TLS and electrons depends on their relative coordinate the interaction matrix element describing scattering of an electron from lead l' in state $k'\sigma$ to a state $k\sigma$ in lead l with a simultaneous TLS transition from β to α takes the form

$$V_{lk,l'k'}^{\alpha\beta} = \iint d^3R d^3r \Psi_{l,k\sigma}^*(\mathbf{r}) \Phi_\alpha^*(\mathbf{R}) V(\mathbf{r} - \mathbf{R}) \Phi_\beta(\mathbf{R}) \Psi_{l',k'\sigma}(\mathbf{r}). \quad (4.16)$$

Similar to earlier works on localized states in metallic glasses we express the interaction in TLS space with Pauli matrices $V_{kk'} = \vec{\sigma} \cdot \vec{V}_{kk'}$ [104, 108]. Here, $\vec{\sigma} = (\sigma^0, \sigma^x, \sigma^y, \sigma^z)^T$ and the corresponding matrix elements in TLS space are defined as

$$\vec{V}_{lk,l'k'} = \left(V_{lk,l'k'}^0, V_{lk,l'k'}^x, V_{lk,l'k'}^y, V_{lk,l'k'}^z \right)^T. \quad (4.17)$$

The σ_0 component can be absorbed in the electron Hamiltonian since it does not act on the TLS. The remaining components of the potential read as

$$V_{lk,l'k'}^x = \frac{1}{2} \left(V_{lk,l'k'}^{LR} + V_{lk,l'k'}^{RL} \right) \quad (4.18)$$

$$V_{lk,l'k'}^y = \frac{1}{2i} \left(V_{lk,l'k'}^{LR} - V_{lk,l'k'}^{RL} \right) \quad (4.19)$$

$$V_{lk,l'k'}^z = \frac{1}{2} \left(V_{lk,l'k'}^{LL} - V_{lk,l'k'}^{RR} \right). \quad (4.20)$$

The matrix elements in x and y direction comprise integrations over products of TLS wavefunctions localized in different wells. Consequently, these matrix elements are suppressed by the overlap between the wavefunctions. For harmonic wells with localized wavefunctions according to Eq. (4.1) the suppression factor depends exponentially on the ratio between well separation d and wavefunction width r_0 , $V^\perp/V^z \sim e^{-d^2/r_0^2}$. For a Hydrogen defect with $d \approx 0.85\text{\AA}$ and $r_0 \approx 0.14\text{\AA}$ this yields $V^\perp/V^z \sim 10^{-32}$. Due to this strong suppression we can reduce the interaction between TLS and electrons to the dipole interaction $\propto \sigma^z$. This interaction between TLS and conduction electrons is well known from the theory of metallic glasses [44, 108]. However, the TLS we are analyzing here are localized in the isolating barrier of the Josephson junction. In this region the electronic wavefunction decays exponentially rendering the inter-

action relatively weak especially for TLS localized further away from the edges. We calculate the interaction matrix elements for a contact interaction $V(\vec{r}) \propto \delta(\mathbf{r})$ and a long-range Coulomb interaction. In both cases we find that the interaction strength between TLS and electrons decays exponentially for TLS away from the edges. The final Hamiltonian of the coupled electron-TLS system reads as

$$H = \sum_{l',k,k'\sigma} (\delta_{ll'} \delta_{kk'} \xi_k + V_{lk,l'k'}^0) c_{l,k\sigma}^\dagger c_{l',k'\sigma} + \sum_{l,k} \left(\Delta_k c_{l,k\uparrow}^\dagger c_{l,-k\downarrow}^\dagger + \Delta_k^* c_{l,-k\downarrow} c_{l,k\uparrow} \right) + \frac{\Delta}{2} \sigma^z + \frac{\Delta_0}{2} \sigma^x + \sigma_z \sum_{l',k,k'\sigma} V_{lk,l'k'}^z c_{l,k\sigma}^\dagger c_{l',k'\sigma}. \quad (4.21)$$

We assume that the interaction with the TLS does not disturb the superconducting state of the metal 'too much' such that we can drop the energy shift $\sim V_{lk,l'k'}^0$. Applying the Bogolioubov transformation we arrive at the final form for the quasiparticle-TLS Hamiltonian.

For a potential that depends only on the difference of the in- and outgoing momenta we have $V_{lk,l'k'} = V_{l'l}(\mathbf{k} - \mathbf{k}')$ and $V_{l'-k',l-k} = V_{l'l}(\mathbf{k} - \mathbf{k}') = V_{lk,l'k'}$ and the interaction Hamiltonian reads as

$$V = \sigma^z \sum_{l',k,k'} \Upsilon_{l,k}^\dagger V_{lk,l'k'}^z M_{lk,l'k'} \Upsilon_{l',k'} \quad (4.22)$$

with the coherence factor in particle-hole space,

$$M_{lk,l'k'} = \begin{pmatrix} u_k^* u_{k'} & u_k^* v_{k'} \\ v_k^* u_{k'} & v_k^* v_{k'} \end{pmatrix} - \begin{pmatrix} v_k v_{k'}^* & -v_k u_{k'}^* \\ -u_k v_{k'}^* & u_k u_{k'}^* \end{pmatrix}. \quad (4.23)$$

4.3.2 Quasiparticle dynamics

TLS decoherence due to quasiparticles strongly depends on the number of quasiparticles in the vicinity of the junction and on the energy distribution of these quasiparticles. These properties of the fermionic many-body system are characterized by the distribution function

$$f_{k\sigma} = \left\langle \gamma_{k\sigma}^\dagger \gamma_{k\sigma} \right\rangle \quad (4.24)$$

and the BCS density of states $\rho(E) = |E|/\sqrt{E^2 - \Delta_{\text{BCS}}^2}$. We introduce the energy distribution function $f(\xi) = (N_F \mathcal{V})^{-1} \sum_{\mathbf{k}} f_{\mathbf{k}} \delta(\xi - \xi_{\mathbf{k}})$ where N_F is the density of states at the Fermi energy including spin and \mathcal{V} is the sample volume [117]. The quasiparticle density can be expressed in terms of the distribution function as

$$n_{\text{qp}} = 2N_F \int d\xi f(\xi). \quad (4.25)$$

Often, it is useful to define the dimensionless quasiparticle density $x_{\text{qp}} = n_{\text{qp}}/n_{\text{cp}}$ where n_{cp} is the density of Cooper pairs $n_{\text{cp}} = 2\Delta_{\text{BCS}}N_F$. We note that the quasiparticle energy is symmetric in particle- and hole-like excitations $E(\xi) = E(-\xi) = \sqrt{\xi^2 + \Delta_{\text{BCS}}^2}$. Thus, for $\xi = +\sqrt{E^2 - \Delta_{\text{BCS}}^2}$ we can define two modes of the quasiparticle distribution function:

$$f^E(E) = \frac{1}{2}[f(\xi) + f(-\xi)] \quad (4.26)$$

$$f^Q(E) = \frac{1}{2}[f(\xi) - f(-\xi)]. \quad (4.27)$$

The energy or symmetric mode f^E named longitudinal mode in earlier works by Schmid and Schön [118] counts the number of excitations with energy $E = \sqrt{\xi^2 + \Delta^2}$ while the charge or antisymmetric mode f^Q (transversal mode) accounts for imbalances between particle- ($\xi > 0$) and hole-like ($\xi < 0$) excitations. In equilibrium the quasiparticle distribution function is symmetric and the charge mode vanishes. In non-equilibrium situations however a finite imbalance can occur for example due to injection of electrons through a normal metal-superconductor junction.

Experiments suggest that non-equilibrium quasiparticles are always present in superconducting devices. Due to the presence of those non-equilibrium quasiparticles the distribution function in typical experimental situations differs from its equilibrium form. Quasiparticles produced at high energies quickly decay to small energies close to the gap due to inelastic phonon scattering and, for quasiparticles at very high energies, due to electron scattering. Quasiparticle recombination on the other hand is a rather slow process. Together with the strongly peaked density of states this results in a strongly increased quasiparticle density close to the gap. The decay of quasiparticles generated at high energies for example from microwave radiation to the gap results in a distribution function that strongly differs from a Fermi distribution in a very narrow region above the gap.

In the next section we will show that TLS relaxation depends linearly on the quasiparticle density x_{qp} while TLS dephasing depends crucially on the exact form of the distribution function at the gap. In order to obtain a better understanding of TLS decoherence due to quasiparticles we simulate quasiparticle dynamics for two BCS superconductors with phonon induced quasiparticle relaxation and recombination. The superconductors are separated by the JJ containing the TLS. For the purpose of TLS decoherence the quasiparticle distribution close to the JJ at a distance of approximately $1/k_F$ is important. We analyze the effect of thermally created quasiparticles and quasiparticles injected through a SQUID. We assume that thermal injection of quasiparticles corresponds to an increase of the temperature T of the phonon bath throughout the entire sample resulting in a homogeneous quasiparticle density. In particular, the

quasiparticle density is identical on both sides of the junction, $x_{\text{qp,L}} = x_{\text{qp,R}}$.

The situation is more elaborate in case of quasiparticle injection. Due to different diffusion length from the SQUID to the junction the density of quasiparticles can be different on both sides $l = L/R$ of the junction. The injection site is around $700\mu\text{m}$ away from the left and around $1400\mu\text{m}$ away from the right side of the junction. We expect to find a difference in the quasiparticle density on both sides, $x_{\text{qp,R}} = \eta x_{\text{qp,L}}$ with $\eta > 1$.

Kinetic equation

In order to simulate quasiparticle distribution function we consider a superconductor with electron-phonon coupling. With the phonon Hamiltonian H_γ and the electron-phonon interaction $H_{el-\gamma}$ the Hamiltonian of the leads takes the form

$$H = H_{\text{bcs}} + H_\gamma + H_{el-\gamma}.$$

From the Dyson equation for the kinetic component of the electron Green's function in Nambu space the kinetic Boltzmann equation for the electron distribution function can be derived. In the diffusive limit the Boltzmann equation for the energy dependent distribution function reads as

$$\frac{\partial f(\xi, r, t)}{\partial t} + D(\xi) \vec{\nabla}_r^2 f(\xi, r, t) = I_{\text{qp}} + \left. \frac{\partial f}{\partial t} \right|_\gamma. \quad (4.28)$$

We introduce the quasiparticle diffusion constant $D(\xi) = D_0 \sqrt{1 - E^2(\xi)/\Delta_{\text{bcs}}^2}$ where $D_0 = 60 \text{ cm}^2/\text{s}$ [34]. I_{qp} describes quasiparticle injection by different sources while the collision integral accounts for electron-phonon scattering and phonon assisted recombination. The chip used in the experiment has been used in experiments by Martinis et al. where it has been confirmed that quasiparticles can be described in the diffusive limit indeed [34, 92]. Additionally, we check that the diffusive limit holds by comparing the quasiparticle density obtained within the diffusive approximation with time resolved measurements from the experiment, see Fig. 4.10.

With the lowest order electron-phonon diagrams shown in Fig. 2.2a, the phonon-collision integral provides the quasiparticle scattering rates [119]

$$I^S(\xi) = -\frac{1}{\tau_0} \int d\xi' \alpha^2(E - E') F(E - E') \left(1 + \frac{\xi\xi' - \Delta_{\text{bcs}}^2}{EE'} \right) \text{sign}(E' - E) \\ \times \left\{ f(\xi)[1 - f(\xi')] n_B(E' - E) - f(\xi')[1 - f(\xi)][1 + n_B(E' - E)] \right\}. \quad (4.29)$$

Here, n_B is the Bose distribution function at the phonon temperature, and $\tau_0 \approx 400ns$

the characteristic timescale of electron-phonon scattering [120]. Using the Boltzmann distribution to characterize the phonon-bath we assume that the phonons remain in equilibrium. This corresponds to a situation where phonons have a very short life-time in the thin aluminum layers and quickly escape into the substrate lying below. The model neglects phonon trapping, i.e. the effect that excess phonons can be absorbed by quasiparticles before they escape into the substrate effectively trapping phonons in the aluminum [119].

The first term in the curly brackets describes scattering from ξ to ξ' while the second term describes the inverse process. For quasiparticles close to the gap the phonons involved in scattering are of low-energy $\Omega \sim E - E'$. For the averaged phonon spectrum $\alpha^2 F(\Omega)$ we assume the low-energy form $\alpha^2 F(\Omega) = \tau_0 \Omega^2 / (k_B T_c)^3$ with the critical temperature of aluminum $T_c \approx 1.19K$ [120]. In the same approximation the phonon induced quasiparticle recombination (first term in curly brackets in Eq. (4.30)) and creation (second term in curly brackets in Eq. (4.30)) rates are

$$I^R(\xi) = -\frac{1}{\tau_0} \int d\xi' \alpha^2(E + E') F(E + E') \left(1 - \frac{\xi\xi' - \Delta_{\text{bcs}}^2}{EE'}\right) \times \left\{ f(\xi)f(\xi')[1 + n_B(E' + E)] - [1 - f(\xi')][1 - f(\xi)]n_B(E' + E) \right\}. \quad (4.30)$$

We note that recombination of two quasiparticles with energies E and E' produces high energy phonons with energy $\Omega = E + E' > 2\Delta_{\text{bcs}}$ while the splitting of a Cooper pair in order to create a quasiparticle requires phonons of energies $\Omega > 2\Delta_{\text{bcs}}$. In our approximation where the phonon bath remains in equilibrium the phonon density at such high energies is small and quasiparticle creation through the phonon bath can be neglected. Experiments suggest that even at small temperatures a finite quasiparticle density remains. Quasiparticles injected at high energies decay quickly to energies close to the gap. It turns out that the exact form of high-energy injection is not crucial. In order to account for background non-equilibrium quasiparticles we add a quasiparticle injection term

$$I_{\text{qp}}^{\text{bg}}(\xi) = r_{\text{qp}} [f_0(E(\xi) - E_1) - f_0(E(\xi) - (E_1 - \delta E))]. \quad (4.31)$$

We denote with f_0 the Fermi distribution function. Non-equilibrium quasiparticles are injected in an energy window between $E_1 - \delta E$ and E_1 and relax to the gap. The injection rate defined above is symmetric in particle-like and hole-like excitations. Thus, the non-equilibrium distribution function remains symmetrical, $f^Q = 0$. In Fig. 4.8 we show results of numerical solution of the stationary distribution function with phonon scattering and quasiparticle injection for different injection energies E_1 and fixed $\delta E = 0.4\Delta_{\text{bcs}}$. These simulations show that the quasiparticle distribution

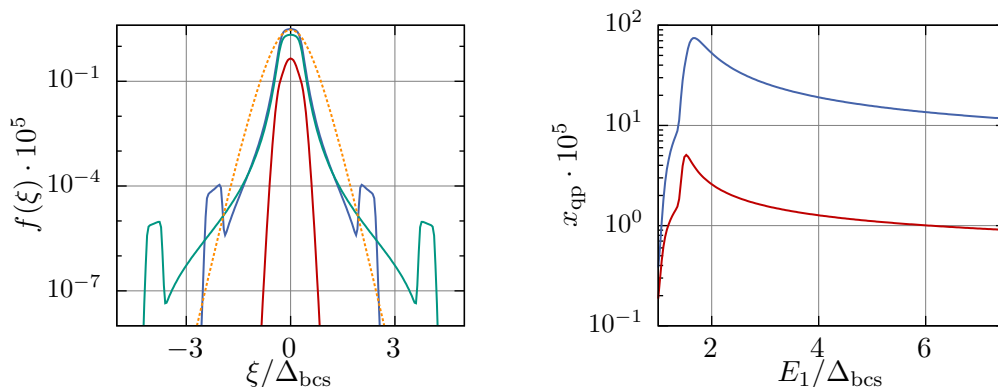


Figure 4.8: Left: Non-equilibrium distribution function $f(\xi)$ for background quasiparticle injection at different energies E_1 . The bumps visible for the blue ($E_1 = 2.6\Delta_{\text{bcs}}$) and green line ($E_1 = 4.3\Delta_{\text{bcs}}$) correspond to the injection-window of quasiparticles. The red line corresponds to $E_1 = 1.0\Delta_{\text{bcs}}$ and significantly differs from the other functions. For quasiparticles injected at high energies the distribution for small energies follows a Fermi distribution with an effective temperature (dashed orange). Right: Quasiparticle density x_{qp} vs. injection energy E_1 for two different injection rates r_{qp} . For injection at energies well above the gap the density x_{qp} weakly depends on E_1 .

in the relevant energy region with $\xi \lesssim \Delta_{\text{bcs}}$ is insensitive to the exact injection energy as long as the injection occurs well above the relevant region. For small energies $\xi \lesssim \Delta_{\text{bcs}}/2$ the actual non-equilibrium distribution corresponds to a Fermi distribution at an effective temperature T_{eff} (dashed lines).

Quasiparticle creation

In the experiment by Bilmes two different methods have been used to produce additional quasiparticles [IV]: heating the sample and quasiparticle injection through a SQUID operated in the resistive regime. We analyze both methods in the framework developed above. We include coupling to phonons and background non-equilibrium quasiparticles as discussed before. We analyze the setup with diffusion in a simplified one dimensional model. This suffices to capture the relevant characteristics of the quasiparticle distribution obtained from the different methods.

Thermally created quasiparticles Heating the sample increases the quasiparticle density homogeneously over the entire sample. Thus, we need not to simulate diffusion. Heating the sample corresponds to an increased phonon temperature T_γ . Keeping the background injection term $I_{\text{qp}}^{\text{bg}}$ we simulate heating of the sample. In Fig. 4.9 we show temperature dependent distribution function and quasiparticle density x_{qp} together with experimental data taken from [IV]. Fitting the simulated quasiparticle density to the values obtained in the experiment we find an injection rate $r_{\text{qp}} \sim 0.05/\mu\text{s}$. Thus, we will use this value for background quasiparticle injection in what follows.

For high temperatures $T \gtrsim 250$ mK quasiparticles follow an equilibrium distribution with temperature determined by the phonon bath. For smaller temperatures a saturation due to background non-equilibrium quasiparticles occurs. Non-equilibrium quasiparticles add a contribution $\delta f_{\text{n-eq}}$ to the distribution function. In good approximation we can describe the non-equilibrium contribution with a Fermi distribution at an effective temperature T_s . For temperatures below the effective temperature of non-equilibrium quasiparticles the distribution function is well described by the Fermi distribution at the effective temperature $f \approx f_0(E, T_s, 0)$ while for phonon temperatures $T > T_s$ the distribution function follows the phonon bath temperature. In this approximation the non-equilibrium quasiparticles add a constant contribution $x_{\text{qp},s}$ to the total density. The experimental data shown in Fig. 4.9 correspond to a non-equilibrium temperature $T_s \approx 0.23\text{K}$. The density of non-equilibrium quasiparticles follows as $x_{\text{qp}}^{\text{n-eq}} \approx 5 \cdot 10^{-5}$. For such a quasi-equilibrium distribution we find the quasiparticle density

$$x_{\text{qp},l} = K_1(\Delta_{\text{bcs}}/k_B T) + x_{\text{qp},s} \quad (4.32)$$

with the modified Bessel function of the second kind $K_n(x)$ and the contribution of background quasiparticles $x_{\text{qp},s}$. We expand the density in the small parameter $k_B T/\Delta_{\text{bcs}}$,

$$x_{\text{qp},l} \approx \sqrt{\frac{\pi k_B T}{2\Delta_{\text{bcs}}}} e^{-(\Delta_{\text{bcs}} - \mu_l)/k_B T_s} \left[1 + \frac{3k_B T}{8\Delta_{\text{bcs}}} + \dots \right] + x_{\text{qp},s}. \quad (4.33)$$

The density of thermal quasiparticles decays exponentially for temperatures below the gap and saturates at the non-equilibrium contribution $x_{\text{qp},s}$ while for higher temperatures the density increases exponentially.

Quasiparticle injection In our model a SQUID is placed at both boundaries of the simulation domain at $x = 0$ and $x = 2100\mu\text{m}$. The JJ containing the TLS is placed at $x = 700\mu\text{m}$. This setup accounts for different diffusion lengths from the SQUID to the different sides of the JJ. We describe quasiparticle injection through the SQUID as a voltage biased superconductor–superconductor (S-S) junction. For a S-S interface the tunnel Hamiltonian reads as

$$H_T = \sum_{kq\sigma} g_{kq} e^{-i\phi} (u_q \gamma_{q\sigma}^\dagger + \sigma v_q \gamma_{-q-\sigma}) (u_k \gamma_{k\sigma} + \sigma v_k \gamma_{-k-\sigma}^\dagger) + h.c., \quad (4.34)$$

where $\phi(t) = \varphi + \int_{t_0}^t dt' V(t')$ is the phase acquired due to the applied voltage difference across the junction and the phase difference φ between the superconducting condensates. The tunneling Hamiltonian comprises quasiparticle operators $\gamma_{q\sigma}$ of the injection superconductor and operators $\gamma_{k\sigma}$ of the superconducting material under

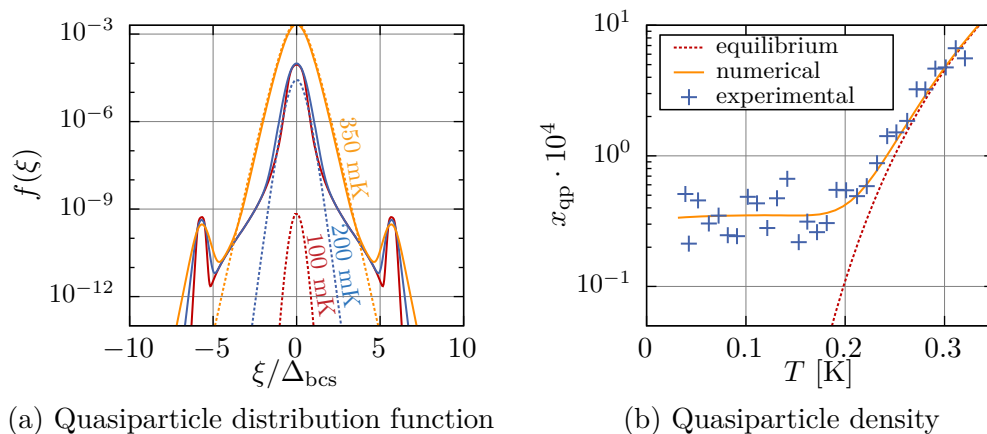


Figure 4.9: (a) Non-equilibrium distribution function for different phonon temperatures with background quasiparticle injection (solid lines) and the corresponding equilibrium distributions (dashed). For higher temperatures the non-equilibrium and equilibrium distribution are identical away from the injection energies while for small temperatures the effect of non-equilibrium quasiparticles is clearly visible. (b) Quasiparticle density x_{qp} vs. temperature. Blue points are experimental data from [IV]. Green is obtained from numerical simulation of the kinetic equation. Dashed red represents equilibrium. For high phonon temperatures the quasiparticles are in equilibrium with the phonon bath while for temperatures below $\sim 200\text{mK}$ saturation due to background injection occurs.

consideration. g_{kq} is the tunneling amplitude. We are interested in the time evolution of the quasiparticle occupation (sum over spin is implied) $f_k = \langle n_{k\sigma} \rangle = \langle \gamma_{k\sigma}^\dagger \gamma_{k\sigma} \rangle$. Coupling with the injection superconductor through the tunneling Hamiltonian induces an additional injection term $I_{\text{qp}}^{\text{inj}} = \partial_t f_k \Big|_{\text{inj}}$ to the Boltzmann equation. Using first order perturbation theory to calculate the mixed expectation values $\langle c_{q\sigma}^\dagger(t) \gamma_{k\sigma}^{(+)}(t) \rangle$ and neglecting coherent Cooper pair contributions to tunneling we find

$$\partial_t f(\xi_k) = \frac{1}{e^2 R_N} \frac{1}{N_F} \left\{ u^2(\xi_k) \rho(E_k - eV) [f_S(E_k - eV) - f(\xi_k)] + v^2(\xi_k) \rho(E_k + eV) [f_S(E_k + eV) - f(\xi_k)] \right\}, \quad (4.35)$$

where f_S is the distribution function of the injection superconductor and R_N is the tunnel resistance of the junction in the normal state. In order to derive previous expression we assumed that the distribution function f_S is symmetric in particle-like and hole-like excitations. Injection through the tunnel barrier is not symmetrical for particle-like ($\xi > 0$) and hole-like ($\xi < 0$) excitations due to the amplitudes $u^2(\xi_k)$ and $v^2(\xi_k)$. We note that the asymmetry increases with the applied bias voltage and vanishes for zero bias.

The quasiparticle injection rate defined above is closely related to the electrical current through the junction: Changing the sign of the hole-amplitude from $v^2(\xi)$ to $-v^2(\xi)$ and integrating over energy yields the electrical current through the junction.

This difference accounts for the opposite charge of holes compared to electrons.

Close to the injection site we acquire a finite charge mode f^Q . The charge mode however decays on the time scale defined by the branch mixing time τ_Q . The branch mixing time is short compared to energy relaxation and recombination processes $\tau_Q \sim 10^{-1}\tau_{r/s}$ [120]. Thus, the charge mode decays quickly during diffusion from injection site to the TLS junction and we assume symmetrical quasiparticle injection. At the TLS site the distribution follows a Fermi distribution with effective chemical potential $\mu(V_{\text{inj}})$ and effective temperature T_{eff} due to injection and background quasiparticles. Another remark concerns with the quasiparticle distribution on either side of the JJ hosting TLS. While the quasiparticle density on both sides is identical for thermal quasiparticles the different diffusion lengths to both junction electrodes causes an imbalance between both sides. Due to the imbalance net quasiparticle tunneling through the junction occurs which we include in our simulation. The tunneling Hamiltonian through the junction corresponds to the SQUID injection Hamiltonian with $V \rightarrow 0$. Just as for quasiparticle injection we calculate tunneling rates in golden rule approximation. This yields for the left-hand (L) and right-hand (R) side distribution

$$\left. \frac{\partial f_L(\xi)}{\partial t} \right|_{\text{tun}} = - \left. \frac{\partial f_R(\xi)}{\partial t} \right|_{\text{tun}} = \frac{1}{e^2 R_T} \frac{1}{N_F} \frac{|\xi|}{E} \{f_R(E) - f_L(E)\}. \quad (4.36)$$

Tunneling tends to compensate the imbalance $\sim f_L - f_R$. Depending on the strength of tunneling the imbalance is suppressed due to tunneling. We find an imbalance ratio $\eta = x_{\text{qp,L}}/x_{\text{qp,R}}$ between $\eta = 1$ for infinitely fast tunneling and $\eta \approx 4$ if there is no tunneling at all.

Rothwarf-Taylor equations

In order to obtain a differential equation for the quasiparticle density x_{qp} we multiply the Boltzmann equation Eq. (4.28) by the density of states N_F and integrate over energies. Neglecting the asymmetric mode this yields the Rothwarf-Taylor equation for the quasiparticle density x_{qp} [119]

$$\dot{x}_{\text{qp}}(r, t) + \bar{D}\nabla^2 x_{\text{qp}}(r, t) = \bar{I}_{\text{qp}}(r, t) - 2R x_{\text{qp}}^2(r, t) + 2B n_\gamma(r, t), \quad (4.37)$$

where $\bar{D} \leq D_0$ is the average diffusion constant. On the right hand side the different terms describe from left to right quasiparticle injection with the average injection current $\bar{I}_{\text{qp}}(r, t) = \int d\xi I_{\text{qp}}(\xi)/\Delta_{\text{bcs}}$, recombination of two quasiparticles with simultaneous creation of a phonon, and creation of two quasiparticles through annihilation of a phonon.

A similar equation for the density n_γ of phonons with energy $\Omega > 2\Delta_{\text{bcs}}$ can be derived. However, in our model the phonon bath remains in equilibrium. The recom-

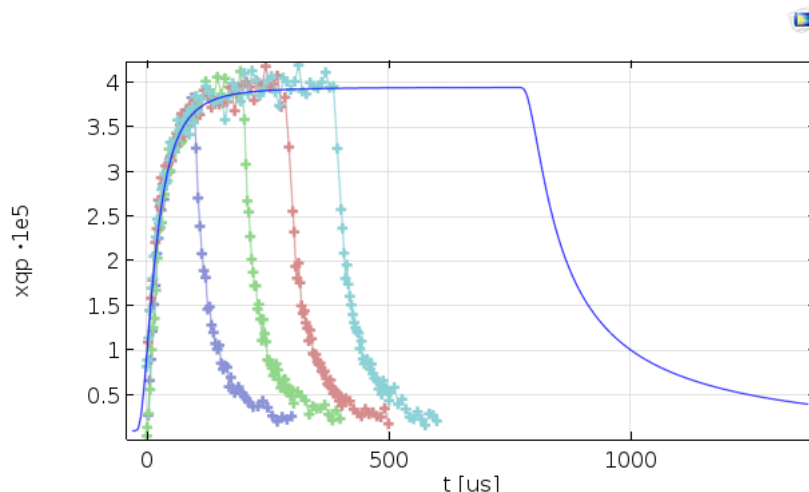


Figure 4.10: Numerical simulation of the Rothwarf-Taylor equation using Comsol[®] multiphysics. We plot the quasiparticle density at the left-hand side of the junction $x_{\text{qp,L}}$ versus time after the beginning of quasiparticle injection. The blue line is obtained from numerical simulation with pulse duration $\tau_{\text{inj}} = 800\mu\text{s}$. Crosses are experimental data obtained with increasing injection pulse duration from $\tau_{\text{inj}} = 100\mu\text{s}$ (magenta) to $\tau_{\text{inj}} = 400\mu\text{s}$ (cyan) [IV].

bination and creation rates can be obtained from the phonon rates given before. The resulting recombination and creation rates can be found in [119]. For energies close to the gap we find the approximate form

$$R \approx \left(\frac{\Delta_{\text{BCS}}}{k_B T_C} \right)^2 \frac{1}{\tau_0} \approx 14/\mu\text{s}. \quad (4.38)$$

For constant and spatially homogeneous injection, i.e. $\bar{I}_{\text{qp}}(r, t \rightarrow \infty) = \bar{I}_{\text{qp}}$, we find the stationary state quasiparticle density $x_{\text{qp},0} = \sqrt{I_{\text{qp}}/2R + n_\gamma B/R}$. Without injection, the stationary solution corresponds to the thermal equilibrium solution $x_{\text{qp}}^{\text{eq}}$. With this we can relate the excitation rate B to the thermal density as $Bn_\gamma = Rx_{\text{qp}}^{\text{eq}} \approx 14x_{\text{qp}}^{\text{eq}}/\mu\text{s}$. Injection through the SQUID yields a quasiparticle injection current $I_{\text{qp},\text{inj}} \approx \frac{1}{e}|I|/\mathcal{V}$, where I is the electrical current applied through the junction and \mathcal{V} the junction volume. This yields an injection rate $I_{\text{qp},\text{inj}} \sim 12|I|/\mu\text{s}$ for I in μA .

In Fig. 4.10 we show results from numerical simulation of the Rothwarf-Taylor equation together with experimental data from [IV]. The results clearly show that the quasiparticles can be described in the diffusive limit. The effective diffusion constant used in the simulation was $\bar{D} = 30\text{cm}^2/\text{s}$. To match experimental data we had to choose a higher effective recombination rate $R = 10 \cdot 14/\mu\text{s}$ and smaller injection current $I \approx 0.01I_{\text{experiment}}$. These differences in our one dimensional simulations stem from sample geometry effects. One of these geometry-induced effects results from quasiparticles that have to pass through shallow bridges. As can be seen in Fig. 4.12

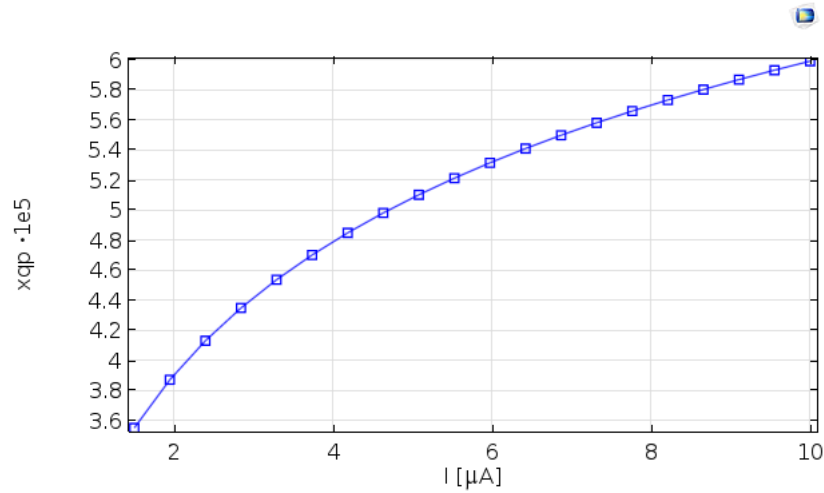


Figure 4.11: Numerical simulation of the Rothwarf-Taylor equation using Comsol[®] multiphysics. We plot the quasiparticle density at the left-hand side of the junction $x_{\text{qp,L}}$ versus injection current.

the quasiparticle density strongly drops at these bridges. The two-dimensional geometry shown in Fig. 4.12 closely resembles the actual chip layout with narrow bridges separating the injection site (bottom) from the phase qubit with the Josephson junction (top part).

Conclusion

We simulated two superconducting leads with electron-phonon interaction and quasiparticle injection through a SQUID as well as thermal heating. We assumed that both, the BCS gap and the density of states are not changing during injection and heating, i.e. we neglected suppression of the BCS gap due to increased quasiparticle density. We found that for a large phonon bath which remains in equilibrium at the base temperature the quasiparticle distribution function can be described as an effective equilibrium distribution function with increased chemical potential at an effective temperature T_{eff}

$$f_{l,k\sigma} = f(E_k, T_{\text{eff}}, \mu_{l,\text{eff}}(V_{\text{inj}})) + f(E_k, T_s, 0). \quad (4.39)$$

T_s accounts for non-equilibrium particles that are always present. From our numerical calculations we conclude that $T_{\text{eff}} = T$ where T is the phonon bath temperature is a good approximation for the system temperature.

We simulated diffusion from the injection site to the Josephson junction with a Boltzmann equation in the diffusive limit. We found that the distribution function at the junction is of the effective form given before with injection voltage dependent

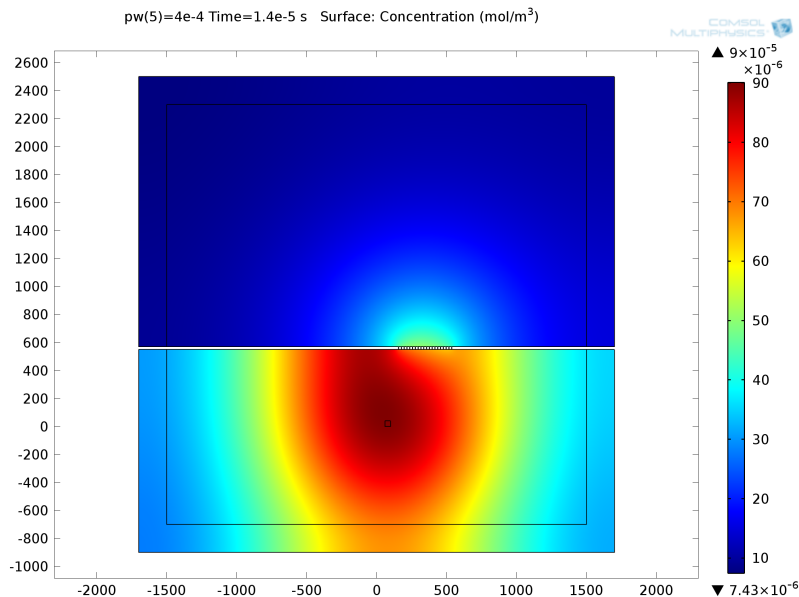


Figure 4.12: 2D numerical simulation of the Rothwarf-Taylor equation using Comsol[®] multiphysics. We plot the quasiparticle density x_{qp} shortly after injection. One can clearly see the drop in quasiparticle density at the small bridges connecting the different parts of the sample. The injection SQUID is represented by the small black square in the bottom part while the Josephson junction is located on the top part close to the bridges.

effective chemical potential $\mu_l = \mu_l(V_{inj})$. We found that for temperatures well below the gap the distribution function decays rapidly for higher energies and $f(E_k) \ll 1$ for quasiparticle energies well above the gap. The width of the distribution function above the gap is $\zeta \sim k_B T \ll \Delta_{bcs}$.

A final remark concerns the measurement of the quasiparticle density. In the experiment the density is measured with help of the frequency shift of the qubit which is proportional to the density of quasiparticles in the junction area, $\delta f \propto x_{qp,meas}$. The qubit, however, is only sensitive to the average density $x_{qp,meas} = (x_{qp,L} + x_{qp,R})/2$ and does not discriminate different densities on the left-hand side or right-hand side electrode. With the ratio between left and right density η the measured density can be related to the left and right side density as

$$x_{qp,L} = \eta x_{qp,R} = \frac{2}{\eta + 1} x_{qp,meas}.$$

In case of quasiparticle injection through thermal heating the density is increased homogeneously and $\eta_{th} = 1$.

4.3.3 Quasiparticle spectral density

The influence of quasiparticles on TLS decoherence is characterized by the spectral density. The interaction Eq. (4.22) between electrons and TLS in the energy eigenbasis of the TLS reads as

$$V = [\tau^z \cos \phi + \tau^x \sin \phi] \sum_{l',kk'} V_{lk,l'k'}^z \Upsilon_{l,k}^\dagger M_{lk,l'k'} \Upsilon_{l',k'}$$

The spectral density of quasiparticles is obtained from Eq. (3.20) with the interaction V . This yields

$$S_{\text{qp}}(\omega) = \sum_{ll'kk'} \sum_{mm'qq'} \int dt \left\langle \left(\Upsilon_{l,k}^\dagger(0) M_{lk,l'k'} \Upsilon_{l',k'}(0) \right) \left(\Upsilon_{m,q}^\dagger(t) M_{mq,m'q'} \Upsilon_{m',q'}(t) \right) \right\rangle e^{-i\omega t}, \quad (4.40)$$

where we dropped the pre-factor $\cos^2 \phi$ for transverse and $\sin^2 \phi$ for longitudinal coupling. We will reintroduce these factors when we calculate the relaxation rate and dephasing function. The mixing angle ϕ is defined in the transformation 4.3. The trace over Bogoliubov operators can be expressed in terms of quasiparticle occupation numbers f_k . Omitting the lead index for brevity we find

$$\begin{aligned} \sum_{qq'} \left\langle \left(\Upsilon_k^\dagger(0) M_{kk'} \Upsilon_{k'}(0) \right) \left(\Upsilon_q^\dagger(t) M_{qq'} \Upsilon_{q'}(t) \right) \right\rangle &= |M_{kk'}^{11}|^2 f_{k\uparrow} (1 - f_{k'\uparrow}) e^{i(E_{k'} - E_k)t} \\ &+ |M_{kk'}^{22}|^2 f_{-k'\downarrow} (1 - f_{-k\downarrow}) e^{-i(E_{-k'} - E_{-k})t} + M_{kk'}^{12} M_{k'k}^{21} f_{k\uparrow} f_{-k'\downarrow} e^{-i(E_{-k'} + E_k)t} \\ &+ M_{kk'}^{21} M_{k'k}^{12} (1 - f_{-k\downarrow}) (1 - f_{k'\uparrow}) e^{i(E_{k'} + E_{-k})t} \end{aligned} \quad (4.41)$$

The first two terms on the right hand side of Eq. (4.41) stem from single-quasiparticle scattering from state $l, k\sigma$ to state $l', k'\sigma$. The quasiparticle occupations account for the fact that the initial state $l, k\sigma$ has to be occupied while the final state needs to be empty. The remaining two terms proportional to the off-diagonal elements of the coherence matrix $M_{kk'}$ describe Cooper pair scattering. We split the spectral density into a pair S_p and a single quasiparticle contribution S_{qp} . Using the relation $\int dt e^{ixt} = 2\pi\delta(x)$ we find the quasiparticle spectral density

$$\begin{aligned} S_{\text{qp}}(\omega) &= 2\pi \sum_{ll'} \sum_{kk'} |V_{lk,l'k'}^z|^2 \left[|M_{lk,l'k'}^{11}|^2 f_{l,k\uparrow} (1 - f_{l',k'\uparrow}) \delta(\omega - E_{k'} + E_k) \right. \\ &\quad \left. + |M_{lk,l'k'}^{22}|^2 f_{l',-k'\downarrow} (1 - f_{l,-k\downarrow}) \delta(\omega + E_{-k'} - E_{-k}) \right]. \end{aligned} \quad (4.42)$$

With Eq. (4.23) for the coherence matrix, relation (4.13) for the coefficients u_k and v_k , and the phase difference $\varphi_{ll'} = \phi_l - \phi_{l'}$ we find

$$|M_{lk,l'k'}^{11}|^2 = |M_{lk,l'k'}^{22}|^2 = 1 + \frac{\xi_k \xi_{k'} - |\Delta_{\text{bcs}}|^2 \cos(\varphi_{ll'})}{E_k E_{k'}}.$$

The phase difference $\varphi_{ll'}$ vanishes for intra lead scattering $l = l'$ while it corresponds to the phase difference between the two superconducting condensates for tunneling quasiparticles $l \neq l'$. Scattering with non-magnetic TLS is independent of spin and we assume a symmetrical distribution for different spins. We introduce the energy dependent quasiparticle distribution $f_l(\xi) = (N_F \mathcal{V})^{-1} \sum_{\mathbf{k}} f_{l,\mathbf{k}} \delta(\xi - \xi_{\mathbf{k}})$ in lead l and use the relation $\sum_{\mathbf{k}} \dots \rightarrow \mathcal{V}^{1/2} \int d^3k / (2\pi)^3 \dots$ to change from momentum summation to a \mathbf{k} -integration. For a direction independent distribution $f_{l,\mathbf{k}} = f_{l,k}$ and direction independent electron energy $\xi_{\mathbf{k}} = \xi_k$ we can separate integration over the solid angle from integration over the absolute value. We denote with N_F the density of states in the normal state at the Fermi energy. We find the spectral density

$$S_{\text{qp}}(\omega) = 2(N_F \mathcal{V})^2 \sum_{ll'} \int_{-\infty}^{\infty} d\xi d\xi' \left[1 + \frac{\xi \xi' - |\Delta_{\text{bcs}}|^2 \cos(\varphi_{ll'})}{E(\xi) E(\xi')} \right] \\ \times f_l(\xi) [1 - f_{l'}(\xi')] I_{ll'}(\xi, \xi') \delta(\omega + E(\xi) - E(\xi')) \quad (4.43)$$

with the quasiparticle energy $E(\xi) = \sqrt{\xi^2 + \Delta_{\text{bcs}}^2}$ of an excitation with energy ξ . We introduced the direction averaged quasiparticle–TLS interaction for scattering between lead l and l'

$$I_{ll'}(\xi, \xi') = \iint \frac{d\Omega}{4\pi} \frac{d\Omega'}{4\pi} |V_{lk(\xi)\mathbf{e}_{\mathbf{k}}, l'k(\xi')\mathbf{e}_{\mathbf{k}'}}^z|^2. \quad (4.44)$$

Only low energy electrons with momentum close to the fermi momentum, $k \approx k_F$, contribute to scattering. This restricts relevant electron energies to small values such that $k(\xi) \approx k(0) \equiv k_F$ and $N(\xi) \approx N(0) \equiv N_F$. With these approximations we find the direction averaged interaction

$$I_{ll'}(\xi, \xi') \approx I_{ll',F} = \iint \frac{d\Omega}{4\pi} \frac{d\Omega'}{4\pi} |V_{lk_F\mathbf{e}_{\mathbf{k}}, l'k_F\mathbf{e}_{\mathbf{k}'}}^z|^2 \quad (4.45)$$

With similar considerations we find the spectral function for Cooper pairs

$$S_{\text{p}}(\omega) = (N_F \mathcal{V})^2 \sum_{ll'} I_{ll',F} \int_{-\infty}^{\infty} d\xi d\xi' \left[1 - \frac{\xi \xi' - |\Delta_{\text{bcs}}|^2 \cos(\varphi_{ll'})}{E(\xi) E(\xi')} \right] \\ \times \{ f_l(\xi) f_{l'}(\xi') \delta(\omega + E(\xi) + E(\xi')) + [1 - f_l(\xi)] [1 - f_{l'}(\xi')] \delta(\omega - E(\xi) - E(\xi')) \} \quad (4.46)$$

Due to energy conservation the Cooper pair spectral density becomes finite for frequencies $|\omega| \geq 2\Delta_{\text{bcs}}$. The relevant energy range for TLS decoherence is defined by the TLS energy splitting which is small compared to the BCS gap. Thus, Cooper pairs do not contribute to TLS decoherence. As shown in section 4.3.2 we can assume particle hole symmetry for the superconducting leads. This means that electron-like $\xi > 0$ and hole-like $\xi < 0$ excitations are equally distributed $f_l(\xi) = f_l(-\xi)$.

Under this assumption integration over the linear part $\propto \xi/E(\xi)$ in the integrand of the quasiparticle density gives no contribution and the spectral density only depends on the energy mode $f_l(E) = f_l(\xi) + f_l(-\xi)$ of the distribution function. This yields

$$S_{\text{qp}}(\omega) = 4(N_F \mathcal{V})^2 \sum_{ll'} I_{ll',F} \int_0^\infty d\xi d\xi' \left[1 - \frac{|\Delta_{\text{bcs}}|^2 \cos(\varphi_{ll'})}{E(\xi)E(\xi')} \right] \times f_l(E(\xi)) [1 - f_{l'}(E(\xi'))] \delta(\omega + E(\xi) - E(\xi')). \quad (4.47)$$

Finally, with the normalized BCS density of states $\rho(E) = E/\sqrt{E^2 - \Delta_{\text{bcs}}^2}$ we can change from integration over electron energies to integration over quasiparticle excitation energies. Evaluating the delta-function we arrive at the final form of the quasiparticle spectral density:

$$S_{\text{qp}}(\omega) = 4(N_F \mathcal{V})^2 \sum_{ll'} I_{ll',F} \int_{\Delta_{\text{bcs}}}^\infty dE \rho(E) \rho(E + \omega) \left[1 - \frac{|\Delta_{\text{bcs}}|^2 \cos(\varphi_{ll'})}{E(E + \omega)} \right] \times f_l(E) [1 - f_{l'}(E + \omega)]. \quad (4.48)$$

TLS properties enter the spectral density through the direction averaged interaction $I_{ll',F}$. The spectral density for quasiparticles strongly depends on the phase $\varphi_{ll'}$. For any value but multiples of π the cosine remains finite and the spectral density diverges for small frequencies ω due to the singularity of the BCS density of states at the gap, see Fig. 4.13. We have seen that pure dephasing evaluates the spectral density for small frequencies already. Thus, for finite $\varphi \neq 2n\pi$ we expect that pure dephasing cannot be described by a simple exponential decay but by a more complex time-dependent dephasing function. However, for TLS inside the Josephson junction the interaction matrix element for tunneling quasiparticles is exponentially suppressed compared to the matrix element of scattering quasiparticles. For such TLS we expect that the main contribution to dephasing stems from quasiparticles that scatter back to their original lead and do not feel the phase difference between the two superconductors. For superconducting qubits the situation is different: the phase difference $\varphi_{ll'}$ arises from the matrix elements of the tunneling Hamiltonian between qubit states and can remain finite [I].

The quasiparticle distribution quickly drops for energies above the gap. Denoting

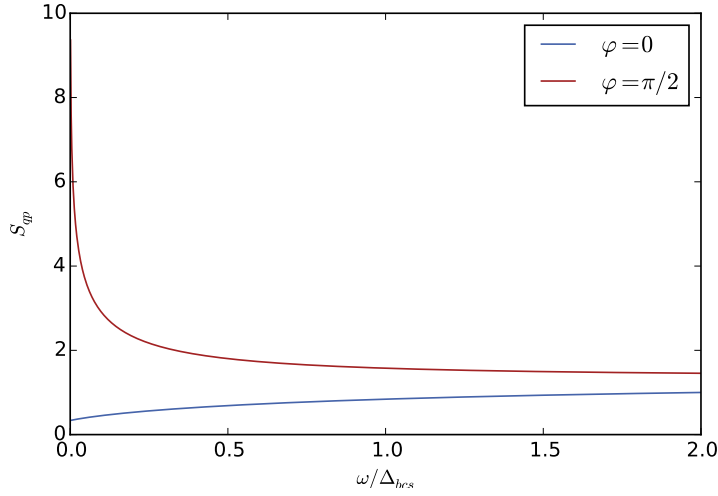


Figure 4.13: Quasiparticle spectral density $S_{\text{qp}}(\omega)$ for $\varphi_{ll'} = 0$ and $\varphi_{ll'} = \pi/2$. For vanishing phase difference, i.e. scattering quasiparticles, the spectral density remains finite even for small frequencies. For $\varphi \neq 0$ the spectral density diverges for small frequencies.

with ζ the width of the distribution function above the gap the spectral density for frequencies $\omega \gtrsim \zeta$ takes the form

$$S_{\text{qp}} = 4 \left((N_F \mathcal{V})^2 \Delta_{\text{bcs}} \sum_{ll'} I_{ll',F} \right) \frac{\omega + \Delta_{\text{bcs}} (1 - \cos \varphi_{ll'})}{\sqrt{(\omega + \Delta_{\text{bcs}})^2 - \Delta_{\text{bcs}}^2}} x_{\text{qp},l} \quad (4.49)$$

where x_{qp} is the density of quasiparticles n_{qp} normalized to the Cooper pair density $n_{\text{cp}} = 2\Delta_{\text{bcs}}N_F$. In equilibrium the width of the distribution function is given by temperature, $\zeta \sim k_B T$. For non-equilibrium quasiparticles the width is determined by the effective temperature T_{eff} introduced in section 4.3.2

We note that influence of quasiparticles on TLS is characterized by the direction averaged interaction $I_{ll',F}$, which we will discuss in more detail in the following section.

4.3.4 Direction Averaged Interaction

We analyze the direction averaged coupling $I_{ll',F}$. We use the Fourier transform

$$V(\mathbf{r}) = \frac{1}{(2\pi)^3} \int d\mathbf{q} e^{-i\mathbf{q}\cdot\mathbf{r}} \tilde{V}(\mathbf{q}) \quad (4.50)$$

of the potential to write the diagonal components of the coupling (4.16) between TLS and electrons as

$$V_{\mathbf{k}\mathbf{k}'}^{\alpha\alpha} = \int \frac{d\mathbf{q}}{(2\pi)^3} V(\mathbf{q}) \int d\mathbf{R} \Phi_{\alpha}^*(\mathbf{R}) \Phi_{\alpha}(\mathbf{R}) e^{i\mathbf{q}\cdot\mathbf{R}} \int d\mathbf{r} \Psi_{\mathbf{k}}^*(\mathbf{r}) \Psi_{\mathbf{k}'}(\mathbf{r}) e^{-i\mathbf{q}\cdot\mathbf{r}}. \quad (4.51)$$

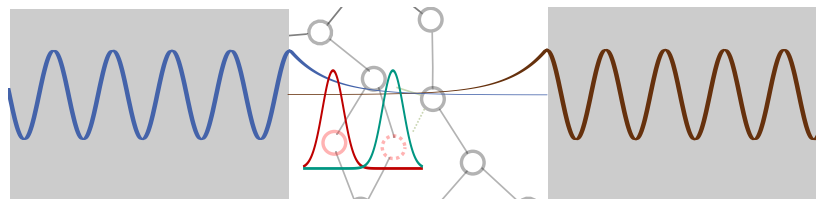


Figure 4.14: Sketch of the JJ with a TLS inside the barrier. We show the TLS wavefunction localized in the junction and the wavefunction of electrons incident from the left and right lead.

Here, α denotes states in the left-right basis of the TLS. We took into account that the overlap between left- and right eigenstates are negligible small. We assume that both superconductors are infinite in the x-y plane while the barrier separates both electrodes in the z-direction for $0 \leq z \leq d$. The electron wavefunctions in the bulk superconductors are plane waves while they decay exponentially in the barrier, see blue and brown curves in Fig. 4.14. Denoting with \mathbf{r}_{\parallel} the x-y components of the three-vector \mathbf{r} and with r_{\perp} the direction perpendicular to the junction we get for the left lead

$$\Psi_{L,k} \sim \mathcal{V}^{-1/2} \begin{cases} e^{i\mathbf{k}\cdot\mathbf{r}} & r_{\perp} < 0 \\ e^{i\mathbf{k}_{\parallel}\cdot\mathbf{r}_{\parallel} - \kappa r_{\perp}} & 0 \leq r_{\perp} \leq d \end{cases}$$

where $\kappa \approx 2m^*U_0/\hbar$. Here, U_0 denotes the barrier height relative to the Fermi energy.

We consider an electron in the junction area of the left lead scattering with the TLS and finally returning to the left lead, i.e., we calculate the coupling for $l = l' = L$. We split the integration region into two regions, $r_{\perp} < 0$ and $r_{\perp} > 0$. For $r_{\perp} < 0$ the effective interaction between TLS and electrons splits into two parts $V_{\mathbf{k}\mathbf{k}'}^{\alpha\beta} = \frac{1}{2} [V_{\mathbf{k}\mathbf{k}',free}^{\alpha\alpha} + \delta V_{\mathbf{k}\mathbf{k}'}^{\alpha\alpha}]$ where

$$V_{\mathbf{k}\mathbf{k}',free}^{\alpha\alpha} = V(\mathbf{k}' - \mathbf{k}) \int d\mathbf{R} \Phi_{\alpha}^*(\mathbf{R}) \Phi_{\alpha}(\mathbf{R}) e^{i(\mathbf{k}' - \mathbf{k})\cdot\mathbf{R}} \quad (4.52)$$

corresponds to the interaction between conduction electrons and TLS in metallic glasses without barrier [44, 108]. The z-component $V_{kk'}^z$ corresponds to $N_{kk'}$ in the work by Kondo. The correction due to the insulating barrier reads as

$$\delta V_{\mathbf{k}\mathbf{k}'}^{\alpha\alpha} = 2i \int d\mathbf{R} \Phi_{\alpha}^*(\mathbf{R}) \Phi_{\alpha}(\mathbf{R}) e^{i(\mathbf{k}' - \mathbf{k})\cdot\mathbf{R}} \left[P \int \frac{dq}{2\pi} \frac{V(\mathbf{k}' - \mathbf{k} + q\hat{\mathbf{e}}_{\perp}) e^{iqR_{\perp}}}{q} \right], \quad (4.53)$$

where $P \int dk f(k) \frac{1}{k} = \lim_{\eta \rightarrow 0} \int dk \frac{k}{\eta^2 + k^2} f(k)$ denotes the Cauchy principal value. Inside the barrier the wavefunctions decay exponentially $\sim e^{-\kappa r_{\perp}}$. The r_{\perp} integration

converges and the interaction inside the barrier can be written as

$$V_{kk'}^{\alpha\alpha} = \int d\mathbf{R} \int dq_{\perp} \frac{V(\mathbf{k}'_{\parallel} - \mathbf{k}_{\parallel} + q_{\perp} \mathbf{e}_{\perp})}{2\kappa - iq_{\perp}} e^{i(\mathbf{k}'_{\parallel} - \mathbf{k}_{\parallel}) \cdot \mathbf{R}_{\parallel} + iq_{\perp} R_{\perp}} \Phi_{\alpha}(\mathbf{R}) \Phi_{\alpha}(\mathbf{R}) \quad (4.54)$$

To gain some insight into these expressions we assume that the TLS wavefunctions are strongly localized with a delta-function-like shape at the well positions $\mathbf{R}_{\alpha} = \mathbf{R}_0 + \alpha \mathbf{d}/2$, i.e. $|\phi_{\alpha}(\mathbf{R})|^2 \sim \delta(\mathbf{R} - \mathbf{R}_{\alpha})$ and that the potential is a contact potential with $V(\mathbf{q}) = V_0$. These assumptions correspond to long electron wavelengths compared to the width r_0 of the localized states, i.e. $k_F r_0 \ll 1$ which is fulfilled for many realizations of TLS. In the long-wavelength limit the dipole element of the coupling reduces to ($\mathbf{Q} = \mathbf{k} - \mathbf{k}'$)

$$V_{kk'}^z = -V_0 e^{-i\mathbf{Q}_{\parallel} \cdot \mathbf{R}_{0,\parallel} - 4\kappa R_{0,\perp}} \sinh \left[i\mathbf{Q}_{\parallel} \cdot \mathbf{d}_{\parallel}/2 + \kappa d_{\perp} \right] \quad (4.55)$$

Calculating the average over directions we find the direction averaged interaction

$$I_{LL,F} = \frac{V_0^2}{2} e^{-4\kappa R_{0,\perp}} \left[\cosh(\kappa d_{\perp}) - \left(\frac{\sin(k_F |d_{\parallel}|)}{k_F |d_{\parallel}|} \right)^2 \right]. \quad (4.56)$$

For an electron scattering on the right side of the junction we have to substitute $R_{0,\perp} \rightarrow W - R_{0,\perp}$ where W is the junction width. For tunneling electrons the coupling element corresponds to the tunneling strength and we have $I_{F,\bar{l}} \sim e^{-2\kappa W}$, where \bar{l} denotes the opposite lead of l . To emphasize the role of TLS position across the junction we define

$$I_0 = \frac{V_0^2}{2} \left[\cosh(\kappa d_{\perp}) - \left(\frac{\sin(k_F |d_{\parallel}|)}{k_F |d_{\parallel}|} \right)^2 \right]$$

and the relative coupling strength of TLS to quasiparticles from the left and the right lead $\gamma_{L/R} = e^{-2\kappa W} e^{\pm\kappa(W-2R_0)}$. With these parameters the coupling takes the form

$$I_{W,F} = I_0 \gamma_l \gamma_{l'} \quad (4.57)$$

The coupling strength of a TLS to the electrons in the leads decays exponentially with the distance $R_{0,\perp}$ of the TLS center from the junction edges. Due to fabrication, however, many TLS reside close to one of the edges. The coupling to the far side electrode and the coupling to tunneling electrons are small compared to the coupling to the near side lead and can be neglected. Interaction with tunneling electrons is suppressed by a factor $\gamma_L \gamma_R \sim e^{-2\kappa W}$. Only TLS close to the center of the junction are equally sensitive to tunneling and scattering particles.

The interaction between conduction electrons in normal metallic glasses and TLS have been analyzed among others by Black [109] and Kondo [108]. Letting $\kappa \rightarrow 0$ and

replacing the component of the separation vector \mathbf{d} parallel to the plane of the barrier with the full distance d between the TLS configurations we recover Kondo's form of the interaction between localized states and conduction electrons $|V_{\text{free}}^z|^2 \sim V_0^2(1 - \sin^2 k_F d / k_F^2 d^2)$. Fitting to experiments, Black estimated the value of the dimensionless coupling parameter $N_F \mathcal{V} V_0 \sim 0.2$ [109, 111]. The dimensionless coupling modified by the exponential decay of the electron wavefunction in the junction determines the strength of the interaction between quasiparticles and TLS in the junction.

To have a more realistic description we calculated the averaged coupling due to a Coulomb potential between the electron and the effective TLS particle. We do not present these calculations in this work. However, we found that the basic characteristics of the long wavelength limit are retained. Thus, we stick with the analytical formulation given above. We neglect any effects of the internal structure of a larger TLS containing several fluctuating charged ions. For TLS inside the insulating barrier of the Josephson junction structural effects could become important due to the exponential dependence on the position of the charges. Further investigation in this direction might prove fruitful.

4.3.5 TLS relaxation due to quasiparticles

Since the quasiparticle spectral density is regular for energies $\omega \geq \zeta$ the relaxation rate $\Gamma_1 = \Gamma_\uparrow + \Gamma_\downarrow$ due to quasiparticles can be obtained with the golden-rule approximation Eq. (3.18). The TLS under consideration have an energy splitting of the order of $E_{\text{tls}} \approx h \cdot 7$ GHz which is large compared to typical quasiparticle energies above the gap while it is small compared to the BCS gap. Thus, TLS excitation with simultaneous relaxation of a high energy quasiparticle to a lower energy is unlikely. Consequently, the up-rate is negligibly small. With the quasiparticle spectral density (4.48) this yields the quasiparticle induced relaxation rate

$$\Gamma_1 \approx \frac{\pi}{2} \cos(\phi) S_{\text{qp}}(E_{\text{tls}}) = 2\pi \frac{\Delta_0^2}{E_{\text{tls}}^2} (N_F \mathcal{V})^2 \sum_{l'l'} I_{l'l', F} \times \int_{\Delta_{\text{BCS}}}^{\infty} dE \rho(E) \rho(E + E_{\text{tls}}) \left[1 - \frac{|\Delta_{\text{BCS}}|^2 \cos(\varphi_{l'l'})}{E(E + E_{\text{tls}})} \right] f_l(E) [1 - f_{l'}(E + E_{\text{tls}})] \quad (4.58)$$

where $\cos \phi = \Delta_0^2 / E_{\text{tls}}^2$ enters the transverse coupling through the transformation from the dipole interaction in the localized basis to the TLS energy basis. For TLS that couple resonantly to the qubit the width of the quasiparticle distribution $\zeta \approx k_B T \approx h \cdot T \cdot 20$ GHz/K above the gap is smaller than the TLS energy splitting in the relevant temperature regime $T \lesssim 0.3K$, i.e., $\zeta \lesssim E_{\text{tls}}$. The quasiparticle spectral density is in good approximation proportional to the quasiparticle density, $S_{\text{qp}} \propto x_{\text{qp}}$, as shown in Eq. (4.49). Using this we find the relaxation rate

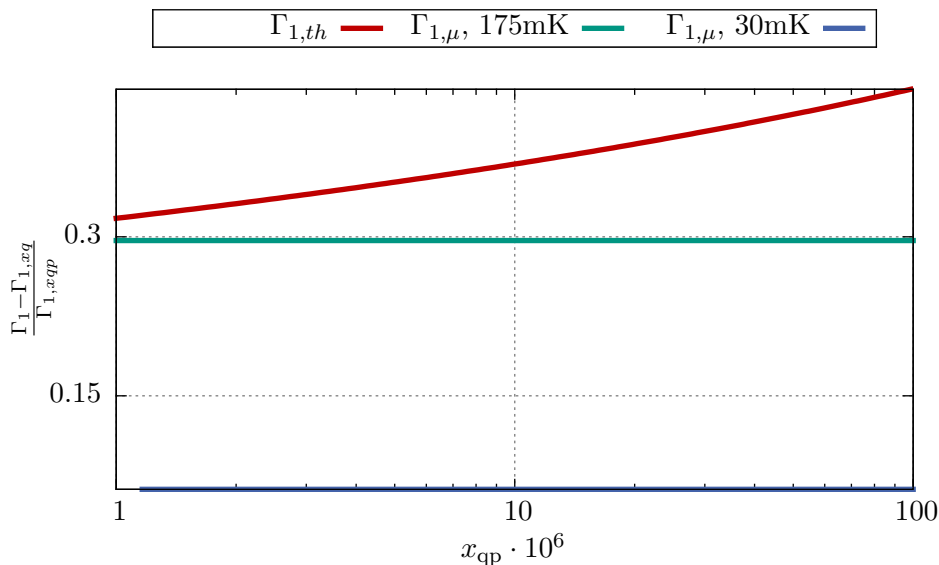


Figure 4.15: Error of the relaxation rate $\Gamma_{1,\text{qp}}$ in x_{qp} approximation according to Eq. (4.60) relative to the numerically calculated relaxation rate Γ_1 for different quasiparticle distributions. The TLS has an energy splitting $E_{\text{tls}} = h \cdot 7$ GHz. Red: a thermal distribution $f(T, 0)$ where the temperature is adjusted to change the quasiparticle density. The maximum temperature is $T_{\text{max}} = 350$ mK. Green and blue: non-equilibrium distributions with fixed temperature and variable chemical potential $f(175\text{mK}, \mu)$ (green), and $f(30\text{mK}, \mu)$ (blue). For the thermal distribution the temperature has to increase to account for the increasing quasiparticle density. Consequently, the width ζ increases and the approximation becomes worse with increasing quasiparticle density. For distributions with fixed temperature the error is independent of the quasiparticle density. For the lower temperature, $T = 30$ mK, the relative error is smaller than for the higher temperature distribution.

$$\Gamma_{qp} = \frac{1}{\tau_0} \frac{\Delta_0^2}{E_{\text{tls}}^2} \sum_{ll'} \frac{I_{ll'} E_{\text{tls}} + \Delta_{\text{bcs}} (1 - \cos \varphi_{ll'})}{I_0 \sqrt{(E_{\text{tls}} + \Delta_{\text{bcs}})^2 - \Delta_{\text{bcs}}^2}} x_{qp,l}. \quad (4.59)$$

In this approximation the relaxation rate due to quasiparticles is proportional to the density of quasiparticles. In Fig. 4.15 we check the quality of the approximation $\Gamma_1 \propto x_{\text{qp}}$ for a TLS with energy splitting $E_{\text{tls}} = h \cdot 7$ GHz. As expected the quality of the approximation is good for small temperatures and degrades with increasing temperature, i.e. increasing width ζ . Since temperature and TLS energy splitting are relatively close for temperatures above 100 mK the deviation from the approximation can already be significant for such temperatures. The time scale of the TLS decoherence due to quasiparticles is given by $\tau_0^{-1} = 2\pi(N_F\mathcal{V})^2\Delta_{\text{bcs}}I_0$ with the coupling strength I_0 defined in Eq. (4.57). Using Black's result for the dimensionless coupling $(N_F\mathcal{V})^2I_0 \sim 0.04$ we find $\tau_0 \approx 0.01\text{ns}$. For typical quasiparticle densities $x_{\text{qp}} \sim 10^{-5}$ this yields TLS relaxation rates of the order of several MHz, $\Gamma_1 \sim \mathcal{O}(1/\mu\text{s})$ which corresponds to experimentally measured relaxation rates [IV]. However, due to the

exponential dependence on the position inside the junction TLS relaxation times for TLS far in the junction can strongly deviate from this time scales. This suggests, that TLS measured in the experiment are close to junction edges. With the averaged interaction Eq. (4.57) we find

$$\Gamma_{\text{qp}} = \frac{1}{\tau_0} \frac{\Delta_0^2}{E_{\text{tls}}^2} \left[\frac{E_{\text{tls}}}{\sqrt{(E_{\text{tls}} + \Delta_{\text{bcs}})^2 - \Delta_{\text{bcs}}^2}} \left(\gamma_L^2 x_{\text{qp,L}} + \gamma_R^2 x_{\text{qp,R}} \right) + \frac{E_{\text{tls}} + \Delta_{\text{bcs}}(1 - \cos \varphi)}{\sqrt{(E_{\text{tls}} + \Delta_{\text{bcs}})^2 - \Delta_{\text{bcs}}^2}} \gamma_L \gamma_R (x_{\text{qp,L}} + x_{\text{qp,R}}) \right]. \quad (4.60)$$

With the imbalance ratio $\eta = x_{\text{qp,L}}/x_{\text{qp,R}}$ the relaxation rate can be expressed in terms of the average quasiparticle density $x_{\text{qp}} = x_{\text{qp,L}} + x_{\text{qp,R}}$. The averaged density corresponds to the quasiparticle density measured in experiments. Additionally, taking into account that the TLS energy splitting is small compared to the superconducting gap we find

$$\Gamma_{\text{qp}} = \frac{1}{\tau_0} \frac{\Delta_0^2}{E_{\text{tls}}^2} \sqrt{\frac{E_{\text{tls}}}{2\Delta_{\text{bcs}}}} \times \left[\gamma_L \gamma_R \left[1 + \frac{\Delta_{\text{bcs}}}{E_{\text{tls}}} (1 - \cos \varphi) \right] + \frac{\eta \gamma_L^2 + \gamma_R^2}{1 + \eta} \right] x_{\text{qp}} \quad (4.61)$$

The quasiparticle density is characterized by the (effective) temperature. For thermally created quasiparticles we have demonstrated that the density is given by $x_{\text{qp}} = x_{\text{qp}}(T) + x_{\text{qp}}(T_s)$ because of the presence of non-equilibrium quasiparticles. Here, T_s is the effective temperature characterizing the non-equilibrium distribution while T is the temperature of the phonon bath. For thermally created quasiparticles the density is homogeneous for the entire superconductor. It follows $x_{\text{qp,L}}^{\text{th}} = x_{\text{qp,R}}^{\text{th}}$, i.e. the ratio between left-hand density and right-hand density is $\eta = 1$. The TLS relaxation rate takes the form

$$\Gamma_1^{\text{th}} = \frac{1}{\tau_0} \frac{\Delta_0^2}{E_{\text{tls}}^2} \left(\sqrt{\frac{\pi k_B T}{2\Delta_{\text{bcs}}} e^{-\frac{\Delta_{\text{bcs}}}{k_B T}} + x_{\text{qp}}(T_s)} \right) \frac{E_{\text{tls}}/\Delta_{\text{bcs}}}{\sqrt{2(E_{\text{tls}}/\Delta_{\text{bcs}} + 1)}} \times \left[\gamma_L \gamma_R \left[1 + \frac{\Delta_{\text{bcs}}}{E_{\text{tls}}} (1 - \cos \varphi) \right] + \gamma_L^2 + \gamma_R^2 \right]. \quad (4.62)$$

For injected quasiparticles the quasiparticle densities are different in both junction electrodes. Neglecting quasiparticle tunneling through the junction we find a ratio $\eta = 4$ between the left and right electrode. With tunneling the ratio decreases to $\eta \approx 2$. With this form of the quasiparticle induced rates we can describe the findings

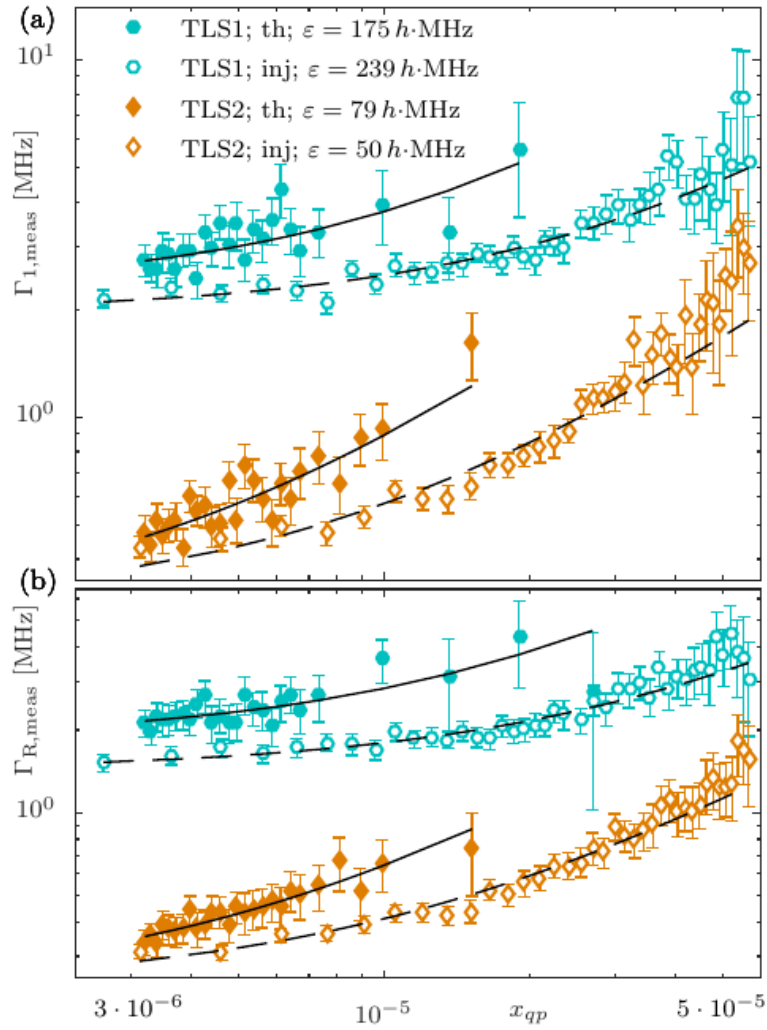


Figure 4.16: TLS relaxation (top) and Rabi decay rates (bottom) vs measured quasiparticle density. Black lines are fits to theory equations (4.61) and (4.79). Taken from reference [IV]. Courtesy of A. Bilmes.

in the experiment by Bilmes [IV]. In Fig. 4.16 we show experimentally measured relaxation rates (top) for thermal and injected quasiparticles. Black lines are fits of our theory to the experimental data. The stunning difference between rates for thermal and injected quasiparticles stems from the imbalance between both junction electrodes. Using our expressions for the relaxation rates the ratio between relaxation through thermally and injected quasiparticles is given by

$$\frac{\Gamma_1^{\text{th}}}{\Gamma_1^{\text{inj}}} = \frac{\gamma_L \gamma_R \left[1 + \frac{\Delta_{\text{tIs}}^{\text{bcs}}}{E_{\text{tIs}}} (1 - \cos \varphi) \right] + \gamma_L^2 + \gamma_R^2}{\gamma_L \gamma_R \left[1 + \frac{\Delta_{\text{tIs}}^{\text{bcs}}}{E_{\text{tIs}}} (1 - \cos \varphi) \right] + (\eta \gamma_L^2 + \gamma_R^2)/(1 + \eta)} \approx \frac{(1 + \eta)(\gamma_L^2 + \gamma_R^2)}{\eta \gamma_L^2 + \gamma_R^2}. \quad (4.63)$$

For $\eta = 4$ the ratios measured in reference [IV] between the rates are well described by our theory. In order to fit our theory to the decay rates observed in reference [43] we assume that acoustic phonons induce decay according to the rate in Eq. (4.89). Fitting the function $\Gamma_1 = a \coth \beta E_{\text{tIs}}/2 + b x_{\text{qp}}$ to the decay times of TLS 1 and TLS 2 of aforementioned reference we obtain values of $b_1 \approx 42 \frac{1}{\text{ns}}$ and $a_1 \approx 2.4 \frac{1}{\mu\text{s}}$ for TLS 1 and $b_2 \approx 35 \frac{1}{\text{ns}}$ and $a_2 \approx 2.6 \frac{1}{\mu\text{s}}$. Comparing b with Eq.(4.62) these values for the parameters b_i correspond to values of the pre-factor

$$\frac{1}{\tau_0} \frac{\Delta_0^2}{E_{\text{tIs}}^2} (\gamma_L^2 + \gamma_R^2 + \gamma_L \gamma_R [1 + \frac{\Delta_{\text{tIs}}^{\text{bcs}}}{E_{\text{tIs}}} (1 - \cos \varphi)]) \sim 10 \frac{1}{\text{ns}}$$

This yields an order of magnitude for the scattering time τ_0 is close to the scattering time obtained from the interaction strength found by black, $\tau_0 \sim 0.01$ ns. We show the experimental data together with the obtained fit in Fig.4.17.

4.3.6 Dephasing: Ramsey and spin-echo protocol

Now, we consider the longitudinal component of the TLS-quasiparticle interaction Eq. (4.22). The self-energy for dephasing due to quasiparticles is given by the diagrams depicted in Fig. 4.18. Contrary to dephasing due to a bosonic noise every quasiparticle vertex contains an incoming and an outgoing fermion line. In principle, it is possible to contract fermion lines in loops containing $2n$ vertices. The subspace of diagrams containing only loops with two vertices, i.e. $n = 1$, describes an effective bosonic noise. The first two diagrams in Fig. 4.18 belong to this subspace of diagrams while the third diagram is a loop containing 4 vertices, i.e., $n=2$. Within the $n = 1$ -subset averages over coupling operators V split in in the bosonic fashion

$$\langle V(t_1)V(t_2) \dots V(t_n) \rangle = \prod_{\text{perm}} \langle V(t_i)V(t_j) \rangle \dots \langle V(t_k)V(t_l) \rangle. \quad (4.64)$$

This defines a coupling to an effective Gaussian bath with bosonic pseudo operators

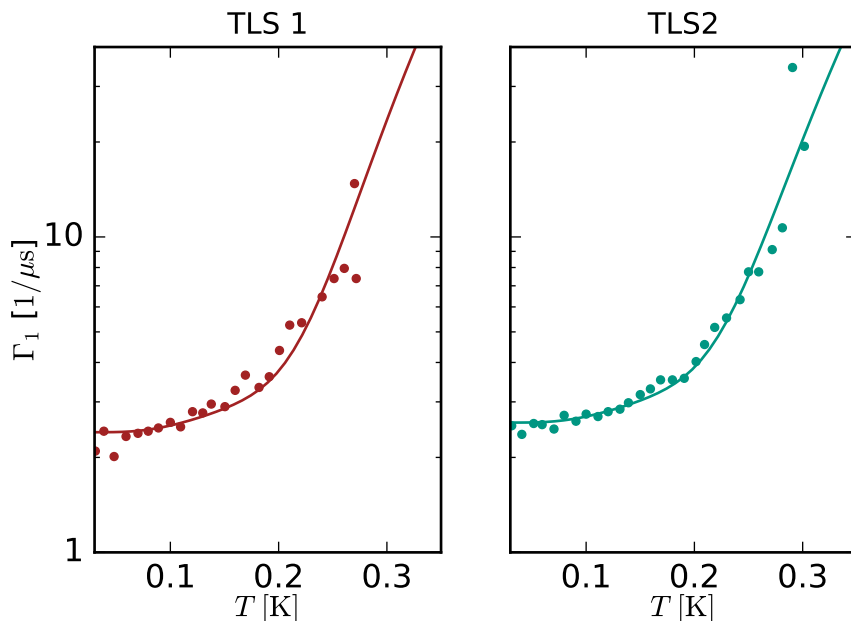


Figure 4.17: Temperature dependent decay rates for two TLS with energy splittings $E_{\text{tls},1} = h \cdot 7.735$ GHz and $E_{\text{tls},2} = h \cdot 7.947$ GHz. Experimental data from [43], solid lines are fit to the superposition of photon-induced decay $\Gamma_1 \propto \coth(\beta E_{\text{tls}}/2)$ and quasiparticle induced decay $\propto x_{\text{qp}}$

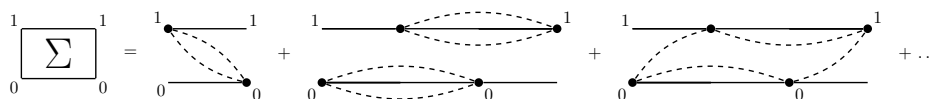


Figure 4.18: Self-energy for dephasing due to a fermionic bath. The first two diagrams contain only fermionic loops with two vertices. The third diagram on the other hand contains a loop comprising four vertices and is neglected in our approximation.

$\hat{X} = \sum_{l',k,k'} \Upsilon_{l,k}^\dagger V_{lk,l'k'}^z M_{lk,l'k'} \Upsilon_{l',k'}$. In reference [I] we motivate the choice of diagrams. There, we show that diagrams with $n > 1$ are suppressed by the number of tunneling channels defined by the ratio of direction averages [121]:

$$\frac{1}{N_{ch}} \sim \frac{\langle t_{k_1 q_1} t_{k_2 q_2} \rangle}{\langle |t_{kq}|^2 \rangle} \quad (4.65)$$

where $t_{\mathbf{k},\mathbf{q}}$ is the tunneling element. Here, we can argue similarly. For $n > 1$ momentum conservation induces more constraints on quasiparticle momentum summations. Diagrams with $n > 1$ are suppressed by the ratio of direction averages over the quasiparticle-TLS interaction $1/N_\Omega \sim \langle V_{lk,l'k'}^z M_{lk,l'k'} V_{r'q,r'q'}^z M_{r'q,r'q'} \rangle / \langle |V_{lk,l'k'}^z M_{lk,l'k'}|^2 \rangle$. Within the Gaussian approximation we can calculate the dephasing function $x(t)$ due

to quasiparticles with the relations given in Eq. (3.28):

$$x_0(t) = \frac{t^2}{2} \int d\omega S_{\text{qp}}(\omega) \text{sinc}^2\left(\frac{\omega t}{2}\right)$$

$$x_1(t) = \frac{t^2}{2} \int d\omega S_{\text{qp}}(\omega) \sin^2\left(\frac{\omega t}{4}\right) \text{sinc}^2\left(\frac{\omega t}{4}\right).$$

The filter functions for Ramsey and spin-echo are peaked at $\omega t \approx 0$ and $\omega t \approx 4.6$ respectively. The width of both filter functions is determined by the relation $\omega t \sim \mathcal{O}(1)$. For typical experiments with measurement times in the microsecond regime this determines a width of several MHz while the spin-echo filter function is peaked at $\omega \sim \mathcal{O}(\text{MHz})$, too. Compared to the superconducting gap $\Delta_{\text{bcs}} \sim h \cdot 40 \text{ GHz}$ and electronic excitation energies the filter functions define small energy scales. Thus, spin-echo and Ramsey protocol evaluate the spectral density at small frequencies compared to electronic energies. The relevant energy scale of the quasiparticles is not given by the gap but defined by the width ζ of the distribution function above the gap which is of the order of several GHz in the relevant temperature regime, $\zeta \approx h \cdot T \cdot 20 \text{ GHz/K}$. Thus, we can distinguish two time regimes, the short time limit defined by $t \lesssim \zeta^{-1}$ and the long time limit $t \gg \zeta^{-1}$. The short time limit corresponds to measurement times of nano-seconds while the long time limit corresponds to usual measurements in the micro second regime. If one could achieve a situation with quasiparticles described by a chemical potential but low temperature the short time regime might be observable at longer measurement times.

Short Times

For short times $\zeta \ll t^{-1}$ the weight functions $g(\omega)$ have broad maximums in frequency space and all quasiparticles contribute to dephasing. Thus, dephasing functions are proportional to the quasiparticle density x_{qp} . The filter functions for Ramsey and spin-echo weight the spectral density at different frequencies. The Ramsey function extends from zero frequency to $\omega \gg \zeta$ and gives the singular part of the spectral density the highest weight. The spin-echo function on the other hand has its maximum at $\omega = \omega_1 = 4.6/t \gg \zeta$ and filters out the divergent contribution. Due to this spin-echo refocusing is very effective. To confirm our intuition we rewrite the quasiparticle spectral density in terms of the dimensionless variables $x = E/\Delta_{\text{bcs}} - 1$ and $y = \omega/\Delta_{\text{bcs}}$:

$$S_{\text{qp}}(\omega) = \frac{\Delta^2}{E_{\text{tIs}}^2} \frac{2}{\pi \tau_0} \sum_W \frac{I_{W,F}}{I_0} \int_0^\infty dx \frac{1}{\sqrt{(x+1)^2 - 1}} \frac{1}{\sqrt{(x+1+y)^2 - 1}}$$

$$\times \left[(x+1)(x+1+y) - \cos(\varphi_W) \right] f_l(\Delta_{\text{bcs}}(1+x)) [1 - f_l(\Delta_{\text{bcs}}(1+x+y))]. \quad (4.66)$$

The distribution function restricts x to small values. Approximating $\sqrt{(x+1)^2-1} \approx \sqrt{2x}$ and $\sqrt{(y+x+1)^2-1} \approx \sqrt{2(x+y-1)}$ we find the Ramsey and spin-echo dephasing function

$$x_{0/1}(t) = \frac{\Delta^2}{E_{\text{tIs}}^2} \frac{(\Delta_{\text{bcs}}t)^2}{2\pi\tau_0\Delta_{\text{bcs}}} \sum_{l'} \frac{I_{l',F}}{I_0} \int_0^\infty dx \int_0^\infty dy \frac{(x+1)(1+y) - \cos(\varphi_{l'})}{\sqrt{x}\sqrt{y}} \\ \times f_l(\Delta_{\text{bcs}}(1+x))[1 - f_{l'}(\Delta_{\text{bcs}}(1+y))] \begin{cases} \text{sinc}^2 \frac{(y-x)\Delta_{\text{bcs}}t}{2} \\ \sin^2 \frac{(y-x)\Delta_{\text{bcs}}t}{4} \text{sinc}^2 \frac{(y-x)\Delta_{\text{bcs}}t}{4} \end{cases} .$$

While the distribution function restricts x to small values no such restriction occurs for y . Thus, we can substitute $x \rightarrow 0$ in every sum with y . With the quasiparticle density $x_{\text{qp}} = \int dx(x+1)/\sqrt{2x}f(\Delta_{\text{bcs}}(1+x))$ we find

$$x_{0/1}(t) = \frac{\Delta^2}{E_{\text{tIs}}^2} \frac{(\Delta_{\text{bcs}}t)^2}{2\pi\tau_0\Delta_{\text{bcs}}} \sum_{l'} \frac{I_{l',F}}{I_0} \sqrt{2}x_{\text{qp},l} \\ \times \int_0^\infty dy \frac{(1+y) - \cos(\varphi_{l'})}{\sqrt{y}} \begin{cases} \text{sinc}^2 \frac{y\Delta_{\text{bcs}}t}{2} \\ \sin^2 \frac{y\Delta_{\text{bcs}}t}{4} \text{sinc}^2 \frac{y\Delta_{\text{bcs}}t}{4} \end{cases} \quad (4.67)$$

The integrals can be evaluated exactly. We find the Ramsey and spin-echo dephasing functions in the short time limit

$$x_0(t) = \frac{\Delta^2}{E_{\text{tIs}}^2} \frac{2\sqrt{\pi\Delta_{\text{bcs}}t}}{\pi\tau_0\Delta_{\text{bcs}}} \left[\sum_{l'} \gamma_l \gamma_{l'} x_{\text{qp},l} \left[1 + \frac{2}{3}(1 - \cos \varphi_{l'}) \Delta_{\text{bcs}}t \right] \right] \quad (4.68)$$

$$x_1(t) = \frac{\Delta^2}{E_{\text{tIs}}^2} \frac{2\sqrt{\pi\Delta_{\text{bcs}}t}}{\pi\tau_0\Delta_{\text{bcs}}} \left[\sum_{l'} \gamma_l \gamma_{l'} x_{\text{qp},l} \left[\sqrt{8} - 1 + \frac{2}{3}(\sqrt{2} - 1)(1 - \cos \varphi_{l'}) \Delta_{\text{bcs}}t \right] \right]. \quad (4.69)$$

Both, spin-echo and Ramsey dephasing do not follow a linear exponential decay with $x(t) \propto \Gamma t$. Instead, for scattering quasiparticles with $\varphi = 0$ both dephasing functions follow a square-root time dependence. The effectiveness of spin-echo refocusing is contained in the ratio $x_1(t)/x_0(t) \approx 1.8$ for scattering quasiparticles. Thus, for short times and scattering quasiparticles spin-echo actually decreases coherence times (increases the dephasing function). This can be seen from the spectral density. For $\varphi = 0$ the spectral density decreases for $\omega \rightarrow 0$ and reaches a minimum at zero frequency. Ramsey dephasing depends on the spectral density at small frequencies while the spin-echo dephasing evaluates the spectral density at higher frequencies where the spectral density increases. For tunneling quasiparticles with $\varphi \neq 0$ an additional term $\propto (\Delta_{\text{bcs}}t)^{3/2}$ appears in the dephasing functions due to the divergent contribution of the spectral density at small frequencies. For times $t \sim 10^{-2}$ ns this factor adds a contribution of $\mathcal{O}(1)$ and becomes dominant compared to the term $\propto \sqrt{t}$. Ramsey

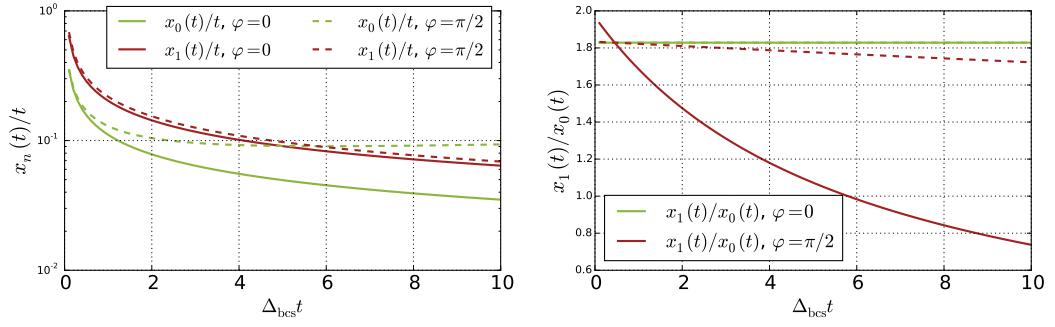


Figure 4.19: *Left:* Ramsey and spin-echo dephasing function normalized to time for $\varphi = 0$ (solid) $\varphi \neq 0$ (dashed). The TLS couples to both leads with $\gamma_L = \gamma_R = 1$. For tunneling quasiparticles the spectral density is divergent at small frequencies. Thus, for equal coupling tunneling quasiparticles become the dominant source of decoherence for $\varphi \neq 0$. The spin-echo protocol filters the divergence resulting in longer coherence times. For scattering quasiparticles the spectral density reaches a minimum at $\omega = 0$ and spin-echo actually decreases coherence times. *Right:* Ratio between spin-echo and Ramsey. Solid lines correspond to $\gamma_L = \gamma_R = 1$, dashed lines to $\gamma_R = 0.01\gamma_L$. For equal coupling tunneling quasiparticles are dominant and spin-echo is effective. Coupling to tunneling quasiparticles is suppressed in the junction and spin-echo becomes less effective (dashed line).

dephasing is sensitive to the divergence while spin-echo filters these low frequencies. Thus, for tunneling quasiparticles spin-echo becomes effective and the ratio between spin-echo and Ramsey decreases. However, for TLS inside the insulating barrier of a Josephson junction the coupling to tunneling quasiparticles is exponentially suppressed and the tunneling contribution plays a minor role. In Fig. 4.19 we plot the short-time dephasing function for a TLS with $\tau_0 = 3 \mu\text{s}$ and $\Delta/E_{\text{tls}} \approx 1$ for $T = 0.2$ mK which corresponds to a quasiparticle density $x_{\text{qp}} \approx 1.1 \cdot 10^{-5}$. At this temperature the short-time limit is valid for times $\Delta_{\text{bcs}} t \lesssim 10$. The left graph shows the dephasing function for equal coupling to the different leads, $\gamma_L = \gamma_R = 1$. The right plot shows the ratio x_1/x_0 for equal coupling (solid) and for $\gamma_R = 0.01\gamma_L$ (dashed). For equal coupling tunneling quasiparticles are dominant and spin-echo is effective. For the more realistic case with very different coupling scattering particles from the left lead are dominant and spin-echo does not yield the same effectiveness. We can define the dephasing time $T_{r/e}$ for Ramsey and spin-echo as the time where $x_{1,0}(t) = 1$. For a TLS with dominant scattering from one side of the junction we find $T_{r/e} \propto [E_{\text{tls}}^2/\Delta^2]^2$, i.e. the dephasing time depends on the ratio between TLS asymmetry and TLS energy to the power of four.

Long Times

In the limit $\zeta \gg 1/t$ the weight functions $g_n(\omega t)$ decay in a narrow region of width $\delta\omega \sim 2\pi/t \ll \zeta$ around their maximum and only quasiparticles with energies very

close to the gap contribute to dephasing. In this limit a different approximation to the spectral density applies. Since the weighting functions decay fast on quasiparticle energy scales we can approximate the quasiparticle distribution function with its value at the gap $f(E) \approx f(\Delta_{\text{bcs}}) = f_0$. The constant f_0 and the width ζ can be related to the quasiparticle density as $f_0 \approx x_{\text{qp}} \sqrt{\Delta_{\text{bcs}}/2\zeta}$. To deal with the divergent spectral density at small frequencies we split the quasiparticle density into a regular contribution $S_{\text{qp},0} = S_{\text{qp}}(\varphi = 0)$ and a divergent contribution $S_{\text{qp},\text{div}} = S_{\text{qp}} - S_{\text{qp},0}$. For the regular part we use that the weighting functions become delta-function like for long times and apply the Born-Markov approximation Eq. (3.30):

$$(x_0(t) - x_{0,\text{div}})/t \approx \Gamma_r = \frac{\pi}{2} S_{\text{qp},0}(0) \quad (4.70)$$

$$(x_1(t) - x_{1,\text{div}})/t \approx \Gamma_e = \frac{\pi}{2} S_{\text{qp},0}(4.6/t). \quad (4.71)$$

We note that for $\omega = 0$ the coherence factors in the spectral density cancel the BCS density of states exactly. This yields the Ramsey dephasing rate ($x = E/\Delta_{\text{bcs}} - 1$ and $y = \omega/\Delta_{\text{bcs}}$)

$$\begin{aligned} \Gamma_r &= \frac{\Delta^2}{E_{\text{tIs}}^2} \frac{1}{\tau_0} \sum_{l'} \frac{I_{l',F}}{I_0} \int_0^\infty dx f_l(\Delta_{\text{bcs}}(1+x)) [1 - f_{l'}(\Delta_{\text{bcs}}(1+x+y))] \\ &\approx \frac{\Delta^2}{E_{\text{tIs}}^2} \frac{1}{\tau_0} \sum_{l'} \frac{I_{l',F}}{I_0} \frac{\zeta f_{0,l}}{\Delta_{\text{bcs}}} \approx \frac{\Delta^2}{E_{\text{tIs}}^2} \frac{1}{\tau_0} \sum_{l'} x_{\text{qp},l} \frac{I_{l',F}}{I_0} \sqrt{\frac{\zeta}{2\Delta_{\text{bcs}}}}. \end{aligned} \quad (4.72)$$

For a Fermi function the width is proportional to the temperature and $\Gamma_r \propto x_{\text{qp}}(T) \sqrt{k_B T / 2\Delta_{\text{bcs}}}$. Similarly, for $\omega_1 = 4.6/\tau \ll \zeta$ we find the spin-echo dephasing rate

$$\begin{aligned} \Gamma_e &\approx \frac{\Delta^2}{E_{\text{tIs}}^2} \frac{1}{\tau_0} \sum_{l'} \frac{I_{l',F}}{I_0} \frac{\zeta f_{0,l}}{\Delta_{\text{bcs}}} \left(1 + \frac{\omega_1}{\zeta}\right) \\ &\approx \frac{\Delta^2}{E_{\text{tIs}}^2} \frac{1}{\tau_0} \sum_{l'} x_{\text{qp},l} \frac{I_{l',F}}{I_0} \sqrt{\frac{\zeta}{2\Delta_{\text{bcs}}}} \left(1 + \frac{\omega_1}{\zeta}\right) \end{aligned} \quad (4.73)$$

Spin-echo tends to increase the pure dephasing rate due to scattering quasiparticles with $\varphi = 0$ compared to free Ramsey decay. To calculate the divergent contribution due to tunneling quasiparticles we calculate the divergent part of the spectral density

$$\begin{aligned} S_{\text{qp},\text{div}}(\omega) &\approx \frac{\Delta^2}{E_{\text{tIs}}^2} \frac{1}{\pi\tau_0} \sum_l \frac{I_{\bar{l},F}}{I_0} f_{0,l} \int_0^{\zeta/\Delta_{\text{bcs}}} dx \frac{1 - \cos \varphi_{\bar{l}}}{\sqrt{x(x + \omega/\Delta_{\text{bcs}})}} \\ &\approx \frac{\Delta^2}{E_{\text{tIs}}^2} \frac{1}{\pi\tau_0} \sum_l \frac{I_{\bar{l},F}}{I_0} f_{0,l} (1 - \cos \varphi_{\bar{l}}) \ln \left| \frac{4\zeta}{\omega} \right| \end{aligned} \quad (4.74)$$

where \bar{l} denotes the opposite lead of l . This form of the spectral density is valid for $\omega \ll \zeta$ which is fulfilled for Ramsey and spin-echo dephasing in the long time limit. The spectral density only depends logarithmically on the cut-off energy. The divergent part of the spectral density yields the dephasing functions

$$x_{0,div}(t) = \frac{\Delta^2}{E_{\text{tls}}^2} \frac{1}{\tau_0} \sum_l \frac{I_{\bar{l},F}}{I_0} f_{0,l}(1 - \cos \varphi_{\bar{l}}) [\gamma_e - 1 + \log(4\zeta t)] t \quad (4.75)$$

$$x_{1,div}(t) = \frac{\Delta^2}{E_{\text{tls}}^2} \frac{1}{\tau_0} \sum_l \frac{I_{\bar{l},F}}{I_0} f_{0,l}(1 - \cos \varphi_{\bar{l}}) [\gamma_e - 1 + \log(\zeta t)] t. \quad (4.76)$$

Both dephasing functions separate into a contribution that is linear in time and adds to the dephasing rate $\Gamma_{r/e}$ and a contribution with logarithmic time dependence. The full dephasing functions can be written as $x_i(t) = \gamma_i \ln(\zeta t)t + \Gamma_i t$, where Γ_i is the sum of rates from the divergent and regular part while γ_i stems from the logarithmic contribution due to the divergent part. Due to the part of the dephasing function that is logarithmic in time the coherences of the TLS density matrix $\rho_{10/01} \propto e^{-x(t)}$ obtain a time dependent pre-factor of the form $\rho_{01}(t) \propto (\zeta t)^{-\gamma_i} e^{-(\Gamma_1/2 + \Gamma_i)t}$ in the long-time limit.

Numerical Results

In this section we calculate the full dephasing functions according to Eq. (3.28) numerically. We assume that quasiparticles are in equilibrium with temperature $k_B T = 0.1 \Delta_{\text{bcs}}$. For aluminum this corresponds to a temperature of 210 mK and a quasiparticle density of $x_{\text{qp}} \approx 1.8 \cdot 10^{-5}$. Due to the relatively large temperature the distribution is smeared out over a wide range of energies above the gap and the short time approximation for a narrow distribution function is likely to fail for short times already. In Fig. 4.20 we plot the numerically obtained dephasing function (solid lines) together with the approximations for long (dot-dashed) and short times (dashed) versus the dimensionless parameter $t\zeta = t \cdot k_B T$ that discriminates the different regimes. All numerical results are obtained for $\tau_0 = 3$ ps. In Fig. 4.20 we assume equal coupling to both leads and analyze dephasing due to scattering and tunneling quasiparticles separately to emphasize the effects of the divergent contribution $\sim (1 - \cos \varphi)$. For scattering quasiparticles both Ramsey and spin-echo-dephasing decay in time until they reach the constant contribution $x(t \gg 1/\zeta)/t = \Gamma_{r,e}$. Thus, dephasing due to scattering quasiparticles in experimentally relevant time scales follows the usual exponential law with golden rule rates Eq. (3.30). Dephasing due to tunneling quasiparticles on the other hand is dominated by the non-linear contribution $x(t) \sim \log(\zeta t)$. While for spin-echo the short time approximation remains valid up to $\zeta t \approx 1$ the approximation breaks down earlier for Ramsey dephasing. For times $\zeta t \gtrsim 10^2$ the full dephasing func-

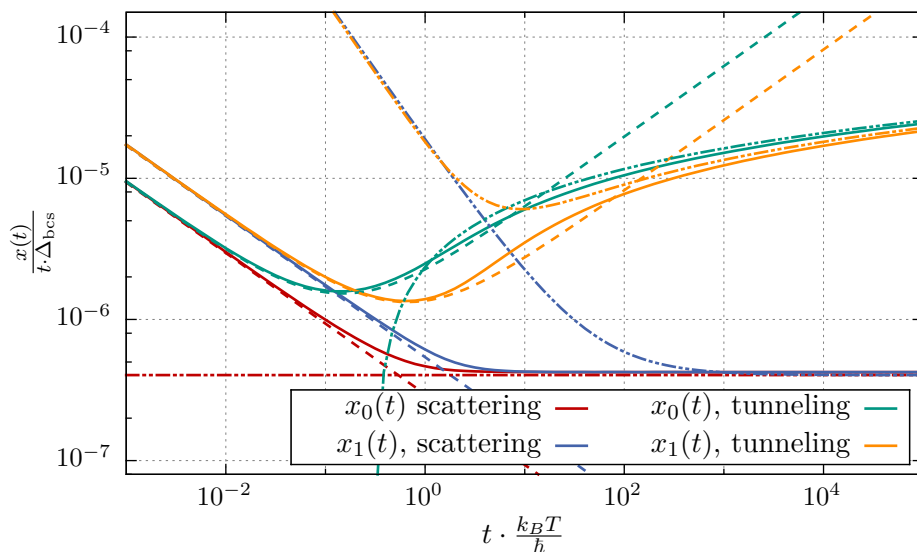


Figure 4.20: Ramsey $x_0(t)$ and spin-echo $x_1(t)$ dephasing functions due to scattering and tunneling quasiparticles versus time. Dephasing rates are normalized to $t \cdot \Delta_{\text{bcs}}$ in order to compare to linear decay with $x(t)/t = \Gamma$. Time is normalized to the width $\zeta = k_B T$ of the distribution function, $t \cdot \zeta / \hbar$ to distinguish different regimes $t \ll \hbar / \zeta$ and $t \gg \hbar / \zeta$. Solid lines are numerical solutions of the full dephasing rate defined in Eq. (3.28). Dashed lines represent the short time solution Eq. (4.68) and Eq. (4.69). Dash-dotted lines show the analytical solutions for long times according to Eq. (4.75) and (4.76). The short time expression remains valid up to $t \cdot \xi / \hbar \sim 1$. For $t \cdot \zeta / \hbar \gtrsim 10^1$ for scattering and $t \cdot \zeta / \hbar \gtrsim 10^2$ for tunneling quasiparticles the approximation for long times becomes reliable. For scattering quasiparticles, i.e. $\varphi = 0$, dephasing in the long-time limit follows the golden rule rates $\Gamma_{r,e}$ while dephasing due to tunneling quasiparticles is dominated by contribution of the divergent part $\propto \log(\zeta t)$.

tion is well described by the long time approximation Eqs. (4.75)-(4.76). In Fig. 4.21 we plot the numerically obtained full dephasing function for different ratios between coupling to left and right lead. For equal coupling $\gamma_L = \gamma_R$ dephasing is dominated by tunneling quasiparticles and closely follows $x(t) \sim \log(\zeta t)$. With decreasing coupling to the right lead tunneling quasiparticles become less important. For large ratios dephasing is dominated by scattering quasiparticles and is well described by the golden rule rates $\Gamma_{r,e}$, Eq. (3.30).

4.3.7 Rabi Decay Rates

We drive the TLS with frequency close to resonance $|\omega - E_{\text{tls}}|/E_{\text{tls}} \ll 1$. Due to the drive the TLS Hamiltonian reads as $H_{\text{tls}} = \frac{E_{\text{tls}}}{2} \tau^z + g_c \tau^x \cos \omega t$. We change to the rotating frame according to the unitary transformation $H_{\text{rot}} = U^\dagger(t) H_{\text{tls}} U(t) - i \dot{U}^\dagger(t) U(t)$ with the free time evolution operator $U(t) = \exp(-i E_{\text{tls}} \tau_z t / 2)$ of the TLS. The rotating frame rotates with the TLS energy splitting around the \hat{z} axis, i.e. without drive the TLS state is static in the rotating frame. Applying the rotating wave approximation

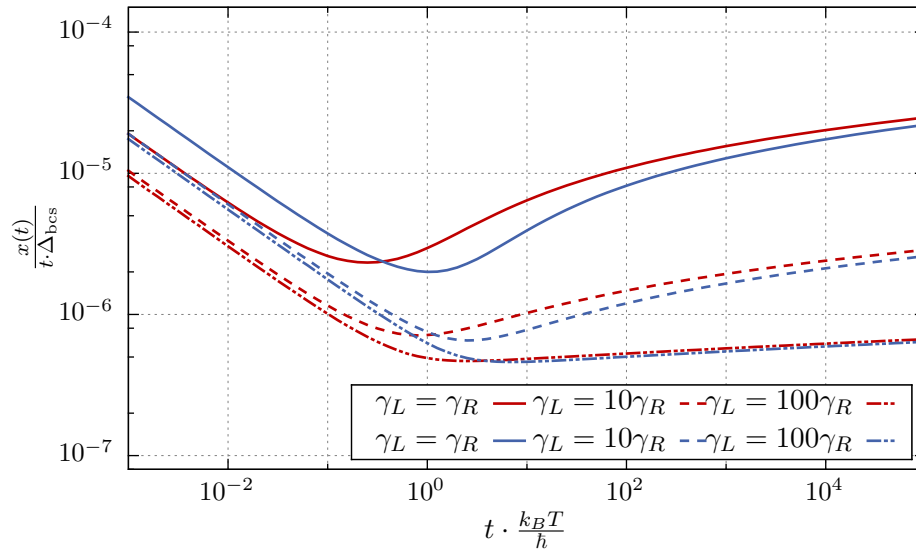


Figure 4.21: Full Ramsey (red) and spin-echo (blue) dephasing $x(t) = x_{\text{scattering}} + x_{\text{tunneling}}$ for different ratios γ_L/γ_R . For equal coupling to both leads dephasing is dominated by scattering quasiparticles $x(t) \propto \log(\zeta t)$. With decreasing coupling to one of the leads, i.e. $\gamma_L/\gamma_R > 1$ scattering quasiparticles become dominant and dephasing of the TLS approaches the golden rule approximation. Thus, for very different couplings to the left and right lead respectively TLS-dephasing follows the exponential law $x(t) \propto \Gamma t$.

(RWA) the TLS Hamiltonian in the rotating frame reads as

$$H_{\text{rot}} \approx \frac{g_c}{2} \tau^x \cos(\delta t), \quad (4.77)$$

where $\delta = |\omega - E_{\text{tls}}|$. In order to have a similar notation as before we apply an additional rotation around the \hat{y} axis of the rotating frame with rotation matrix $\hat{R} = \exp(i\frac{\pi}{4}\tau^y)$. This yields $H_{\text{rot}} = \frac{g_c}{2}\tau^z$. The coupling matrix element between TLS and electrons in the rotating frame after additional rotation around \hat{y} reads as

$$V = \left\{ -\frac{\Delta^2}{E_{\text{tls}}^2} \tau^x + \frac{\Delta_0^2}{E_{\text{tls}}^2} \cos(E_{\text{tls}} t) \tau^z + \frac{\Delta_0^2}{E_{\text{tls}}^2} \sin(E_{\text{tls}} t) \tau^y \right\} \sum_{l', k, k'} \Upsilon_{l', k}^\dagger V_{l', k, k'}^z M_{l', k, k'} \Upsilon_{l', k'}. \quad (4.78)$$

Since oscillations with frequency E_{tls} are fast compared to the slow oscillations with frequency determined by the difference frequency δ the time dependent contributions to the coupling drop out in the RWA and we are left with pure transversal coupling $\propto \tau^x$. Contrary to relaxation of the free TLS the coupling matrix element is proportional to the asymmetry Δ^2 instead of the tunneling amplitude Δ_0^2 . The corresponding Rabi

decay rate is obtained within golden rule approximation as

$$\Gamma_{\text{Rabi}} = \frac{\pi}{2} \frac{\Delta^2}{E_{\text{tls}}^2} (S_{\text{qp}}(g_c) + S_{\text{qp}}(-g_c)). \quad (4.79)$$

Besides the substitution $\Delta_0 \rightarrow \Delta$ in the matrix element the only further difference compared to the free TLS relaxation rate is that the energy difference between ground and excited state in the rotating frame corresponds to the coupling strength g_c rather than the energy splitting E_{tls} . Consequently, the spectral density is evaluated at the effective energy splitting g_c instead of E_{tls} . While the TLS energy splitting is of the order of several gigahertz, the coupling g_c amounts only some tens or hundreds of megahertz in a typical experiment. For example, in [IV] the coupling strength is $g_c \approx h \cdot 10$ MHz. The quasiparticle energy scale ζ determined by temperature remains unaffected by the change to the rotating frame. Even for temperatures as small as 30 mK the width ζ/h is of the order of several hundred MHz and thus comparable to or even larger than the coupling strength g_c . Thus, Rabi decay realizes a transition regime between dephasing and relaxation. Since the coupling is very small, Rabi decay is even closer to dephasing than to relaxation. Thus, for $g_c \gtrsim \zeta$ Rabi decay due to quasiparticles is given by the decay rate Eq. (4.60) with the substitution $E_{\text{tls}} \rightarrow g_c$. For $g_c \lesssim \zeta$ Rabi decay rates due to scattering quasiparticles can be obtained from the spin-echo dephasing rate Eq. (3.30) with the substitution $\omega_1 \rightarrow g_c$. For tunneling quasiparticles the spectral density $S(g_c)$ has to be evaluated numerically. In the bottom graph of Fig. 4.16 we show experimentally obtained data for Rabi decay together with fits to our theory [IV]. Fits to Rabi and relaxation decay rates yield identical TLS parameters within the error limits [IV].

4.3.8 Decoherence of superconducting qubits due to quasiparticles

Superconducting qubits are among the most promising candidates for a scalable quantum computer. Quasiparticles provide an inherent channel of decoherence for superconducting qubits. The results obtained for decoherence of TLS due to tunneling quasiparticles can be straightforwardly applied to superconducting qubits as well [I]. A superconducting qubit comprises at least one Josephson junction with tunneling Hamiltonian

$$H_T = \sum_{kq\sigma} g_{kq} e^{-i\varphi} (u_q \gamma_{q\sigma}^\dagger + \sigma v_q \gamma_{-q-\sigma}) (u_k \gamma_{k\sigma} + \sigma v_k \gamma_{-k-\sigma}^\dagger) + h.c., \quad (4.80)$$

The superconducting phase φ and its conjugate variable, the number of Cooper pairs \hat{n} describe the qubit dynamics. Thus, the tunneling Hamiltonian couples to the qubit via the phase φ accumulated by a tunneling quasiparticle. The resulting quasiparticle

spectral density for decoherence of a superconducting qubit is identical to Eq. 4.48 with the substitutions $4N_F\mathcal{V} \rightarrow E_J|z|^2/\Delta_{\text{bc}s}\pi$ and $\cos\varphi \rightarrow (\text{Re } z^2 - \text{Im } z^2)/|z|^2$. Here, E_J is the Josephson energy of the junction and $z = (\langle 1|e^{i\varphi}|1\rangle - \langle 0|e^{i\varphi}|0\rangle)/2$ is the matrix element of the tunnel operator between qubit states. With these substitutions all statements concerning decoherence of TLS due to tunneling quasiparticles can be applied directly to superconducting qubits. Especially, qubit Ramsey and spin-echo dephasing in the long and short time limit obeys the same time dependence as dephasing of a TLS.

4.4 Decoherence due to different sources of noise

Measurements on TLS inside a Josephson junction revealed unexpected behavior of decoherence rates of the TLS with the applied mechanical strain [III]. Spin-echo refocusing proved remarkably effective. Compared to Ramsey dephasing spin-echo dephasing times were increased by a factor of up to twenty-two. Additionally, the ratios Γ_e/Γ_r varied over a wide range for different TLS. These results suggest that TLS in the junction couple to strong quasi-static noise. Furthermore, the quasi-static noise strongly varies for different TLS suggesting that it arises from local perturbations and not from a global effect.

In this section we compare several microscopic models in order to explain these characteristics of decoherence of junction-TLS. We are looking for systems which provide a divergent spectral density at low frequencies and additionally vary for different TLS. The strong variation of decoherence rates between different TLS suggests that coupling to nearby secondary TLS induces these unexpected characteristics. Besides, TLS are known as a source of $1/f$ noise, i.e., they provide a divergent spectral density [122].

Another source of decoherence we analyze in this section are acoustic phonons. Phonons provide a channel of damping, i.e. relaxation, of TLS. This has been analyzed for example by Jäckle [112] and Anderson [36]. Phonon induced relaxation rates were confirmed experimentally for example by Black [123]. Phonons can also explain the distinct features found for the strain dependent relaxation rates suggesting coupling to some resonant modes.

In the previous section we have analyzed decoherence due to quasiparticles in great detail. Here, we comment on the possibility that quasiparticles can be responsible for the findings of the experiment.

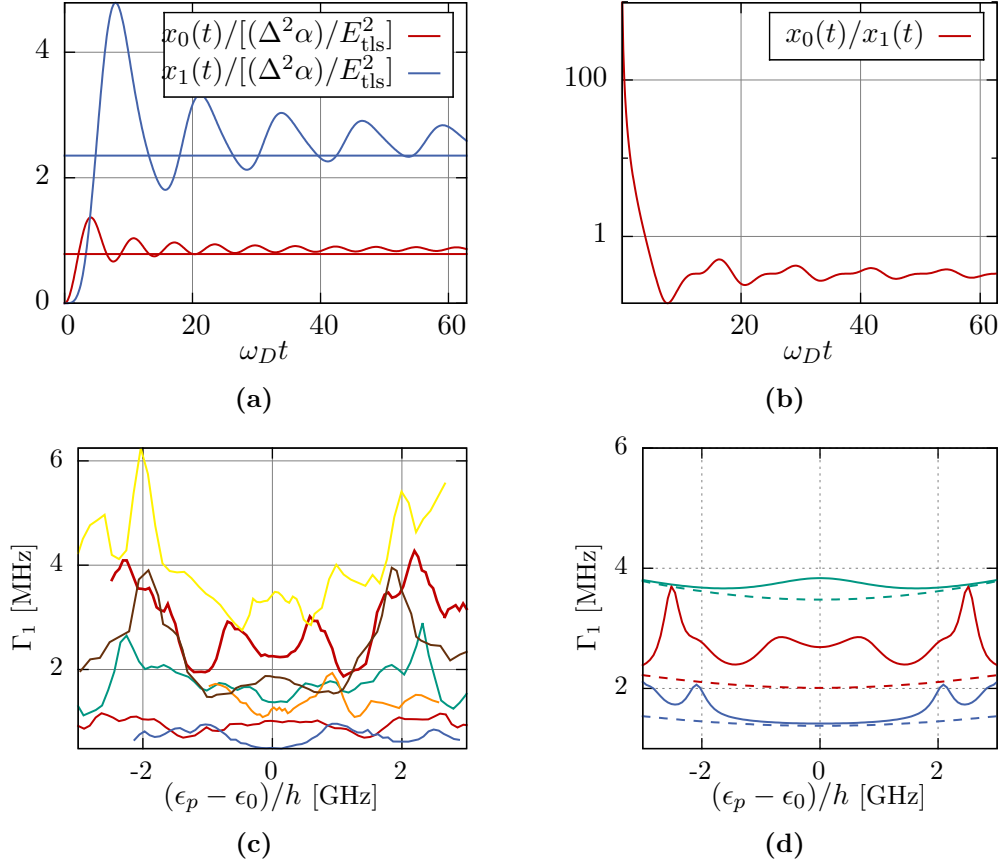


Figure 4.22: Decoherence induced by phonons. **a** Dephasing functions $x_0(t) \cdot E_{\text{tls}}^2/\alpha\Delta^2$ (red) and $x_1(t) \cdot E_{\text{tls}}^2/\alpha\Delta^2$ (blue) versus time normalized to the Debye frequency ω_D . This corresponds to a timescale of some femto-seconds. **b** Ratio x_0/x_1 vs time. Spin-echo dephasing increases for long times and surpasses Ramsey dephasing which is stronger for very short times of the order $t\omega_D \sim 1$. **c** Measured relaxation rates Γ_1 versus applied strain for several microscopic TLS. Data taken from [III]. Strain in arbitrary units and shifted to the symmetry point. **d** Phonon induced relaxation rates versus applied strain without resonant phonon modes (dashed) as well as with resonant phonon modes (solid). The phonons are characterized by $\alpha = 5 \cdot 10^{-9}\text{GHz}^{-2}$ and $\tilde{\alpha} = 0.5 \cdot 10^{-5}\text{GHz}$. Different colors correspond to different tunneling strength. The plot shows qualitative agreement with the experimentally observed rates.

4.4.1 Decoherence due to acoustic phonons

Phonons couple via the same mechanism to the TLS as does static mechanical strain. They provide an important damping mechanism for TLS in insulating materials [86]. In order to derive the form of the coupling between TLS and acoustic phonons we follow the derivation by Würger in reference [86]. Despite the disordered structure of the amorphous host material we can describe low-frequency vibrations in terms of harmonic oscillators. At position \mathbf{x} in the junction the vibrational amplitude reads as [124]

$$\mathbf{u}(\mathbf{x}) = \frac{1}{\sqrt{\mathcal{V}}} \sum_{\mathbf{k},s} \mathbf{e}_{\mathbf{k}s} \sqrt{\frac{1}{2\rho\omega_{\mathbf{k}s}}} \left[e^{i\mathbf{k}\cdot\mathbf{x}} b_{\mathbf{k}s} + e^{-i\mathbf{k}\cdot\mathbf{x}} b_{\mathbf{k}s}^\dagger \right], \quad (4.81)$$

where \mathcal{V} is the volume, ρ is the mass density of the host material, $\mathbf{e}_s(\mathbf{k})$ is the polarization vector of a mode with wave vector \mathbf{k} that belongs to branch s and has a frequency $\omega_{\mathbf{k}s}$. The TLS couple to the (local) strain tensor $\epsilon_{\mu\nu} = \frac{1}{2}(\partial_\mu u_\nu + \partial_\nu u_\mu)$:

$$\epsilon_{\mu\nu} = \frac{1}{\mathcal{V}} \sum_{\mathbf{k}s} \frac{\mathbf{e}_{s,\nu}(\mathbf{k})k_\mu}{\sqrt{2\rho\omega_{\mathbf{k}s}}} \left[i e^{i\mathbf{k}\cdot\mathbf{x}} b_{\mathbf{k}s} - i e^{-i\mathbf{k}\cdot\mathbf{x}} b_{\mathbf{k}s}^\dagger \right]. \quad (4.82)$$

In general two approximations to the coupling are made: Firstly, the tunnel matrix element Δ_0 is independent of the strain, and secondly, the change in the asymmetry is linearized [78]:

$$\Delta[\epsilon_{\mu\nu}] = \Delta + 2 \sum_{\mu\nu} \gamma_{\nu\mu} \epsilon_{\mu\nu} \approx \sum_s \gamma_s \epsilon_s. \quad (4.83)$$

In the last step we used that the disordered character of the solid hosting the TLS implies that no selection rules due to the tensorial character of the strain tensor arises. Thus, we replaced the tensor product with an average value γ_s for each branch. We place the TLS at the origin and evaluate the coupling at position $\mathbf{x} = 0$ to find the interaction between TLS and phonons [112]:

$$V = \sigma^z \sum_s \gamma_s \epsilon_s \equiv \sigma^z \frac{1}{2} \sum_{\mathbf{k}s} \lambda_{\mathbf{k}s} \left(i b_{\mathbf{k}s} - i b_{\mathbf{k}s}^\dagger \right) \quad (4.84)$$

The sum runs over two transverse and one longitudinal phonon branch and the coupling constants are defined as

$$\frac{1}{2} \lambda_{\mathbf{k}s} = \frac{1}{\sqrt{\mathcal{V}}} \frac{\gamma_s k}{2\rho\omega_{\mathbf{k}s}}. \quad (4.85)$$

The phonon spectral density is given by

$$J_\gamma(\omega) = \sum_s \gamma_s^2 \int dt e^{i\omega t} \langle [\epsilon_s(t), \epsilon_s(0)] \rangle = \frac{\pi}{2} \sum_{\mathbf{k}s} \lambda_{\mathbf{k}s}^2 \delta(\omega - \omega_{\mathbf{k}s}). \quad (4.86)$$

It is related to the symmetrized spectral density S_γ of the noise operator $\frac{i}{2} \sum \lambda_{ks} (b_{ks} - b_{ks}^\dagger)$ as $S_\gamma(\omega) + S_\gamma(-\omega) = J_\gamma(|\omega|) \coth(\beta\omega/2)$. Using Debye's approximation for acoustic phonons $\omega_{\mathbf{k}s} = v_s k$ we find

$$J_\gamma(\omega) = \left(\frac{\gamma_t^2}{v_t^5} + \frac{2\gamma_l^2}{v_l^5} \right) \frac{\omega^3}{2\pi\hbar\rho} = \pi\alpha\omega^3 = \pi\bar{\alpha}(\hbar^2/k_B^2)\omega^3. \quad (4.87)$$

Here, $\alpha = \sum_s \gamma_s^2 / (4\pi^2 \rho c_s^5)$ is a material dependent parameter. Black and Halperin estimated the deformation potential in Suprasil W. Their experiments yielded $\frac{1}{2}\gamma_t = \gamma_l = 1.6$ eV [123]. For aluminum oxide the material dependent parameters are $\rho \approx 4\text{g/cm}^3$, $c_l \approx 9.9\text{km/s}$, $c_t \approx 5.8\text{km/s}$ and $\gamma \sim \mathcal{O}(1\text{eV})$. This yields an effective coupling strength $\alpha \approx 5 \cdot 10^{-10}\text{GHz}^{-2}$. The cubic spectral density doesn't induce an infrared singularity and tends to zero for small frequencies. Thus, we expect weak dephasing due to acoustic phonons. On the other hand the form of the spectral density causes strong enhancement of damping with temperature. There is no well defined small parameter. But the temperature scale

$$T_0 = (2\pi^2\bar{\alpha})^{-1/2} \sim 1 - 100 \text{ K} \quad (4.88)$$

provides a useful parameter to specify ranges of weak and strong coupling [86]. Since $T_0 \propto \gamma^{-1}$ a small temperature T_0 corresponds to a large coupling potential γ . There are four relevant parameters in determining the effective coupling strength: Δ_0 , T , T_0 and the Debye temperature Θ . In general, $\Delta_0 \ll k_B\Theta \approx 400$ K in aluminum oxide. The low and intermediate temperature range $k_B T < \Delta_0$ and $\Delta_0 < k_B T < k_B T_0$ relevant for coherent TLS measurements are reasonably well described with lowest order perturbation theory.

The phonon induced TLS relaxation rates within golden rule are given by [36, 112]

$$\begin{aligned} \Gamma_1 &= \frac{\Delta_0^2}{E_{\text{tls}}^2} (S_\gamma(E_{\text{tls}}) + S_\gamma(-E_{\text{tls}})) = \frac{\Delta_0^2}{E_{\text{tls}}^2} J(E_{\text{tls}}) \coth \frac{E_{\text{tls}}}{2k_B T} \\ &\approx \pi\alpha E_{\text{tls}} \Delta_0^2. \end{aligned} \quad (4.89)$$

The factor $\propto (\Delta_0^2/E_{\text{tls}}^2)$ in front of the spectral density stems from transforming the dipole interaction $\propto \sigma^z$ into the energy-basis of the TLS. The strain dependence of the relaxation rate due to phonons enters only through the energy splitting $E_{\text{tls}}(\epsilon)$ which yields $\Gamma_1(\epsilon) = \pi\alpha\Delta_0\sqrt{1 + (\epsilon - \epsilon_0)^2/\Delta_0^2}$. For a TLS tunneling rate $\Delta_0 \sim h \cdot 7$ GHz the decay rate is of the order of $\Gamma_1 \sim 0.1\sqrt{1 + (\epsilon - \epsilon_0)^2/\Delta_0^2}\text{MHz}$. This form of the relaxation rate well describes the general trend of the relaxation rate found in the experiment.

However, the TLS relaxation rates found in the experiment show distinct resonances.

These resonances appear symmetric in strain ruling out secondary TLS as candidates for the resonant coupling. Another possible explanation is that the TLS are in resonance with some phonon modes. For a phonon mode with inverse lifetime Γ_γ and frequency ω_γ we find an additional contribution of the form

$$\Gamma_{1,\gamma,\text{res.}} = \tilde{\alpha} \frac{\Delta_0^2 \omega_\gamma}{E_{\text{tls}}^2} \frac{\Gamma_\gamma}{(E_{\text{tls}} - \omega_\gamma)^2 + \Gamma_\gamma^2}. \quad (4.90)$$

The coupling $\tilde{\alpha} = \gamma^2/(\mathcal{V}2\rho c^2)$ depends on the velocity of sound c , mass density ρ , and the deformation potential γ . The volume \mathcal{V} can be estimated by the velocity and lifetime of the phonon as $\mathcal{V} \sim (c/\Gamma_\gamma)^3$. In Fig. 4.22d we show strain dependent TLS relaxation rates $\Gamma_{1,\gamma} + \Gamma_{1,\gamma,\text{res.}}$. Coupling to a homogeneous bath of phonons together with coupling to some resonant modes well describes the distinct resonances observed in the experimentally obtained rates as shown in Fig.4.7.

Since the spectral density tends to zero with ω^3 we expect small dephasing due to phonons. Especially for Ramsey dephasing which measures the spectral density at $\omega \approx 0$. Since the spectral density rapidly increases with frequency we expect a larger dephasing rate for spin-echo which measures the density at higher frequencies $\omega \sim \mathcal{O}(\text{MHz})$. Compared to the Debye frequency this is a very small frequency scale and spin-echo remains small, too. Using Eq. (3.28) we find the Ramsey and spin-echo dephasing functions

$$\frac{2E_{\text{tls}}^2}{\alpha\Delta^2} x_0(t) = \omega_D^2 + \frac{4 \sin^2 \frac{\omega_D t}{2}}{t^2} - \frac{2\omega_D \sin \omega_D t}{t} \quad (4.91)$$

$$\frac{2E_{\text{tls}}^2}{\alpha\Delta^2} (x_1(t) + x_0(t)) = 4 \left[\omega_D^2 + \frac{\sin^2 \frac{\omega_D t}{4}}{t^2} - \frac{4\omega_D \sin \frac{\omega_D t}{2}}{t} \right], \quad (4.92)$$

where ω_D is the Debye frequency. In aluminum the Debye frequency is $\omega_D \approx 5.6 \cdot 10^4$ GHz. We note that for very short times $\omega_D t \lesssim \pi$ Ramsey decay is faster than spin-echo, $x_0(t)/x_1(t) > 1$ while for longer times we find $x_1 > x_0$. Furthermore, we find that for short times the Ramsey rate is quadratic in time $x_0 \sim t^2$ while $x_1 \sim t^4$. For experimentally relevant times we find $\lim_{t \rightarrow \infty} x_1 = \lim_{t \rightarrow \infty} 3x_0 = 3\alpha(\epsilon/E_{01})^2 \omega_D^2$ and hence $x_0/x_1 = 1/3$, i.e. the ratio between spin-echo and Ramsey is small and reversed because spin-echo dephasing is stronger than free Ramsey dephasing.

In conclusion, phonon induced relaxation is most likely the dominant relaxation process in the experiment while phonon induced dephasing is negligible.

4.4.2 Decoherence due to TLS

A TLS in an amorphous host material induces an elastic strain field which distorts the equilibrium positions of surrounding atoms and depends on the current state of the

TLS. Other TLS couple to this perturbation of the strain field according to Eq. (4.83) and their energy splitting becomes sensitive to the state of the first TLS. This induces a long range dipole-dipole interaction between TLS due to the exchange of phonons similar to the exchange of virtual photons in electric dipole-dipole interaction. For two TLS coupling to the phonon field according to Eq. (4.84) the effective interaction mediated through acoustic phonons is given by [125]

$$H_{\text{int}} = -\frac{1}{2}U_{12}\sigma_1^z\sigma_j^z. \quad (4.93)$$

The interaction between two TLS decays with the distance r_{12} between TLS as $U_{12} = u_{12}/r_{12}^3$ [126]. The angle-averaged coupling strength is obtained as $\langle |u_{12}| \rangle = U_0 \approx \gamma^2/\rho c^2$ with averaged deformation potential γ and averaged velocity of sound c [127]. For an ensemble of TLS in the standard tunneling model with probability P_0 to find a TLS with parameters in the range $[\Delta, \Delta + d\Delta]$ and $[\lambda, \lambda + d\lambda]$, the dimensionless parameter $\chi = P_0 U_0 \sim 10^{-3}$ characterizes the relative coupling strength between TLS and the energy splitting of TLS [127]. The effective Hamiltonian of the ensemble of TLS that inherits the interaction between TLS reads as

$$H = \sum_i \left(\frac{1}{2}\Delta_i\sigma_i^z + \frac{1}{2}\Delta_{0,i}\sigma_i^x \right) + \frac{1}{2} \sum_{i \neq j} U_{ij}\sigma_i^z\sigma_j^z$$

Each TLS still couples to the bath of phonons. The phonons induce random state flips for each TLS with rates described in the previous section. We pick a certain TLS with energy splitting in the range of $E_{\text{tls}} \sim h \cdot 7$ GHz. This energy range corresponds to the TLS that couples to the qubit in a resonant way and has been analyzed in the experiment by Lisenfeld. The other TLS act as a bath for this particular TLS. The coupling of our specific TLS which we label i to the remaining TLS reads as

$$V_i = \sigma_i^z \sum_j U_{ij}\sigma_j^z = \sigma_i^z \sum_{j \neq i} U_{ij} \left[\frac{\Delta_j}{E_{\text{tls},j}}\tau_j^z - \frac{\Delta_{0,j}}{E_{\text{tls},j}}\tau_j^x \right]. \quad (4.94)$$

where we changed to the eigenbasis of the bath-TLS. In the previous section we have demonstrated that phonons induce state flips for each TLS while they do not contribute to dephasing. In order to calculate the spectral density of the bath of TLS we only take leading order in the TLS coupling into account. In this approximation TLS induced decoherence rates in the spectral density of the bath of TLS can be neglected. The spectral density of the bath of TLS comprises the contributions of individual TLS which can be calculated with the quantum regression theorem [66, 128]. Taking into account the decoherence rates of the individual TLS the spectral density of the bath

of TLS reads as [128]

$$\begin{aligned}
 S_{\text{tls}}(\omega) = \sum_{j \neq i} S_j(\omega) = \frac{1}{\pi} \sum_{j \neq i} U_{ij}^2 \left[\frac{\Delta_j^2}{E_j^2} \frac{\Gamma_{1,j}}{\omega^2 + \Gamma_{1,j}^2} \frac{1}{\cosh^2 \frac{E_j}{2k_B T}} \right. \\
 + \frac{\Delta_{0,j}^2}{E_j^2} \frac{\Gamma_{2,j}}{\Gamma_{2,j}^2 + (\omega + E_j)^2} \frac{1}{1 + e^{E_j/k_B T}} \\
 \left. + \frac{\Delta_{0,j}^2}{E_j^2} \frac{\Gamma_{2,j}}{\Gamma_{2,j}^2 + (\omega - E_j)^2} \frac{1}{1 + e^{-E_j/k_B T}} \right] \quad (4.95)
 \end{aligned}$$

For the sake of notational brevity we denote the energy splittings of TLS that belong to the bath as E_j and skip the subscript 'tls'. The first term in the square brackets is symmetric in frequency and describes classical noise [128]. For TLS with energies $E_j > k_B T$ this contribution is suppressed by the thermal factor $\propto \cosh^{-2} E_j/2k_B T$. The second term describes emission of an excitation from TLS j and is suppressed by temperature, too. The last term describes absorption of an excitation by TLS j and induces decay of TLS i . As we have shown in previous sections pure dephasing due to phonons remains small and the decoherence rate is dominated by relaxation, $\Gamma_{2,j} \approx \Gamma_{1,j}/2$.

Similar to Shnirman et al. we find TLS induced relaxation rate of TLS 'i' [128]

$$\Gamma_{1,i} \approx \frac{\Delta_{0,i}^2}{E_{\text{tls},i}^2} \sum_j U_{ij}^2 \frac{\Delta_{0,j}^2}{E_j^2} \frac{\Gamma_{2,j}}{\Gamma_{2,j}^2 + (E_{\text{tls},i} - E_j)^2}.$$

The strain dependence is determined by the pre-factors $\propto \frac{1}{E_{\text{tls},i}^2} \cdot \frac{1}{E_j^2}$. Since every TLS differently depends on strain different TLS are tuned into resonance with TLS i and away again while the applied strain changes. This could explain resonances in the TLS relaxation rate. However, due to the strain dependence of all TLS energy splittings the resulting relaxation rate would not be symmetric in strain. With this, we rule out TLS induced relaxation as the main contribution to the relaxation rate.

The low-frequency sector of the spectral density of the ensemble of TLS is dominated by the first term in Eq. (4.95). Only TLS with energies $E_{\text{tls}} \ll k_B T$ contribute to the low-frequency spectral density. These TLS randomly switch between excited and ground state and can be understood as a classical telegraph noise. The quantum operators τ^z behave as a classical random variable with values $\tau^z(t) = \pm 1$. These two-level fluctuators (TLF) dominate pure dephasing. In order to analyze dephasing due to the TLF we have to distinguish two different situations: dephasing to a self-averaging, i.e. Gaussian, ensemble and dephasing due to strong coupling to a single TLF. At first, we investigate dephasing due to an ensemble of TLF. From this considerations one finds a parameter which determines whether the ensemble actually is self-averaging

or not [122]. Following these calculations we provide the theory of dephasing due to a strongly-coupled individual TLF.

Ensemble of TLF A large ensemble of TLF is characterized by the distribution of a set of parameters. These parameters are the tunneling amplitude Δ_0 , the energy splitting E_{tls} , and the coupling U to the TLS under consideration. Following the STM we assume a uniform distribution of the Gamow parameter λ and the asymmetry Δ , $P(\lambda, \Delta) = P_0$. The corresponding distribution of energy splittings and tunneling amplitudes is given by $P(E, \Delta_0) = P_0 E / \Delta_0 \sqrt{E^2 - \Delta_0^2}$. The coupling between TLS i and j depends on the distance between the TLS with a power law behavior $U_{ij} \propto r_{ij}^{-b}$. In a d -dimensional system this yields a probability distribution for the coupling strength $P(U) \propto U^{-(1+d/b)}$ [122]. For a coupling mediated by phonons this yields a distribution $P(U) \propto U^{-(1+3/d)}$. For a large ensemble with continuous and dense parameters we can replace the sum with an integral over parameters to find the spectral density of the bath of TLS

$$S_{\text{tls}}(\omega) = \frac{1}{\pi} \int dE d\Delta_0 dU P(E, \Delta_0) P(U) U^2 \frac{\Delta^2}{E_{\text{tls}}^2} \frac{\Gamma_1}{\omega^2 + \Gamma_1^2} \frac{1}{\cosh^2 \frac{E_{\text{tls}}}{2k_B T}} \quad (4.96)$$

Assuming phonon induced decay rates $\Gamma_1(E, \Delta_0) \approx \pi \alpha E \Delta_0^2$, see Eq. (4.89), we find the spectral density at zero temperature and for small frequencies

$$S(\omega) = \frac{4\langle U^2 \rangle P_0}{\pi} \int_{\Delta_{0,\text{ir}}}^{\Delta_{0,\text{uv}}} d\Delta_0 \int_{E_{\text{ir}}(\Delta_0)}^{E_{\text{uv}}(\Delta_0)} dE \frac{1}{\Delta_0} \frac{\sqrt{4E^2 - \Delta_0^2}}{E} \frac{\alpha \Delta_0^2 E}{(\alpha \Delta_0^2 E)^2 + \omega^2}. \quad (4.97)$$

Here, $E_{\text{ir/uv}} = \sqrt{\Delta_{\text{ir/uv}}^2 + \Delta_0^2}$ is the lower and upper cut-off energy determined by the low-energy (infrared) and high-energy (ultra violet) cut-off of the asymmetry Δ . The averaged interaction is defined as $\langle U^2 \rangle = \int dU P(U) U^2$. The integration over excitation energies E yields $S_{\text{tls}}(\omega) = S_0 + S_1(\omega)$ with a white noise contribution

$$S_0 = \frac{4\langle U^2 \rangle P_0}{\pi} \int_{\Delta_{0,\text{min}}}^{\Delta_{0,\text{max}}} d\Delta_0 \frac{2}{\alpha \Delta_0^3} \log \frac{2E_{\text{max}}(\Delta) + \Delta_{\text{max}}}{2E_{\text{min}}(\Delta) + \Delta_{\text{min}}} \quad (4.98)$$

and a frequency dependent contribution

$$S_1(\omega) = -\frac{4\langle U^2 \rangle P_0}{\pi} \int_{\Delta_{0,\min}}^{\Delta_{0,\max}} d\Delta_0 \frac{\sqrt{4\omega^2 + \alpha^2 \Delta_0^6}}{\alpha \omega \Delta_0^2} \times \arctan \frac{(E_{\max}(\Delta_0) + E_{\min}(\Delta_0)) \sqrt{4\omega^2 + \alpha^2 \Delta_0^6}}{1 - E_{\min}(\Delta_0) E_{\max}(\Delta_0) \sqrt{4\omega^2 + \alpha^2 \Delta_0^6}}. \quad (4.99)$$

Dephasing experiments measure the spectral density for small frequencies $\omega \ll 1$. In this regime the spectral density of the bath of TLS is proportional to $1/\omega$, $S_{\text{tls}}(\omega) = S_0 + \frac{S_{1/\omega}}{\omega}$. Here, the energy scale characterizing the 1/f noise is given by

$$S_{1/\omega} = \frac{4\langle U^2 \rangle P_0}{\alpha \pi} \int_{\Delta_{0,\min}}^{\Delta_{0,\max}} d\Delta_0 \arctan \frac{\alpha \Delta_0^3 (E_{\max}(\Delta_0) - E_{\min}(\Delta_0))}{\alpha \Delta_0^3 E_{\min}(\Delta_0) E_{\max}(\Delta_0) - 1}. \quad (4.100)$$

For a 1/f-noise Ramsey and spin-echo dephasing functions are given by [122, 129]

$$x_0(t) = t^2 \frac{\Delta^2}{E_{\text{tls}}^2} \frac{S_{1/\omega}}{2} \left(\ln \frac{1}{\omega_{\text{ir}} t} + \gamma_e - \frac{3}{2} \right) \quad (4.101)$$

$$x_1(t) = t^2 \frac{\Delta^2}{E_{\text{tls}}^2} \frac{S_{1/\omega}}{2} \ln 2 \quad (4.102)$$

which can describe neither the large ratios x_1/x_0 up to 22 nor the huge variation of the ratios ranging from one up to 22. The ratio depends logarithmically on the infrared cutoff ω_{ir} , where the infrared cut-off is determined by the experimental setup but doesn't vary for different TLS.

Assuming that the TLS do not decay due to phonon interaction but with a different mechanism, e.g. other TLS or quasiparticles, we have to slightly modify the calculation. Following the discussion given by Schön et al. in [122] we assume a distribution of coupling strengths U and switching rates Γ_1 on the domain $[U_{\min}, \infty) \times [\Gamma_{\min}, \Gamma_{\max}]$ for N fluctuators as

$$P(U, \Gamma_1) = \frac{c}{\Gamma_1} \frac{\mu \eta^\mu}{U^{1+\mu}} \quad (4.103)$$

where $\mu = d/b$ with dimension d and $U \propto r^{-b}$ and $\eta = g_{\min} N^{1/\mu}$ [122]. Following the discussion in [122] we can distinguish $\mu < 2$ and $\mu > 2$. In the first case the integral over coupling strengths is dominated by the upper limit and dephasing is dominated by few fluctuators which strongly couple to the TLS under consideration. We discuss this situation in the next section. On the other hand for $\mu > 2$ the ensemble is self-averaging and one can treat the TLS as a Gaussian ensemble. For this case one obtains

for the spectral density

$$S(\omega) = \frac{\Delta^2}{E_{\text{tls}}^2} A \begin{cases} \frac{1}{\Gamma_{\min}} - \frac{1}{\Gamma_{\max}}, & \omega \ll \Gamma_{\min} \\ \frac{\pi}{2\omega}, & \Gamma_{\min} \ll \omega \ll \Gamma_{\max} \\ \frac{\Gamma_{\max} - \Gamma_{\min}}{\omega^2}, & \Gamma_{\max} \ll \omega \end{cases} \quad (4.104)$$

where the pre-factor $A = A(\epsilon_p)$ is obtained from integration over the TLF ensemble and is a function of the applied mechanical strain ϵ_p .

We find that the ensemble of TLS is $1/f$ like for intermediate to small frequencies and approaches white noise behavior for even smaller frequencies. For spin-echo and Ramsey dephasing typical frequencies are of the order of several MHz which corresponds to the intermediate regime, i.e. $1/f$ -like behavior. We define the dephasing time for a protocol with dephasing function $x_n(t)$ as the time where $x(t_n) = 1$ holds. Assuming that Ramsey dephasing corresponds to the limiting case $\omega \ll \Gamma_{\min}$ while spin-echo dephasing corresponds to the $1/f$ -like scenario, we find Ramsey and spin-echo dephasing times according to

$$T_r = \frac{E_{\text{tls}}^2}{\Delta^2} \frac{\Gamma_{\min}}{A} \quad (4.105)$$

$$T_e = \frac{E_{\text{tls}}}{\Delta} \frac{1}{\sqrt{A \ln 2}} \quad (4.106)$$

In this limiting case Ramsey and spin-echo rates have a different strain-dependence. While the Ramsey dephasing time depends on the matrix element E_{tls}/Δ squared, the spin-echo time depends linearly on the matrix element. This feature can actually be seen in the strain-dependent rates presented in Fig. 4.7 but with exchanged roles: linear strain-dependence for Ramsey dephasing. However, the different strain dependence is more likely due to another mechanism: strong-coupling to a single TLF. We do not expect that different regimes for Ramsey and spin-echo dephasing are realized. In fact, the ensemble of TFL induces $1/f$ noise and we conclude that dephasing due to a self-averaging ensemble cannot explain the experimental results.

Strong Coupling to a Dominant TLF In three dimensions and phonon-mediated interaction we find $\mu = 1$. Thus, the ensemble of TLF is not self-averaging [122]. A single TLF in spacial proximity to the TLS under consideration dominates dephasing. This spacial proximity of TLS and TLF induces a strong coupling. Due to this strong coupling we cannot treat dephasing to the dominant TLF as a Gaussian noise. Instead we treat the strongly coupled TLF as a classical random telegraph noise with switching rate γ between the states. For TLS with energy $E \ll k_B T$ at the experimental temperature $T = 35$ mK, phonon induced switching rates obtained from Eq. 4.89 are

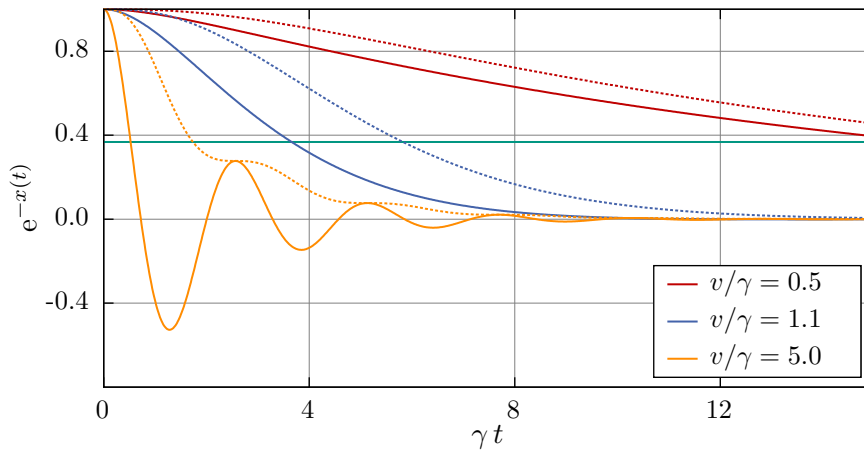


Figure 4.23: Ramsey (solid) and spin-echo (dashed) signal $e^{-x_N(t)}$ due to a single TLF in the weak (red), intermediate (blue) and strong (orange) coupling regime versus time normalized to the switching rate γ . The green horizontal line denotes $1/e$. The intersection between the signal and this line corresponds to the dephasing time shown in Fig. 4.24.

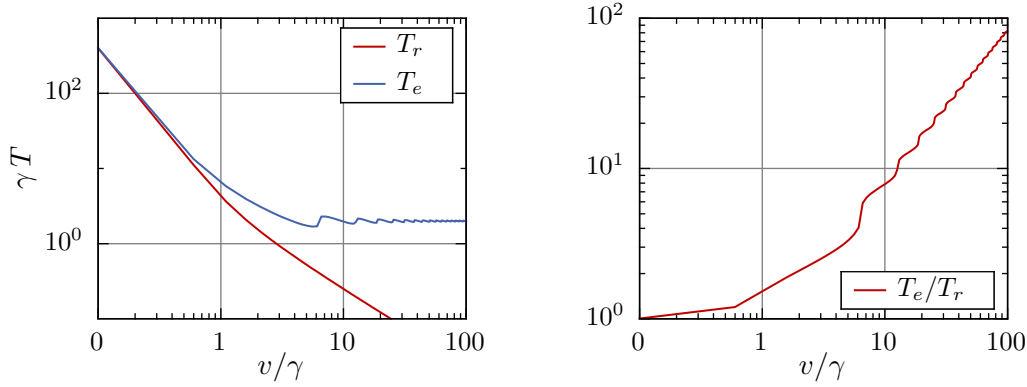
of the order of several kHz. Since $T \gg E_{\text{tlf}}$ the switching rates from ground to excited state and vice versa are identical. They can be related to the relaxation rate of the TLF as $\gamma = \Gamma_1/2$. Dephasing due to a classical non-Gaussian noise can be obtained from the phase memory functional [130]

$$\Phi(t) = \left\langle \exp \left[i \int_0^t dt' g_N(t') \chi(t') \right] \right\rangle, \quad (4.107)$$

which accounts for the random phase accumulated through the random noise fluctuations. Here, $g_N(t)$ is a filter function that depends on the measurement protocol and $\chi(t) = \pm U_{12} \frac{\Delta}{E_{\text{tlf}}}$ is a random variable accounting for the random fluctuations of the TLF. In order to calculate the phase memory we have to integrate over all possible histories of the random variable $\chi(t)$ [131]. We find the Ramsey and spin-echo dephasing functions due to strong coupling with the single TLF j as calculated before by Paladino et al. and Galperin et al. [122, 130, 132]:

$$x_0^{(j)}(t) = \frac{1}{2} \gamma_j t - \log \left[\cos \left(\frac{u_j}{2} \gamma_j t \right) + \frac{1}{u_j} \sin \left(\frac{u_j}{2} \gamma_j t \right) \right] \quad (4.108)$$

$$x_1^{(j)}(t) = \frac{1}{2} \gamma_j t - \log \left(1 + \frac{1}{u_j} \sin \left(\frac{u_j}{2} \gamma_j t \right) + \frac{1}{u_j^2} \left(1 - \cos \left(\frac{u_j}{2} \gamma_{1,j} t \right) \right) \right). \quad (4.109)$$



(a) Ramsey T_r and spin-echo T_e dephasing times

(b) Ratio T_e/T_r

Figure 4.24: (a) Spin-echo T_e and Ramsey T_r dephasing times due to a single TLF with coupling strength v and switching rate γ . (b) Ratio between Ramsey dephasing time T_r and spin-echo dephasing time T_e due to a single TLF versus coupling strength v .

Here, $u_j = \sqrt{\left(v_j/\gamma_{1,j}\right)^2 - 1}$ and $v_j = \frac{\Delta}{E_{\text{tls}}} \frac{\Delta_j}{E_{\text{tlf},j}} U_j$. The effective coupling strength is determined by the dimensionless parameter v_j/γ_j . In Fig. 4.23 we show the signal $e^{-x_N(t)}$ due to a single TLS. The overall decay is given by the rate $\gamma/2$ while the log-contribution induces deviations from this general trend. We show the ratio between Ramsey and spin-echo dephasing times in Fig. 4.24. The dephasing times are obtained from the relation $x_n(T) = 1$. The graph shows that dephasing due to a single strong-coupling TLS can explain the strong effect of spin-echo refocusing. If several TLS are coupled to the TLS of interest with similar coupling strength the final dephasing function is the sum of individual contributions:

$$x_{0,1}(t) = \sum_{j \in \text{strong}} x_{0,1}^j(t) \quad (4.110)$$

M. Schechter and S. Matityahu developed a more detailed theory. They argued that for $v \gg \gamma$ and slow switching rates $\gamma \sim 1$ kHz, the signal $e^{-x(t)}$ is dominated by the log-contribution of the dephasing functions for relevant times $t \sim 1 \mu\text{s}$. In the limit $v \gg \gamma$ this yields

$$e^{-x_0(t)} \approx \cos \frac{vt}{2} \quad (4.111)$$

$$e^{-x_1(t)} \approx 1. \quad (4.112)$$

For $vt < 1$ this yields $\Gamma_r \approx v/\sqrt{8}$ and $\Gamma_e \approx 0$. Ramsey dephasing due to a single strongly coupled TLS is proportional to the TLS asymmetry Δ/E_{tls} . Thus, the matrix element is linear in the applied strain. They calculated the ensemble average over the

strong coupling dephasing functions Eq. (4.109) in two and three dimensions. They found that while Ramsey-dephasing is indeed not self-averaging, spin-echo dephasing due to the ensemble of TLS is self-averaging. With this, they found even higher ratios than in the experiment [133]. This suggests, that another source of decoherence is present [III]. We explain this by the coupling to non-equilibrium quasiparticles in the sample.

4.4.3 Quasiparticle induced decoherence

In section 4.3 we analyzed decoherence due to non-equilibrium quasiparticles. For scattering quasiparticles from one lead we found the Ramsey and spin-echo dephasing rates

$$\Gamma_r \approx \frac{\Delta^2}{E_{\text{tls}}^2} \frac{1}{\tau_0} \gamma_l^2 \frac{\zeta f_{0,l}}{\Delta_{\text{bcs}}} \quad (4.113)$$

$$\Gamma_e \approx \frac{\Delta^2}{E_{\text{tls}}^2} \frac{1}{\tau_0} \gamma_l^2 \frac{\zeta f_{0,l}}{\Delta_{\text{bcs}}} \left(1 + \frac{\omega_1}{\zeta}\right). \quad (4.114)$$

The width of quasiparticles is determined by the effective temperature $\zeta = k_B T_{\text{eff}}$. In these equations, γ_l is the effective coupling strength to lead l and not the deformation potential of a longitudinal phonon mode. Dephasing due to quasiparticles is proportional to $\Delta^2/E_{\text{tls}}^2$. Thus, for small mechanical strain the rate is proportional to the square of the applied strain, $\Gamma_{r,e} \propto (\epsilon_s - \epsilon_0)^2$. This corresponds to the additional white noise found in the spin-echo dephasing rates in [III]. In the experiment a white noise contribution $\Gamma_e = A\Delta^2/E_{\text{tls}}^2$ was found with $A \sim 0 - 14 \mu\text{s}^{-1}$. The typical time-scale of the quasiparticle induced dephasing rates assuming typical non-equilibrium quasiparticle densities is of the same order as the parameter A . Thus, non-equilibrium quasiparticles likely are responsible for the additional white-noise-like contribution.

Calculating the ratio between quasiparticle induced spin-echo and Ramsey dephasing in the long time limit we find

$$\frac{x_0(t)}{x_1(t)} = \begin{cases} 1, & \cos \varphi = 1 \\ 2, & \text{else} \end{cases}. \quad (4.115)$$

For quasiparticle induced dephasing the spin-echo protocol is not as efficient as was measured in the experiment. This rules out quasiparticles as the main source of decoherence at low temperatures.

5 Chapter 5

Conclusion

Simulating large quantum mechanical systems using quantum simulators promises a wide range of applications from the simulation of molecules and solids to interesting phenomena in strongly correlated spin systems and other quantum systems. Thus, research on quantum simulation is amongst the most active and exciting fields in physics. Many proof-of-principle experiments have already demonstrated elementary quantum simulations of small quantum mechanical systems using different physical realizations [13, 20, 21, 25, 27, 134], while an increasing number of proposals suggesting further experiments are being published [15, 61, 67, 135]. The advance in qubit technology [33] regularly extends the possible applications of up-to-date quantum simulators.

Nonetheless, many obstacles are barring the way to large scale quantum simulators which will be able to tackle problems of physically relevant size. One of the major challenges is the effect of decoherence [32, 136]. Experimental imperfections in control and read-out as well as undesired interactions with the environment induce errors into quantum simulations. These errors distort results and raise questions on the reliability of quantum simulations. Consequently, understanding sources and effects of decoherence is of great importance in order to avoid errors and to develop reliable quantum simulators.

This thesis contributes to a better understanding of decoherence from two perspectives. Firstly, sources of decoherence in superconducting circuits were analyzed in detail in chapter 4, namely microscopic two-level systems and superconducting quasiparticles. Secondly, a theoretical method suitable to dealing with quantum simulators comprising large numbers of qubits subject to noise was developed in chapter 2.

Microscopic two-level systems that arise from bistable defects are not only responsible for universal low-temperature properties of amorphous materials [35, 36], but they are also one of the major sources of decoherence in superconducting circuits. Despite extensive research the microscopic nature of these two-level systems is not fully under-

stood yet. In the past, experiments were limited to measurements on large ensembles of two-level systems.

The recently demonstrated coherent control of individual two-level systems using superconducting qubits allows for very detailed measurements on individual two-level systems [42]. Coherence time measurements yield information about the coupling of two-level systems to their environment, from which conclusions about their microscopic properties and their surroundings can be drawn. In chapter 4 we analyzed decoherence of individual two-level systems residing in the amorphous aluminum oxide layer of a Josephson junction due to coupling to several sources of noise. The Josephson junction comprises an amorphous aluminum oxide layer which is sandwiched between two superconducting aluminum electrodes (leads). Our theoretical analysis was motivated by experiments by J. Lisenfeld [III, 43] and A. Bilmes [IV]. In these experiments the dependence of decoherence of two-level systems on strain, on temperature, and the dependence on the density of quasiparticles in the superconducting aluminum were measured.

Non-equilibrium quasiparticles, that are present even at low temperatures, are a well known source of decoherence in superconducting qubits [I, 80, 99, 102, 107]. Similar to metallic glasses where conduction electrons provide an important damping channel for two-level systems [44], we expect influence of quasiparticles on two-level systems in the junction. In section 4.3 we developed a detailed theory of the interaction of two-level systems residing in the amorphous layer of a Josephson junction with quasiparticle excitations in the superconducting leads.

The interaction between a two-level system and quasiparticles exponentially decays with the distance of the two-level system from the respective junction edges. Consequently, for a two-level system closer to one edge, scattering with quasiparticles from the lead further away and interaction with tunneling quasiparticles is strongly suppressed. We found that the relaxation rates and Rabi-decay rates of two-level systems due to quasiparticles are proportional to the quasiparticle densities in the leads in vicinity of the junction and proportional to the respective coupling strength. Our theoretically obtained Rabi- and relaxation rates fit well to the rates experimentally obtained in reference [IV]. The quasiparticle densities are suppressed by the superconducting gap but increase exponentially with the temperature. This strong temperature dependence of relaxation caused by quasiparticles explains the temperature dependence of two-level systems relaxation rates observed in an experiment by J. Lisenfeld [43].

The characteristics of the relaxation rate due to quasiparticles, i.e., strong dependence on the position of the two-level system relative to the junction edges and dependence on the individual quasiparticle densities in the different leads, allows for new experiments to analyze, for example, the spatial distribution of two-level systems

inside the junction by selective quasiparticle injection in one of the leads. Indeed, in an experiment by A. Bilmes quasiparticles were created in the superconducting aluminum layers either by heating or by injection through a SQUID [IV]. The observed relaxation and Rabi decay rates showed a striking difference between injected and thermally created quasiparticles: rates due to injected quasiparticles were always smaller than rates due to thermally created quasiparticles. Analyzing the diffusion and recombination processes of quasiparticles on their way from the injection-SQUID to the junction, we found an imbalance between quasiparticle densities on both sides of the junction. Together with the exponential suppression of coupling to one of the leads this explains the striking differences between the decoherence rates. We conclude that two-level systems preferably are created during a certain fabrication process and are mainly located close to one of the junction edges.

The spectral density of tunneling quasiparticles diverges for small frequencies. Since dephasing is a process that is sensitive to the low-frequency spectral density this divergent behavior leads to strongly enhanced dephasing. We found that dephasing due to quasiparticles follows a decay law of the form $\rho_{01}(t) \propto e^{-x(t)}$, with the protocol-dependent 'dephasing function' $x(t)$. The dephasing functions have a non-trivial time dependence. Using a diagrammatic approach we calculated dephasing functions for the Ramsey protocol (free induction decay) and the spin-echo protocol. For dephasing due to tunneling quasiparticles the time dependence of the dephasing function changes from a square-root like behavior $x(t) \sim t^{3/2}$ for short times to a $t \log t$ -behavior for long times. The characteristic time scale of the quasiparticles is determined by their effective temperature, $t_0 \approx \hbar/k_B T$. The theory for dephasing of a two-level system due to tunneling quasiparticles applies for microscopic two-level systems as published in [II] but also to superconducting qubits as published in [I]. The coupling-matrix elements between qubit states and the tunneling Hamiltonian herein replace the interaction between microscopic two-level system and quasiparticles. We note, that for scattering quasiparticles the spectral density remains finite at small frequencies and the square-root-like time dependence transforms into typical exponential time dependence $\Gamma_{r/e} t$ for long times.

Finally, in section 4.4 we compared decoherence rates of microscopic two-level systems due to different sources of noise. We found that relaxation rates measured in [III] are readily explained by coupling of two-level systems to acoustic phonons. From our analysis it follows that the large ratios and the wide range of ratios between spin-echo and Ramsey dephasing rates, that were observed in the same experiment, can be explained by strong coupling to an individual two-level thermal fluctuator. This thermal fluctuator randomly switches between two configurations inducing a random telegraph noise, which spin-echo effectively filters. By averaging over an ensemble of two-level fluctuators M. Schechter and S. Matityahu found that, while for spin-

echo measurements the ensemble of fluctuators is self-averaging, this does not hold for Ramsey measurements [III, 133], which explains the surprisingly large ratios between measured Ramsey and spin-echo dephasing rates that were observed in the experiment.

In chapter 2 we analyzed decoherence in a perturbed analog quantum simulator, which is used to simulate a fermionic system. In order to simulate the fermionic system on the quantum simulator, it has to be mapped onto the qubits of the quantum simulator. We assume that this mapping is achieved in terms of a Jordan-Wigner transformation. The qubits couple to the environment via different types of noise changing the effective system that is simulated by the quantum simulator.

We used the Jordan-Wigner transformation to map the quantum simulator and its interaction with the environment onto a fermionic system. While the unperturbed quantum simulator maps back onto the fermionic system, that it is supposed to simulate, different types of noise map to different effective perturbations in the fermionic Hamiltonian. Longitudinal coupling of qubits to the environment induces fluctuations of qubit energies and the corresponding perturbation in the fermionic system couples to the occupation number, $V^z \propto c_i^\dagger c_i$. Transversal coupling on the other hand describes the exchange of excitations between qubits and environment. Mapping this type of coupling onto fermions produces fermion source terms $V^x \propto c_i^\dagger + c_i$, which lead to unphysical Hamiltonians that explicitly violate fermion number conservation. We showed that transversal coupling to a fermionic environment or to two-level systems avoids unphysical terms. The effective system, comprising the original fermionic Hamiltonian and additional perturbations arising from the coupling to the environment, $H_{\text{eff}} = H_{\text{system}} + V$, corresponds to the system the perturbed quantum simulator actually mimics in an experiment.

Using fermionic non-equilibrium Green's function methods we calculated the non-equilibrium Green's functions of the perturbed quantum simulator and showed, that the Dyson equation establishes a connection between the results of the ideal quantum simulator and the results obtained from a noisy quantum simulator. The Green's functions obtained via these calculations correspond to the Green's functions of the effective system.

In order to verify our approach, we compared numerical master equation calculations with results derived using the aforementioned fermionic mapping. In this context, we discussed a quantum simulator with nearest neighbor transversal qubit-qubit couplings and longitudinal single qubit terms, which maps onto a non-interacting fermionic system. The quantum simulator is subject to dephasing due to a bosonic environment characterized by a power-law spectral density, or subject to relaxation due to an ensemble of TLS at low temperatures. In all regimes where the master equation approach is valid, that is, regimes where the Born-Markov approximation holds, the results ob-

tained with our method and the results obtained with master equation calculations match exactly.

A quantum simulator can only distinguish features separated by energies larger than the scale defined by its spectral resolution. We applied our method to larger systems and we found that the minimal spectral resolution of a quantum simulator is determined by a frequency dependent rate function $\Gamma(\omega)$ which has the same order of magnitude as the single qubit decoherence rates. Due to size-effects features of a simulated system usually become denser with increasing system size and an effective resolution of a quantum simulator comprising N qubits can be defined as $N \cdot \Gamma(\omega)$. A system characterized by parameters like hopping terms or on-site energies that are smaller than the effective resolution cannot be simulated on such a quantum simulator.

Slow fluctuations of physical parameters of the quantum simulator are described in terms of quenched disorder. Mapping the quantum simulator subject to disorder onto a fermionic system we calculated disorder-averaged Green's functions of the quantum simulator. Usually, perturbation expansions in the disorder strength are inaccurate, especially in one-dimensional systems. For systems subject to decoherence, we found that due to an interplay between decoherence and disorder a self-consistent approach yields accurate results even for strong disorder. We confirmed our calculation by comparing results from our diagrammatic expansion with Monte-Carlo simulations of the quantum simulator. We found good agreement between self-consistently obtained Green's functions and the Monte-Carlo results.

In order to quantitatively understand decoherence in a quantum simulator used to simulate fermionic systems it will be important to analyze effects of decoherence in a quantum simulator with fermion-fermion interaction. As motivated in the last section of chapter 2 we expect that general features found for non-interacting systems remain valid as long as the coupling to the environment remains weak. Furthermore, in recent work J. Reiner found that gate errors in a quantum simulator used to analyze a fermionic system leads to disorder in the fermionic interaction as described in the last part of the chapter. A more detailed analysis of disorder and interacting systems is still ongoing research promising interesting applications for quantum simulation. The findings presented in this chapter are suited to estimate the error of a quantum simulator [VI]. Under certain conditions they might also be used to reconstruct the ideal result from a perturbed quantum simulation [VII].

Bibliography

1. D. Poulin, M. B. Hastings, D. Wecker, A. C. Doherty, N. Wiebe & M. Troyer. Improving quantum algorithms for quantum chemistry. *QIC* **15**, 1–21 (2015) (cit. on p. iii).
2. Foresman, J. B. & Frisch, Æ. *Exploring Chemistry with Electronic Structure Methods* 2nd ed. (Pittsburgh, PA: Gaussian Inc., 1996) (cit. on p. iii).
3. Bednorz, J. G. & Müller, K. A. Possible highTc superconductivity in the Ba–La–Cu–O system. *Z. Phys. B* **64**, 189–193 (1986) (cit. on p. iii).
4. Jiang, W., DeYonker, N. J., Determan, J. J. & Wilson, A. K. Toward Accurate Theoretical Thermochemistry of First Row Transition Metal Complexes. *J. Phys. Chem. A* **116**. doi: 870–885 (2012) (cit. on p. iii).
5. Feynman, R. P. Simulating physics with computers. *Int. J. Theor. Phys.* **21**, 467–488 (1982) (cit. on p. iv).
6. Johnson, T. H., Clark, S. R. & Jaksch, D. What is a quantum simulator? *EPJ Quantum Technol* **1**, 10 (2014) (cit. on p. iv).
7. Buluta, I. & Nori, F. Quantum Simulators. *Science* **326**, 108 (2009) (cit. on p. iv).
8. Cirac, J. I. & Zoller, P. Goals and opportunities in quantum simulation. *Nat. Phys.* **8**, 264–266 (2012) (cit. on p. iv).
9. Lloyd, S. Universal Quantum Simulators. *Science* **273**, 1073 (1996) (cit. on p. iv).
10. Zalka, C. Simulating quantum systems on a quantum computer. *Proc. R. Soc. A* **454**, 313 (1998) (cit. on p. iv).
11. Whitfield, J. D., Biamonte, J. & Aspuru-Guzik, A. Simulation of electronic structure Hamiltonians using quantum computers. *Mol. Phys.* **109**, 735–750 (2011) (cit. on p. iv).
12. Kassal, I., Whitfield, J. D., Perdomo-Ortiz, A., Yung, M.-H. & Aspuru-Guzik, A. Simulating Chemistry Using Quantum Computers. *Annu. Rev. Phys. Chem.* **62**, 185–207 (2011) (cit. on pp. iv, 21).

13. Barends, R., Lamata, L., Kelly, J., Garcia-Alvarez, L., Fowler, A. G., Megrant, A., Jeffrey, E., White, T. C., Sank, D., Mutus, J. Y., *et al.* Digital quantum simulation of fermionic models with a superconducting circuit. *Nat. Commun.* **6**, 7654 (2015) (cit. on pp. iv, 141).
14. Wecker, D., Hastings, M. B., Wiebe, N., Clark, B. K., Nayak, C. & Troyer, M. Solving strongly correlated electron models on a quantum computer. *Phys. Rev. A* **92**, 062318 (2015) (cit. on p. iv).
15. Bauer, B., Wecker, D., Millis, A. J., Hastings, M. B. & Troyer, M. Hybrid Quantum-Classical Approach to Correlated Materials. *Phys. Rev. X* **6**, 031045 (2016) (cit. on pp. iv, 21, 141).
16. Johnson T. H., Biamonte J. D., Clark S. R. & Jaksch D. Solving search problems by strongly simulating quantum circuits. *Scientific Reports* **3**, (2013) (cit. on p. iv).
17. Grover, L. K. A fast quantum mechanical algorithm for database search. *eprint arXiv:quant-ph/9605043*. eprint: quant-ph/9605043 (1996) (cit. on p. iv).
18. Shor, P. W. Polynomial-Time Algorithms for Prime Factorization and Discrete Logarithms on a Quantum Computer. *SIAM Journal on Computing* **26**, 1484–1509 (1997) (cit. on p. iv).
19. Jaksch, D. & Zoller, P. The cold atom Hubbard toolbox. *Ann. Phys* **315**, 52–79 (2005) (cit. on p. iv).
20. Bloch, I., Dalibard, J. & Nascimbene, S. Quantum simulations with ultracold quantum gases. *Nat. Phys.* **8**, 267–276 (2012) (cit. on pp. iv, 141).
21. Blatt, R. & Roos, C. F. Quantum simulations with trapped ions. *Nat. Phys.* **8**, 277–284 (2012) (cit. on pp. iv, 141).
22. Aspuru-Guzik, A. & Walther, P. Photonic quantum simulators. *Nat Phys* **8**, 285–291 (2012) (cit. on p. iv).
23. Makhlin, Y., Schön, G. & Shnirman, A. Quantum-state engineering with josephson-junction devices. *Rev. Mod. Phys.* **73**, 357–400 (2 2001) (cit. on p. iv).
24. Devoret, M. H. & Schoelkopf, R. J. Superconducting circuits for quantum information: an outlook. *Science* **339**, 1169–1174 (2013) (cit. on pp. iv, v).
25. Houck, A. A., E., T. H. & J., K. On-chip quantum simulation with superconducting circuits. *Nat. Phys* **8**, 292–299 (2012) (cit. on pp. iv, 141).
26. Heras, U. L., Mezzacapo, A., Lamata, L., Filipp, S., Wallraff, A. & Solano, E. Digital Quantum Simulation of Spin Systems in Superconducting Circuits. *Phys. Rev. Lett.* **112**, 200501 (20 2014) (cit. on p. iv).

27. Hart, R. A., Duarte, P. M., Yang, T.-L., Liu, X., Paiva, T., Khatami, E., Scalettar, R. T., Trivedi, N., Huse, D. A. & Hulet, R. G. Observation of antiferromagnetic correlations in the Hubbard model with ultracold atoms. *Nature* **519**, 211–214 (2015) (cit. on pp. iv, 141).
28. Navon, N., Nascimbène, S., Chevy, F. & Salomon, C. The Equation of State of a Low-Temperature Fermi Gas with Tunable Interactions. *Science* **328**, 729–732 (2010) (cit. on pp. iv, v).
29. Greif, D., Uehlinger, T., Jotzu, G., Tarruell, L. & Esslinger, T. Short-Range Quantum Magnetism of Ultracold Fermions in an Optical Lattice. *Science* **340**, 1307 (2013) (cit. on pp. iv, 21).
30. Lanyon, B. P., Whitfield, J. D., Gillett, G. G., E., G. M., P., A. M., Kassal, I., Biamonte, J., Mohseni, M., Powell, B. J., Barbieri, M., *et al.* Towards quantum chemistry on a quantum computer. *Nat Chem* **2**, 106–111 (2010) (cit. on p. v).
31. Barends, R., Shabani, A., Lamata, L., Kelly, J., Mezzacapo, A., Heras, U. L., Babbush, R., Fowler, A. G., Campbell, B., Chen, Y., *et al.* Digitized adiabatic quantum computing with a superconducting circuit. *Nature* **534**, 222–226 (2016) (cit. on pp. iv, 21).
32. Hauke, P., Cucchiatti, F. M., Tagliacozzo, L., Deutsch, I. & Lewenstein, M. Can one trust quantum simulators? *Rep. Prog. Phys.* **75**, 082401 (2012) (cit. on pp. iv, v, 21, 141).
33. Barends, R., Kelly, J., Megrant, A., Veitia, A., Sank, D., Jeffrey, E., White, T. C., Mutus, J., Fowler, A. G., Campbell, B., *et al.* Superconducting quantum circuits at the surface code threshold for fault tolerance. *Nature* **508**, 500–503 (2014) (cit. on pp. v, 82, 141).
34. Simmonds, R. W., Lang, K. M., Hite, D. A., Nam, S., Pappas, D. P. & Martinis, J. M. Decoherence in Josephson Phase Qubits from Junction Resonators. *Phys. Rev. Lett.* **93**, 077003 (7 2004) (cit. on pp. vi, 82, 93, 99).
35. Phillips, W. Tunneling states and the low-temperature thermal expansion of glasses. *Journal of Low Temperature Physics* **11**, 757–763 (1973) (cit. on pp. vi, 81, 83, 141).
36. Anderson, P. W., Halperin, B. I. & Varma, C. M. Anomalous low-temperature thermal properties of glasses and spin glasses. *Philosophical Magazine* **25**, 1–9 (1972) (cit. on pp. vi, 81, 83, 128, 131, 141).

37. Gunnarsson, D., Pirkkalainen, J.-M., Li, J., Paraoanu, G. S., Hakonen, P., Sil-lanpää, M. & Prunnila, M. Dielectric losses in multi-layer Josephson junction qubits. *Superconductor Science and Technology* **26**, 085010 (2013) (cit. on pp. vi, 82).
38. DuBois, T. C., Russo, S. P. & Cole, J. H. Atomic delocalization as a microscopic origin of two-level defects in Josephson junctions. *New J. Phys.* **17**, 023017 (2015) (cit. on pp. vi, 82).
39. Holder, A. M., Osborn, K. D., Lobb, C. J. & Musgrave, C. B. Bulk and Surface Tunneling Hydrogen Defects in Alumina. *Phys. Rev. Lett.* **111**, 065901 (6 2013) (cit. on pp. vi, 82).
40. De Sousa, R., Whaley, K. B., Hecht, T., von Delft, J. & Wilhelm, F. K. Mi-croscopic model of critical current noise in Josephson-junction qubits: Subgap resonances and Andreev bound states. *Phys. Rev. B* **80**, 094515 (9 2009) (cit. on pp. vi, 82).
41. Lisenfeld, J., Müller, C., Cole, J. H., Bushev, P., Lukashenko, A., Shnirman, A. & Ustinov, A. V. Rabi spectroscopy of a qubit-fluctuator system. *Phys. Rev. B* **81**, 100511 (10 2010) (cit. on pp. vi, 82).
42. Grabovskij, G. J., Peichl, T., Lisenfeld, J., Weiss, G. & Ustinov, A. V. Strain Tuning of Individual Atomic Tunneling Systems Detected by a Superconducting Qubit. *Science* **338**, 232–234 (2012) (cit. on pp. vi, 82, 87, 89, 90, 93, 142).
43. Lisenfeld, J., Müller, C., Cole, J. H., Bushev, P., Lukashenko, A., Shnirman, A. & Ustinov, A. V. Measuring the Temperature Dependence of Individual Two-Level Systems by Direct Coherent Control. *Phys. Rev. Lett.* **105**. Hiess vorher 'CoherentControl', 230504 (23 2010) (cit. on pp. vi, 83, 87, 89, 90, 93, 118, 119, 142).
44. Black, J. L. & Gyorffy, B. L. Interaction of the Conduction Electrons with Tunneling States in Metallic Glasses. *Phys. Rev. Lett.* **41**, 1595–1598 (23 1978) (cit. on pp. vi, 93, 96, 112, 142).
45. Rammer, J. & Smith, H. Quantum field-theoretical methods in transport theory of metals. *Rev. Mod. Phys.* **58**, 323 (1986) (cit. on pp. 3, 13, 14, 35).
46. Stefanucci, G. & van Leeuwen, R. *Nonequilibrium Many-Body Theory of Quantum Systems* (Cambridge University Press, 2013) (cit. on pp. 3, 4, 7, 8, 12, 51, 53).
47. Wick, G. C. The Evaluation of the Collision Matrix. *Phys. Rev.* **80**, 268–272 (1950) (cit. on p. 7).

48. Martin, P. C. & Schwinger, J. Theory of Many-Particle Systems. I. *Phys. Rev.* **115**, 1342–1373 (1959) (cit. on pp. 7, 8).
49. Kubo, R. Statistical-Mechanical Theory of Irreversible Processes. I. General Theory and Simple Applications to Magnetic and Conduction Problems. *Journal of the Physical Society of Japan* **12**. doi: 10.1143/JPSJ.12.570, 570–586 (1957) (cit. on p. 8).
50. Abrikosov, A. a., Gorkov, L. P. & Dzyaloshinski, I. E. *Methods of Quantum Field Theory in Statistical Physics* (Dover Books on Physics, 1975) (cit. on p. 8).
51. Altland, A. & Simons, B. *Condensed Matter Field Theory* (Cambridge University Press, Cambridge, 2006) (cit. on pp. 8, 15, 24).
52. Langreth, D. C. & Wilkins, J. W. Theory of Spin Resonance in Dilute Magnetic Alloys. *Phys. Rev. B* **6**, 3189–3227 (9 1972) (cit. on p. 12).
53. Larkin, A. L. & Ovchinnikov, Y. N. Nonlinear conductivity of superconductors in the mixed state. *JETP* **41**, 960 (1975) (cit. on p. 13).
54. Kamenev, A. (Cambridge University Press, 2011) (cit. on pp. 14, 15, 29, 59).
55. Gell-Mann, M. & Low, F. Bound States in Quantum Field Theory. *Phys. Rev.* **84**, 350–354 (1951) (cit. on p. 15).
56. Mills, R. *Propagators For Many Particle* (Gordon and Breach, New York, 1969) (cit. on p. 15).
57. Hall, A. G. Non-equilibrium Green functions: generalized Wick’s theorem and diagrammatic perturbation with initial correlations. *Journal of Physics A: Mathematical and General* **8**, 214 (1975) (cit. on p. 15).
58. Keldysh, L. V. Diagram Technique for Nonequilibrium Processes. *Sov.Phys.JETP.* **20**, 1018 (1965) (cit. on p. 15).
59. Lanyon, B. P., Hempel, C., Nigg, D., Müller, M., Gerritsma, R., Zähringer, F., Schindler, P., Barreiro, J. T., Rambach, M., Kirchmair, G., *et al.* Universal Digital Quantum Simulation with Trapped Ions. *Science* **334**, 57 (2011) (cit. on p. 21).
60. Wecker, D., Bauer, B., Clark, B. K., Hastings, M. B. & Troyer, M. Gate-count estimates for performing quantum chemistry on small quantum computers. *Phys. Rev. A* **90**, 022305 (2 2014) (cit. on p. 21).
61. Reiner, J.-M., Marthaler, M., Braumüller, J., Weides, M. & Schön, G. Emulating the one-dimensional Fermi-Hubbard model by a double chain of qubits. *Phys. Rev. A* **94**, 032338 (3 2016) (cit. on pp. 21, 28, 141).

62. Mei, F., Stojanović, V. M., Siddiqi, I. & Tian, L. Analog superconducting quantum simulator for Holstein polarons. *Phys. Rev. B* **88**, 224502 (2013) (cit. on p. 21).
63. Trotzky, S., Chen, Y.-A., Flesch, A., McCulloch, I. P., Schollwöck, U., Eisert, J. & Bloch, I. Probing the relaxation towards equilibrium in an isolated strongly correlated one-dimensional Bose gas. *Nat. Phys.* **8**, 325–330 (2012) (cit. on p. 21).
64. Wenz, A. N., Zürn, G., Murmann, S., Brouzos, I., Lompe, T. & Jochim, S. From Few to Many: Observing the Formation of a Fermi Sea One Atom at a Time. *Science* **342**, 457 (2013) (cit. on p. 21).
65. Friedenauer, A., Schmitz, H., Glueckert, J. T., Porras, D. & Schaetz, T. Simulating a quantum magnet with trapped ions. *Nat. Phys.* **4**, 757–761 (2008) (cit. on p. 21).
66. Carmichael, H. J. *Statistical Methods in Quantum Optics 1: Master Equations and Fokker-Planck Equations* (eds Balian, R., Beiglböck, W., Grosse, H., Lieb, E., Reshetikhin, N., Spohn, H. & Thirring, W.) (Springer, 2002) (cit. on pp. 22, 24, 44, 74, 133).
67. Du, L.-H., You, J. Q. & Tian, L. Superconducting circuit probe for analog quantum simulators. *Phys. Rev. A* **92**, 012330 (1 2015) (cit. on pp. 22, 141).
68. Tian, L., Schwenk, I. & Marthaler, M. Detector Readout of Analog Quantum Simulators. *ArXiv e-prints*, (2016) (cit. on p. 22).
69. Almog, I., Loewenthal, G., Coslovsky, J., Sagi, Y. & Davidson, N. Dynamic decoupling in the presence of colored control noise. *Phys. Rev. A* **94**, 042317 (4 2016) (cit. on p. 22).
70. Schad, P., Makhlin, Y., Narozhny, B., Schön, G. & Shnirman, A. Majorana representation for dissipative spin systems. *Ann. Phys.* **361**, 401–422 (2015) (cit. on pp. 24, 26).
71. Mills, R., Kenan, R. & Korrington, J. Perturbation theory of antiferromagnetism. *Physica* **26**, S204–S214 (1960) (cit. on p. 26).
72. Wang Yung-Li, Shtrikman S. & Callen Herbert. Wick’s Theorem for Spin- $\frac{1}{2}$ Operators, with an Application to Spin Waves in Antiferromagnets. *Phys. Rev.* **148**, 419–432 (1966) (cit. on p. 26).
73. Jordan, P. & Wigner, E. Über das Paulische Äquivalenzverbot. *ZS. f. Phys.* **47**, 631–651 (1928) (cit. on p. 26).

-
74. Affleck Ian, Zou Z., Hsu T. & Anderson P. W. SU(2) gauge symmetry of the large- U limit of the Hubbard model. *Phys. Rev. B* **38**, 745–747 (1988) (cit. on p. 26).
 75. Dagotto Elbio, Fradkin Eduardo & Moreo Adriana. SU(2) gauge invariance and order parameters in strongly coupled electronic systems. *Phys. Rev. B* **38**, 2926–2929 (1988) (cit. on p. 26).
 76. Martin, J. L. Generalized Classical Dynamics, and the 'Classical Analogue' of a Fermi Oscillator. *Proceedings of the Royal Society of London. Series A. Mathematical and Physical Sciences* **251**, 536 (1959) (cit. on p. 26).
 77. Bravyi, S. B. & Kitaev, A. Y. Fermionic Quantum Computation. *Ann. Phys.* **298**, 210–226 (2002) (cit. on p. 26).
 78. Leggett, A. J., Chakravarty, S., Dorsey, A. T., Fisher, M. P. A., Garg, A. & Zwerger, W. Dynamics of the dissipative two-state system. *Rev. Mod. Phys.* **59**, 1–85 (1 1987) (cit. on pp. 33, 130).
 79. Ithier, G., Collin, E., Joyez, P., Meeson, P. J., Vion, D., Esteve, D., Chiarello, F., Shnirman, A., Makhlin, Y., Schrieffer, J., *et al.* Decoherence in a superconducting quantum bit circuit. *Phys. Rev. B* **72**, 134519 (13 2005) (cit. on p. 33).
 80. Catelani, G., Nigg, S. E., Girvin, S. M., Schoelkopf, R. J. & Glazman, L. I. Decoherence of superconducting qubits caused by quasiparticle tunneling. *Phys. Rev. B* **86**, 184514 (18 2012) (cit. on pp. 41, 93, 142).
 81. Johansson, J., Nation, P. & Nori, F. QuTiP 2: A Python framework for the dynamics of open quantum systems. *Comput. Phys. Commun.* **184**, 1234–1240 (2013) (cit. on p. 44).
 82. Martin, I., Bulaevskii, L. & Shnirman, A. Tunneling Spectroscopy of Two-Level Systems Inside a Josephson Junction. *Phys. Rev. Lett.* **95**, 127002 (2005) (cit. on pp. 75, 87).
 83. Bylander, J., Gustavsson, S., Yan, F., Yoshihara, F., Harrabi, K., Fitch, G., Cory, D. G., Nakamura, Y., Tsai, J.-S. & Oliver, W. D. Noise spectroscopy through dynamical decoupling with a superconducting flux qubit. *Nat Phys* **7**, 565–570 (2011) (cit. on pp. 75, 77).
 84. Uhrig, G. S. Keeping a Quantum Bit Alive by Optimized π -Pulse Sequences. *Phys. Rev. Lett.* **98**, 100504 (2007) (cit. on pp. 75, 77).
 85. Zeller, R. C. & Pohl, R. O. Thermal Conductivity and Specific Heat of Non-crystalline Solids. *Phys. Rev. B* **4**, 2029–2041 (6 1971) (cit. on p. 81).
 86. Esquinazi, P. *Tunneling Systems in Amorphous and Crystalline Solids* (Springer, 1998) (cit. on pp. 81–84, 130, 131).

87. Zimmerman, J. & Weber, G. On the excess specific heat of vitreous silica at low temperatures. *Physics Letters A* **86**, 32–34 (1981) (cit. on p. 82).
88. Sahling, S. Low temperature long-time energy relaxation in LiCl 7H₂O. *Solid State Communications* **72**, 497–500 (1989) (cit. on p. 82).
89. Nittke, A., Scherl, M., Esquinazi, P., Lorenz, W., Li, J. & Pobell, F. Low temperature heat release, sound velocity and attenuation, specific heat and thermal conductivity in polymers. *Journal of Low Temperature Physics* **98**, 517–547 (1995) (cit. on p. 82).
90. White, B. & Pohl, R. Elastic properties of amorphous solids below 100 K. *Zeitschrift für Physik B Condensed Matter* **100**, 401–408 (1997) (cit. on p. 82).
91. Topp, K. & Cahill, D. G. Elastic properties of several amorphous solids and disordered crystals below 100 K. *Zeitschrift für Physik B Condensed Matter* **101**, 235–245 (1996) (cit. on p. 82).
92. Martinis, J. M., Cooper, K. B., McDermott, R., Steffen, M., Ansmann, M., Osborn, K. D., Cicak, K., Oh, S., Pappas, D. P., Simmonds, R. W., *et al.* Decoherence in josephson qubits from dielectric loss. *Phys. Rev. Lett.* **95**, 210503 (21 2005) (cit. on pp. 82, 87, 93, 99).
93. Faoro, L. & Ioffe, L. B. Internal Loss of Superconducting Resonators Induced by Interacting Two-Level Systems. *Phys. Rev. Lett.* **109**, 157005 (15 2012) (cit. on p. 82).
94. Cole, J. H., Müller, C., Bushev, P., Grabovskij, G. J., Lisenfeld, J., Lukashenko, A., Ustinov, A. V. & Shnirman, A. Quantitative evaluation of defect-models in superconducting phase qubits. *Appl. Phys. Lett.* **97**, 252501 (2010) (cit. on p. 82).
95. Müller, C., Lisenfeld, J., Shnirman, A. & Poletto, S. Interacting two-level defects as sources of fluctuating high-frequency noise in superconducting circuits. *Phys. Rev. B* **92**, 035442 (3 2015) (cit. on p. 82).
96. Wang, C., Gao, Y., Pop, I., Vool, U., Axline, C., Brecht, T., Heeres, R., Frunzio, L., Devoret, M., Catelani, G., *et al.* Measurement and Control of Quasiparticle Dynamics in a Superconducting Qubit. *ArXiv e-prints*. arXiv: 1406.7300v1 [quant-ph] (2014) (cit. on p. 83).
97. Sun, L., DiCarlo, L., Reed, M. D., Catelani, G., Bishop, L. S., Schuster, D. I., Johnson, B. R., Yang, G. A., Frunzio, L., Glazman, L., *et al.* Measurements of Quasiparticle Tunneling Dynamics in a Band-Gap-Engineered Transmon Qubit. *Phys. Rev. Lett.* **108**, 230509 (23 2012) (cit. on p. 83).

98. Shaw, M. D., Lutchyn, R. M., Delsing, P. & Echternach, P. M. Kinetics of nonequilibrium quasiparticle tunneling in superconducting charge qubits. *Phys. Rev. B* **78**, 024503 (2 2008) (cit. on p. 83).
99. Pop, I. M., Geerlings, K., Catelani, G., Schoelkopf, R. J., Glazman, L. I. & Devoret, M. H. Coherent suppression of electromagnetic dissipation due to superconducting quasiparticles. *Nature* **508**, 369–372 (2014) (cit. on pp. 83, 142).
100. Martinis, J. M., Ansmann, M. & Aumentado, J. Energy Decay in Superconducting Josephson-Junction Qubits from Nonequilibrium Quasiparticle Excitations. *Phys. Rev. Lett.* **103**, 097002 (9 2009) (cit. on pp. 83, 93).
101. Lutchyn, R., Glazman, L. & Larkin, A. Quasiparticle decay rate of Josephson charge qubit oscillations. *Phys. Rev. B* **72**, 014517 (1 2005) (cit. on pp. 83, 93).
102. Lenander, M., Wang, H., Bialczak, R. C., Lucero, E., Mariani, M., Neeley, M., O’Connell, A. D., Sank, D., Weides, M., Wenner, J., *et al.* Measurement of energy decay in superconducting qubits from nonequilibrium quasiparticles. *Phys. Rev. B* **84**, 024501 (2 2011) (cit. on pp. 83, 142).
103. Catelani, G. Parity switching and decoherence by quasiparticles in single-junction transmons. *Phys. Rev. B* **89**, 094522 (9 2014) (cit. on p. 83).
104. Vladár, K. & Zawadowski, A. Theory of the interaction between electrons and the two-level system in amorphous metals. I. Noncommutative model Hamiltonian and scaling of first order. *Phys. Rev. B* **28**, 1564–1581 (3 1983) (cit. on pp. 84, 93, 96).
105. Cole, J. Personal Correspondence. 2016 (cit. on p. 84).
106. Catelani, G., Schoelkopf, R. J., Devoret, M. H. & Glazman, L. I. Relaxation and frequency shifts induced by quasiparticles in superconducting qubits. *Phys. Rev. B* **84**, 064517 (6 2011) (cit. on pp. 88, 89).
107. Leppäkangas, J. & Marthaler, M. Fragility of flux qubits against quasiparticle tunneling. *Phys. Rev. B* **85**, 144503 (14 2012) (cit. on pp. 88, 93, 142).
108. Kondo, J. Localized atomic states in metals. *Physica B+C* **84**, 40–49 (1976) (cit. on pp. 93, 96, 112, 113).
109. Black, J. L., Gyorffy, B. L. & Jäckle, J. On the resistivity due to two-level systems in metallic glasses. *Philosophical Magazine Part B* **40**, 331–334 (1979) (cit. on pp. 93, 113, 114).
110. Korringa, J. Nuclear magnetic relaxation and resonance line shift in metals. *Physica* **16**, 601–610 (1950) (cit. on p. 93).

111. Golding, B., Graebner, J. E., Kane, A. B. & Black, J. L. Relaxation of Tunneling Systems by Conduction Electrons in a Metallic Glass. *Phys. Rev. Lett.* **41**, 1487–1491 (21 1978) (cit. on pp. 93, 114).
112. Jäckle, J. On the ultrasonic attenuation in glasses at low temperatures. *Zeitschrift für Physik* **257**, 212–223 (1972) (cit. on pp. 93, 128, 130, 131).
113. Kondo, J. Localized atomic states in metals. II. Resistivity and free energy. *Physica B+C* **84**, 207–212 (1976) (cit. on p. 93).
114. Weiss, G. & Golding, B. Phonon Echoes in Superconducting Amorphous Pd₃₀Zr₇₀. *Phys. Rev. Lett.* **60**, 2547–2550 (24 1988) (cit. on p. 93).
115. Morr, W., Müller, A., Weiss, G., Wipf, H. & Golding, B. Isotope dependence of hydrogen tunneling in niobium. *Phys. Rev. Lett.* **63**, 2084–2087 (19 1989) (cit. on p. 93).
116. Olivares, D. G., Yeyati, A. L., Bretheau, L., Girit, C. Ö., Pothier, H. & Urbina, C. Dynamics of quasiparticle trapping in Andreev levels. *Phys. Rev. B* **89**, 104504 (10 2014) (cit. on p. 93).
117. Heimes, A. *Non-equilibrium quasiparticles and topological excitations in hybrid superconducting structures* Phd Thesis (Karlsruhe Institute of Technology, 2014) (cit. on p. 97).
118. Schmid, A. & Schön, G. Linearized kinetic equations and relaxation processes of a superconductor near T_c . *Journal of Low Temperature Physics* **20**, 207–227 (1975) (cit. on p. 98).
119. Chang, J.-J. & Scalapino, D. J. Kinetic-equation approach to nonequilibrium superconductivity. *Phys. Rev. B* **15**, 2651–2670 (5 1977) (cit. on pp. 99, 100, 104, 105).
120. Kaplan, S. B., Chi, C. C., Langenberg, D. N., Chang, J. J., Jafarey, S. & Scalapino, D. J. Quasiparticle and phonon lifetimes in superconductors. *Phys. Rev. B* **14**, 4854–4873 (11 1976) (cit. on pp. 100, 104).
121. Dittrich, T., Hänggi, P., Ingold, G.-L., Kramer, B., Schön, G. & Zwirger, W. in. And references within. Chap. 3. Single-Electron Tunneling (Wiley-VCH, 1998) (cit. on p. 119).
122. Schrieffer, J., Makhlin, Y., Shnirman, A. & Schön, G. Decoherence from ensembles of two-level fluctuators. *New J. Phys.* **8**. former MSS06, 1 (2006) (cit. on pp. 128, 135–138).
123. Black, J. L. & Halperin, B. I. Spectral diffusion, phonon echoes, and saturation recovery in glasses at low temperatures. *Phys. Rev. B* **16**, 2879–2895 (6 1977) (cit. on pp. 128, 131).

124. Kittel, C. *Quantum Theory of Solids* (Wiley, New York, 1963) (cit. on p. 130).
125. Burin, A. L. Dipole gap effects in low energy excitation spectrum of amorphous solids. Theory for dielectric relaxation. *Journal of Low Temperature Physics* **100**, 309–337 (1995) (cit. on p. 133).
126. Grannan, E. R., Randeria, M. & Sethna, J. P. Low-temperature properties of a model glass. I. Elastic dipole model. *Phys. Rev. B* **41**, 7784–7798 (11 1990) (cit. on p. 133).
127. Burin, A. L. & Kagan, Y. Low-energy collective excitations in glasses. New relaxation mechanism for ultralow temperatures. *JETP* **80**, 761 (1994) (cit. on p. 133).
128. Shnirman, A., Schön, G., Martin, I. & Makhlin, Y. Low- and High-Frequency Noise from Coherent Two-Level Systems. *Phys. Rev. Lett.* **94**, 127002 (12 2005) (cit. on pp. 133, 134).
129. Shnirman, A., Makhlin, Y. & Schön, G. Noise and Decoherence in Quantum Two-Level Systems. *Physica Scripta* **2002**, 147 (2002) (cit. on p. 136).
130. Galperin, Y. M., Altshuler, B. L., Bergli, J. & Shantsev, D. V. Non-Gaussian Low-Frequency Noise as a Source of Qubit Decoherence. *Phys. Rev. Lett.* **96**, 097009 (9 2006) (cit. on p. 138).
131. Hu, P. & Hartmann, S. R. Theory of spectral diffusion decay using an uncorrelated-sudden-jump model. *Phys. Rev. B* **9**, 1–13 (1 1974) (cit. on p. 138).
132. Paladino, E., Faoro, L., Falci, G. & Fazio, R. Decoherence and $1/f$ Noise in Josephson Qubits. *Phys. Rev. Lett.* **88**, 228304 (22 2002) (cit. on p. 138).
133. Matityahu, S., Shnirman, A., Schön, G. & Schechter, M. Decoherence of a quantum two-level system by spectral diffusion. *Phys. Rev. B* **93**, 134208 (13 2016) (cit. on pp. 140, 144).
134. Zohar, E., Cirac, J. I. & Reznik, B. Quantum simulations of gauge theories with ultracold atoms: Local gauge invariance from angular-momentum conservation. *Phys. Rev. A* **88**, 023617 (2013) (cit. on p. 141).
135. Dallaire-Demers, P.-L. & Wilhelm, F. K. Method to efficiently simulate the thermodynamic properties of the Fermi-Hubbard model on a quantum computer. *Phys. Rev. A* **93**, 032303 (3 2016) (cit. on p. 141).
136. Sarovar, M., Zhang, J. & Zeng, L. Reliability of analog quantum simulation. *EPJ Quantum Technol* **4**, 1 (2017) (cit. on p. 141).

